13

RADC-TR-83-51
Final Technical Report

AD-A133 411

ACOSS FOURTEEN (ACTIVE CONTROL OF SPACE STRUCTURES)

TRW

Sponsored by
Defense Advanced Research Projects Agency (DOD)
ARPA Order No. 3654

APPROVED FOR PUBLIC RELEASE; DISTRIBUTION UNLIMITED

The views and conclusions contained in this document are those of the authors and should not be interpreted as necessarily representing the official policies, either expressed or implied, of the Defense Advanced Research Projects Agency or the U.S. Government.

DTIC ELECTE OCT 1 1 1983 S A D

ROME AIR DEVELOPMENT CENTER
Air Force Systems Command
Griffiss Air Force Base, NY 13441

83 10 04 073

This report has been reviewed by the RADC Public Affairs Office (PA) and is releasable to the National Technical Information Service (NTIS). At NTIS it will be releasable to the general public, including foreign nations.

RADC-TR-83-51 has been reviewed and is approved for publication.

APPROVED: Richard W. Carman

RICHARD W. CARMAN
Project Engineer

APPROVED: Louis E. White

LOUIS E. WHITE, Lt Col, USAF
Chief, Surveillance Division

FOR THE COMMANDER: John P. Huss

JOHN P. HUSS
Acting Chief, Plans Office

If your address has changed or if you wish to be removed from the RADC mailing list, or if the addressee is no longer employed by your organization, please notify RADC (OCSE) Griffiss AFB NY 13441. This will assist us in maintaining a current mailing list.

Do not return copies of this report unless contractual obligations or notices on a specific document requires that it be returned.

ACOSS FOURTEEN (ACTIVE CONTROL OF SPACE STRUCTURES)

Robert J. Benhabib
Henry K. Flashner
Frank C. Tung

Contractor: TRW
Contract Number: F30602-81-C-0194
Effective Date of Contract: 23 June 1981
Contract Expiration Date: 30 October 1982
Short Title of Work: ACOSS Fourteen (Active Control of Space Structures)
Program Code Number: 2E20
Period of Work Covered: Jun 81 - Oct 82

Principal Investigator: Robert J. Benhabib
Phone: 213 536-1871

Project Engineer: Richard W. Carman
Phone: 315 330-3148

Approved for public release; distribution unlimited.

This research was supported by the Defense Advanced Research Projects Agency of the Department of Defense and was monitored by Richard W. Carman (RADC/OCSE), Griffiss AFB NY 13441 under Contract F30602-81-C-0194.

UNCLASSIFIED

SECURITY CLASSIFICATION OF THIS PAGE (When Data Entered)

REPORT DOCUMENTATION PAGE		READ INSTRUCTIONS BEFORE COMPLETING FORM
1. REPORT NUMBER RADC-TR-83-51	2. GOVT ACCESSION NO.	3. RECIPIENT'S CATALOG NUMBER
4. TITLE (and Subtitle) ACOSS FOURTEEN (ACTIVE CONTROL OF SPACE STRUCTURES)		5. TYPE OF REPORT & PERIOD COVERED Final Technical Report 23 Jun 81 - 30 Oct 82
		6. PERFORMING ORG. REPORT NUMBER N/A
7. AUTHOR(s) Robert J. Benhabib Henry K. Flashner Frank C. Tung		8. CONTRACT OR GRANT NUMBER(s) F30602-81-C-0194
9. PERFORMING ORGANIZATION NAME AND ADDRESS TRW One Space Park Redondo Beach CA 90278		10. PROGRAM ELEMENT, PROJECT, TASK AREA & WORK UNIT NUMBERS 62301E C6540114
11. CONTROLLING OFFICE NAME AND ADDRESS Defense Advanced Research Projects Agency 1400 Wilson Blvd Arlington VA 22209		12. REPORT DATE March 1983
		13. NUMBER OF PAGES 282
14. MONITORING AGENCY NAME & ADDRESS(if different from Controlling Office) Rome Air Development Center (OCSE) Griffiss AFB NY 13441		15. SECURITY CLASS. (of this report) UNCLASSIFIED
		15a. DECLASSIFICATION/DOWNGRADING SCHEDULE N/A

16. DISTRIBUTION STATEMENT (of this Report)

Approved for public release; distribution unlimited.

17. DISTRIBUTION STATEMENT (of the abstract entered in Block 20, if different from Report)

Same

18. SUPPLEMENTARY NOTES

RADC Project Engineer: Richard W. Carman (OCSE)

19. KEY WORDS (Continue on reverse side if necessary and identify by block number)

Control Theory
Large Space Structure
Structural Dynamics
Flexible Vehicles
On-Orbit Testing
Noncolocated Control Design

20. ABSTRACT (Continue on reverse side if necessary and identify by block number)

ACOSS Fourteen is one of a series of studies for the development of a unified structural dynamics and control technology base to support future development of large space systems. The major emphasis in these studies in the past has been on generic control law development for active vibration suppression. The emphasis is now shifting towards hardware development and experimental verification of the technology. ACOSS Fourteen studies the definition, design and plan for an on-orbit, Shuttle-based

DD FORM 1 JAN 73 1473 EDITION OF 1 NOV 65 IS OBSOLETE

UNCLASSIFIED

SECURITY CLASSIFICATION OF THIS PAGE (When Data Entered)

Proof of Concept demonstration and stability enduring designs which extend previous designs and treat noncolocated actuator-sensor control systems, while remaining insensitive to modal truncation and inaccurate structural models.

ACKNOWLEDGEMENT

This work was performed by TRW Space and Technology Group under Contract No. F30602-81-C-0194 for the U.S. Government. The research was sponsored by the Defense Advanced Research Projects Agency (DARPA) of the Department of Defense and was monitored by the Rome Air Development Center (RADC), Air Force Systems Command. This final technical report covers the period from June 1981 through October 1982. The technical monitors of this program were Lt. Col. A. Herzberg (DARPA) and Mr. R. Carman (RADC).

The program manager at TRW was Mr. Robert J. Benhabib. This study was performed within the Control Systems Engineering Department of TRW's Spacecraft Engineering Division. The Control Systems Engineering Department is managed by Mr. D. P. Hoffman.

The contributors to this report are:

Mr. Robert J. Benhabib:	Sections 1, 2, 3, 6.0 to 6.2, 7, 8.0 to 8.3, Appendices A, B, and D
Dr. Henryk Flashner:	Sections 4, 5, 6.3, 8.4, 9, Appendix C
Dr. Frank C. Tung:	Section 6.4

TABLE OF CONTENTS

TABLE OF CONTENTS (Continued)

TABLE OF CONTENTS (Continued)

TABLE OF CONTENTS (Continued)

TABLE OF CONTENTS (Continued)

LIST OF FIGURES

LIST OF FIGURES (Continued)

LIST OF FIGURES (Continued)

LIST OF TABLES

LIST OF TABLES (Continued)

1.0 INTRODUCTION AND SUMMARY

1.1 Background

Future DoD large space system concepts such as High Altitude Large Optics (HALO), High Energy Laser Optics (HELO) and Millimeter (MM) Wave applications have stringent line-of-sight (LOS) pointing and jitter performance requirements which cannot readily be met with existing technology. These systems of interest have common features in terms of their large size, extreme complexity, low mass, low stiffness and precision structural tolerances. Under the Active Control of Space Structures (ACOSS) Program, the Defense Advanced Research Projects Agency (DARPA) has sponsored a number of studies for the development of a unified structural dynamics and control technology base to support the future development of these large space system missions. The major emphasis in these studies in the past has been placed on generic control law development for active vibration suppression. However, the emphasis is now shifting towards hardware development and experimental verification of the technology.

This document reports the results of one of these studies, namely ACOSS-14, conducted by TRW Space and Technology Group for DARPA from June 1981 through October 1982. The study addressed two areas of interest:

- PREMOD Contract - the definition, design and plan for an on-orbit, Shuttle-based Proof-of-Concept demonstration
- MOD Contract - stability ensuring designs which extend to treat noncolocated actuator-sensor control systems, while remaining insensitive to modal truncation/inaccurate structural models.

1.2 Summary of PREMOD Contract

One of the challenges in active control of large space structures (LSS) is to assure the stability and performance of structural control system designs. The problem stems from the relation between modeling information and performance. Generally, the control system must make up for increasing modeling uncertainty by commensurately giving up performance. In the systems of interest, the requirement for performance in the presence of uncertainty is carried to an extreme. First, the finite element methods currently used to predict structural behavior truncate and provide poor knowledge of the

structural modal frequencies, shapes and damping. Moreover, they do not account for nonlinear structural behavior effects which can often dominate behavior. Second, the desired performance levels are sub μrad for precision pointing and sub μm for structural control. Under DARPA sponsorship, it is currently believed that the control theory required to simultaneously satisfy these requirements has been developed but it has not been experimentally demonstrated. Therefore, it has become evident that hardware tests are needed to verify the existing results.

The objectives of the ACOSS-14 PREMOD study were to define, design and plan an on-orbit experiment to further develop DARPA's understanding of generic structural dynamics and control of LSS. The primary reason for wanting to conduct the tests on-orbit is the realization that currently neither analysis nor the combination of analysis and ground test data predicts the on-orbit behavior of a structure well enough to establish that the desired on-orbit performance goals can be met. Also, for large and flexible structures, ground tests are not always feasible. Therefore, since verifying performance is of utmost importance to DARPA, on-orbit tests have two immediate goals. One is to learn how to make accurate structural models. The other is to verify that the performance objectives can be met.

The major results of the PREMOD study were: the identification of the set of experiments needed to meet the modeling and performance verification goals; the selection and design of a simple, moderately priced structure which can be used as the test bed for executing these experiments; and the analytical verification that the chosen structure and experiment concept are feasible and compatible.

Figure 1-1 and Table 1-1 show and summarize the key features of the resulting experiment system. The distinguishing characteristic of the concept is its capability to provide data necessary for modeling of future spacecraft of interest, while demonstrating a technology

1.3 PREMOD Contract Conclusions/Recommendations

This study shows that a moderately priced, on-orbit experiment system can be designed to provide the data necessary to design future surveillance and weapon systems. The key ingredient to keeping the cost down is an

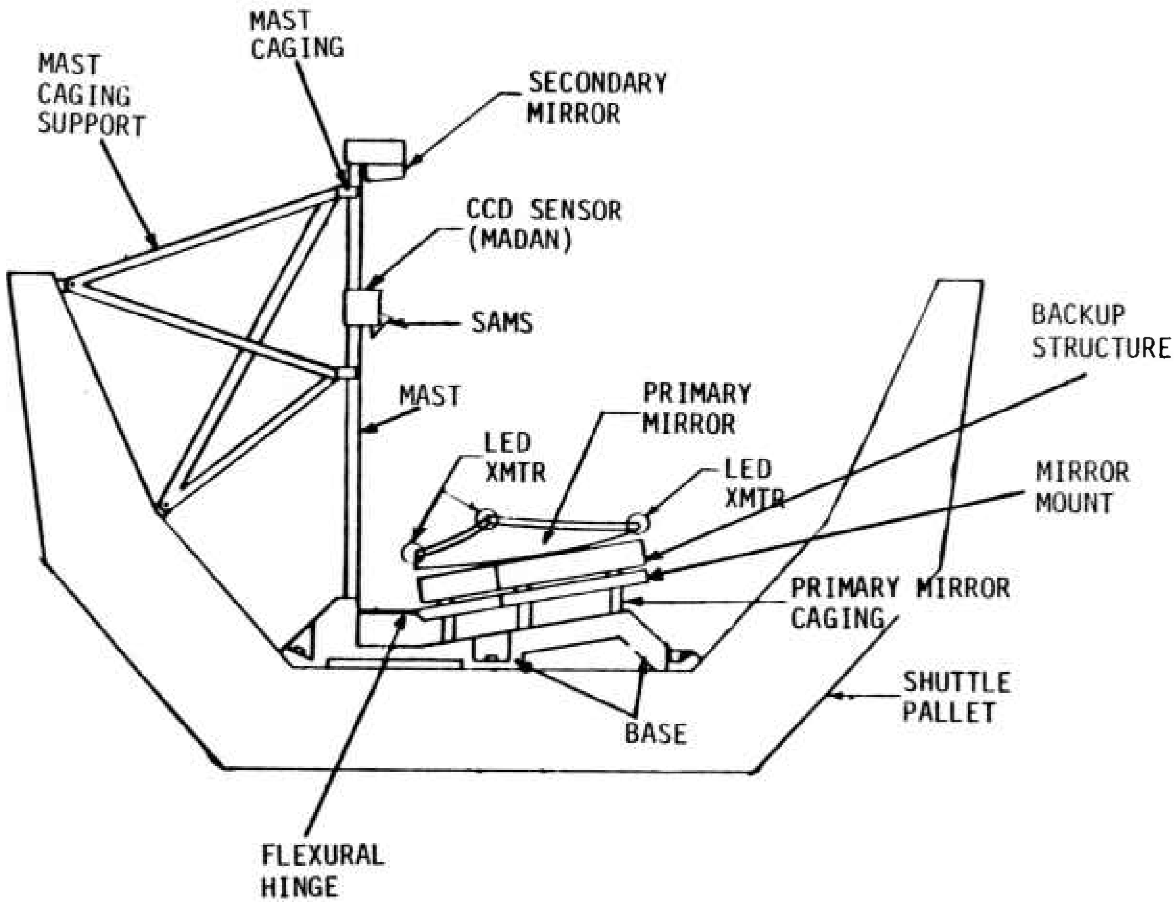

Figure 1-1. Baseline Offset Cassegrain Telescope Test Structure

Table 1-1. Salient Features of Baseline Offset Cassegrain Telescope Experiment System

Provides the data necessary to design future surveillance and weapon systems

- Modeling verification/extrapolation objectives are met together with a technology demonstration
- Maximum use of existing hardware is made
- Fits comfortably on one Shuttle pallet
- Program lasts for 4 years
- Estimated cost is $43.5M (1982 $)

Key Features and Capabilities:

- Ground and on-orbit experiments are compatible at the outset
- State-of-the-art performance is demonstrated
  - 1000:1 vibration reduction
  - structural control to .2 μm, 3σ
  - open/closed loop LOS control to .8/.2 μrad
- Stellar and earth imaging are the final, on-orbit performance measures
- Passive and active control technologies are integrated, validated and evaluated
- Vibration suppression and isolation are demonstrated together with high speed optical autoalignment and figure control
- Actuator and sensor technologies are integrated and demonstrated

Other:

- Concept is dynamically, electronically, thermally and power compatible with Shuttle - it is safe
- Experiments are autonomous, with manual override from the astronauts and ground

integrated, ground and on-orbit test plan, with focused objectives at each stage. The hardware required in the test are not off-the-shelf but, in many cases, has been built and has been demonstrated to work. The experiment plan exploits this situation to permit execution in four years.

Execution of the experiment program is recommended. If this is not possible, the goals and objectives set forth in this study merit consideration. In particular, modeling verification/extrapolation experiments may not be cost effective to do for their own sake. The cost of a Shuttle flight is just too expensive. It therefore appears to be more cost effective to do the experiments together with a technology demonstration. Also, the integrated ground and on-orbit test approach here is noteworthy. The ground experiment will be required to provide the link between analysis and ground test data and also provide the basis for future extrapolation to on-orbit behavior (once the extrapolation model is derived in the post experiment analysis of the on-orbit test). The ground experiment should therefore be designed compatible with the on-orbit experiment at the outset. This simplifies model comparisons, ensures power, thermal and computational system compatibility with true, on-orbit capability, and reduces integrated cost. Finally, it is recommended that, if funding limitations are severe, a low cost ground experiment incorporating the essential features described in this document is still useful. Excluding certain elements of the optical train, for example, will reduce cost significantly. This approach will allow for growth as funding becomes available; it serves to compare analytical and ground based structural models in the near term; and permits selection of the most promising technologies to be demonstrated on-orbit from the several that are available.

1.4 Summary of MOD Contract

As a result of an earlier study by TRW, ACOSS-8, a methodology for designing stable control systems for inaccurately modeled structures was developed. This stability ensuring design methodology is based on the positivity of operators and has the advantage that it does not rely on modal truncation, it has only low sensitivity to the exact knowledge of the structural model, and can accommodate for nonlinear effects. Moreover, it leads to time and frequency domain solutions which can be implemented

using current microprocessor technology. Its main disadvantage was that it required all the actuators and sensors in the control system to be colocated. In a number of applications of interest, however, colocation is not possible and further development was required.

The main objective of the ACOSS-14 MOD study was to extend the stability ensuring design methodology of ACOSS-8 to include systems not permitting colocated actuators and sensors.

A major result of this study is the successful generalization of the ACOSS-8 design technique to include noncolocated LSS systems with possibly unequal numbers of actuators and sensors. In order to do this, the Sector Theory, from which the positivity approach was derived, was reexamined and the assumptions requiring colocation removed. The generalized method degenerates exactly to the colocated design approach as a special case. In addition, the revised stability ensuring design condition provides a quantifiable indication of the trade between design insensitivity and performance. A flow chart is shown in Figure 1-2.

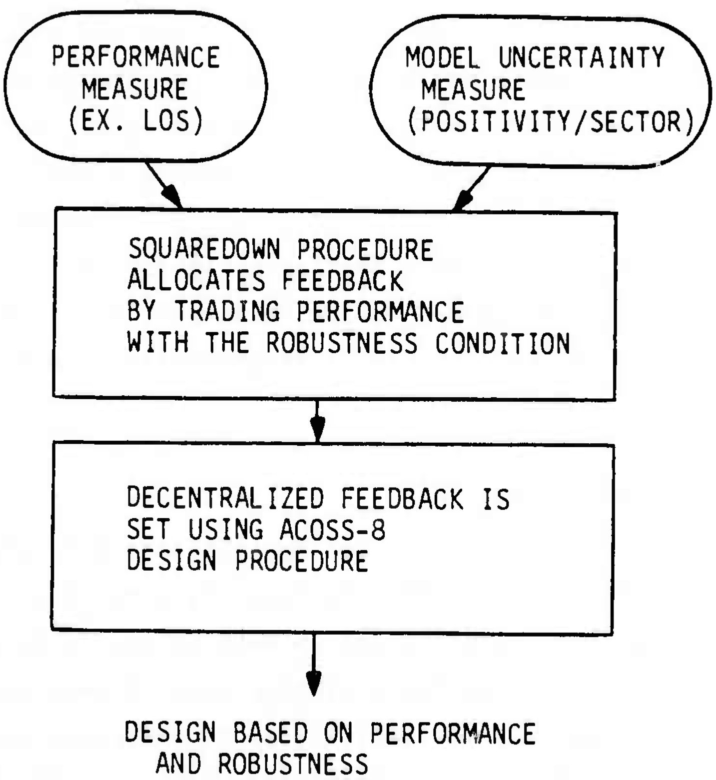

Figure 1-2. Flow Chart of Generalized Stability Ensuring Design Methodology

The generalized methodology was then illustrated on two design examples and shown to work well. In the "Flat Plate" example, the damping augmentation of the critical modes improved significantly. Moreover, when the sensitivity of the noncolocated design was compared with an existing, very insensitive colocated design, the results were comparable. Computational complexity was also comparable. The results were also similar for the Draper Model #1 (Draper Tetrahedron) example. The damping of the tetrahedron apex more than doubled over an existing colocated design which already met design goals. The design sensitivity and computational requirements here were also found comparable to the colocated design. The price paid in both examples, over the colocated design, was the addition of a single sensor—no new actuators were added.

1.5 MOD Contract Conclusions/Recommendations

The generalized design procedure has been shown to work well. In particular, it is concluded that noncolocated control systems can be designed to be insensitive with respect to stability (stability robustness). Also, noncolocated designs may actually be desirable from a performance standpoint, if it is the only way to measure the variables that must be controlled. We had expected the colocated designs to have better stability and performance properties because of their ability to operate at a higher loop gain without sacrificing stability. However, this was not true in the examples considered. We found that the colocated system must sometimes work harder to predict and control poorly observable signals. This means that it may need a higher bandwidth and higher loop gain. The noncolocated design, on the other hand, was found to afford to be less robust at the outset because it did not need as high a bandwidth and loop gain. It inherently got a better representation of the critical signals because of the designer's freedom to place a sensor at critical locations. Hence, when the overall compensation required to meet performance goals were considered, the noncolocated design was better. The price one pays for this is the additional sensor and the loss of decentralization in the control law computations.

A corollary which includes the above observation and the ACOSS-8 result is that there exists a quantifiable trade between stability robustness of a design and its performance: one is obtained at the expense of the other. Model uncertainty of what one is measuring, controlling and their relation may be large, but the accuracy must be known within specifiable limits. If the model uncertainty is small, robustness may be traded for performance. The degree to which one succeeds in designing performance will depend on the degree to which one is measuring and controlling what one really wants to control and measure. Given two equivalently accurate models (e.g., one colocated and one noncolocated), both have the same stability robustness and output control performance limitations but the one that measures and controls the desired control variable more directly (noise-free, observable and controllable) will be superior.

In as far as lessons learned, it is concluded, and justified from the theory developed here, that a good rule of thumb is to split the design problem into two pieces. First, the frequency dependent loop gain is allocated (loop by loop) proportionally to performance and the knowledge of the model, and inversely proportional to the uncertainty and noise. The loop gain matrix is then scaled to the highest gain (norm) permitted by the positivity/Sector condition ensuring stability robustness.

Finally, we conclude that the ACOSS-8 proposed three-step, stability ensuring design approach for LSS systems appears to be the correct approach in the sense that it continues to minimize risk with the potential for maximizing performance.

1) It assures stability robustness at the outset, when it is required the most.

2) It identifies model parameters through on-orbit tests whenever the starting model accuracy is too high to a priori design the required performance.

3) It tunes the controller to maximize performance.

It is therefore recommended that the developed design approach be studied further in order to streamline it and automate it. This will facilitate its use in more complex, realistic problems. It is also recommended that a representative design be evaluated on actual hardware.

1.6 Organization of Report

Sections 2 through 9 address the technical work performed under the ACOSS-14 PREMOD contract. It covers the ACOSS-14 baseline experiment from the initial conceptual and trade stages to its analysis and evaluation. The flight experiment program plan and cost estimate for the baseline system has been inserted in Appendices A and B as requested in the contract's statement of work.

Sections 8 and 9 address the technical work performed under the ACOSS-14 MOD contract. Section 8 covers the theoretical development of noncolocated control. Section 9 covers the design examples and their evaluation.

Quoted references are listed following Section 9. Appendix C describes the Orbiter's digital autopilot model, as used in this study. Appendix D contains a published paper detailing the digital, colocated design of the Draper Tetrahedron used in Section 9.

2.0 IDENTIFICATION AND DEFINITION OF EXPERIMENTS

Task one identified and defined a generic set of POC experiments that would be useful to both DARPA and NASA. The implied joint venture was considered as a way of meeting technical objectives at a reduced cost. This possibility was researched by examining NASA's and the AF's "generic" LSS missions listed in References [1, 2]. The interests and requirements described in these documents were analyzed and the set of common technologies that need to be demonstrated to ensure mission success were identified. The underlying premise in this research was that a joint venture would only be feasible if both parties' interests were satisfied. In order to meet this objective, the common technical unknowns and uncertainties in the systems of interest were identified first [the identified technologies directly determine the knowledge that must be gained through experimentation]. The methods needed to gather the data to reduce or eliminate the uncertainties then make up the experiments.

2.1 Determination of Technologies to be Demonstrated

The results of the NASA document search leads one to perceive that its interests are ideally driven by the desire to explore and exploit space and the sciences it induces. More practically however, it is evident that these objectives are modulated by politics, DoD and Congressional funding. Some of the "generic" representative systems that one can identify are: solar power stations, platforms, communications systems, permanent man-in-space systems, terrestial/extra terrestial research and resource exploration, and astrophysics research. In these categories one can further identify systems which are LSS. Therefore, any true desire to build these systems induces a need for demonstrating LSS technologies. The most important technologies identified are: structural modeling and verification, dynamic interaction and stability during assembly and construction, man-machine "loop" in space, passive and active damping augmentation in space, distributed actuation and sensing, and ground predicted performance verification.

A similar search through AF and DARPA documents resulted in the perception that they are driven by "threats" to the security of the U.S. In particular, DARPA's role appears to be coordination and support of the technology development of advanced communication, surveillance and weapon systems. In some cases, the systems of interest to DARPA and the AF are LSS but the requirements can sometimes be very different from NASA's missions: DARPA's missions will not only push the state-of-the-art in materials and structure but also in various advanced control technologies. The most important of these are: structural modeling and verification, dynamic interaction and stability of dynamic subsystem, passive and active damping augmentation in space, distributed actuation and sensing, ground predicted performance verification, and advanced control. The last includes precision pointing, vibration isolation, figure control, slew control, and off-line controller tuning.

The set of common technologies that must be demonstrated by DARPA and NASA are therefore:

- structural modeling and verification
- dynamic interaction and stability
- active and passive damping
- distributed actuation/sensing
- predicted performance verification.

The objective of structural modeling and verification tests should be to demonstrate that current analytical models are sufficient to predict, at least grossly, structural behavior in space. Secondly, the demonstration should provide the experimental data required to permit the confident use of models to predict the behavior of systems that have not been built yet.

The dynamic interaction and stability within the system is also important to understand and demonstrate. Classically, weak dynamic interaction is reduced by using local controls with large loop gains. This is difficult to do with flexible structures, however, because the structure theoretically strong-couples the system at resonance and stability concerns preclude the

use of high gains. It is therefore necessary to validate the current understanding of the problem and verify that proposed modern control concepts are a solution.

Next, the integration of active and passive damping into a structure must be demonstrated in space if it is to be a viable approach to solving various LSS problems. Current ignorance of the relationships between ground and on-orbit passive damping is currently too high and could lead later to confusing and costly trades that are false.

Distributed sensing and actuation are also commonly accepted concepts planned for solving various LSS problems. Yet, because of the large bandwidth and dynamic range encountered in LSS, the integration of coarse and vernier devices will be non-standard and must be validated.

Finally, what is the real current performance limit of the integrated LSS technology? Nobody seems to know. Moreover, it is not likely that paper analyses are going to be credible until current uncertainties are resolved in an integrated test.

2.2 Generic Set of Experiments

Two generic sets of experiments have been identified in response to the technology demonstrations outlined in Section 2.1.

The primary set includes:

- identification of structural dynamic model
- identification of structural damping
- passive damping augmentation
- dynamic interaction with the orbiter
- active damping augmentation/control and verification
- pointing performance verification.

These experiments are interrelated and often one experiment is the logical step to the next. Most of the tests can be readily conducted on the ground. This is desirable as the difference between ground and on-orbit results, especially for performance verification and determining existing and augmented damping, is what one needs to know to improve modeling abilities. Current vibration and pointing control capability is also to be verified.

The secondary set includes

- figure control and associated performance verification
- slew maneuvers
- control law tuning

and have been chosen to add realism. The figure control experiment would show the interaction of the vibration control system with the figure control system. The interaction of the attitude control system and the vibration control system during a slew maneuver adds realism to the acquisition and tracking problem. A control law tuning experiment demonstrates indirect adaptive control.

2.3 Generic Set of Procedures for the Experiments

2.3.1 Assumptions about the Generic Procedures

The generic experiments were assumed conducted from the Space Shuttle Orbiter and therefore hypothesized to be automated. However, human assistance with the Remote Manipulator System (RMS), or through Extra Vehicular Activities (EVA), were not initially excluded when the generic procedures were defined. Some other assumptions initially used were:

i) The experiment structure can be deployed incrementally or sub-structures can be uncaged to change the dynamic characteristics of the structure.

ii) The experiment structure's critical modes are lower than the Orbiter digital autopilot (DAP) so that the structure can be excited by the DAP.

iii) A conservative, active controller is used to stabilize the structure and to damp out vibrations between experiments.

iv) The Orbiter DAP signals are available to the LSS control system.

v) Actuators installed on the structure are used to generate disturbance for evaluating control system disturbance rejection.

vi) The controller performance measurement is sensed using the line-of-sight error from a dummy payload to the Orbiter cargo bay or to an inertial reference point. This information did not necessarily have to be available to the control system.

and vii) All the actuator/sensor data, including DAP signals, are recorded on tape for post-flight analysis.

2.3.2 Test Procedure Concepts

Conceptual procedures to the experiments identified in Section 2.2 were derived next. The results are summarized in Table 2-1. Listed are the candidate experiments, their procedures, and required ground/on-orbit activities. The table is subsequently used in this report to guide the selection of a suitable test structure and as the framework for the detailed experiment procedures described in Appendix A for the baseline test structure.

Referring to Table 2-1, the experiments described follow the ACOSS-8 approach to LSS control: first, a robust, stable control system is designed; then, after one identifies the on-orbit dynamical behavior more accurately, the control system is tuned to obtain the best achievable performance. From this approach, the following experiments are derived:

1) Identification of Structure Dynamic Model - A more accurate structural dynamic model is obtained from actuator/sensor measurements by using parameter estimation techniques. The preferred techniques are the maximum likelihood method and the transfer function method.

2) Structural Damping - Ground measurement of structural damping does not accurately estimate the on-orbit damping. Thus, structural damping is determined on-orbit to ensure the control system stability and performance. Damping is measured from free vibration decay or from frequency of peak coincident response.

3) Component and Substructure Testing - One of the lessons that will be learned from the experiment is how one can predict the behavior of a larger structure by testing an individual component or substructure. The component and substructure can be tested using the same technique as the full scale structure.

4) Passive Damping Augmentation - Effective use of passive damping augmentation concepts depends on their being designed into the structure rather than added as an after-thought. The design process includes detailed modal analysis of the entire structure to find those members possessing significant amounts of elastic energy and therefore suitable for damping augmentation. The selection of damping material should consider the material loss factor as a function of frequency and temperature range. The experiment structure can have cageable/deployable appendages which have the ability to change the structure's modal characteristics and damping.

Table 2-1. Generic Experiment Procedures

Test Objective	Procedure	EVA/RMS Activities	Post-Flight Analysis	Remarks
1) Identification of structural dynamic model	• Excite the experiment structure with: – Actuation on the test structure – Orbiter thrusters	• Assist the deployment of experiment structure: – Change the characteristics of the experiment structure	• Maximum likelihood parameter estimations: – Physical parameters – Modal parameters • Transfer function/frequency response method	• Experiments are conducted during and after the deployment of test structure • Structural model may include Orbiter
2) Structural Damping	• Excite the structure with: – Sinusoidal signals – Frequency sweep sinusoidal signals	Same as above	• Determine damping from free vibration decay • Determine damping from frequency of peak coincident response	• May require long time of no Orbiter thruster activity • Relatively "clean" data are required
3) Component Testing	• Set up special test bench • Test the dynamic properties of individual component (truss, damper, actuator, sensor) by observing the response to an input signal	• Place test article on test bench	• Determine component physical properties (stiffness, damping) and dynamic properties (frequency response)	• Test can be conducted independently
4) Substructure Testing	• Test the dynamic properties of substructure	Same as above	• Determine the dynamic properties of each individual substructure and combine the results to predict total structure response	• Provides data on model synthesis techniques
5) Passive Damping Augmentation	• Excite the structure before and after the replacement of an existing truss with a damping-enhanced one • Excite the structure before and after the addition of passive damper	• Replace or install passive damping elements	• Determine structural damping before and after passive damping augmentation • Evaluate the effects of damping-enhanced devices	
6) Control law and pointing performance verification	a) Select controller • Open-loop response – Increase input signal magnitude to test linearity • Closed-loop response – Increase delay to test phase margin – Increase gain to test gain margin • Simulate disturbance – Measure disturbance rejection – Tune controller • Closed-loop response for tuned controller • Simulate actuator/sensor malfunction b) Change structure characteristics, repeat item a) c) Assess pointing performance	None	• Compute open-loop response • Check linearity • Compute closed-loop response – Compare with predictions from open-loop response – Verify phase/gain margins • Estimate closed-loop damping • Compute disturbance rejection	• LOS error from test structure to Orbiter cargo bay can be used as performance index • Disturbance can be simulated by actuators installed on the structure • Disturbance signal can be sinusoidal or band-limited random noise
7) Dynamic Interaction with the Orbiter	• Firing orbiter thrusters and observing the structure response with active controller on/off • Using inertial-type actuators to excite the total structure and observing the response with combinations of Orbiter OAP on/off and active controller on/off • Repeat, after changing the structure characteristics	• Change experiment structure characteristics	• Orbiter fuel consumption • Dynamic coupling between Orbiter and experiment structure	
8) Comparison of Actuators (relative vs inertial)	• Evaluate controller performance using relative type actuators (linear force actuators) • Evaluate controller performance using inertial type actuators (reaction wheels and/or proof mass)	None	• Estimate closed-loop damping • Evaluate disturbance rejection (control performance)	• Locations and characteristics of these two types of actuators are different, only qualitative comparisons can be made • Relative actuator will not affect the rigid body motion • Rigid body will respond to inertial actuator. This is important when LOS pointing is to be controlled

5) Control Law and Pointing Performance Verification - Control law characteristics that should always be tested are stability, robustness, and meeting of performance design goals. Robustness and stability can be verified by varying control parameters until the system is on the verge of instability, provided, of course, that this can be done safely. Damping design goals can be directly measured from sensed responses. Pointing control performance can be measured from the LOS error between a dummy payload to Orbiter cargo bay. This information is intended for assessing pointing performance only; it is not available to the control system. The vibration control or disturbance rejection can be tested by installing special actuators on the structure that have output characteristics resembling the on-orbit disturbance source, e.g., cryocoolers.

6) Dynamic Interaction with the Orbiter - The dynamic interaction with the Orbiter must be well understood for the following reasons: 1) safety of the Orbiter and its crew, 2) excessive fuel consumption of the Orbiter DAP, 3) effects of the dynamic interaction on the test structure and the outcome of the experiments, and 4) being attached to the Orbiter will be the normal mode of operation for some future LSS missions. Of particular interest is the relations among VRCS thruster firing, Orbiter DAP, and LSS control system.

7) Comparison of Actuators - There are two types of actuators that can be used for LSS control: relative (e.g., linear force actuator) and inertial (e.g., reaction wheel, proof mass). The major difference between these two types of actuators in theory is that the relative type actuator will not affect the center of mass rigid body motion while the rigid body will respond to inertial actuators.

Tests of components, substructures, and actuators have been included in the list because of their unique modeling importance. It is precisely the relation between the characteristics of the components, the substructure, and the total structure that is needed to be able to develop analytical models in LSS. Also, some of these experiments can be performed on the ground or in orbit but the results can differ significantly in some cases (e.g., damping). Therefore, these tests should be performed in both locations so that analytical prediction methods can be improved and future on-orbit predictions based on ground data can be more accurate.

3.0 SELECTION OF SUITABLE TEST STRUCTURE

Having defined the generic experiments to be conducted, the next task in the study was to select a structure to accommodate them. Existing, planned and new designs were considered. The approach taken was to first obtain a list of the planned Shuttle payloads. This list was compiled from information contained in NASA STAR from 1977 to 1980, from NASA literature search #45835 ("Space Shuttle Payloads") [1, 3, 4, 20, 21] and from various DoD documents [2, 4]. The last was necessarily limited due to "need to know" constraints. From this base list, structures which could accommodate the experiments were next identified. The criteria was to select systems which are consistent with the NASA and DoD Technology Models [1, 2] and which have reasonable time frames and level of commitment. At the end, new possibilities consistent with NASA and DoD were added and considered.

3.1 NASA Missions

3.1.1 Mission Definition Process for NASA

NASA missions were examined first. As one might have guessed, the "wish list" was very large and it became important to try to rank missions according to credibility. The block diagram in Figure 3-1 was found useful in performing this operation. It models the NASA mission definition process. It is based on sheer perception and consistency with available data.

Referring to Figure 3-1, the process starts at NASA and DoD think tanks. Their organizations look at current objectives, what has been successful in the past, and speculate about the future. The output of the think tanks are termed unvalidated missions and there is no time frame associated with them. Then, depending on the "ideas", unvalidated models are discarded or validated by NASA major offices. The offices also determine, depending on usefulness and cost, whether the validated models are O-models or C-models. O-models are potential/speculative missions with possible starts beyond 10 years. C-models are candidates for possible start within 10 years. The validated models, together with a speculated DoD coordinating input, are next processed by NASA to determine P-models. These are missions planned to start within 5 years. The final NASA process takes P-models,

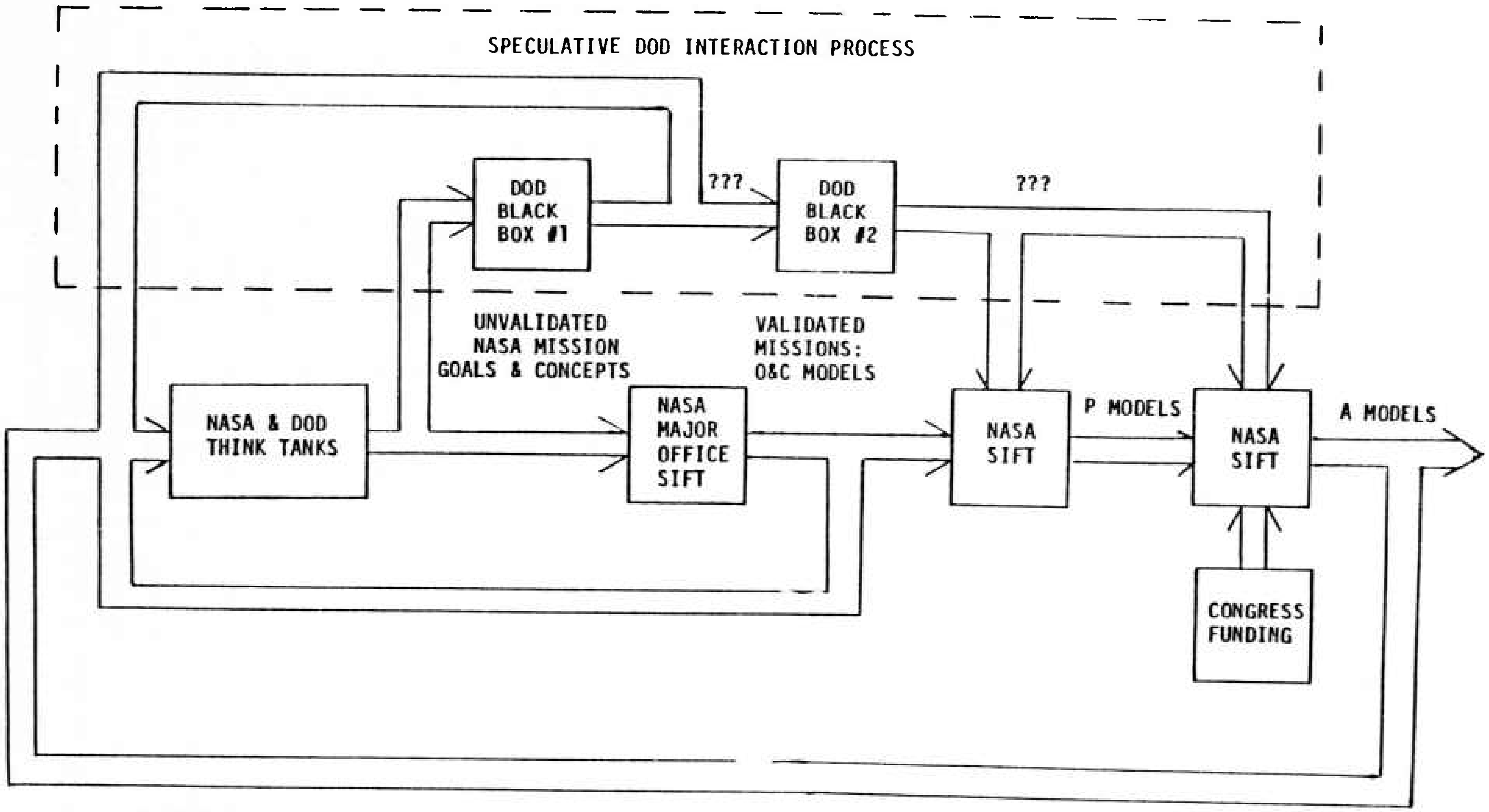

A MODELS: FUNDED, <5 YEARS

P MODELS: PLANNED, START <5 YEARS

C MODELS: CANDIDATES, POSSIBLE START <10 YEARS

O MODELS: POTENTIAL/SPECULATIVE, POSSIBLE START >10 YEARS

Figure 3-1. Perception of Mission Definition Process for NASA

DoD coordination and congressional approval/funds into A-models. These are approved and funded systems, scheduled for launch within 5 years.

3.1.2 Feasible NASA Missions

A preliminary set of criteria used to "sift" the NASA models of interest was defined to determine which missions are feasible. It was determined that politically, only USA, NASA missions could be realistically considered. This would exclude, for example, an International Solar Polar Mission (ISPM) like mission. The system would also have to be Shuttle launched and earth orbiting to permit monitoring and exclude planetary spacecraft which could not be retrieved. Finally, the structure in the mission would have to have the LSS-like features of the "true" system of interest.

Validated Systems. The set of approved and planned NASA missions that satisfy the feasibility criteria above is shown on Table 3-1. The raw data is taken from [1]. The alpha-numeric code designates the NASA mission number. It is interesting that only one mission, the Solar Electric Power Array test flight, had been approved (is funded for launch) at the time this research was made, 1981.* The remaining missions were "planned". The more interesting missions identified are the radiometers (RI12, RI13, and EI67), LSST (Large Space Structure Technology program), and 30/20 GHz. However, none of these are expected to require ultra-precision structural control.

Continuing the search through the remaining validated, feasible missions, the systems become more and more LSS-like. Table 3-2 shows the "candidate" and "opportunity" missions. It is evident that these systems are more speculative than the ones in Table 3-1. Nevertheless, it is important to observe that the Space Operation Center, which had no set date in 1980, is the current Space Station for which NASA has recently initiated Phase A study. Hence, abrupt status changes are very possible.

---

* Many of the NASA missions described have since been delayed or eliminated.

Table 3-1. Feasible NASA Missions (1980 Data)

Approved:			
OI12	SEP Solar Array Shuttle Flight	1983	Launch
Planned:			
L2	Space Science Platform	1982	Start
RI12	Passive Microwave Radiometer	Mid 1980's	
RI13	Active Microwave Sensor	Mid 1980's	
EI67	Pushbroom Radiometer	<1985	Start
C4	30/20 GHz Antenna Wideband Communications Satellite Program	1982	Start
C5	Geostationary Platform Demonstration	1983	Start
T9	Solar Electric Propulsion Stage (SEPS)	1981	Start
U4	Tethered Satellite System	1981	Start
U5	LSST	1981	Start
U6	Power Extension Package (PEP)	1981	Start
U7	Science and Applications Space Platform	1982	Start
U8	25 KW Power System	1983	Start
U9	Material Experiment Carrier	1983	Start
U10	Material Experiment Carrier II	1986	Start
U11	Large Power Module	1990	Start

Table 3-2. Speculative, Feasible NASA Missions (1980 Data)

Candidates:

A15	Very Long Baseline Radio Interferometer	<1990	Start
A16	Orbiting Submillimeter Telescope	1985-90	Start
A17	Large Ambient Deployable IR Telescope	1985-90	Start
S12	Solar Terrestial Observatory	1985	Start
R8	Soil Moisture Research and Assessment	Mid 1980's	Start

Opportunity:

A18	Infrared Interferometer	>1990	Start
A19	Gravity Wave Interferometer	>1990	Start
A20	Coherent Optical System of Modular Imaging Collectors	>1990	Start
A21	Large Optical/UV Telescope, Diffraction Limited	>1990	Start
A22	100-Meter Thinned Aperture Telescope	>1990	Start
C6	Multi-Service Thin Route Narrowband Program	1984	Start
C8	Orbiting Deep Space Relay Station	>1990	Start
T14	Advanced Electric Propulsion	1990	Start
U13	Materials Experimentation Module	1990	Start
U14	Space Operation Center	No Date Set	

The final set of possibly feasible, validated missions are shown in Table 3-3. The available descriptions of these systems were too ambiguous to determine whether they were feasible or not. The list consists primarily of instruments (as opposed to spacecraft) and a few Earth resources spacecraft.

Unvalidated Systems. Unvalidated missions were also considered in the search for a suitable test structure. These missions are primarily proposed and evaluated by "think tank" organizations through various funded studies. Some of the more extensive studies include: "Advanced Space Concepts and Their Orbital Support Needs" [4], "Space Resources and Space Settlements" [5], "Space Horizons" [6], and "Post LANDSAT-D, Advanced Concept Evaluation" [7]. It is evident from the "NASA Technology Models" [1] document that NASA used many of the missions described in these documents, but only after they had been further studied by two think tanks: General Research Corporation and Planning Research Corporation. The number of identified unvalidated systems is also rather large ($\sim$ 50) but NASA OAST goes through a ranking exercise to determine which should become validated missions. The missions listed in Table 3-4 meet the feasibility criteria and are in the top 30 of the rankings. The Permanent Orbiting Outpost is number one and the "Geosynchronous" spacecraft are numbers three and four.

3.1.3 Most Promising NASA, Feasible Systems

All of the feasible NASA systems described above were carefully examined and only the most promising were selected for further evaluation. The following twelve candidates were judged to be the most promising with respect to near-term starts (< 5 years):

OI12	SEP Solar Array Shuttle Flight
U5	LSST
T9	SEPS
U6	PEP
U8	25 KW
C4	30/20 GHz
RI12	Passive Microwave Radiometer
RI13	Active Microwave Radiometer
A16	Orbiting submillimeter Telescope
A17	Large Ambient Deployable IR Telescope

Table 3-3. Possibly* Feasible NASA Missions

Approved:

RI6	Shuttle Imaging Radar	1981	Launch

Planned:

A14	Large Area Modular Array of Reflectors	<1990	Start
RI10	Gravity Gradiometer	1982	Start
RI11	Multispectral Mid-IR Imager	1983	Start
RI14	Thermal IR Sensor	Mid 1980's	Start
RI15	Visible IR Sensor	Mid 1980's	Start
RI16	Earth Resources Synthetic Aperture Radar	Undetermined Start Date	
E6	National Oceanic Satellite System (NOSS)	1981	Start
E7	Upper Atmospheric Research Satellite	1982	Start
E8	NOSS Research Program	1982	Start
E9	Ocean Circulation Mission Topography Experiment	1983	Start
E10	Operational Meteorology Satellite	Mid 1980's	Start
EI25	Large Antenna Multifrequency Microwave Radiometer	1981	Start
EI26	Scatterometer	1981	Start
EI27	Scanning Multichannel Microwave Radiometer	1981	Start
EI31-EI41	Instruments on E7	1982	Start
EI45	Cryogenic Limb Scanning Interferometer Radiometer	1984	Start
EI62	Salinity Radiometer	<1985	Start
EI66	Ocean Synthetic Aperture Radar	<1985	Start
EI67	Pushbroom Radiometer	<1985	Start

Candidates:

A14	Large Area Modular Array Reflectors	1990	Start
E11	Ocean Research	1985	Start

Opportunity:

L3	Search for Extraterrestrial Intelligence	Undetermined Start Date	
S14	Pinhole Satellite	1984	Start
C7	Tracking and Data Relay Satellite II	1986	Start
T15	Unconventional Orbital Transfer Vehicle	1990	Start

* Description in documents too vague to make judgement.

Table 3-4. Feasible, NASA Unvalidated Missions

Permanent Orbiting Outpost

Geosynchronous Telephone Switching Utility

Geosynchronous Broadband Computer Links

Global Search and Rescue Location

Orbiting Civil Command and Control Station

High Resolution Earth Mapping Radar

10-m Optical Interferometer

Advanced Resources/Pollution Observatory

All of the others were judged either too far into the future, too speculative, or possessed less than average desirability with respect to the "envisioned" POC test.

3.2 AF Missions

Representative DoD missions were examined next to determine their requirements and also their suitability as test structures. It was found that many of the systems are classified and that one realistically has to settle for some very limited, available information from the Air Force [2, 4].

Table 3-5 shows the set of AF missions which were determined to be feasible (in the same sense as the NASA missions). The missions are listed according to underlying functions: radar, communication, passive and active optics. The time frames for these missions are unavailable and therefore could not be assessed. In general, all of these systems are excellent test beds. The radar and communication systems listed are LSS having stringent structural control requirements. Moreover, the passive and active optical missions probably represent the most needful of the technology that is proposed to be demonstrated by this study.

The document "Advanced Space System Concepts and Their Orbital Needs" [4] proposes an extensive set of potential AF missions. Those that can serve as a test bed are listed in Table 3-6. These systems must be viewed, however, as much more speculative than the missions listed in Table 3-5.

3.3 Preliminary Assessment of Existing or Planned Systems

The systems listed in Subsections 3.1 and 3.2 were all feasible. The next step taken in the task was to determine a criterion with which to select the baseline POC structure and choose one.

The desirable properties for a POC experiment are that it be of interest to NASA and DoD, yield as much information about LSS as is possible, and be low cost and simple. In order to rank the identified systems according to these attributes, each system was to be graded in each of the following nine categories:

Table 3-5. Feasible AF Mission Models

Radar:

Mechanically Steered Space Based Radar Surveillance (U)

Medium Altitude Parabolic Cylinder Radar Surveillance (U)

Synchronous Altitude Active Lens Radar Surveillance (U)

Medium Altitude Tactical Surface Reconnaissance Radar (U)

Distributed Array Radiometer Surveillance (U)

Medium Altitude Surveillance Radar (U)

Communications:

Maneuverable Strategic MILSATCOM (U)

Passive Optics:

Staring IR Missile Tracking (U)

IR Step-Stare Mosaic Surveillance (U)

IR Panoramic Pushbroom Space Surveillance (U)

Active Optics:

Space Based Laser for ASAT/DSAT (U)

Space Based Laser Relay (U)

Space Based Laser for Boost Phase ABM (U)

Table 3-6. Additional, Feasible AF Missions

Communications:

MC4	Deep Space Survivable COMSAT (U)
MC5	Proliferated and Netted Survivable COMSATS (U)
MC10	G.I. Personal Communications (U)
MC15	Submerged Submarine to Satellite Laser Communications (U)

Active and Passive Radar:

MO13	Sonobuoy Readout Submarine Surveillance (U)
MO14	Sensor Readout System (U)
MO15	Global Logistics Information System (U)
MO16	Over-Horizon Aircraft Surveillance (U)
MO17	Ocean Surveillance Radar (U)
MO18	Multi-Mission Space-Based Radar (U)
MO19	Quadristatic Missile Detection Radar (U)
MO20	Battlefield Surveillance (U)
MW3,4	ABM Radar Jamming (U)
MW5	Tactical Microwave Weapon (U)

Active and Passive Optics:

MO5	Ocean Surveillance (U)
MO7,8	Detection of Submerged Submarines Via Laser Sonobuoys (U)
MO9	Aircraft Passive IR Surveillance (U)
MO10	Advanced Strategic Surveillance Sensor (U)
MO11	Deep Space Backup Surveillance (U)
MO12	Laser Detection of Submerged Submarines (U)
MS1,2	Target Designator for Homing Missiles (U)
MS4	Far Term RPM Control/Readout (U)
MS6,9	Battlefield Illuminator (U)
MS11	Bomber Beam Power (U)
MW6	Space Laser ABM (U)
MW7	Space Mirror Laser ABM (U)
MW8	Synchronous Mirror Laser ABM (U)
MW9	Synchronous Pulsed Laser ABM (U)
MW10	Synchronous CW Laser ABM (U)

Other:

MW2

1) Interest to DoD and NASA objectives

2) Representative of LSS - many closed spaced, low frequency, low damped modes

3) Acceptable dynamic interaction with orbiter

4) Low cost and simplicity

5) Ground testability

6) Low impact on intended mission

7) Potential for future growth

8) Low weight and small Shuttle stowed volume

and

9) Easy restowability

The total score was then to be collected and compared.

It became evident very quickly, however, that the stated approach for choosing a structure would not succeed. The problem is that there are really no candidates. More specifically, hard timeframes and commitments for the systems identified are lacking. A multitude of competing NASA missions are being advanced, yet there is a great uncertainty as to which ones, if any, will fly. The DoD were highly suitable candidates, nevertheless the timeframe and commitment needed to judge them is not accessible. Another challenging problem was to determine if the sponsor of a multi-million dollar spacecraft could be convinced that a set of experiments, deliberately exciting his structure, is risk-free and to his benefit. Finally, a majority of the missions required major, expensive modification and added instrumentation to permit the experiment. Hence, the preliminary conclusion was that a dedicated POC structure was too competitive an alternative to ignore and, therefore, had to be considered before final trades are made.

3.4 Dedicated POC Structure Alternatives

Dedicated structures were considered next as means of getting more control on commitment and timeframe and also to improve the support of the sponsor. Two different viewpoints were taken in generating these dedicated POC structure alternatives. One is a simple, modular approach

aimed at demonstrating technology through emulations of a real system. The other is geared at demonstrating technology on pieces of a potentially real system.

The idea of the modular approach is to split the structure into two pieces, the support structure and the payload. One then, depending on the desired technology demonstration, interchanges various support structures with the alternative payloads. As will be shown later, the approach offers simplicity and at potentially low cost.

The idea of the second approach is to use pieces of existing or funded hardware which are likely to be used in future systems. The advantage of this is that pieces of real hardware can be tested and later be integrated into the real missions. The disadvantage is that it is limited to the demonstration of system unique technologies and is potentially more complex and expensive than the modular approach.

3.4.1 Modular, Emulation Concepts

Two support structures were identified for use in the modular concept. One, shown in Figure 3-2a, is an Astromast like structure that has one end attached to a shuttle pallet and the other end has a gimbal. The gimbal is free to accept one of several payloads to be identified next. The mast itself can be used to demonstrate vibration suppression and figure control. The second support structure, shown in Figure 3-2b, consists of two concentric volumes. The inner volume contains disturbance generating devices. The outer volume is attached to the inner volume through isolation mechanisms. One end of the other volume can be attached to the Shuttle through another isolation mechanism or the whole structure can be tethered. At the other end of the outer volume is a gimbal free to accept one of several payloads. The second support structure can be used to demonstrate vibration isolation, suppression, and to some extent, figure control.

One method conceived for adding vibration suppression and figure control to the mast support structure is to attach collars. Referring to Figure 3-3, force actuators connecting the collars can be used to apply a controllable bending moment. Alternatively, one may add momentum exchange devices that are linear or rotational. A similar approach may be taken with the concentric volume structure.

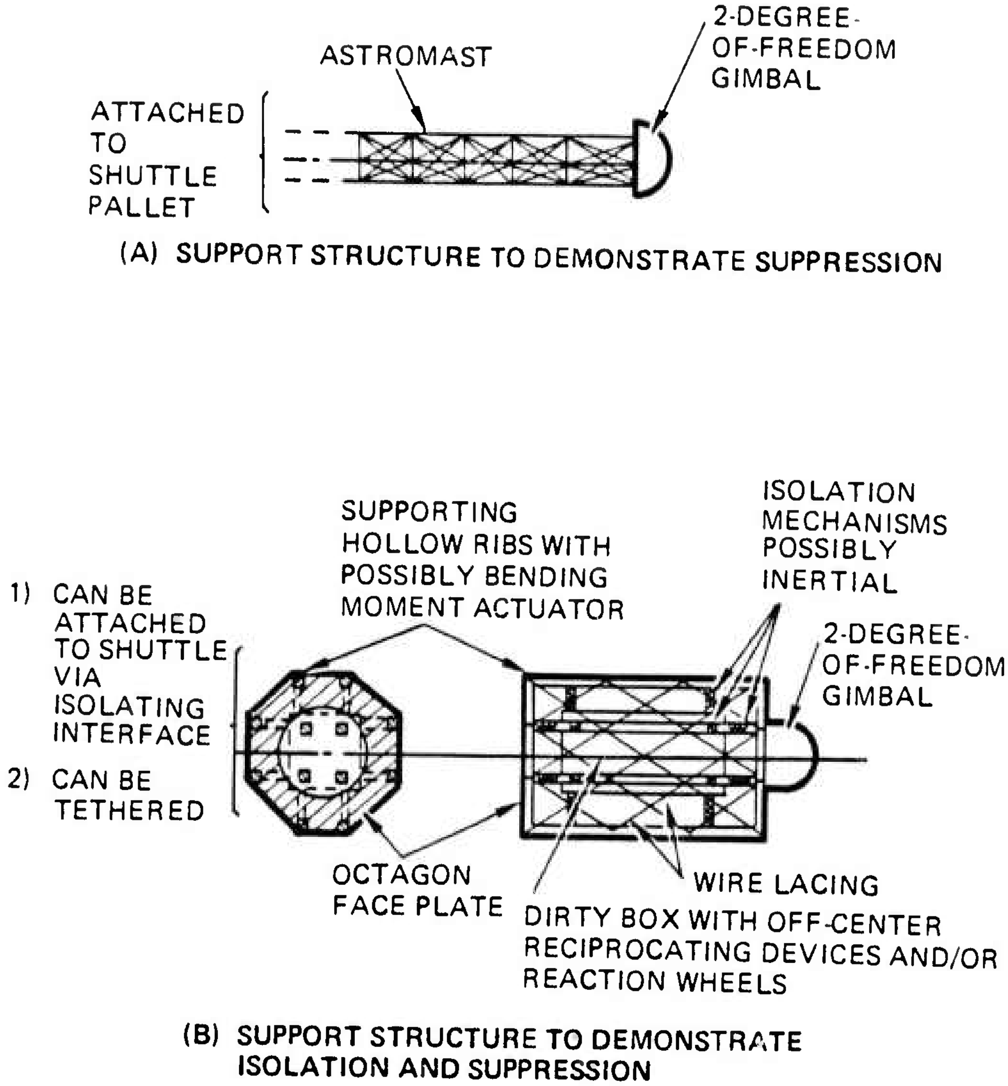

Figure 3-2. Modular, Emulation Support Structures

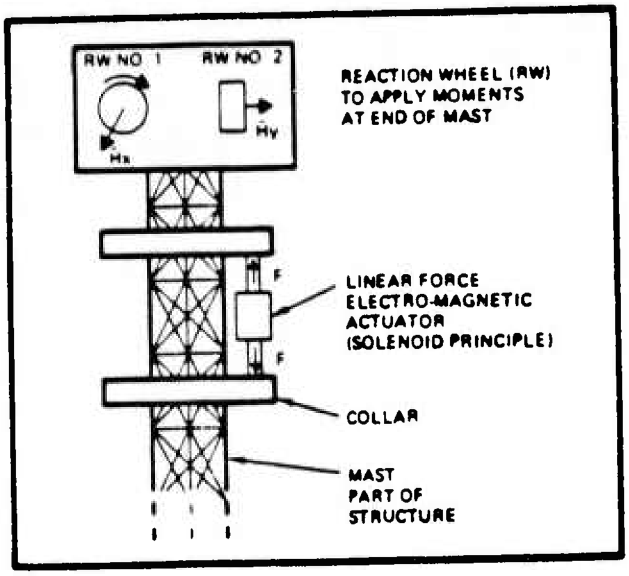

Figure 3-3. Concept for Evaluating Active Structural Control

Several modular payload structures were identified next for use with either of the described support structures. These are shown in Figures 3-4 and 3-5. They are the thin rectangular plate, the thin planar structure with inexpensive segmented mirrors, the thin rectangular plate with tetrahedron, and the thin twin beam. They all attach directly to the support structure gimbal.

The three structures, shown in Figure 3-4, can be used to emulate the dynamics of antennas, segmented optics, and, with some imagination, antennas or mirrors with reflectors. Bending moment and momentum exchange actuation attached on the planar part of the structure can be used to demonstrate vibration suppression, figure control, and, when the gimbal is rotated, post slew damping. The addition of the tetrahedron in Figure 3-4b adds another level of emulation and can be used to demonstrate isolation and the control of weakly controllable modes. The tetrahedron can also be added to the structure with segmented mirrors. The picture of the Sunflower antenna in Figure 3-4d is shown to demonstrate what is meant by

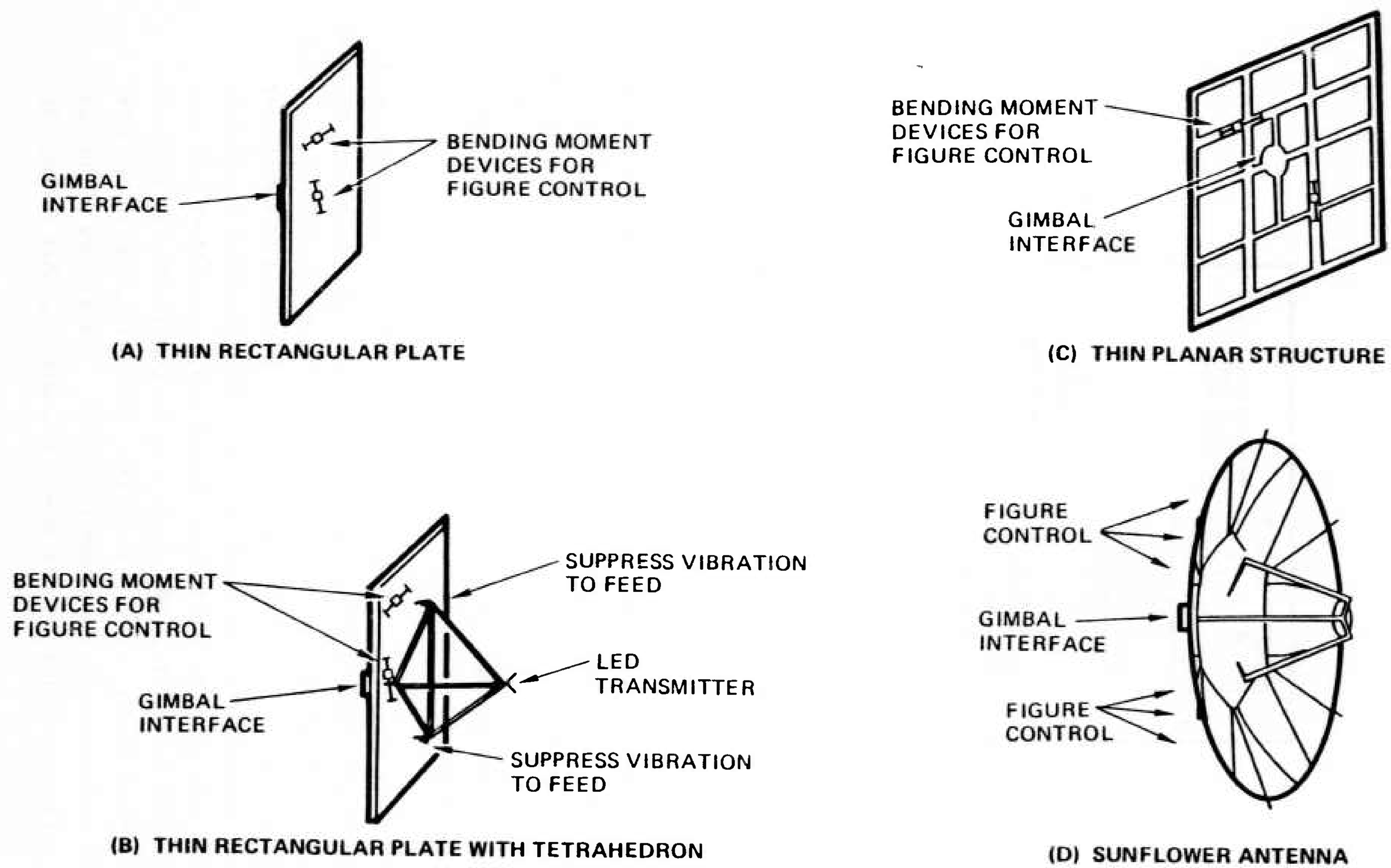

Figure 3-4. Modular, Emulation Payload Structures

emulation. The topological resemblance between the plate with tetrahedron and the Sunflower is self-evident.

The thin beam payload shown in Figure 3-5 also attaches to the support structure gimbal. It represents a concept capable of demonstrating optimum slew of LSS with large solar panels but it can be configured to demonstrate vibration suppression, figure control, rotational vibration isolation and multibody alignment. The structure consists of two parallel, very thin beams. The beams are hinged (in-plane) to each other to reduce the effects of torsional modes. The two beams attach to the support structure gimbal through an interface consisting of two concentric motors. The inner motor is used to disturb the structure, the outer motor is used to rotationally isolate the disturbance and also effect the slew. Bending moment and/or momentum exchange devices are used to suppress "leaked" vibration and preserve figure. The LED and receiver are used to monitor the test. The multibody alignment experiment adds additional LED transmitters, light receiver and a motorized gimbal. The motor is used to effect alignment of one end of the beam to body center. The motorized gimbal would be attached at one end of the beam and the rotational momentum exchange would be controlled to perform the alignment.

Figure 3-6 illustrates how the shuttle attached and tethered configuration would look using the modular approach. The motion of the structure would be monitored by attaching LED transmitters to selected points and then observing the motion from a shuttle based receiver. Pointing experiments would reverse this: a receiver could be added to the structure and an LED transmitter would be placed in the shuttle cargo bay.

3.4.2 Semi-Real Concepts

Alternative concepts incorporating pieces of planned, funded, or existing hardware were also considered. With few exceptions, the majority are large antennas: e.g., the General Dynamics "Precision Erectable Truss Antenna" PETA), the Lockheed "Wrap-Rib Antenna", the Harris "Hoop-and-Column", and the TRW "Sunflower". These systems were invariably rejected because of their cost and complexity (for an experiment) and because it is not clear if active control is even required in these systems. For this reason, the decision to depart from antennas and into optical systems was made.

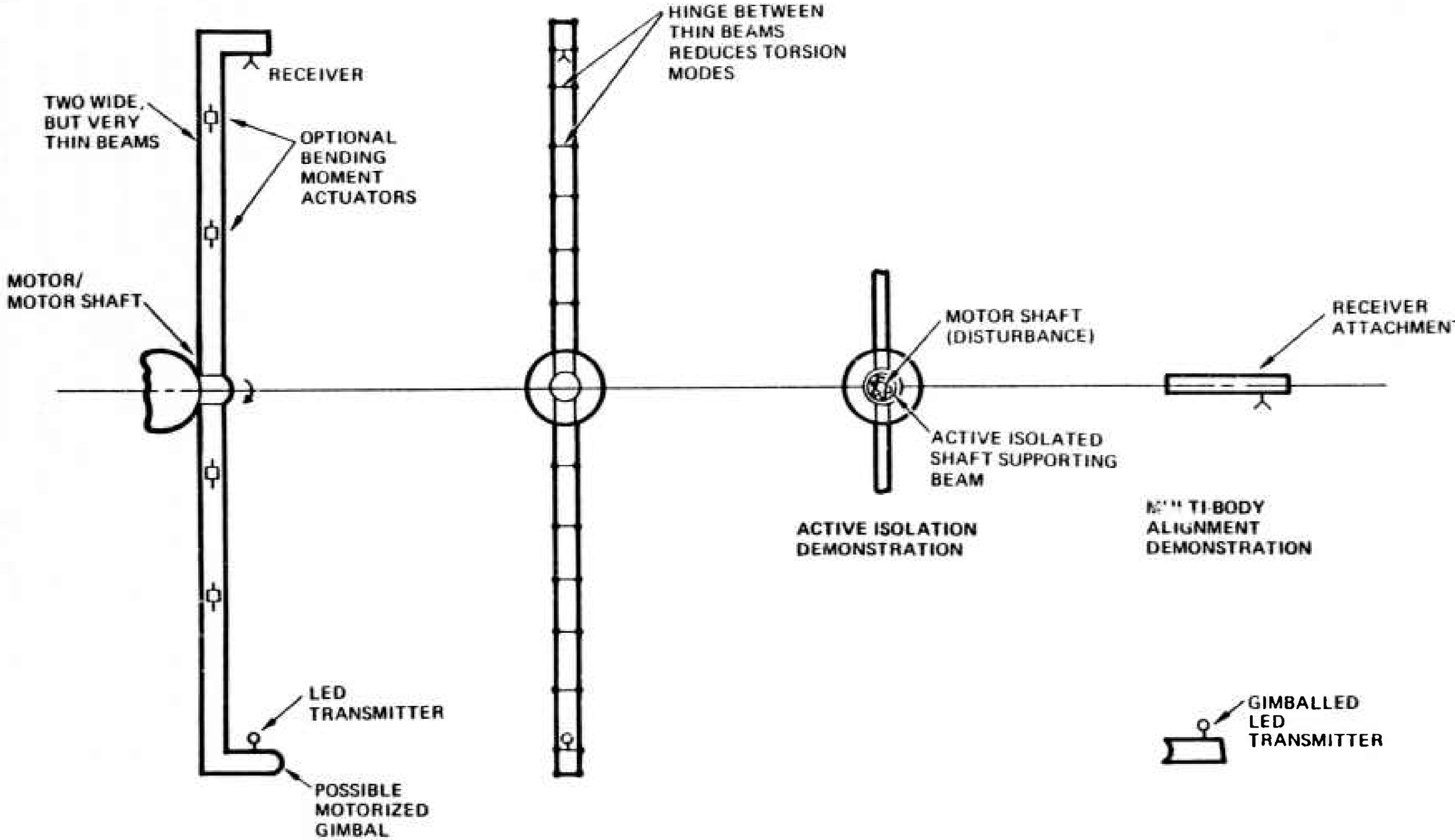

Figure 3-5. Modular, Thin Beam Payload

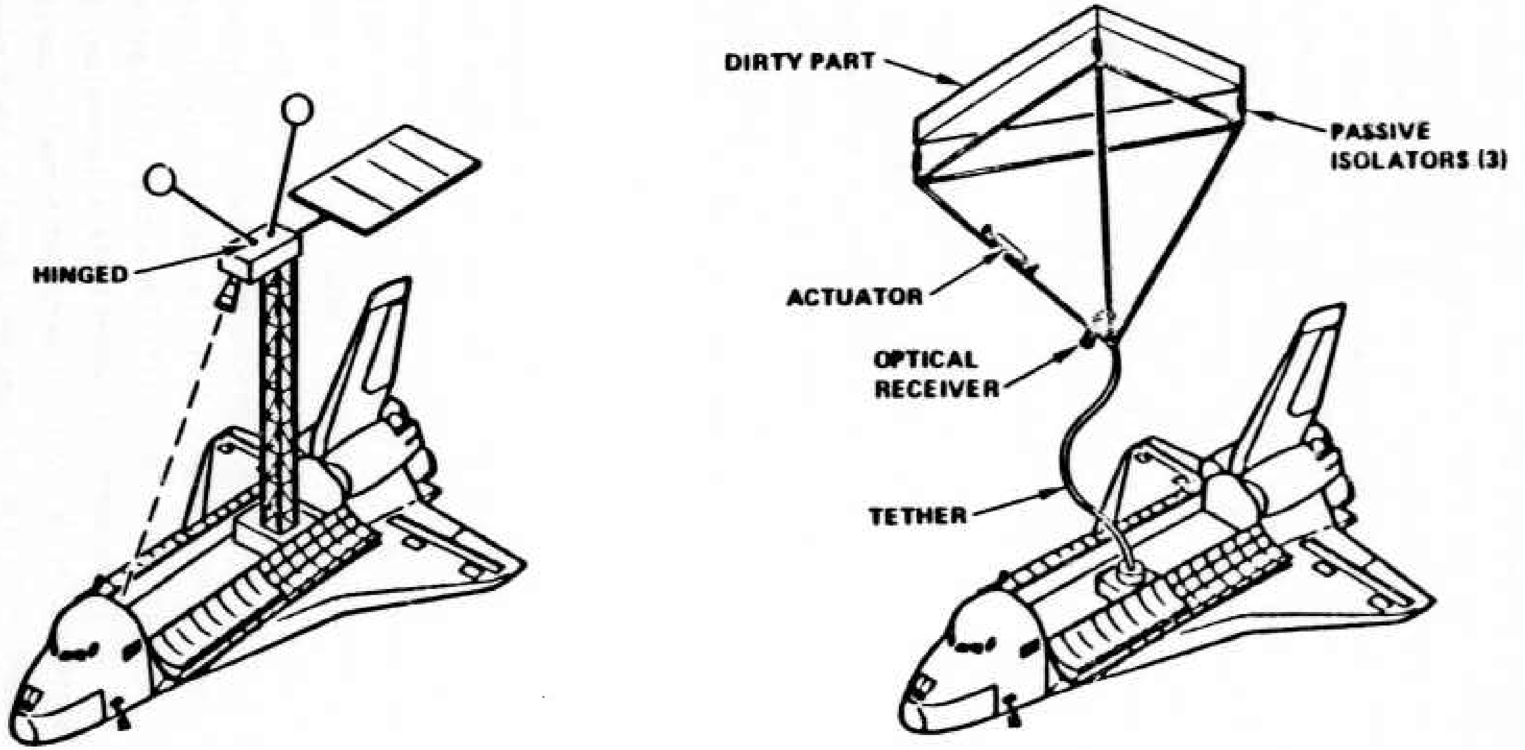

A. Rigidly Attached to Pallet

B. Tethered

Figure 3-6. Illustration of Attached and Tethered Configuration Using the Modular Approach

Two optical structures were conceptualized. The first, sketched in Figure 3-7, is of an Offset Cassegrain structure. The primary is parabolic, the secondary is hyperbolic and the focal plane/detector is sideways behind the primary mirror. The entire structure fits in one shuttle pallet. The concept was equipped with actuators, sensors, and an optical train to enable one to test vibration control, isolation, figure control and, via monitored shuttle motion, active damping. The optical field-of-view of this was expected to be small, perhaps $0.5° \times 0.5°$. The main experiment therefore envisioned to image a star as a point light source at infinity. The quality of the image in the presence of various disturbance acting on the optical train would then be used to assess the effectiveness of active structural control. Earth imaging was a secondary experiment.

The second optical structure conceptualized is sketched in Figure 3-8. This configuration retains the essence of the two mirror system but eliminates the secondary mirror and relocates the focal plane/detector to where the secondary used to be. It was initially believed that this approach would result in a more reasonable optical geometry while retaining the geometric/jitter sensitivities projected for future systems. It will be shown in Section 4.0 that this is not true.

3.5 Test Structure Candidates

The addition of the dedicated systems to the NASA and AF missions made the trades described in Section 3.3 possible. The results of these trades are: no near term NASA structures suitable to meet DARPA POC objectives could be identified. Those that are of interest are in the future and are too uncertain to commit a POC experiment design. Many of the DoD missions examined could be used but the data required to decide on whether the structure is really usable is unavailable. Hence, reliance on projected missions to design a POC test is too risky. Strictly generic structures were also considered but these are hard to justify for a costly flight experiment. The POC test has to simultaneously demonstrate a technology to make it worthwhile. Existing and funded systems were additionally considered to meet this later requirement but these systems were found to be antennas; too complex, too expensive, and it was not even clear that they required the

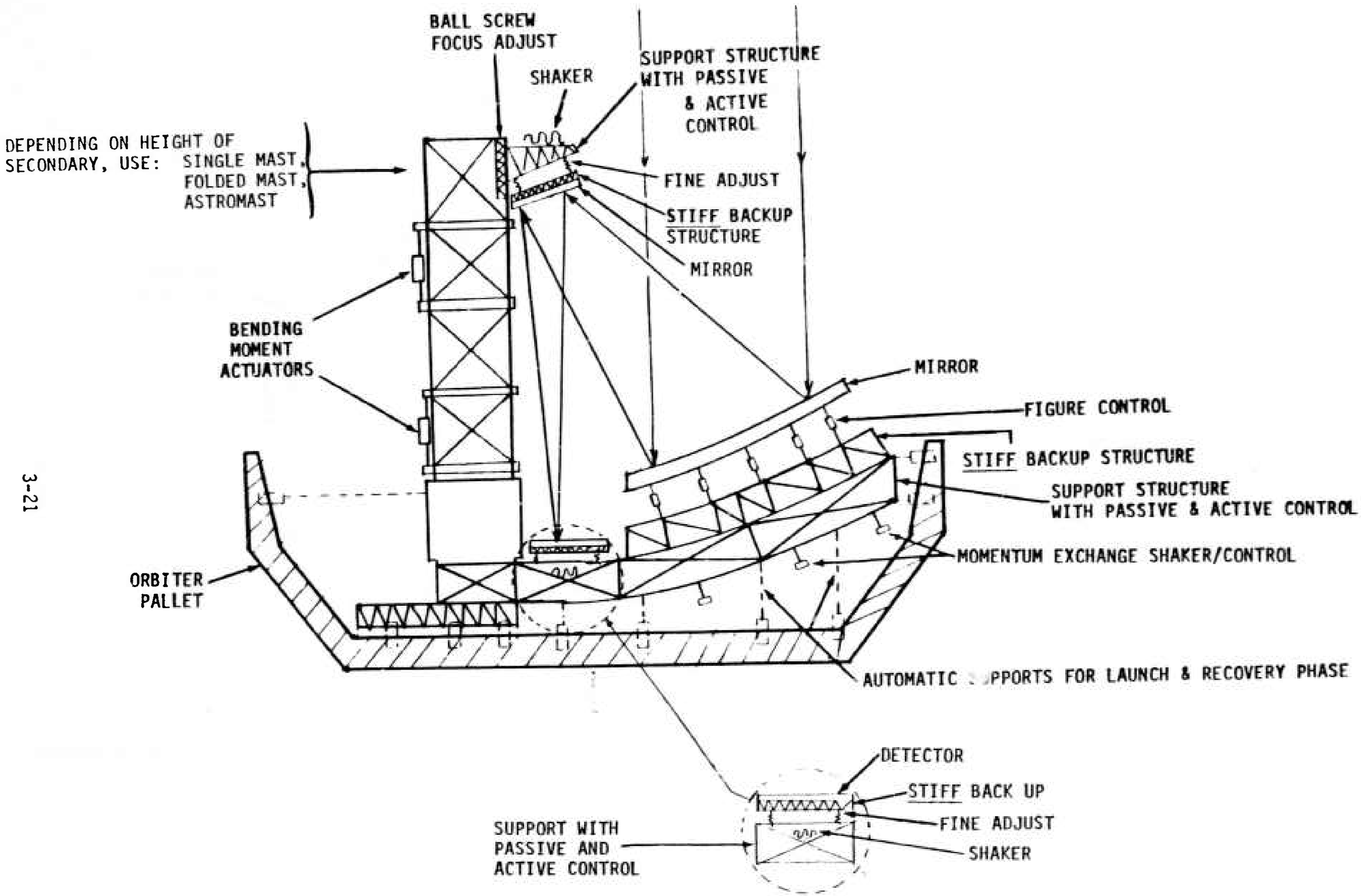

Figure 3-7. Offset Cassegrain, Two Mirror Telescope Concept

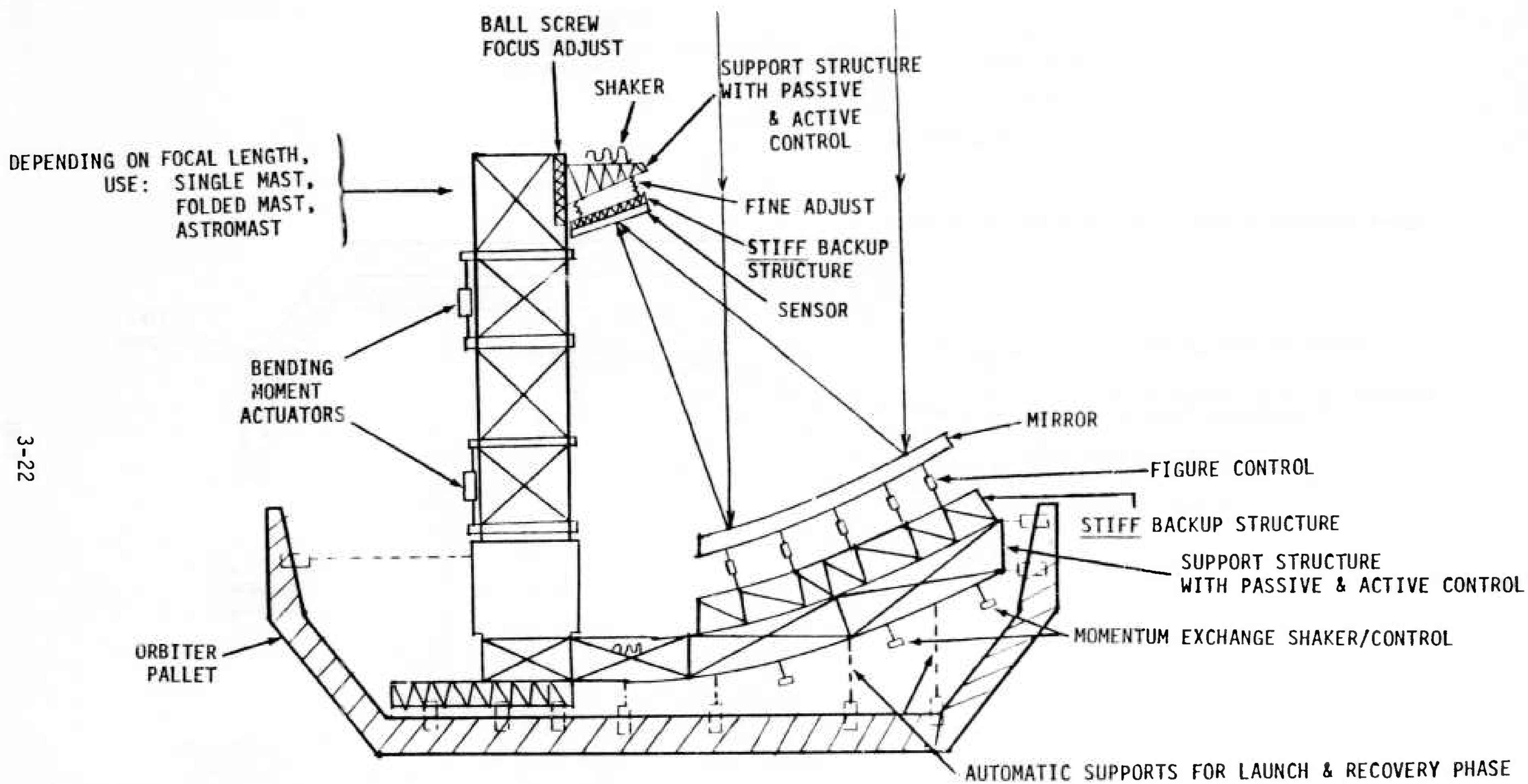

Figure 3-8. Single Mirror Telescope Concept

technology. Therefore, since DARPA's interests seem to lie in large optical systems, we recommended the study of an on-orbit POC structure supporting this technology. The two telescope structures incorporating a lightweight mirror were therefore chosen for further, more detailed analysis.

4.0 TEST STRUCTURE DESIGN AND ANALYSIS

Two concepts for the optical system configuration were considered: the single mirror concept and the two mirror cassegrain configuration. In the following the two concepts are discussed and the advantages and drawbacks of each approach are explained. The reasons for the selection of the two mirror approach and the details of the chosen configuration are given. The model data obtained from finite element program is presented.

4.1 Optical Prescription for Single Mirror Concept

In designing the optical system we are trying to achieve two goals:
(i) To arrive at an optical system exhibiting similar sensitivity to geometric distortions and jitter anticipated in optical trains of future systems.
(ii) To make use of existing optical hardware, with possibly some modifications.

The single mirror configuration was considered as a possible candidate for the optical system because its simple geometry results in a less complicated structure. The simplicity of the single mirror design is apparent in the ray traces of its optical prescription as shown in Figure 4-1. The effectiveness of the active structural control system will be assessed by imaging a star as a point light source at infinity. The quality of the image in the presence of various disturbances acting on the optical train will serve as the performance measure of the control system.

Although the single mirror configuration has a simple structure, it suffers from an inherent nonuniformity of the image resolution over the field of view (field angle) as can be seen in Figure 4-2. This inherent drawback of the single mirror optical system makes it unacceptable as a POC test structure: The vernier thruster (VRCS) shuttle limit cycle has excursions of $\pm 0.1°$. Thus at least a $0.3° \times 0.3°$ field of view will be required to image a star. The motion of the star image in the focal plane due to the shuttle limit cycle occurs at a very slow (0.01 deg/sec) and predictable rate and can be easily removed

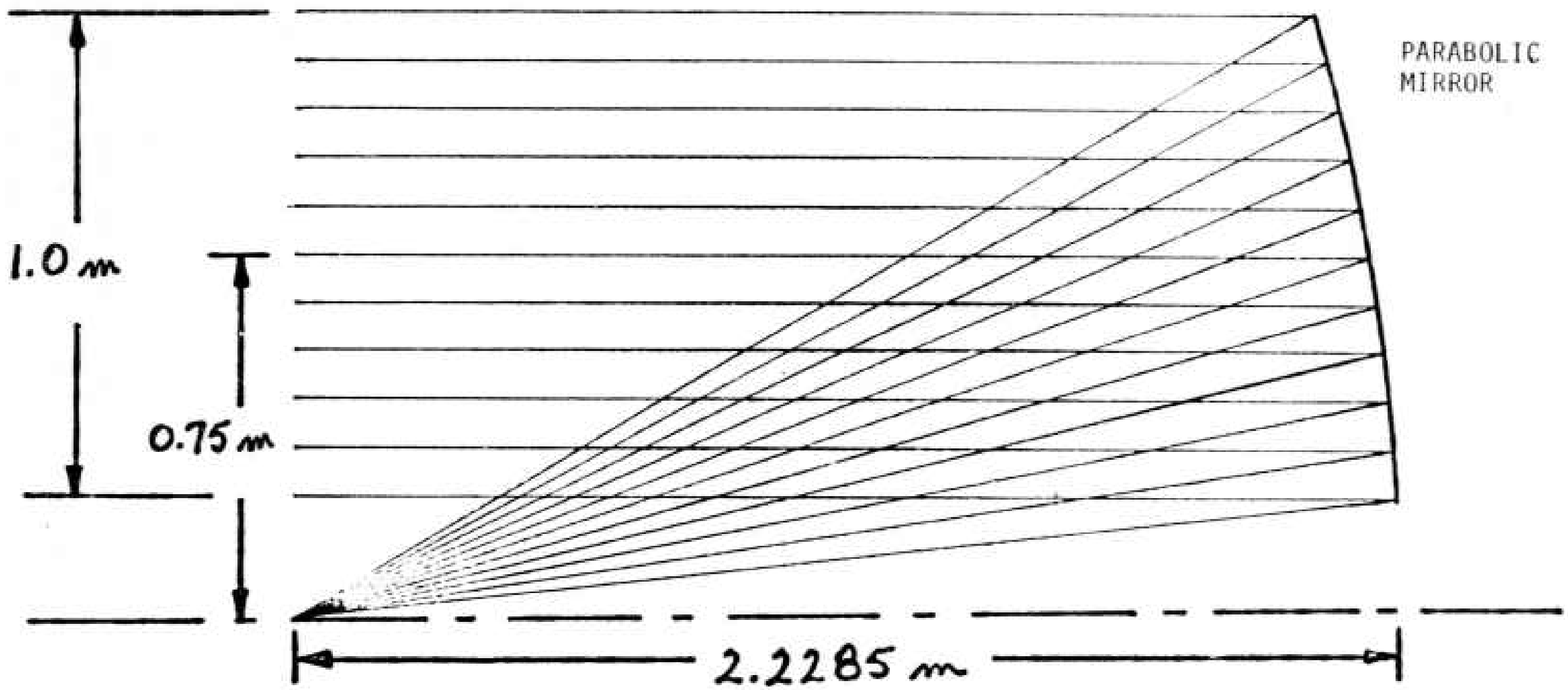

Figure 4-1. Optical Prescription of Single Mirror Concept

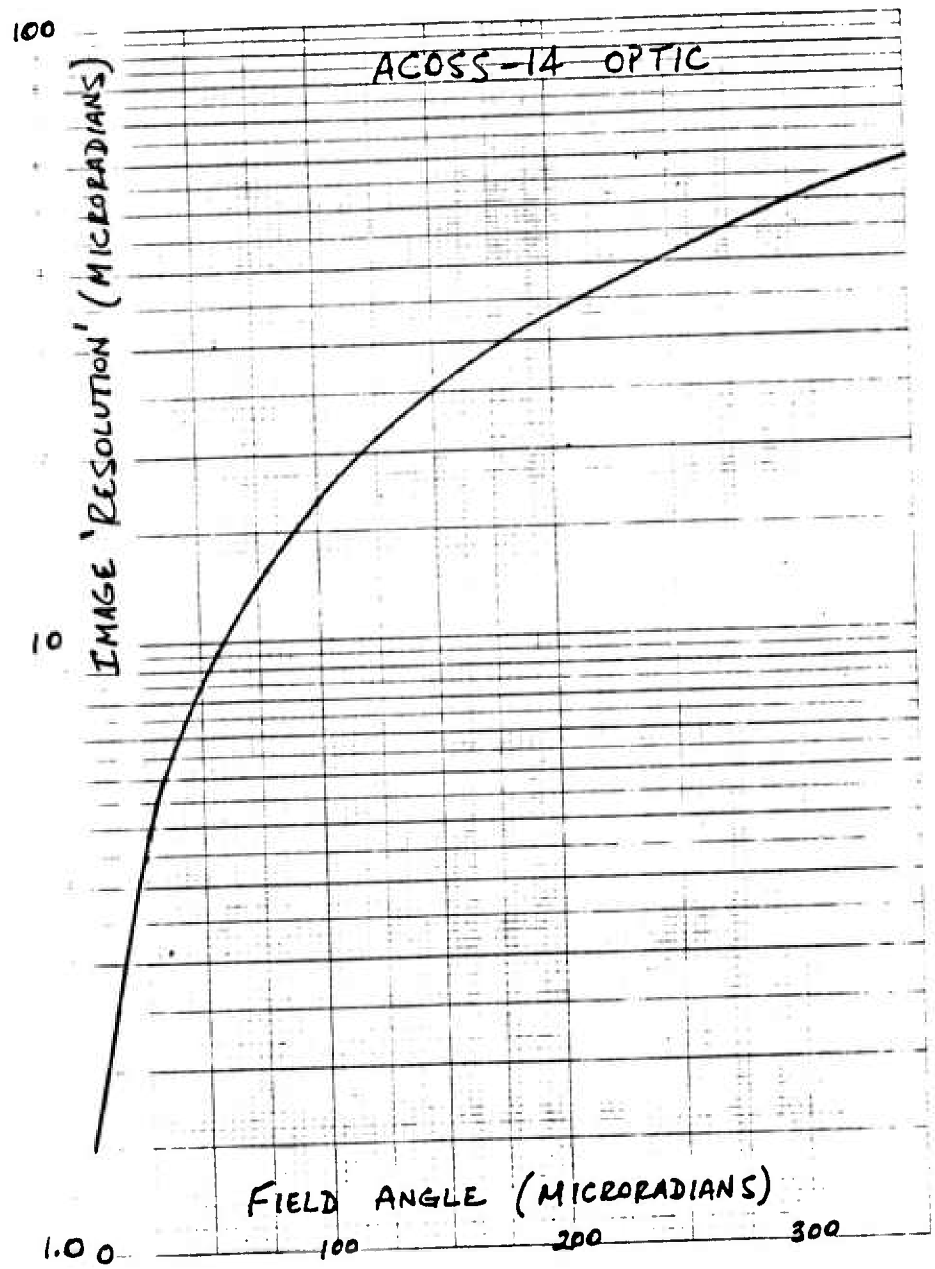

Figure 4-2. Performance of the Single Mirror Concept

post facto from the observation data. However, it is extremely difficult, if not impossible to decide how much of the loss of resolution is caused by vibrations in the optical structures which are to be controlled or by the resolution deterioration incurred as the star image moves away from the center of the field of view (FOV).

4.2 The Two Mirror, Offset Cassegrain Structure

Because of the drawbacks of the single mirror concept explained in Section 4.1, it was decided to go with a two mirror, offset Cassegrain system. This configuration allows for an optical design which provides a more uniform resolution over the FOV as compared to the single mirror approach. The structure for the Cassegrain system is designed to have the focal plane assembly in between the primary and the secondary mirrors. The total distance along the optical center between the primary and secondary surfaces is only 1.77 m, assuming a mast not exceeding 2.5 meters. Thus, the entire structure fits within the Shuttle cargo bay envelope with cargo bay doors closed and therefore no deployment mechanisms are needed.

The optical prescription of the two mirror, offset Cassegrain structure is shown in Figure 4-3. It represents a preliminary optical design, which is more than adequate for our present purpose of defining an opto-mechanical test structure. The optical configuration of the Cassegrain structure consists of two mirrors: a parabolic primary mirror and a hyperbolic secondary. The salient data of the system is given in the following:

<u>System</u>

Effective Focal Length: 3.5m
Field-of-View: 0.01x0.01 rad
Focal Plane: 3.5x3.5 cm

<u>Primary: Parabolic Surface</u>

Diameter of Off-Axis Segment: 1.0m
Radius of Curvature: -4.1464m
Focal Length: 2.0732m

<u>Secondary: Hyperbolic Surface</u>

Aperture Diameter: 0.15m
Radius of Curvature: -1.4718m
Focal Length: 0.4032m
Eccentricity: 3.906

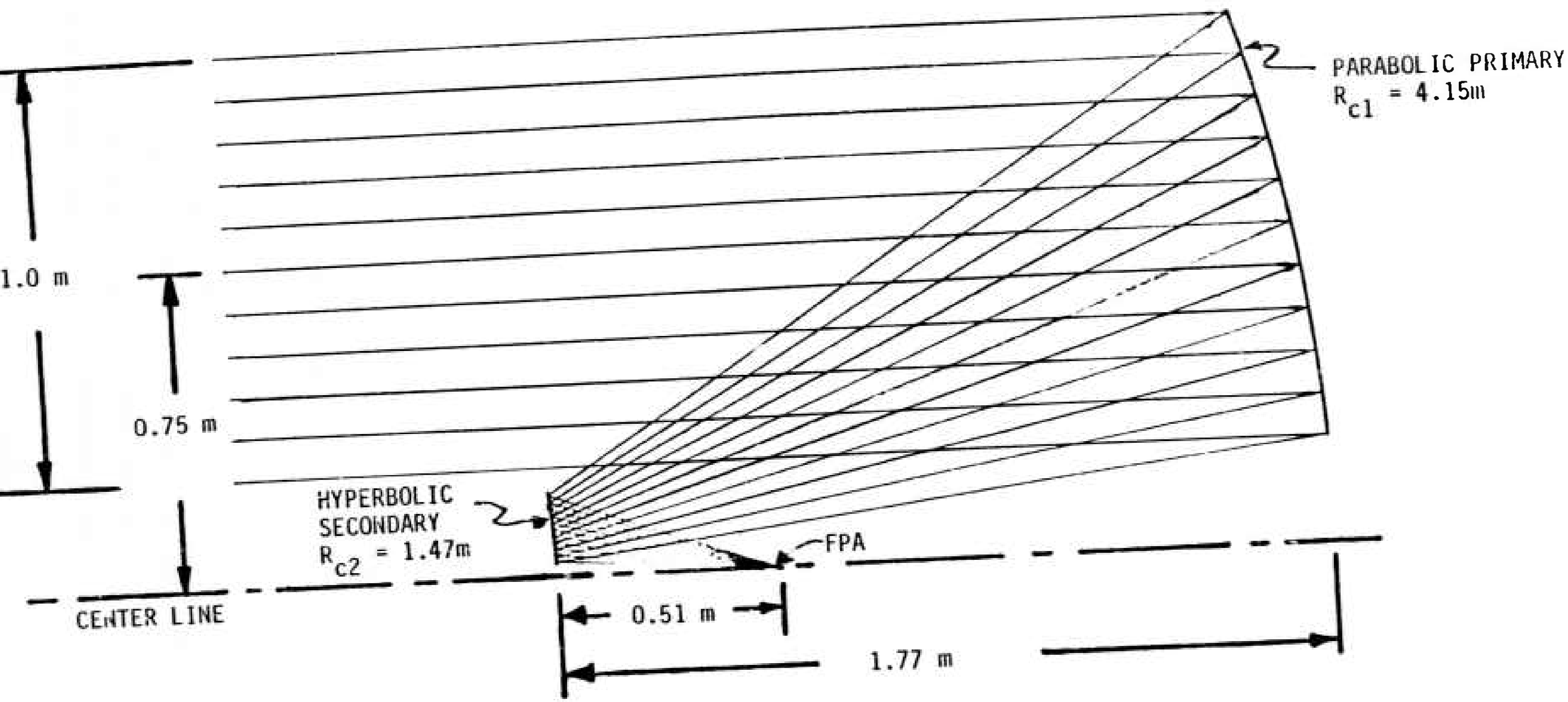

EFL: 3.5m
FOV: 0.57x0.57 DEG
FPA: 3.5x3.5 cm (1.38x1.38 inches)

SCALE: 1/15

Figure 4-3: Optical Prescription of Offset Cassegrain Concept

The FOV in this configuration is 0.01x0.01 rad (0.57x0.57 deg). It allows imaging a star while the Shuttle undergoes $\pm.1$ degree limit cycle motions. As mentioned before, this highly predictable and very slow Shuttle rate of 0.01 deg/sec can be removed from the data post facto. Another advantage is that the reasonable FOV size also makes earth viewing a meaningful experiment.

The performance of this preliminary optical design is shown in Figure 4-4. By shifting the focal plane by +1.8mm out of focus a relatively uniform resolution of 100 μrad over the FOV can be achieved. This resolution is not sufficient for an actual on-orbit test structure and a fine tuned optical design. Improvement of resolution and the uniformity of resolution are needed before such a system could be built. This, however, is not the intent at this point. At this stage it is merely important that the system concept selected and the resulting structure allow for a high quality optical design. This can be accomplished by either figuring the primary and secondary surfaces as aspherics, or by adding a third reflective element. A very desirable approach for an on-orbit POC structure would be to leave the large primary surface as a parabola, add a refractive element between the secondary and the focal plane, aspherize the secondary surface and design the refractive element to optimize the optical performance. Of key interest here is the fact that such optical design improvements will not affect the structural concept nor its physical dimensions.

4.3 Baseline Structure Design of the Two-Mirror Offset Cassegrain Concept

The baseline test structure was designed to withstand launch and landing loads while being extremely complient in space. To accomplish this task, flexible structures are used to support the mirrors and the sensor package. These structures are in turn supported by caging devices during period of critical loading.

The design of the test structure is shown in Figure 4-5. It consists of an L shaped structure which supports the primary and secondary mirrors, a mast and primary mirror caging mechanisms, primary mirror's coarse and fine actuators, and secondary mirror control

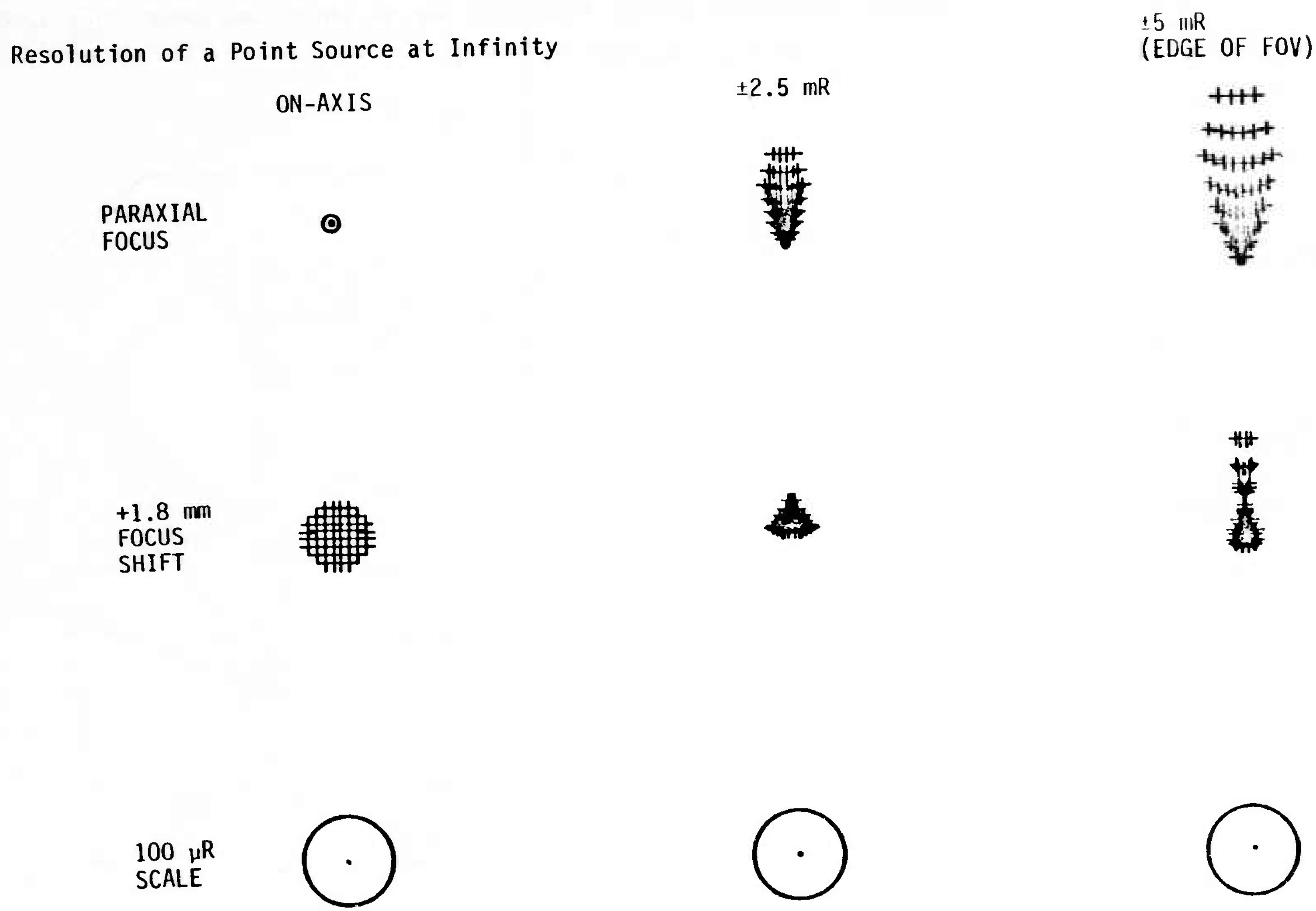

Figure 4-4. Performance of the Offset Cassegrain Concept

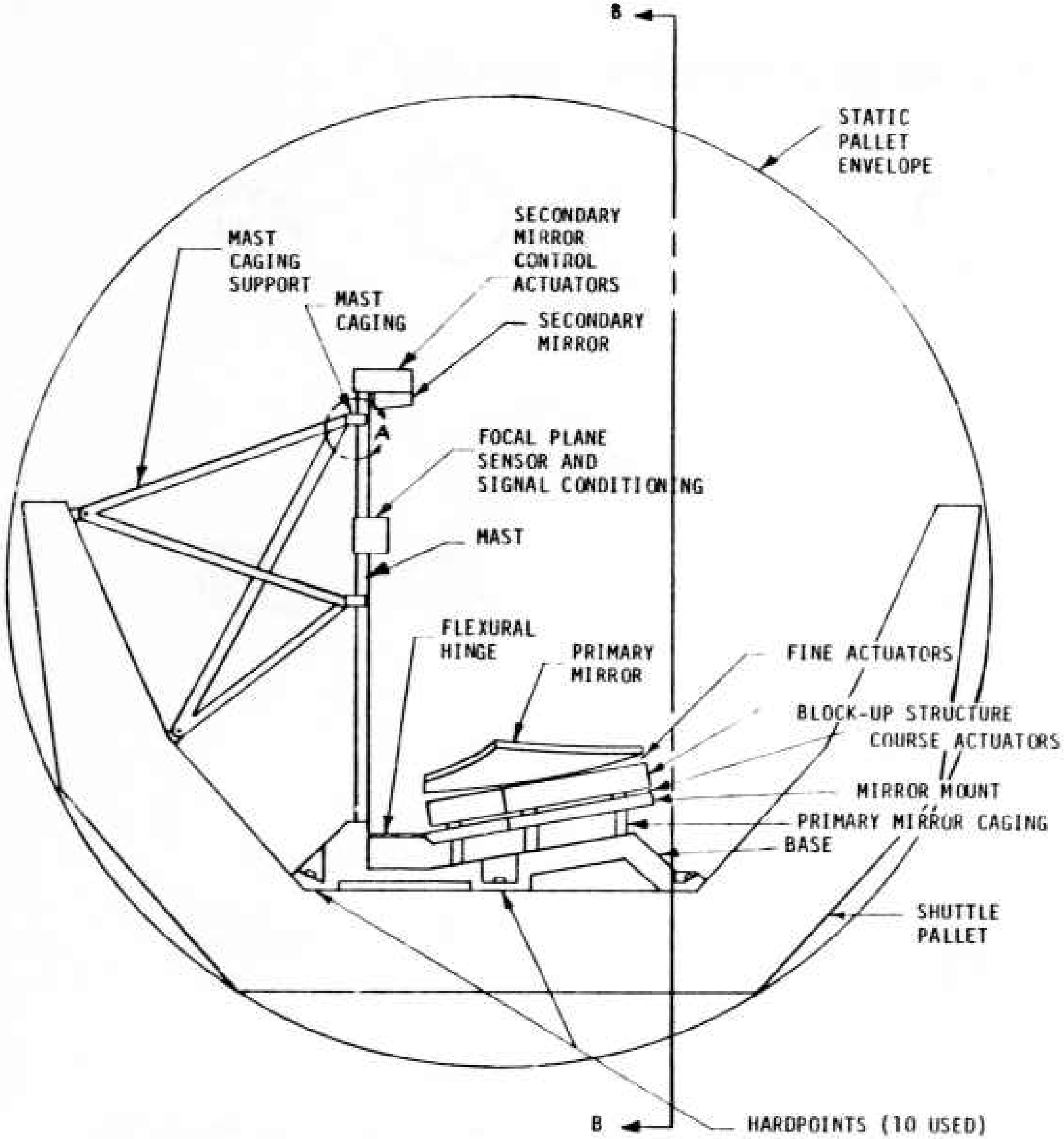

Figure 4-5. Baseline Design of the Two-Mirror Offset Cassegrain Concept

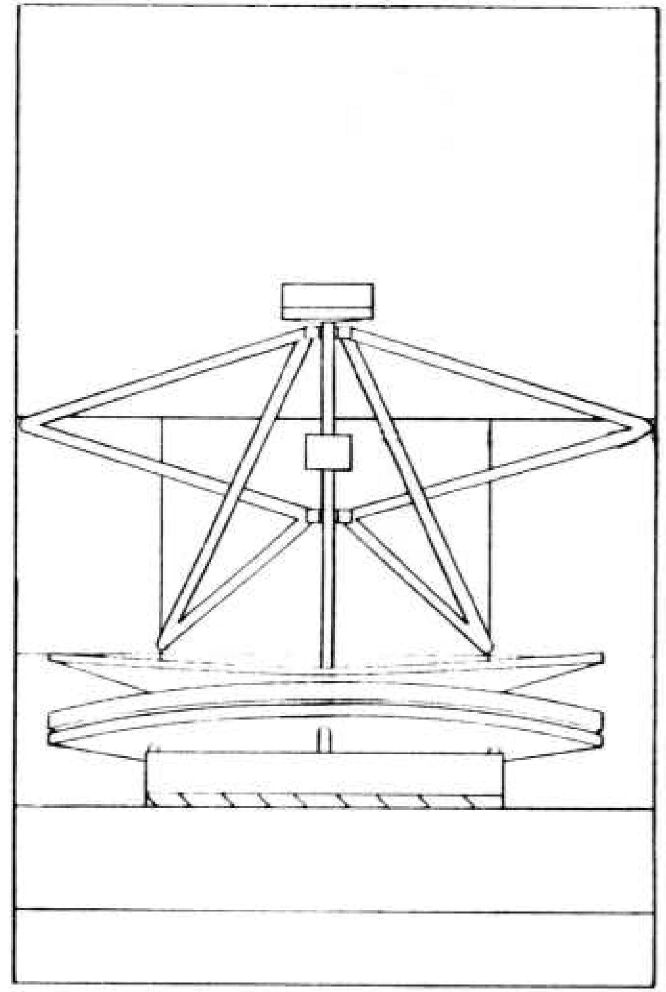

SECTION B-B

actuators. The structure is mounted on a base which is connected to the Shuttle pallet at ten attachment points.

The coarse actuators of the primary mirror system are mounted on a graphite-epoxy honeycomb panel. This panel is attached to the base by two paths. When the experiment is not being used, a set of caging devices is closed, rigidly connecting the mirror mount to the base. When testing, these caging devices are opened to allow limited free movement of the mirror ($\pm$3mm). However, movement large enough to damage the structure is prevented by a pair of low thermal expansion graphite epoxy flexural hinges that support the primary mirror system. The fundamental frequency of the hinge mirror system is ~2 Hz.

The primary mirror caging mechanism is shown in Figure 4-6a. It consists of a motor and gearhead combination which automates the opening and closing of jaws through a rack and pinion gear train. The jaws close on a T-bar which is connected to the mirror support. The major forces exerted by the T-bar on the jaws are perpendicular to the allowed movement of the jaws, so the motor does not carry the load where the jaws are open. The primary mirror is allowed limited free motion in all axes.

The support mast for the secondary mirror and sensor package has a fundamental resonance frequency of 2.7 Hz. The mast is caged and is also made of low thermal expansion graphite-epoxy. It is a tube approximately 6 cm in diameter by 2mm thick. The secondary mirror is attached to the top of the mast and has variable height and angle actuators. The sensor package is one third of the way down, see Figure 4-5.

The caging devices for the mast are shown in Figure 4-6b. These devices have two movable, beveled jaws on each side of the mast. The jaws fit into matching "V" slots in a bar through the mast. This provides caging in all axes when the jaws are closed. The caging devices are attached to the pallet by a truss of tubes from the pallet.

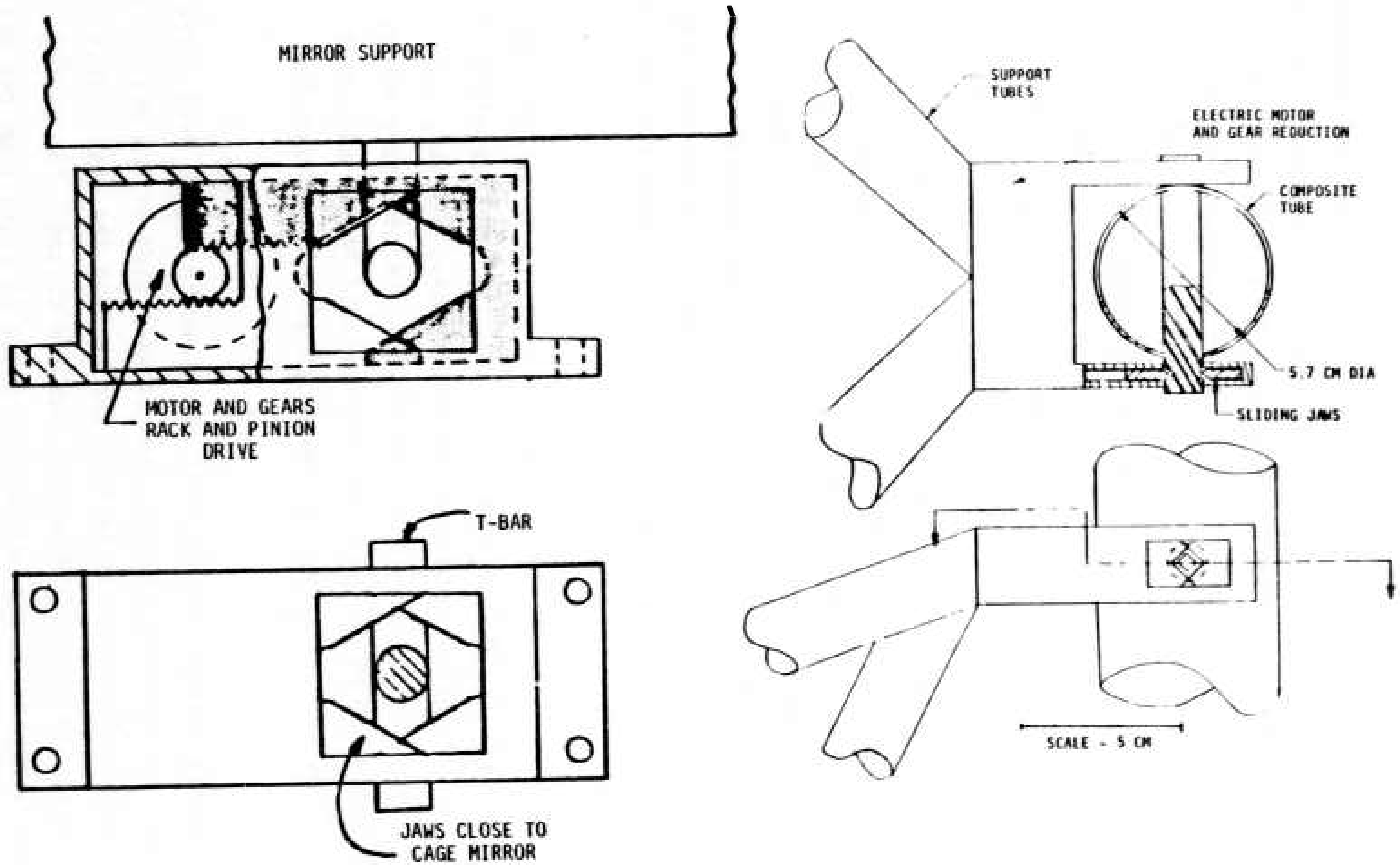

(a) Primary Mirror Caging

(b) Mast Caging

Figure 4-6. Caging Mechanisms

4.4 Modal Analysis of the Test Structure

A finite element model of the structure with the two mirrors attached to it was developed. The structural model included 43 truss elements and 31 two dimensional elements. The resultant dynamic model included 50 nodes each one having six degrees of freedom in space, giving a total of 300 degrees of freedom. In developing the test structure's model, it was assumed that both mirrors were very stiff, the fundamental frequency of the primary mirror was assumed to be ~400 Hz. The modal analysis was performed using the TRW finite element program TRWSAP.

Two sets of modal frequencies and mode shapes were generated:

(i) The free-free modal representation of the test structure including mirrors.

(ii) The modal representation of the test structure (mirror included) assuming that the base is attached to the ground. These modes will be referred to as the cantilevered modes.

Tables 4-1 and 4-2 show some of the modal frequencies for both the free-free and cantilevered boundary conditions. The first four mode shapes of each case are shown in Figures 4-7 and 4-8. As it can be seen from the tables, there is a significant jump in free-free model frequencies after the first two modes. However, when the structure is cantilevered two more modal frequencies are lowered. In general, it can be said that the structure behaves like two cantilevered beams.

Table 4-1. Free-free Modal Frequencies of Test Structure

MODE NUMBER	FREQUENCY $f_s(H_z)$	DESCRIPTION
1-6	0	Rigid body modes
7	2.896	Secondary mirror moves along x, primary moves along z
8	3.767	Primary mirror rotates around x, Secondary mirror moves along y
9	17.860	Secondary moves along x, primary rotates around y
10	20.413	Secondary mirror moves in y direction
11	40.644	Mast motion in yz plane
12	45.148	Mast bending in xz plane, primary mirror motion in z direction
13	127.831	Rotation of secondary mirror about the y-axis
14	147.467	Rotation of secondary mirror around x-axis
15	157.887	Rotation of secondary mirror around x-axis and motions of primary mirrors support

Table 4-2. Cantilever Modal Frequencies of Test Structure

MODE NUMBER	FREQUENCY f_s(Hz)	DESCRIPTION
1	1.970	Bending of Primary mirror in xz plane
2	2.637	Bending of mast (and secondary mirror) in zy plane
3	2.640	Bending of mast (and secondary mirror) in xz plane
4	4.872	Torsion of primary mirror around the y-axis
5	22.360	Bending of mast (and secondary mirror) in xz plane
6	23.014	Bending of mast in yz plane
7	40.881	Bending of mast in xz plane
8	48.444	Torsion of primary mirror around y-axis
9	50.654	Motion of primary mirror in z direction
10	124.505	Motion of secondary mirror in t direction

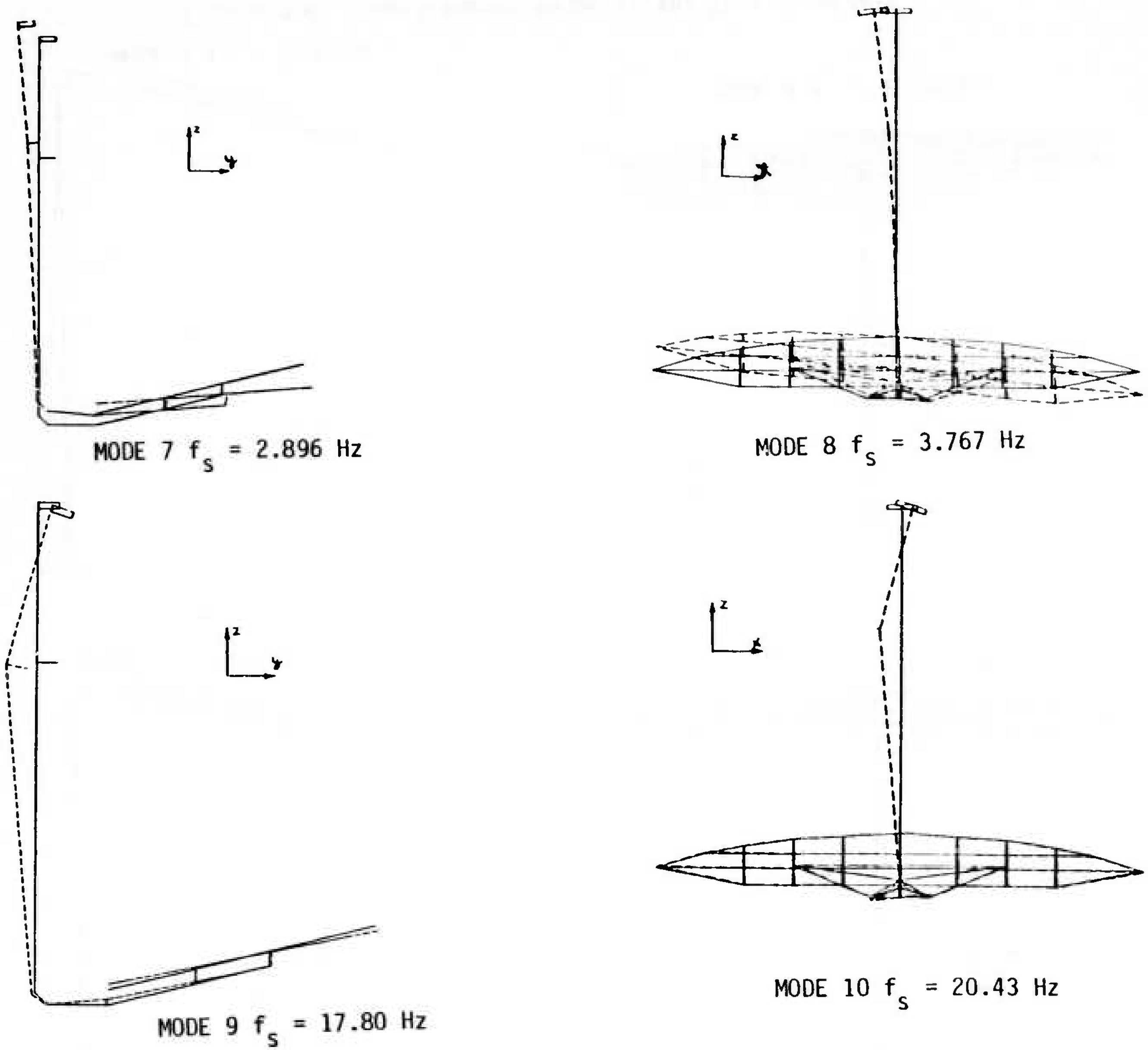

Figure 4-7. Free-free Modes of the Test Structure

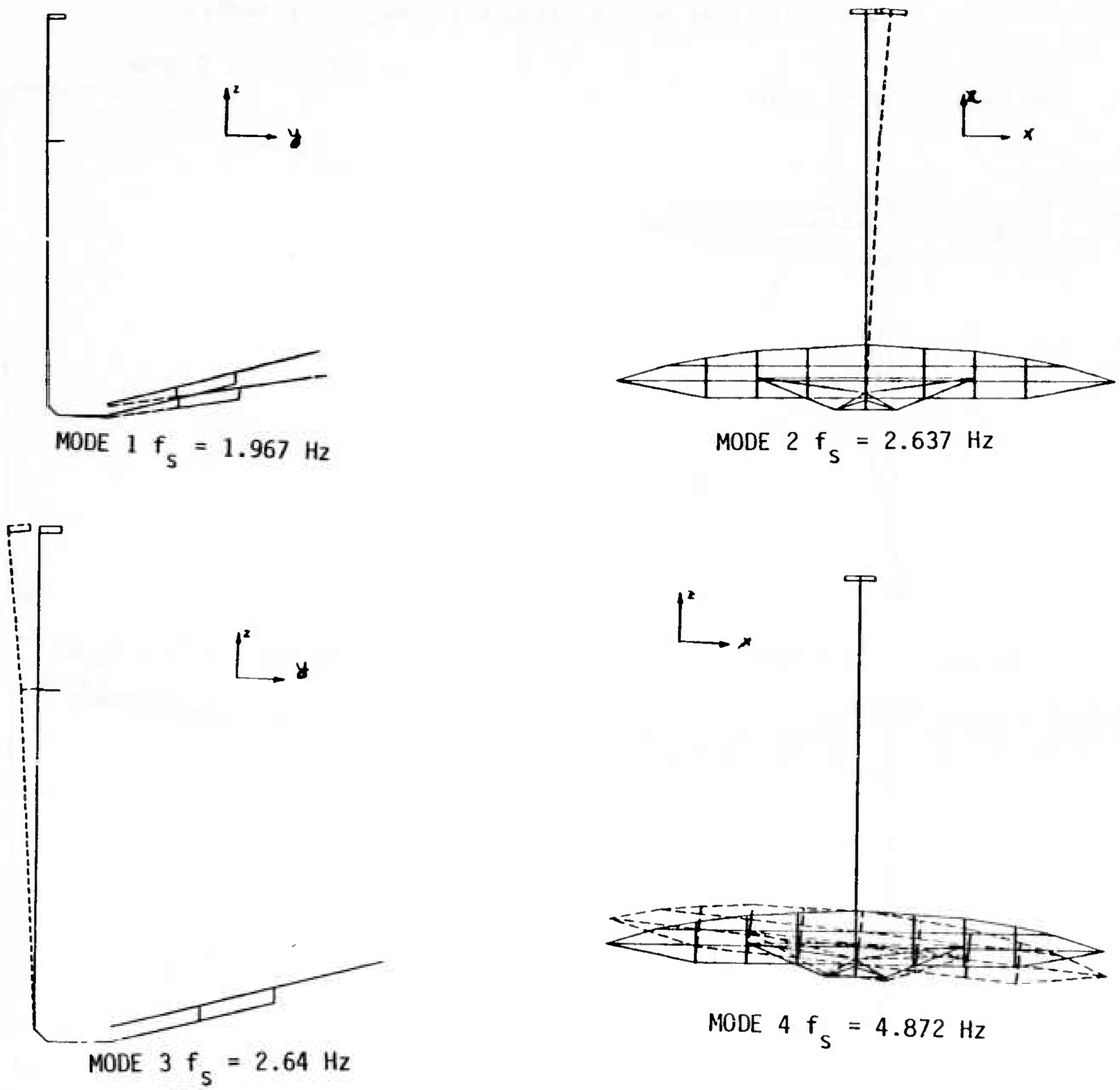

Figure 4-8. Cantilevered Modes of the Test Structure

5.0 DYNAMIC INTERACTION WITH THE ORBITER

The motivation for the dynamic interaction study is to assess the effect of mounting the structure on the normal operation of the Shuttle Orbiter. In addition, one would like to determine the influence of the Shuttle thrusters firings on the structure's oscillation so that they can be taken into account in the design of the control law demonstration experiments.

Areas of special interest are the effect of added structural flexibility on the system's dynamic behavior and the influence of excitation forces applied to the structure during experiments on the normal operation of the Digital Autopilot (DAP). It will be shown that the additional vibrational modes of the test structure mounted on the Orbiter do not couple with the Shuttle's modes and therefore do not result in high amplitude vibrations. It will be also shown that the excitation forces which act on the structure during experiments do not affect the Shuttle's RCS system operation. The simulation study shows that the number of thrusters firings does not change significantly with the addition of the test structure and thus the fuel consumption remains virtually unchanged.

Another area of interest investigated was the amount of excitation exerted on the structure by the RCS firings. The level of this excitation must be assessed in order to correctly design the experiments and to determine the additional excitations needed to demonstrate the control law performance.

A dynamic simulation study was performed using a TRW developed digital simulation program. The dynamic model of the coupled system was obtained by combining the modal representations of the Orbiter and the test structure using a TRW modal synthesis program, KOMBINE. A detailed model of the DAP was implemented using the up-to-date parameters obtained from JSC. Special features were added to the program to simulate the conditions during the experiments. The simulation program is highly modular and can be easily modified by adding and/or changing specific subroutines which might be needed. This feature allows one to perform simulation studies on different structures and various flight conditions with minimum additional programming effort.

5.1 Systems's Dynamic Representation

The system's dynamic model was obtained by combining the modal data of the Orbiter and the test structure. The modal synthesis approach allows one to make changes in the test structure without running an expensive finite element program each time a dynamic model of the total system is required. The combination procedure was performed by a TRW developed program KOMBINE which will be described in the following section. Since the dynamic model of the Shuttle obtained from Rockwell International was given in terms of the Orbiter's structural coordinate system [8], this coordinate system was adopted as the reference system for the current study (see Figure 5-1). In order to avoid confusion, all quantities and locations were transformed into this coordinate system. This includes DAP parameters and thruster firing directions expressed in different coordinate systems in Shuttle's original documents.

5.1.1 Modal Synthesis Program KOMBINE

Most of the existing structure modeling computer programs are general purpose programs and therefore are very expensive to run. The modal synthesis program developed in TRW permits fast and efficient modeling of a flexible assembly which consists of any number of interconnected flexible and rigid bodies. The program reads the free-free modal representation of each body in the assembly and combines them sequentially into one system. The program can accommodate very general interfaces between any two adjacent bodies, including gimballed and flexible connections. Moreover, any two bodies can be connected at more than one point which allows for closed topological loops. The resultant dynamic model is linear since the bodies modal representation is used as input. However, the program allows large angle relative rotations between any two adjacent bodies. Therefore, it is possible to conduct sensitivity studies of the dynamic representation as a function of system's configuration. The program has also an option of calculating the mass properties of the combined body and of any of the given substructures. This feature is useful in propulsion system and fuel consumption studies. The program accepts modal data calculated by standard finite element programs such as NASTRAN and TRWSAP. Moreover, KOMBINE is

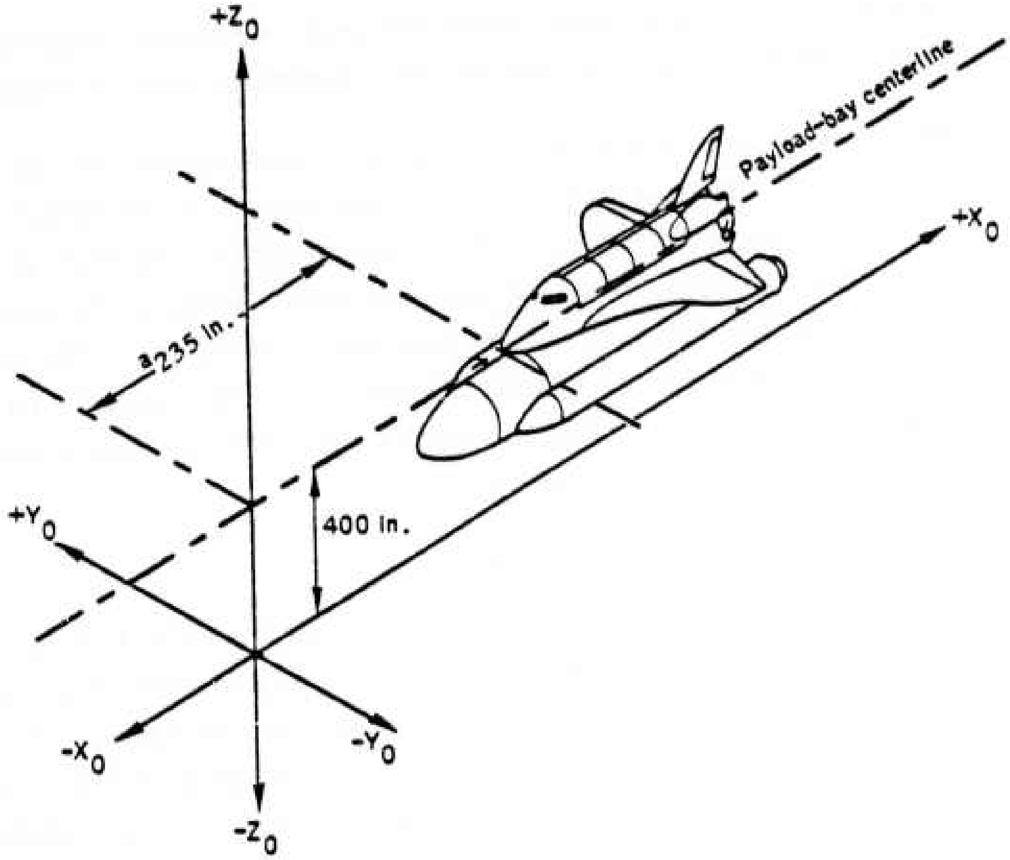

ORIGIN: In the orbiter plane of symmetry, 400 inches below the center line of the payload bay and 235 inches forward of the tip of the orbiter nose fairing.

ORIENTATION: The X_0 axis is in the vehicle plane of symmetry, parallel to and 400 inches below the payload bay centerline. Positive sense is from the nose of the vehicle toward the sail.

The Z_0 axis is in the vehicle plane of symmetry, perpendicular to the X_0 axis. Positive upward in landing attitude.

The Y_0 axis completes a right-handed system.

Figure 5-1. The System's Reference Coordinate System

compatible with existing control system analysis and design programs such as FLYNSYS. The flow chart diagram of the program is shown in Figure 5-2.

KOMBINE is as accurate as a finite element program but its run costs are 1-2 orders of magnitude less. This is achieved by using numerically stable and efficient algorithms. The procedure avoids inversion of ill-conditioned matrices by eliminating the constrained modes using singular value decomposition which does not require matrix inversion. The program can be run in either batch or timeshare modes, although for most applications the memory available in the timeshare mode is sufficient. The average cost for combining 2 to 4 bodies is \$1-\$5.

5.1.2 Combined Systems' Modal Representation

The dynamic representation of the orbiter was obtained from Rockwell International in the form of free-free modal frequencies and displacements. The given model included 200 modes and 567 modal displacements. The structure was modeled as being attached to one of the existing cargo ports. The cargo port chosen is one of the right-hand side attach points at $X_0 = 1017.870$, $Y_0 = 94$, $Z_0 = 424$ (node number 369 in the Orbiter's model). The attachment to this node is representative and is used to generate a typical system's behavior. Attachment to any other point would not alter the conclusions of the study.

The model of the complete system, Orbiter and test structure was obtained by combining 30 free-free modes of the Orbiter with 30 free-free modes of the structure by using the modal synthesis program KOMBINE. This particular number of modes was chosen after concluding that a higher number of modes does not change the dynamic representation of the complete system. In order to keep the combined system's model at a manageable size for simulation and analysis studies, only selected nodes were retained in the final model. Table 5-1 shows the numbering of the selected nodes and their locations. A schematic drawing of the structure indicating nodes' locations is given in Figure 5-3. The CPU run time of the modal synthesis process was $\sim$ 2 sec and the total run cost on the CDC CYBER175 was \$3.00. Thus, model generation is easy and inexpensive and, if future changes are needed either in the structural model or in the number of modes used, they can be easily implemented in the simulation.

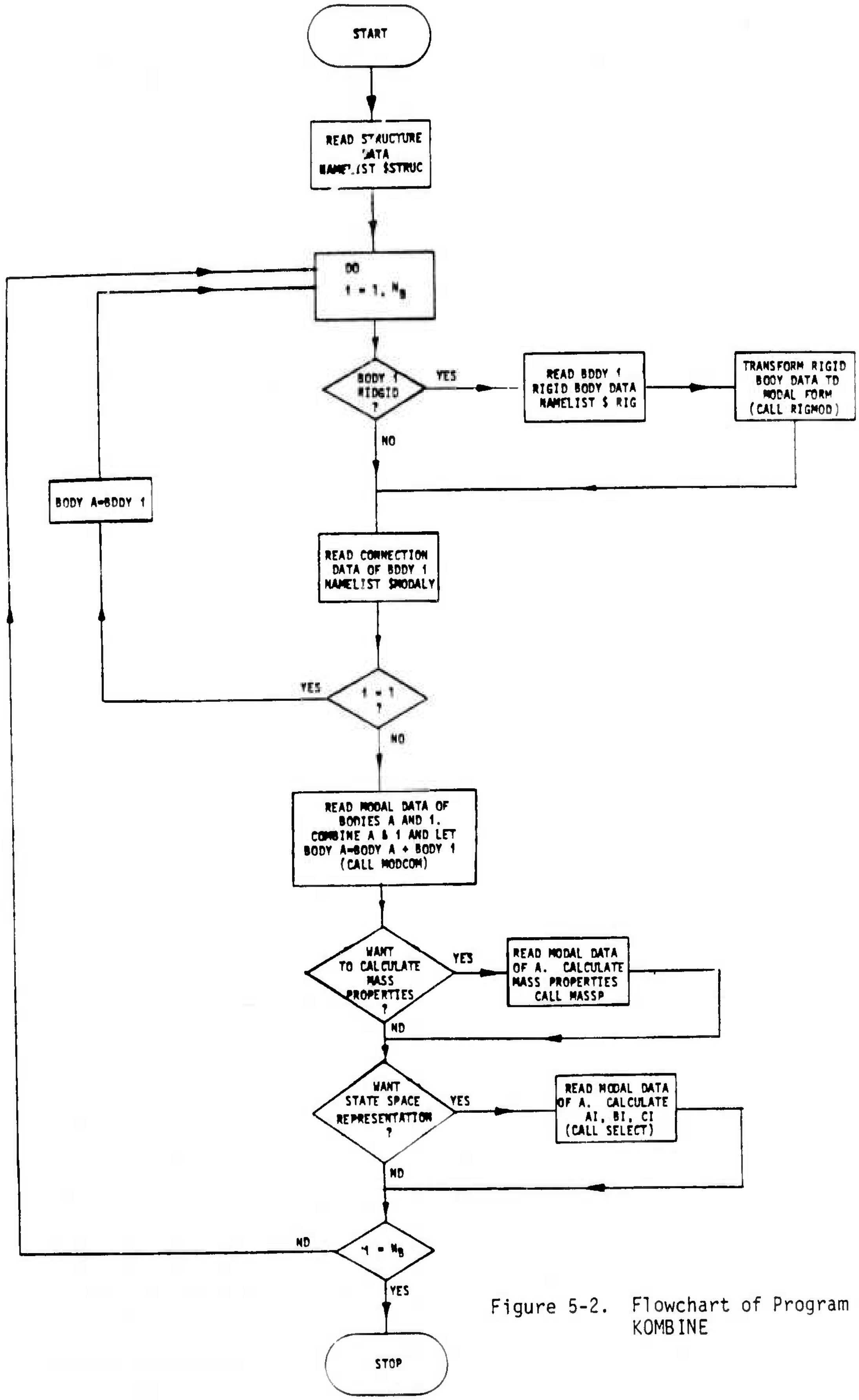

Figure 5-2. Flowchart of Program KOMBINE

Table 5-1. System's Node Location

NODE NO.	LOCATION (in)			DESCRIPTION	NODE NO.	LOCATION (in)			DESCRIPTION
	x_o	y_o	z_o			x_o	y_o	z_o	
1	1028.80	105.80	496.60	MAJOR ATTACHMENT POINT	14	1087.70	72.90	479.60	PRIMARY MIRROR SUPPORT
2	1028.80	159.00	549.80	FOCAL PLANE POINT	15	1044.70	72.90	522.60	PRIMARY MIRROR SUPPORT
3	1028.80	184.60	575.40	TOP OF MAST	16	1028.80	123.50	514.30	POINT ON MAST
4	1032.20	155.60	549.80	FOCAL PLANE POINT	17	1028.80	141.10	531.90	POINT ON MAST
5	1030.80	101.80	494.60	ATTACHMENT POINT	18	1028.80	171.80	562.60	POINT ON MAST
6	1035.20	180.20	571.40	POINT ON SECONDARY MIRROR	19	324.35	59.70	350.12	FRONT VRCS THRUSTER
7	1029.20	180.20	577.40	POINT ON SECONDARY MIRROR	20	324.35	-59.70	350.12	FRONT VRCS THRUSTER
8	1054.40	81.70	498.10	PRIMARY MIRROR SUPPORT	21	1565.00	-118.00	455.44	REAR VRCS THRUSTER
9	1028.90	183.50	574.40	POINT ON SECONDARY MIRROR	22	1565.00	118.00	455.44	REAR VRCS THRUSTER
10	1040.60	92.00	494.60	ATTACHMENT POINT	23	1565.00	-149.87	459.00	REAR VRCS THRUSTER
11	1054.40	84.10	500.50	POINT ON PRIMARY MIRROR	24	1565.00	149.87	459.00	REAR VRCS THRUSTER
12	1087.70	75.30	525.00	POINT ON PRIMARY MIRROR	25	497.00	0.00	395.00	IMU SENSOR LOCATION
13	1044.70	75.30	525.00	POINT ON PRIMARY MIRROR					

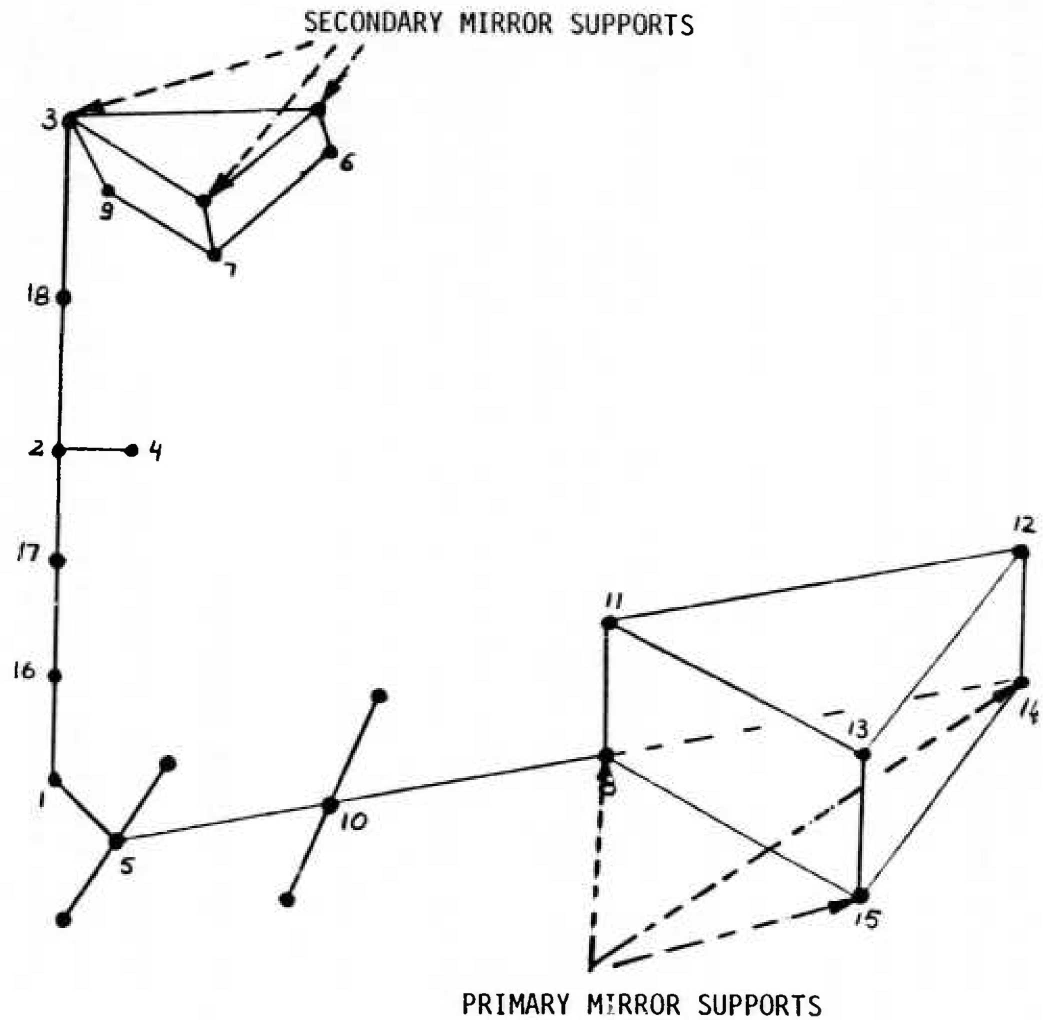

Figure 5-3. Structure's Node Definition

Table 5-2 summarizes the modal representation of the combined structure. In addition to the system's modal frequencies, the free-free natural frequencies of the Orbiter and of the structure are given. The modal frequencies of the structure rigidly attached to the ground are given for comparison. It can be seen that the modes of the combined system are very close to the modes of the cantilevered structure. This is to be expected since the mass of the Shuttle-Orbiter is very large compared to the structure and, hence, for all practical purposes the structure behaves as if it were cantilevered. It can also be observed that the Shuttle's modal frequencies are not affected by the addition of the test structure. This is due to the large mass of the Orbiter and also because of the relatively low flexibility at the attachment point.

The vibrational modes of the structure as attached to the Orbiter can be divided into three distinct groups:

(i) Modes with modal frequencies 1.970, 2.639, 2.645, 4.879 Hz
(ii) Modes with modal frequencies 22.732, 23.040 Hz
(iii) Modes with modal frequencies 40.884, 51.33 Hz.

In designing the vibration suppression control system, this natural division of vibrational modes is taken into account. The control system will be designed to control the first four vibrational modes. As it will be shown later, two additional modes have to be taken into account during the identification study.

5.2 Simulation Program Description

5.2.1 Simulation Program Functional Description

A detailed simulation program based on the TRW's general simulation program XSIM was developed. The program was written in a modular form which facilitates additions of new options into the program without altering its general structure. Moreover, if changes have to be made, only the modified part of the program is affected. The program was divided into seven autonomous sections, each one of them implemented by a separate subroutine. Figure 5-4 shows the functional description of the simulation program. The function of each part of the program is written inside each block and the name of the subroutine implementing it is denoted above the corresponding block.

Table 5-2. Natural Frequencies of Vibrational Modes

	ORBITER FREE-FREE FREQUENCY (Hz)	STRUCTURE FREE-FREE FREQUENCY (Hz)	STRUCTURE CANTILEVERED FREQUENCY (Hz)	COMBINED SYSTEM FREE-FREE FREQUENCY (Hz)
1	3.703	2.896	1.967	1.970
2	5.318	3.766	2.637	2.639
3	6.688	17.860	2.740	2.645
4	6.938	20.41	4.872	3.703
5	7.206	40.644	22.360	4.879
6	7.469	45.147	23.013	5.317
7	7.682	127.891	40.880	6.687
8	8.740	147.466	48.444	6.938
9	9.156	157.887	50.650	7.206

Note: For the combined system, Modes 1, 2, 3, 5 are vibrational modes of the structure. Modes 4, 6, 7, 8, 9 are vibrational modes of the orbiter. Hence, Modes 1, 2, 3, 5 of the combined structure are compared to Modes 1-4 of the cantilevered structure and Modes 4, 6, 7, 8, 9 compared to Modes 1-5 of the Orbiter.

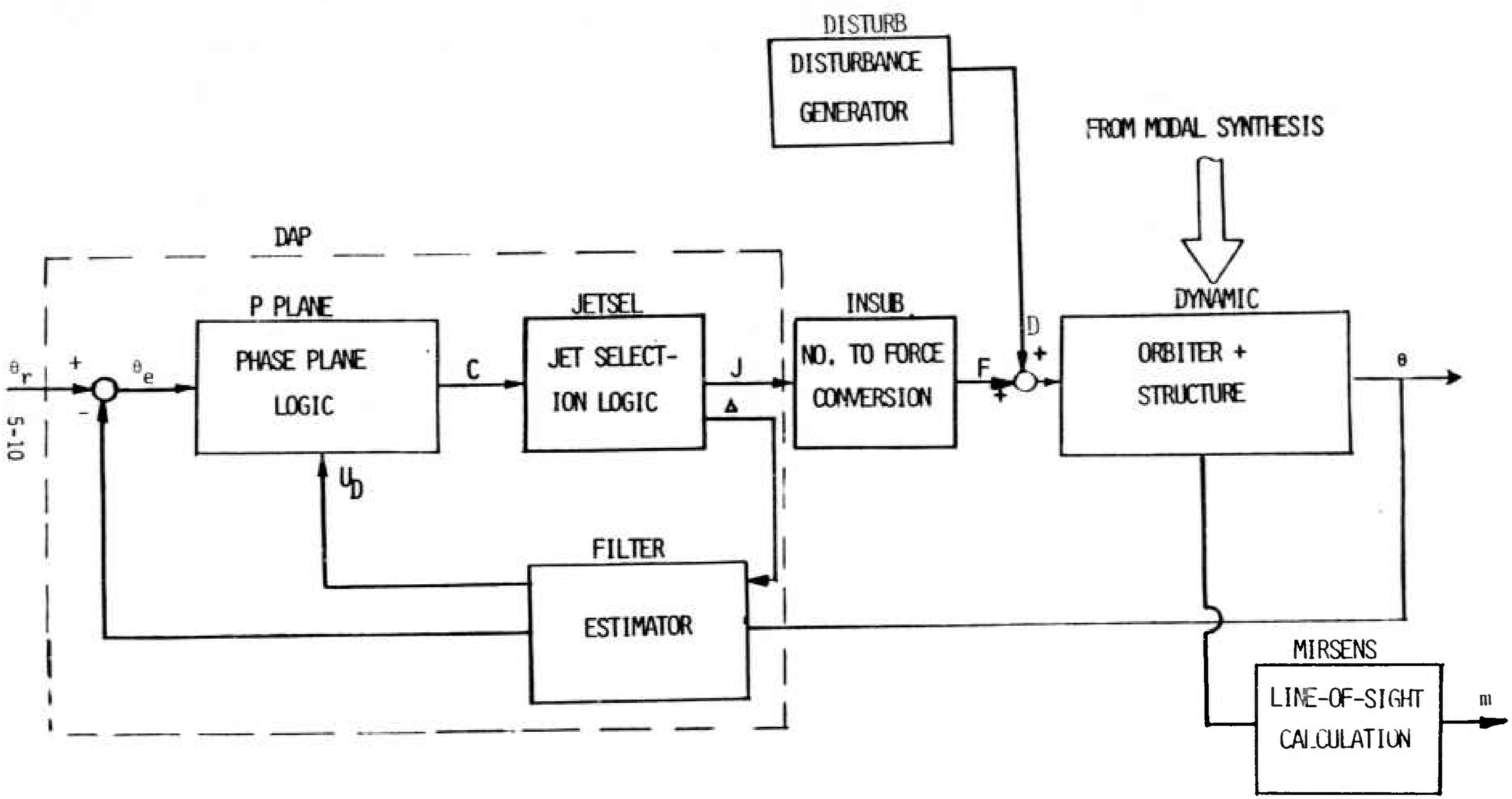

Figure 5-4. Functional Diagram of the Simulation Program

The different functional parts of the program and the subroutines which implement each part are as follows: (I) The plant (DYNAMIC) - The state space model of the Orbiter and the test structure as obtained from the model synthesis program KOMBINE. The inputs to DYNAMIC are the thrust forces of the VRCS system and disturbance forces acting on the structure. The outputs are the three attitude angles at the IMU sensor location and the deflections of the nodal points on the test structure. (II) Phase plane logic (PPLANE) - calculates the required control torques needed to maintain a given attitude. Subroutine PPLANE accepts the estimated attitude error, (θ_e), attitude rate error ($\dot{\theta}_e$), and acceleration caused by disturbances (U_D) and computes the control torque (C) needed for attitude correction. The objective is to limit the attitude error to less than 0.1 degree and attitude rate error to less than 0.01 deg/sec. (III) Jet selection logic (JETSEL) selects the vernier jets that must fire to maintain the system's attitude. JETSEL obtains the control torques command C and calculates the jet numbers J which are then supplied as inputs to subroutine INSUB. (IV) Conversion of jet numbers to corresponding forces (INSUB) - This subroutine converts the numbers of the jets that fire at any given time into corresponding force components acting on the plant. (V) State estimator model (FILTER) - Two filters which estimate and interpolate the Orbiter's attitude rate and disturbance acceleration. Subroutine FILTER accepts the attitude parameters of the plant and performs the following operations: (a) Estimates the attitude parameters and disturbance acceleration given their measurements (sample at 6.25 Hz) implemented by subroutine FILTER1; (b) Extrapolates attitude parameters over half the sampling period of FILTER1, implemented by subroutine FILTER2. (VI) Disturbance generator (DISTURB) - Simulates the disturbance forces acting on the structure during experiments. It models the disturbance forces (D) acting on the structure during control law performance demonstration (band limited gaussian noise) and during the parameter identification experiment (pulse sequence). (VII) Line-of-sight calculations (MIRSENS) - calculates LOS motion, given the motion of various mirrors' support points.

Subroutines PPLANE, JETSEL and FILTER constitute the Digital Autopilot (DAP) of the Orbiter. The various parts of the DAP operate at a sampling rate of 12.5 Hz, except the estimation part of subroutine FILTER (FILTER1) which operates at 6.25 Hz. The parameters used in the implementation of

the DAP were obtained recently from JSFC and are up to date. The detailed description of the DAP is given in various Shuttle documents [9]. A brief description of the DAP is given in Appendix C. In the following, the subroutines specific to the current simulation study are described.

5.2.2 Disturbance Generating Subroutine DISTURB

DISTURB is a subroutine which generates the required disturbance forces as a function of time and applies them to various points on the structure. In the current study two types of functions were simulated:

(i) A band limited Gaussian process which simulates artificial disturbance forces acting on the structure. These disturbance forces (Shakers) induce the vibration used to assess the performance of the proposed control law. The shakers themselves simulate expected environmental disturbances, e.g., pumps, CMG's, etc., which act on a spacecraft during normal operation. The subroutine which generates the random process permits specification of the standard deviation, the cutoff frequency, and the mean of the process. An important feature of the subroutine is the fact that the noise bandwidth is preserved when the process is sampled at non-increasing instances of time. This feature is important in simulation studies, for example, when Runge-Kutta integration algorithm is used.

(ii) A pulse sequence simulating the excitation signals used in the parameter estimation studies. The subroutine allows adjustment of various pulse sequence parameters such as amplitude, pulsewidth, period and start time.

5.2.3 Line-of-Sight Calculations

A ray tracing program for the two mirror Cassegrain configuration was developed. The program computes the mirror misalignments as function of the mirrors' motion. Two alternative ways of measuring misalignments are possible. One is in terms of the ray scatter (r_{av}) and the location of trace's center on the focal plane (y_m, z_m). The other method of measuring is in terms of focal plane perturbation (Δz) and the change of LOS direction (θ_y, θ_z). The two alternative ways of LOS measurement are illustrated in Figure 5-5.

In order to avoid time consuming calculations of LOS motion in the simulation program, a linear approximation was performed. It was assumed that the mirrors motion is small and only the linear terms of Taylor series

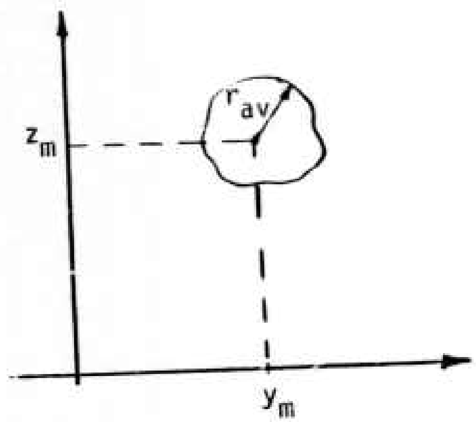

(a) Scatter and Trace Motion

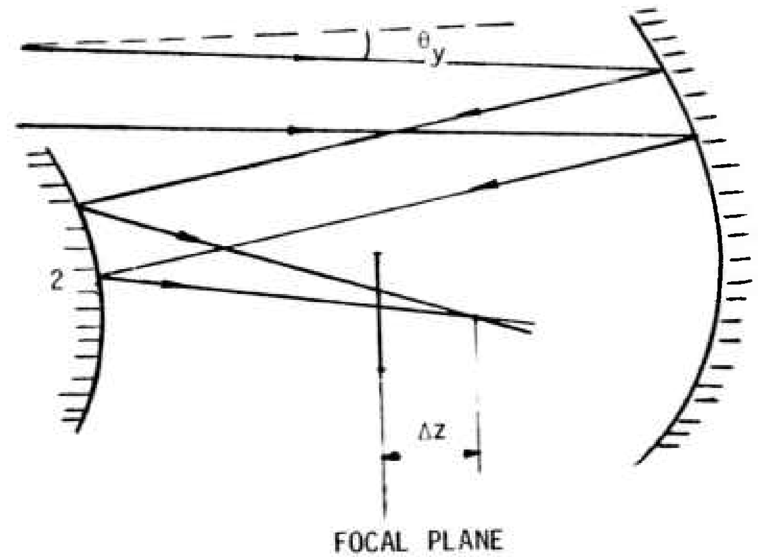

(b) Focal Plane Motion and Direction Change

Figure 5-5. LOS Motion Description

are needed to evaluate LOS motion. Therefore, the various perturbations can be written as:

$$\Delta F = \begin{bmatrix} r_{av} \\ y_m \\ z_m \end{bmatrix} = [\phi_1]\ \Delta x_1 + [\phi_2]\ \Delta x_2 \tag{5.1}$$

and

$$\Delta L = \begin{bmatrix} \Delta z \\ \theta_y \\ \theta_x \end{bmatrix} = [\psi_1]\ \Delta x_1 + [\psi_2]\ \Delta x_2 \tag{5.2}$$

where:

Δf, ΔL:	Perturbed LOS vectors
ϕ_1, ψ_1:	Sensitivities of LOS to mirror 1 motion
ϕ_2, ψ_2:	Sensitivites of LOS to mirror 2 motion
Δx_1, Δx_2:	Vector 9 x 1 expressing the three dimensional motion of three points on mirrors 1 and 2.

The sensitivity matrices were obtained by perturbing each mirror support points separately and computing the trace motion on the focal plane using the ray tracing program. The various sensitivity matrices are given in Table 5-3.

5.3 Simulation Results

5.3.1 Setting the Initial Conditions

In order to create the worst case structure excitation caused by VRCS thruster firings, the initial conditions of the Orbiter ought to be set in a way which will cause frequent firings. Moreover, in order to reduce simulation costs, the firings should occur in the initial stage of the simulation.

Table 5-3. LOS Sensitivity Matrices

$$\phi_1 = \begin{matrix} 3.23E-01 & 1.03E+00 & -7.41E-01 & -6.72E-01 & 7.99E-01 & 7.41E-01 & 7.11E-01 & -1.75E+00 & 2.48E-04 \\ 1.11E+01 & -4.99E+00 & 1.13E+00 & 1.27E+01 & -9.35E+00 & -1.13E+00 & -2.43E+01 & 1.59E+01 & -1.94E-05 \\ -6.23E+00 & -3.82E-01 & -3.75E+00 & 6.23E+00 & 3.82E-01 & -8.30E+00 & -3.51E-08 & -6.23E-08 & 1.37E+01 \end{matrix}$$

$$\phi_2 = \begin{matrix} 2.63E-01 & -1.61E+01 & 7.43E-05 & -5.31E+00 & 7.18E+00 & -8.64E+00 & 4.54E+00 & 8.83E+00 & 8.64E+00 \\ 3.16E+01 & 2.26E+01 & 3.68E-05 & -7.48E+00 & -1.74E+01 & 1.39E+01 & -2.33E+01 & -5.87E+00 & -1.39E+01 \\ -3.24E-08 & -1.00E-07 & -1.61E+00 & 1.65E+01 & -7.12E-01 & -5.92E+00 & -1.65E+01 & 7.12E-01 & 6.87E+00 \end{matrix}$$

$$\psi_1 = \begin{matrix} 2.33E+00 & 7.43E+00 & -5.35E+00 & -4.85E+00 & 5.77E+00 & 5.35E+00 & 5.13E+00 & -1.26E+01 & 1.79E-03 \\ 3.16E+00 & -1.43E+00 & 3.24E-01 & 3.62E+00 & -2.67E+00 & -3.24E-01 & -6.95E+00 & 4.55E+00 & -5.55E-06 \\ -1.78E+00 & -1.09E-01 & -1.07E+00 & 1.78E+00 & 1.09E-01 & -2.37E+00 & -1.00E-08 & -1.78E-08 & 3.92E+00 \end{matrix}$$

$$\psi_2 = \begin{matrix} 1.89E+00 & -1.16E+02 & 5.36E-04 & -3.83E+01 & 5.18E+01 & -6.23E+01 & 3.28E+01 & 6.37E+01 & 6.23E+01 \\ 9.04E+00 & 6.47E+00 & 1.05E-05 & -2.14E+00 & -4.96E+00 & 3.97E+00 & -6.67E+00 & -1.68E+00 & -3.97E+00 \\ -9.25E-09 & -2.87E-08 & -4.59E-01 & 4.71E+00 & -2.03E-01 & -1.69E+00 & -4.71E+00 & 2.04E-01 & 1.96E+00 \end{matrix}$$

Since the system dynamics is represented in terms of modal coordinates, a procedure was developed to obtain the initial conditions of the modal coordinates given a set of physical initial states. The procedure assumes that only the rigid body initial conditions are different from zero. Let q be the physical coordinates and η_R and η_e be the rigid body and flexible modal coordinates, respectively. One can write:

$$q = [\phi_R \mid \phi_e] \begin{bmatrix} \eta_R \\ \hline \eta_e \end{bmatrix} \tag{5.3}$$

then

$$q(o) = [\phi_R \mid \phi_e] \begin{bmatrix} \eta_R(o) \\ \hline 0 \end{bmatrix} \tag{5.4}$$

or

$$\eta_R(o) = \phi_R^{-1}\, q(o) \tag{5.5}$$

In general, $q(o)$ is a 6 dimensional vector expressing initial displacements and rotations at a given location. However, if only a subset of the physical coordinates is initialized, only the corresponding number of rigid body modes is calculated. In our case only three modes are given initial conditions because only the three angular attitudes are initialized. The initial rate is obtained directly from Equation (5.5).

$$\dot{\eta}_R(o) = \phi_R^{-1}\, \dot{q}(o) \tag{5.6}$$

It was decided to impose the largest attitude deviation on the roll axis. This is because the roll moment of inertia is the smallest and rotation around this axis will conceivably cause the largest disturbances. The initial conditions on the other axes were set to also violate the limit cycle limits, thus causing frequent thruster firings. The initial conditions are summarized in Table 5-4.

Table 5-4. Attitude Initial Conditions

	ROLL	PITCH	YAW
ATTITUDE (deg)	0.128	0.11	0.11
RATE (deg/sec)	0.01	0.01	0.01

As expected, the above initial conditions caused frequent firings in the initial stage of the simulation. The various vernier thruster firings during the first 20 seconds are shown in Figure 5-6. Figure 5-7 shows the attitude of the Shuttle during the first 50 seconds of a simulation run. The behavior shown is typical of the Shuttle when disturbances cause the attitude to drift outside the bounds of the limit cycle. Obviously, the exact behavior of the Orbiter is highly dependent on the initial conditions and the disturbances acting on it during normal operation. However, the behavior presented here is representative and, since it is a "worst case" study, it gives an upper limit on the motion of the test structure. As it can be seen, the limit cycle is irregular and a definite time period is difficult to observe. This is due to the fact that the various thrusters do not produce a pure moment around one axis only. A compromise is made by the jet selection logic algorithm which produces a torque that is not exactly in the direction of the commanded torque. After the initial stage of frequent transfer firings, the Orbiter enters the limit cycle deadband and coasts without VRCS activity for a relatively long period of time. Therefore, during normal operation of the Shuttle, there will be long periods of time in which there will not be structural excitation caused by thruster firings.

Figure 5-8 shows the vibrations induced by system's flexibility at the location of the IMU sensor. As it can be seen, the dynamic interaction of the test structure with the Orbiter does not cause noticeable vibrations. The change of attitude due to the vibrational motion is of the order of 10^{-9} rad which cannot be even detected by the IMU sensor. Moreover, this level of vibration is within the modeling error of the finite element model.

Figures 5-9 and 5-10 show the vibrations induced by the VRCS firings on the primary and secondary mirrors. The motion of the structure due to the rigid body rotation of the Orbiter is of the order of 10^{-2}m. The amplitude of the vibrational motion excited by the VRCS thrusters is of the order of 10^{-5} meters. This is a relatively low level of disturbance which will not interfere with the experiments performed on the structure. Moreover, for long periods of time the thrusters are not firing because the Orbiter is within the deadband of the limit cycle. Hence, during periods of inactivity the vibrations are damped out by the existing structural damping.

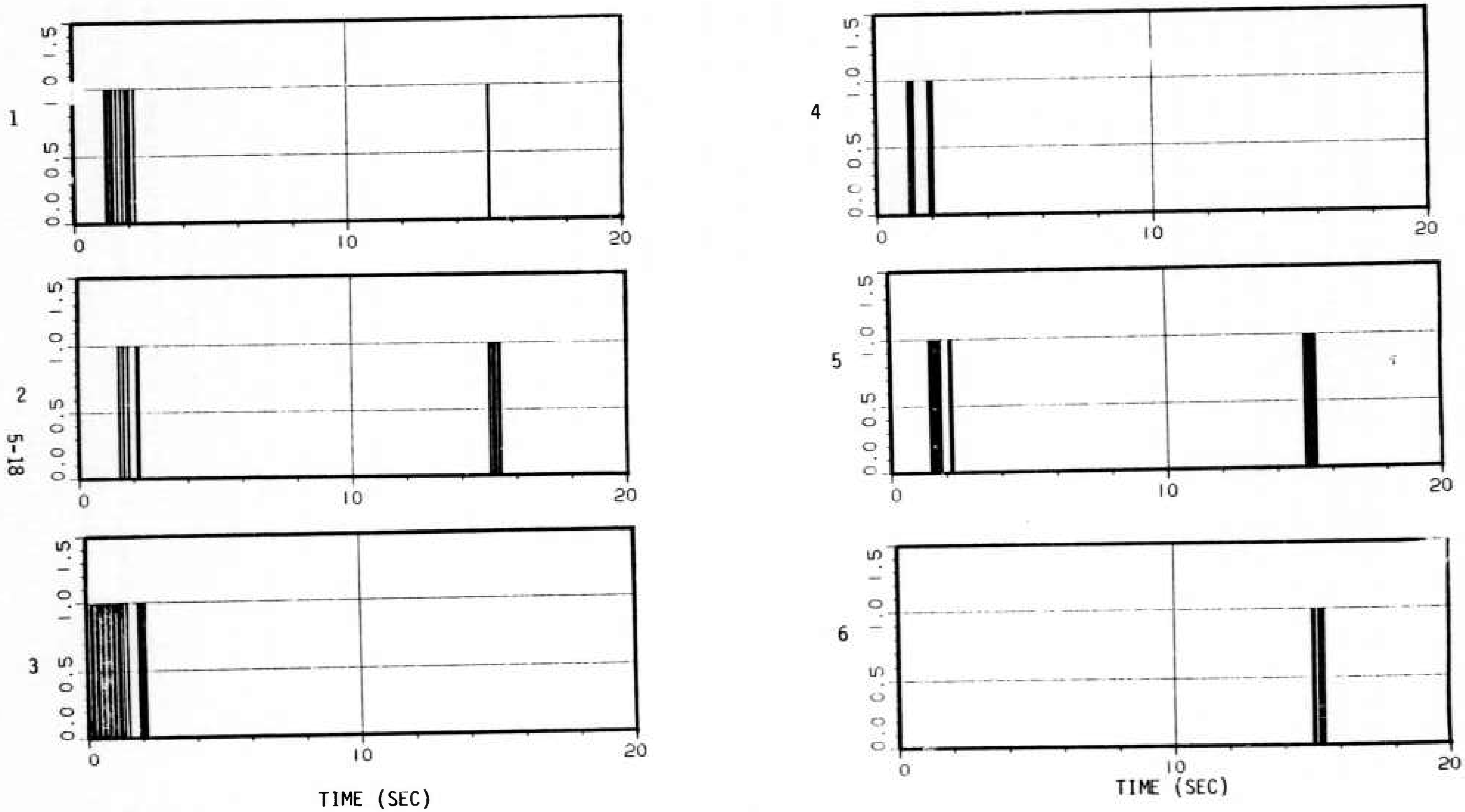

Figure 5-6. Thrusters' Firing Sequence

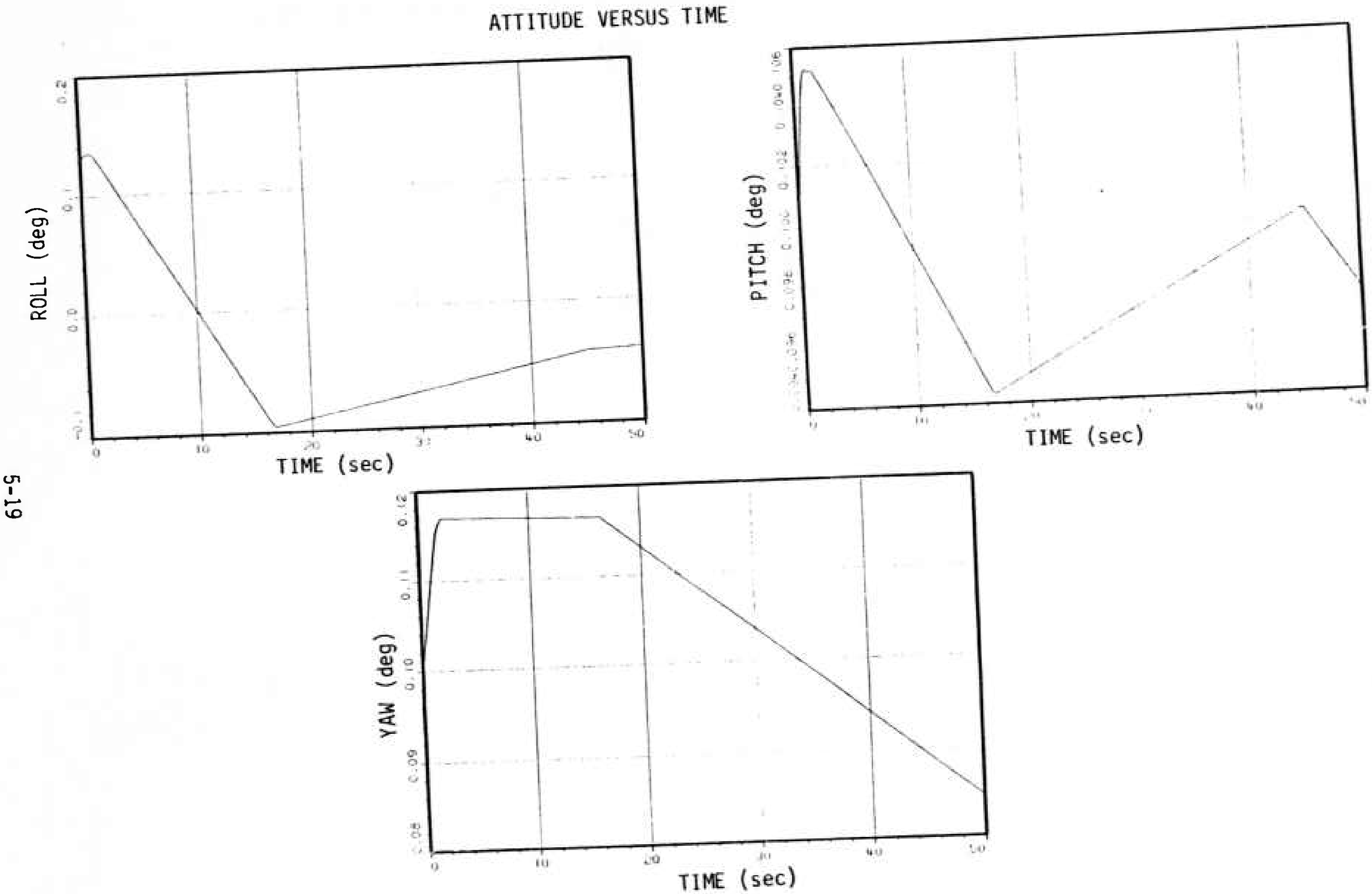

Figure 5-7. Orbiter's Attitude During VRCS Limit Cycle

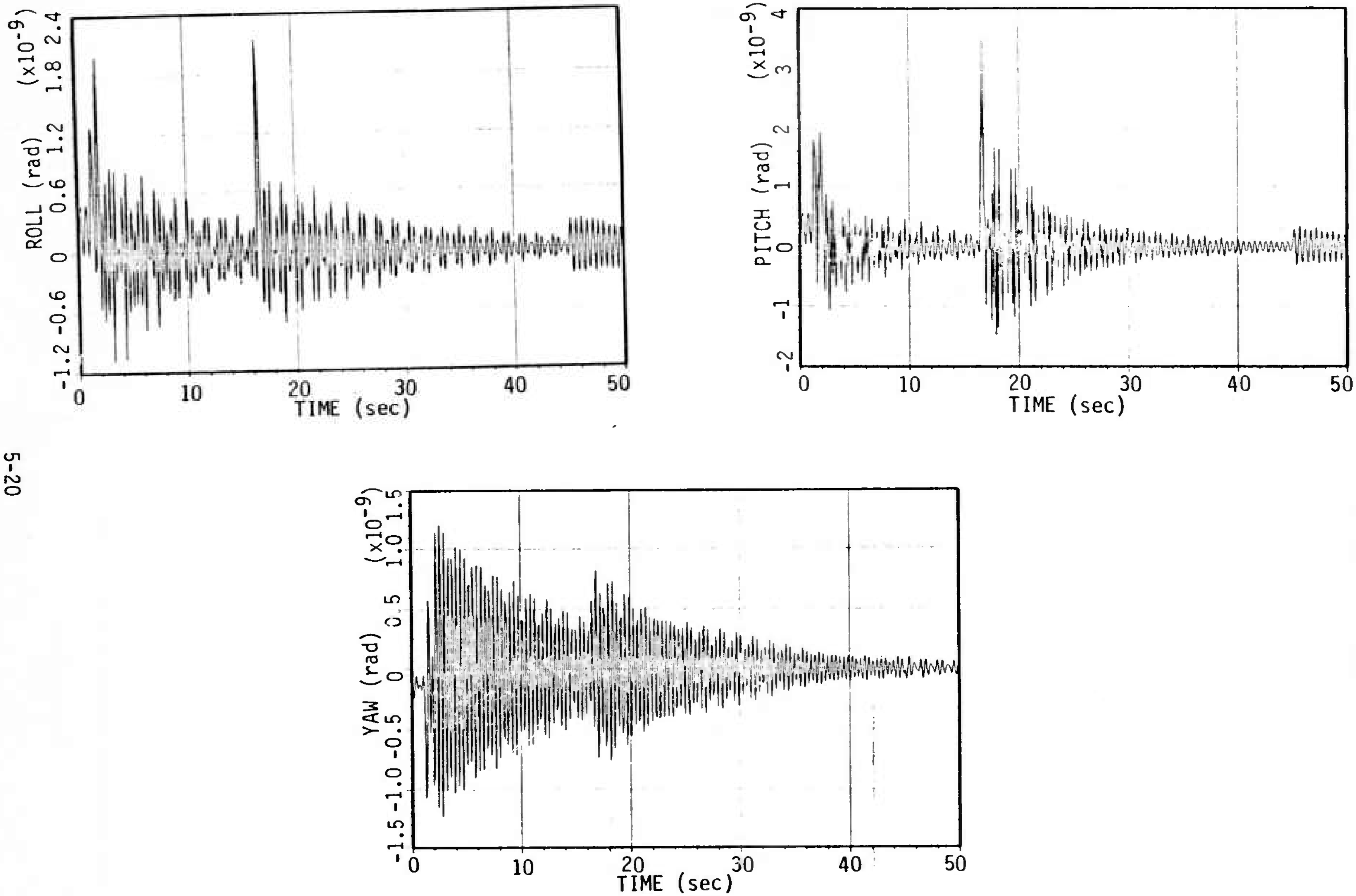

Figure 5-8. Vibrations of the Shuttle Induced by Structural Coupling

PRIMARY MIRROR (NODE 14)

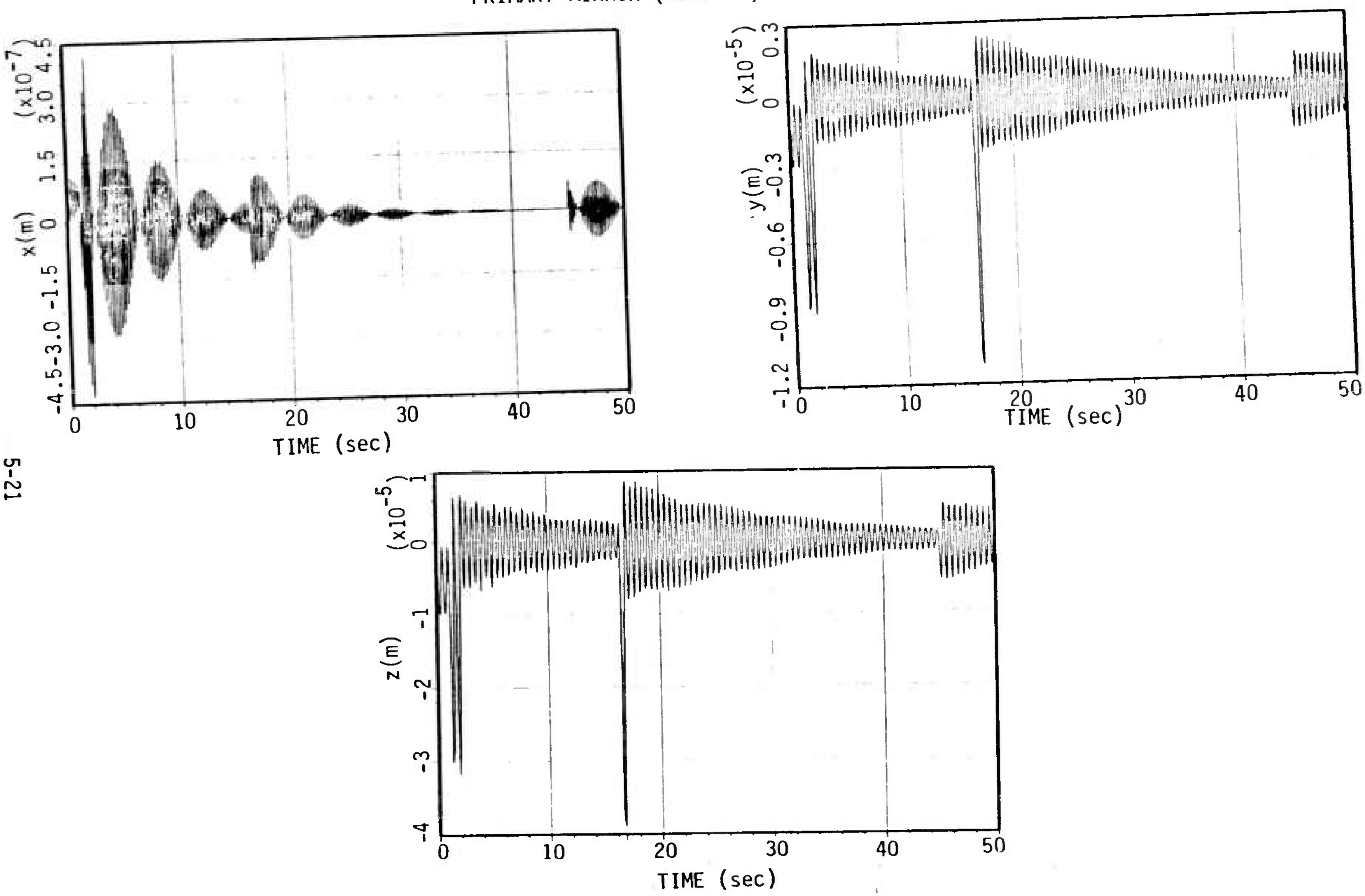

Figure 5-9. Vibrations of Primary Mirror During VRCS Firings

SECONDARY MIRROR (NODE 6)

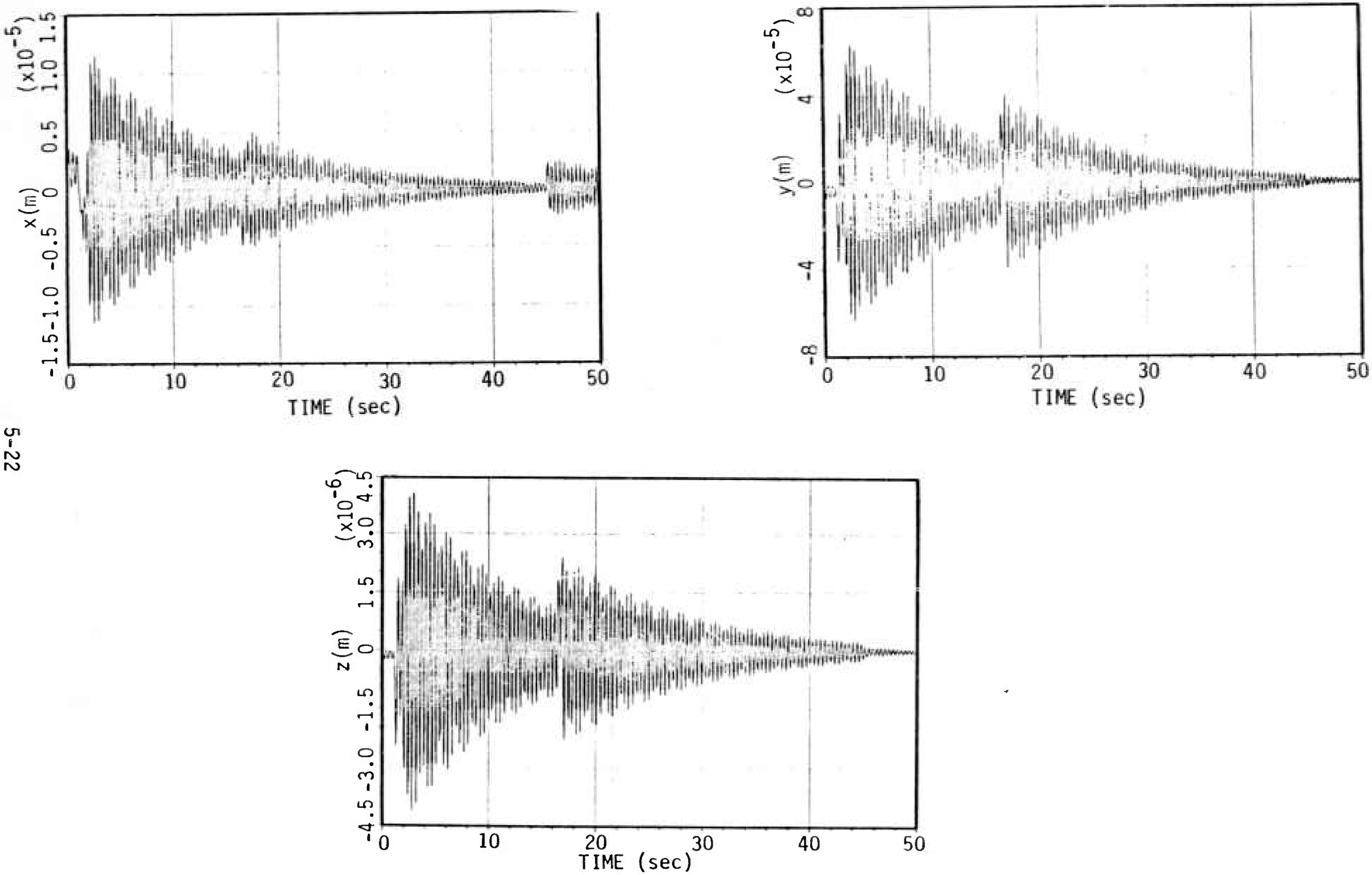

Figure 5-10. Vibrations of Secondary Mirror During VRCS Firings

As can be observed in the figures, four vibrational modes are important:

i) The bending mode of the secondary mirror in the xz plane. The vibrations due to the VRCS limit cycle are of the order 10 μm.

ii) The bending mode of the secondary mirror in the yz plane. The VRCS thruster firings caused vibration with amplitude up to 65 μm. The vibrations in this direction are higher than for the previous mode because the induced roll motion is larger than the pitch motion.

iii) The bending mode of the primary mirror in the xz plane. This causes vibrations with an amplitude of up to 40 μm.

iv) Combined bending and torsion of the primary mirror, which gives deflections of up to 10 μm.

In conclusion, as it was predicted, the test structure behaves like two cantilevered beams with concentrated masses at their ends.

The qualitative behavior of the system will not change for different sets of initial conditions. The change that might occur for different thruster firing sequence is the relative deflection of the mirrors. In particular, if the yaw motion is larger, the vibration mode (iv) will have a larger amplitude.

In addition to the interaction study, another goal of the simulation was to determine the level of excitation needed for demonstrating the control system performance. Preliminary calculations indicated that deflections of 0.2 μm of the mirrors will cause line-of-sight (LOS) error of 0.8 μrad. Therefore, in order to demonstrate vibration suppression by a factor of 1000, the imposed excitation should cause deflections of $\sim$ 300 μm. Based on previous results, it was determined that, in order to excite the significant structural modes, the disturbance forces should be applied at the top of the mast and on one of the side support points of the primary. The simulation study determined that the following set of Gaussian, band-limited (25 Hz) forces causes the required deflections:

a) Force in x direction acting on top of the mast (node 3), 0-mean, $\sigma_m^2(0) = 10^{-3}(Hz^{-1})$.

b) Force in y direction acting on top of the mast, 0-mean $\sigma_m^2(0) = 10^{-3}(Hz^{-1})$.

c) Force in z direction acting on one of the side supports of the primary mirror (node 14), 0-mean, $\sigma_m^2(0) = 10^{-3}(Hz^{-1})$.

Figures 5-11 and 5-12 show the vibrations of the two mirrors as the result of the above disturbance forces. The primary mirror's support (node 14) undergoes vibrations with amplitude up to 100 μm in the z direction, $\sim$ 40 μm in the y direction, and $\sim$ 10 μm in the x directions. The secondary mirror's deflections are $\sim$ 50 μm in the x direction, $\sim$ 40 μm in the y direction and $\sim$ 10 μm in the z direction.

The resulting LOS perturbation is shown in Figure 5-13. It can be seen that the LOS error is in the range which will permit control law demonstration of vibration suppression by a factor of a 1000. The open loop LOS error is of the order of 500 μrad which is within the desired range.

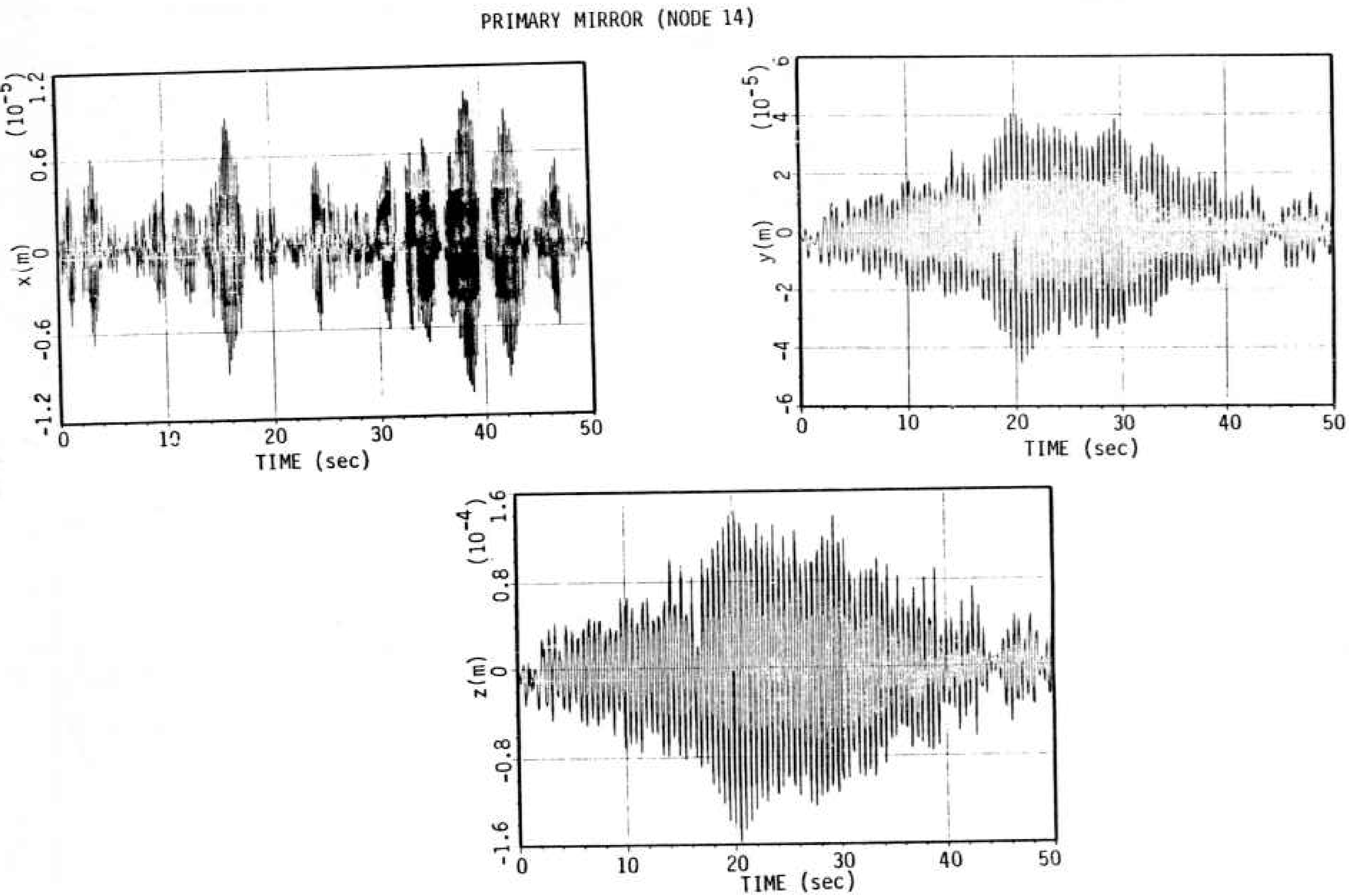

Figure 5-11. Deflections of the Primary Mirror in the Presence of Disturbance Forces

SECONDARY MIRROR (NODE 6)

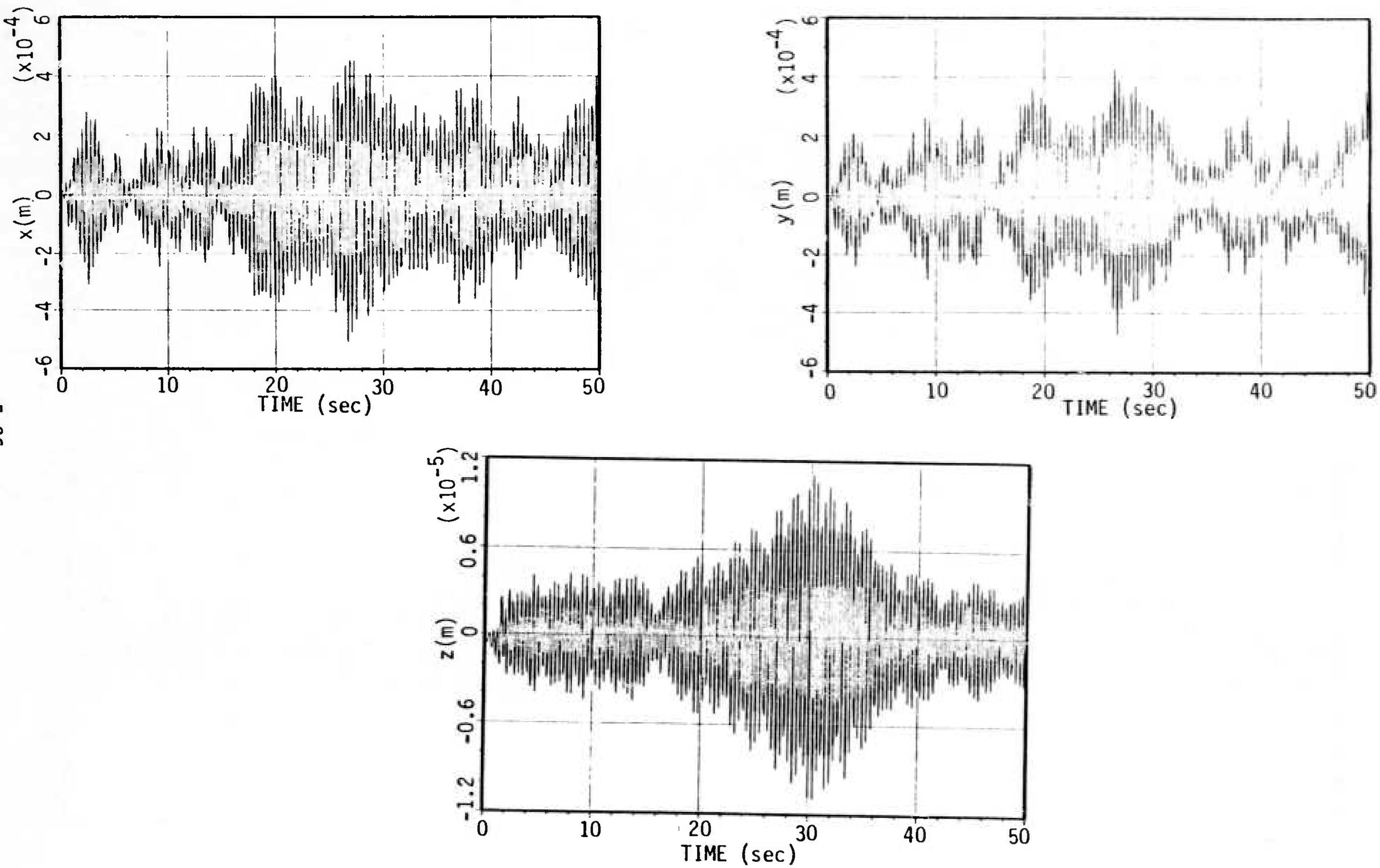

Figure 5-12. Deflection of the Secondary Mirror in Presence of Disturbance Forces

SECONDARY MIRROR (NODE 6)

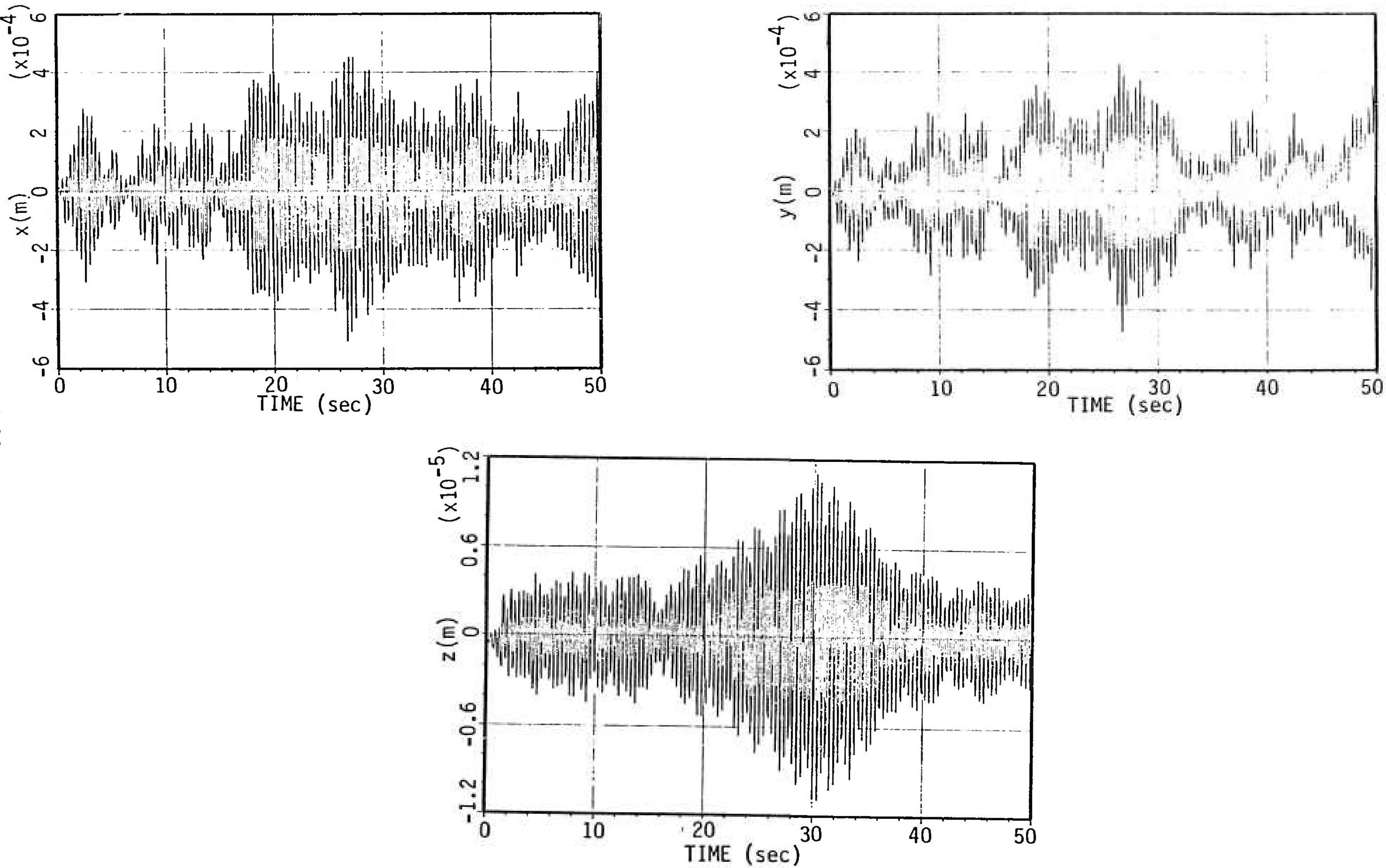

Figure 5-12. Deflection of the Secondary Mirror in Presence of Disturbance Forces

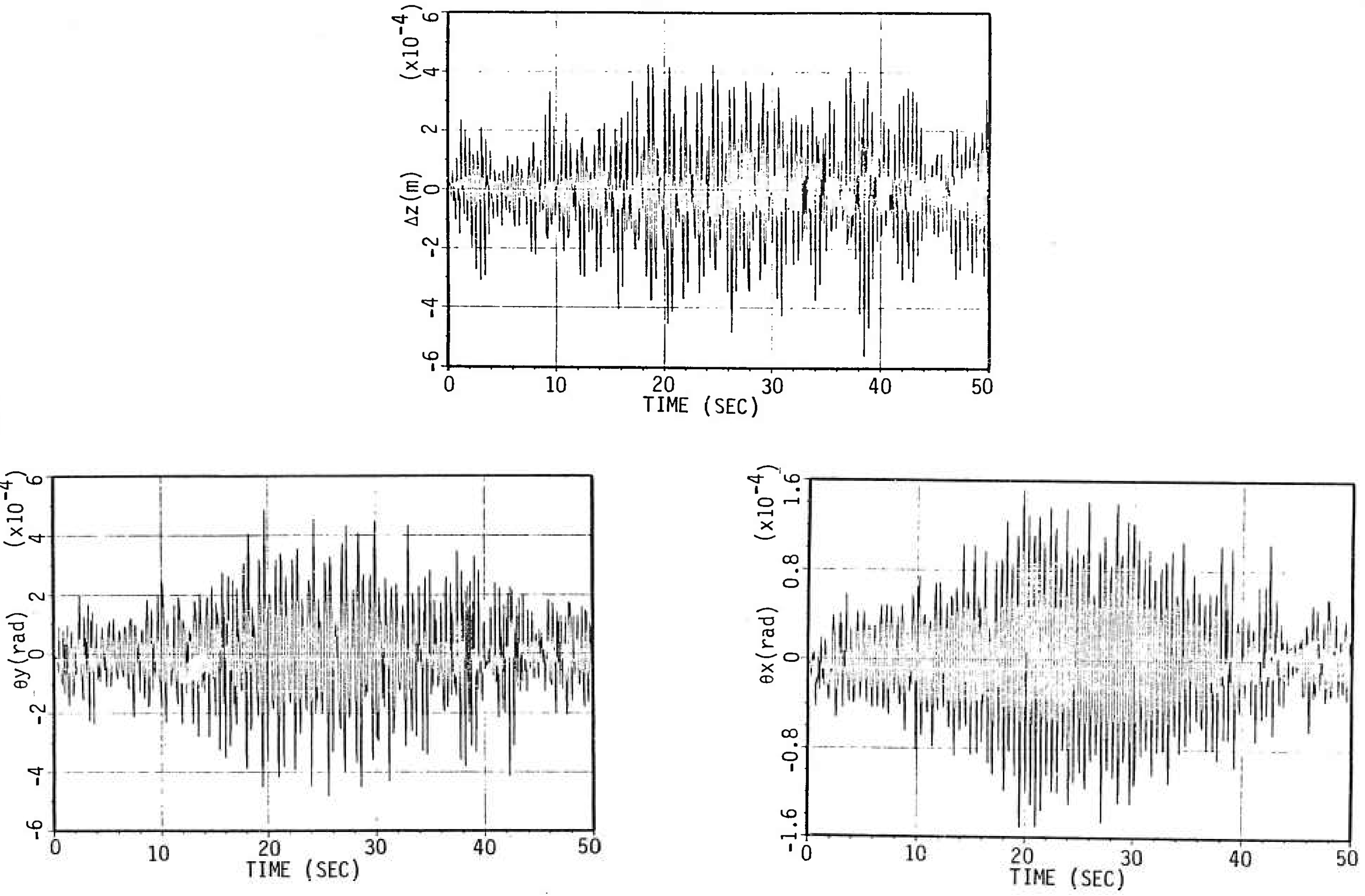

Figure 5-13. Line-of-Sight Perturbations

6.0 DESIGN AND ANALYSIS OF EXPERIMENTS

With the basic, dynamical compatibility between the baseline test structure and the Orbiter established in Section 5, this section tailors the generic experiments identified in Section 2 to the test structure. Details of these experiments are described in Section 6.1, followed by the design and analysis of the control and estimation subsystems. Particular attention is paid to define and baseline key elements of these subsystems. Simulation of critical elements were then used to establish conceptual design feasibility.

6.1 Baseline Experiments and Objectives

The generic list of experiments described in Section 2 was expanded, and, a candidate list of ground and orbit tests has been compiled and detailed for use with the baseline test structure. The tests include: a procedure for extracting the information necessary to derive more accurate analytical LSS models from the analysis of smaller, structural components; experiments for validating the achievable robustness and performance of on-orbit structural control; and a method for comparing alternative approaches which improve optical, imaging quality.

Referring to Table 6-1, the set of ground experiment headings are:

I. Component Tests
II. Substructure Tests
III. System Tests (Ground, No Shuttle)
and IV. Technology Demonstrations.

The on-orbit tests are to repeat parts of III and IV and add number V, Miscellaneous. The two primary reasons for performing numbers III and IV on the ground and on-orbit is to: i) provide data necessary for validating models which extrapolate ground to on-orbit behavior, and ii) provide a means for discarding poor approaches on ground from those that merit further evaluation on-orbit. Costs will be reduced if only the most promising technologies (determined by the ground experiments) are tested on-orbit.

Table 6-1. Candidate List of Experiments

I. <u>COMPONENT TESTS (GROUND)</u>

OBJECTIVE: TO DETERMINE ANALYTICAL MODELS AT THE POC STRUCTURE COMPONENT LEVEL.

SET OF TESTS:

A. DETERMINE TRUSS MATERIAL PROPERTIES AND GEOMETRY NECESSARY TO DEVELOP FINITE ELEMENT MODELS (FEM) AT EXPECTED TEST AND OPERATING ENVIRONMENT (E.G., TEMPERATURE, PRESSURE, RADIATION, ETC.).

B. DETERMINE ACTUATOR AND SENSOR DYNAMICS OVER OPERATING RANGE

1. LINEARITY
2. RESOLUTION
3. DYNAMIC RANGE
4. NOISE CHARACTERISTICS
5. BANDWIDTH AND FREQUENCY RESPONSE AS A FUNCTION OF SIGNAL AMPLITUDE IN THE OPERATING RANGE

C. DETERMINE ENVIRONMENTAL DISTURBANCES THAT WILL NOT PARTICIPATE IN POC TEST AND "RECORD"

1. CRYOCOOLER "NOISE" AND COOLANT MASS SHIFTS
2. CMG IMBALANCE AND NOISE
3. RW IMBALANCE AND NOISE
4. SOLAR PANEL MOTION AND SLIPRING NOISE
5. IMPULSIVE DISTURBANCES

II. <u>SUBSTRUCTURE TESTS (GROUND)</u>

OBJECTIVE: TO DETERMINE ANALYTICAL MODELS AT THE SUBSTRUCTURE LEVEL.

SET OF TESTS:

A. SHUTTLE PALLET

1. I.D. MODAL DATA
2. I.D. DAMPING
3. COMPARE "REAL" VERSUS FEM MODEL

B. PRIMARY MIRROR + SUPPORT

1, 2, AND 3. SAME AS II.A.

C. TEST STRUCTURE

1, 2, AND 3. SAME AS II.A.

D. MISCELLANEOUS FLEXIBLE (< X10 CONTROL BW) COMPONENTS TO BE ATTACHED TO TEST STRUCTURE

1, 2, AND 3. SAME AS II.A.

III. <u>SYSTEM TESTS (GROUND, NO SHUTTLE AND ON-ORBIT)</u>

OBJECTIVE: TO CALIBRATE THE SYSTEM AND TO VALIDATE OPEN AND CLOSED LOOP SYSTEM MODELING.

A. CALIBRATE OPTICAL MEASUREMENT AND ALIGNMENT SYSTEM

OBJECTIVE: ESTABLISH NOMINAL CAPABILITY AND OPERATING POINT FOR DISTURBANCE FREE SYSTEM

METHOD: APPLY KNOWN ROTATIONAL AND TRANSLATIONAL PERTURBATIONS TO ELEMENTS IN OPTICAL LOS PATH, THEN COMPARE MEASURED COMPONENT MOTION VS REAL. USE TRW SURFACE ACCURACY MEASURMEENT SENSOR (SAMS) IN TRIANGULATION MODE. THIS SENSOR WILL MONITOR SIX-DEGREE-OF-FREEDOM MOTION OF RIGID POINTS ON PRIMARY AND SECONDARY MIRROR STRUCTURE (AND ANY OTHER ELEMENTS ALONG THE OPTICAL PATH) IN FOCAL PLANE COORDINATES.

Table 6-1. Candidate List of Experiments (Continued)

B. CALIBRATE IMAGE MOTION SENSOR SYSTEM

OBJECTIVE: ESTABLISH NOMINAL CAPABILITY AND OPERATING POINT FOR DISTURBANCE FREE SYSTEM. ALSO, TEST AND CALIBRATE OPTICAL ELEMENT MOTION TO LOS MOTION TRANSFORMATION.

METHOD: USE IMAGING CHARGE COUPLED DEVICE LIKE USED IN TRW'S MADAN AND FOCUS CENTROID OF "TRUTH" TARGET; THEN APPLY KNOWN ROTATIONAL AND TRANSLATIONAL PERTURBATIONS TO ELEMENTS IN OPTICAL LOS PATH AND COMPARE PREDICTED LOS MOTION VERSUS REAL.

C. CALIBRATE ACTUATOR TO SENSOR "DC" TRANSFORMATION

OBJECTIVE: CALIBRATE AND VALIDATE THE INFLUENCE THE ACTUATORS (E.G., CONTROL, DISTURBANCE, I.D.) HAVE ON LOS, OPTICAL ELEMENT MOTION, AND STRUCTURE.

METHOD: APPLY KNOWN STATIC PERTURBATIONS TO EACH ACTUATOR IN A SEQUENTIAL MANNER AND MONITOR DC CHANGE ON ALL SENSORS. COMPARE PROJECTED VERSUS REAL.

D. MODAL SYNTHESIS EXPERIMENT, PHASE I

OBJECTIVE: VALIDATE ANALYTICAL MODAL SYNTHESIS PROCEDURES AND ESTABLISH A REFERENCE FOR THE METHOD'S MODELING ERROR PROPAGATION.

CONDITIONS: GROUND, NO SHUTTLE, CONTROL OFF, PASSIVE CONTROL OFF (MEMBER DAMPERS AND ISOLATORS "LOCKED"), DISTURBANCES OFF.

METHOD:

1. PLACE ASSEMBLED STRUCTURE PLUS PALLET (IF POSSIBLE) ON TEST BED, AND IDENTIFY MODAL DATA AND DAMPING
2. COMPARE WITH FEM MODEL, EXPERIMENT I.A.
3. COMPARE WITH MODAL SYNTHESIS FEM MODEL
4. COMPARE WITH MODAL SYNTHESIS USING "REAL" SUBSTRUCTURE DATA -- EXPERIMENT II.

E. DISTURBANCE RECORDING VALIDATION

OBJECTIVE: VERIFY THAT DISTURBANCE "RECORDING" IS REPRESENTATIVE OF EXPECTED DISTURBANCES.

CONDITIONS: SAME AS III.2.D BUT WITH DISTURBANCES ON AS REQUIRED.

METHOD: TURN ON DISTURBANCE ACTUATORS IN A SEQUENTIAL MANNER AND MONITOR EFFECT USING ALL SENSORS. COMPARE WITH ANALYTICAL PREDICTION.

F. VERIFICATION OF LUMPED PASSIVE ELEMENT MODELING/PASSIVE CONTROL EXPERIMENT, PHASE I

OBJECTIVE: VERIFY ANALYTICAL METHODS USED TO MODEL STRUCTURES WITH INTEGRATED, LUMPED, PASSIVE ELEMENTS.

CONDITIONS: GROUND, NO SHUTTLE, CONTROL OFF, PASSIVE CONTROL ON AS REQUIRED, DISTURBANCES ON AS REQUIRED.

METHOD:

1. VALIDATE EFFECT OF PASSIVE ISOLATOR MODELING: MEMBER DAMPERS LOCKED, ISOLATORS UNLOCKED. ID WITH AND WITHOUT DISTURBANCES. MONITOR LOS AND STRUCTURAL DEFLECTIONS AND COMPARE WITH PREDICTED.
2. VALIDATE EFFECT OF PASSIVE MEMBER DAMPERS MODELING: MEMBER DAMPERS UNLOCKED, ISOLATORS LOCKED. ID WITH AND WITHOUT DISTURBANCES. MONITOR LOS AND STRUCTURAL DEFLECTIONS AND COMPARE WITH PREDICTED.
3. VALIDATE PASSIVE CONTROL SYSTEM PERFORMANCE PREDICTION: MEMBER DAMPERS AND ISOLATORS UNLOCKED. ID WITH AND WITHOUT DISTURBANCES. MONITOR LOS AND STRUCTURAL DEFLECTIONS AND COMPARE WITH PREDICTED.

Table 6-1. Candidate List of Experiments (Continued)

G. VERIFICATION OF ACTIVE STRUCTURAL CONTROL MODELING

OBJECTIVE: VERIFY ANALYTICAL METHODS USED TO MODEL ACTIVE CONTROL

CONDITIONS: GROUND, NO SHUTTLE, PASSIVE CONTROL ON, ACTIVE STRUCTURAL CONTROL ON AS REQUIRED, DISTURBANCES ON AS REQUIRED.

METHOD:

1. COMPUTE SIMPLE ACTIVE LAWS (E.G., PIB) FOR FEM MODEL (I.A.), "REAL" MODAL SYNTHESIZED MODEL (II.D), AND "REAL" SYSTEM (III.F.3).
2. FOR EACH SET OF GAINS ABOVE: ID WITHOUT DISTURBANCES, MEASURE STABILITY MARGINS, MONITOR LOS AND STRUCTURAL DEFLECTIONS WITH DISTURBANCES.
3. COMPARE WITH ANALYTICAL PREDICTION AND III.F.3.

IV. TECHNOLOGY DEMONSTRATIONS (GROUND WITH NO SHUTTLE AND/OR ON-ORBIT WITH SHUTTLE AS REQUIRED)

A. ADVANCED CONTROL LAWS

OBJECTIVE: DETERMINE STABILITY AND PERFORMANCE LIMITATIONS OF ADVANCED CONTROL LAWS

CONDITIONS: PASSIVE CONTROL ON AS REQUIRED, ACTIVE CONTROL ON AS REQUIRED, DISTURBANCES ON AS REQUIRED.

METHOD:

1. IDENTIFY MODAL DATA AND DAMPING OF UNCONTROLLED STRUCTURE WITH NO DISTURBANCES.
2. MEASURE UNCONTROLLED SYSTEM RESPONSE TO DISTURBANCES.
3. FOR COMPETING FIXED GAIN COLOCATED CONTROL LAWS, NON-COLOCATED CONTROL LAWS, DIRECT ADAPTIVE, AND FIXED GAIN LAW BASED ON "REAL" MODAL DATA (INDIRECT ADAPTIVE):
   A. DETERMINE STABILITY ROBUSTNESS BY INSERTING GAIN AND PHASE PERTURBATIONS INTO THE CONTROL LOOP.
   B. DETERMINE PERFORMANCE BY MEASURING LOS AND OPTICAL TRAIN RESPONSE TO DISTURBANCE ENVIRONMENT.
4. DETERMINE PERFORMANCE (AS ABOVE) USING RELATIVE AND INERTIAL CONTROL LAWS DESIGNED USING THE SAME CONTROL PHILOSOPHY AND MODEL INFORMATION.

B. WAVE PROPAGATION EXPERIMENT

OBJECTIVE: EVALUATE PERFORMANCE AND RELATIVE MERITS BETWEEN CONTROLLING AT SOURCE, CONTROLLING ALONG PROPAGATION PATH (STRUCTURAL CONTROL) AND CONTROLLING AT DESTINATION (HIGH BANDWIDTH OPTICAL AUTOALIGNMENT SYSTEM). ALSO, ESTABLISH PERFORMANCE LIMITATIONS.

METHOD:

THE PERFORMANCE OF THE THREE CONTROL APPROACHES WILL BE COMPARED INDIVIDUALLY AND IN COMBINATION. LOS AND OPTICAL TRAIN RESPONSE TO DISTURBANCES WILL BE THE CRITERIA.

C. IMAGING EXPERIMENT

OBJECTIVE: EVALUATE PERFORMANCE AND RELATIVE MERITS BETWEEN DITHERED ACTIVE OPTICS, WAVEFRONT COMPENSATION, AND ACTIVE STRUCTURAL CONTROL. ALSO, ESTABLISH PERFORMANCE LIMITATIONS.

METHOD:

IMAGE QUALITY WILL BE EVALUATED USING A TRUTH TARGET AND EACH OF THE THREE IMAGE CONTROL TECHNIQUES ABOVE, ALSO WITH NO CONTROL. ACTIVE STRUCTURAL CONTROL WILL THEN BE USED IN COMBINATION WITH ONE OF THE OPTICAL METHODS TO ESTABLISH PERFORMANCE LIMITS.

Table 6-1. Candidate List of Experiments (Continued)

V. <u>MISCELLANEOUS (ON-ORBIT WITH SHUTTLE)</u>

A. POC STRUCTURE DYNAMICAL INTERACTION WITH ORBITER

OBJECTIVE: VALIDATE ANALYTICAL MODELS FOR DYNAMICAL INTERACTION BETWEEN PRECISION STRUCTURE AND HOST SPACECRAFT. ALSO, ESTABLISH THE SHUTTLE ENVIRONMENT MODEL.

METHOD:

1. MONITOR OPEN LOOP, DISTURBANCE FREE DEFLECTIONS OF POC STRUCTURE AS SHUTTLE IS IN NORMAL OPERATION. ALSO MONITOR SHUTTLE CONTROL SIGNALS.
2. MONITOR CLOSED LOOP, DISTURBANCE DEFLECTIONS OF POC STRUCTURE AS SHUTTLE IS IN NORMAL OPERATION. MONITOR SHUTTLE CONTROL SIGNALS.

B. RAPID SLEW-TRACK-SETTLE

OBJECTIVE: VALIDATE RAPID SLEW-TRACK-SETTLE ALGORITHMS REQUIRED IN SOME MISSIONS.

METHOD:

1. USE SHUTTLE TO PERFORM OPTIMUM OPEN LOOP SLEW.
2. COUPLE SIGNALS FROM SHUTTLE AUTOPILOT INTO POC OPTICAL ALIGNMENT SYSTEM AND EXECUTE FINE SLEW CONTROL AND TRACK WITH ACTUATED OPTICAL ELEMENTS. SETTLE BY COUPLING SLEW AND TRACK SIGNALS INTO STRUCTURAL CONTROLLER.

The ultimate figure of merit to be used in the technology demonstrations will be optical element motion, line-of-sight (LOS) motion, and image quality. The goals are to control the relative motion of the optical train to .2 μm, and, to control the LOS pointing accuracy to .8 μrad (without closed loop target tracking). It is intended that the openloop system performance be 1000 fold out of specification. That is, the vibration suppression system goal is to reduce the vibrations by a factor of 1000 as measured by LOS motion.

Referring again to Table 6-1, the following subsections provide additional details.

6.1.1 Component Tests

The objective of the component tests is to determine good analytical models for all subsystem components. These include material properties, actuators and sensors, and disturbance sources. It is intended that analytical models of these components be analytically combined to create substructure models and then be experimentally validated during the substructure tests.

Another important objective of the component test is "record" the spectrum of the disturbance sources expected in the true systems of interest. The recordings can be played back in later tests through actuation devices. Hence, representative disturbances can be used to later test the complete system without actually having the true sources.

6.1.2 Substructure Tests

The objectives of the substructure tests are to: i) provide a substructure by substructure validation of analytical, finite element modeling (FEM); and ii) provide the truth models for composing structures through modal synthesis. Both the synthesized FEM and the synthesized substructure models are to be created and compared. Both are later to be compared with ground and on-orbit system structural models.

6.1.3 System Tests

The objective of these sequence of tests is to validate open and closed loop structural control models.

The need to validate open-loop structural models is self evident. To do it, all actuators and sensors are first calibrated, then the test structure is identified. The resulting test data is compared with the predictions made with the two modal synthesis models from the substructure tests.

The need to validate closed-loop structured models at sub μm and μrad levels is also of utmost importance. Up until the present time only the rigid body modes of a spacecraft have actively been controlled. All of the flexible modes have only been stabilized (mainly gain stabilized). Hence it hasn't been too important whether closed-loop flexible modes act according to linear, lumped parameter feedback theory or not. With the current emphasis on precision structural control however, there is a need to determine this information. It is expected that the baseline, truss like system will act as the mechanical analog of a transmission line with wave delays and energy absorbing "stubs" (active and passive control).

The proposed validation experiment is to first verify passive control modelling. Here the actual open and closed loop responses of the system to known disturbance inputs are compared with those predicted by linear feedback models. Once the analytic feedback model has been validated, active control models will be evaluated in a similar fashion. Passive control is described first so that a gross error in the analytical model will result in only a benign miscalculation rather than a potential hardware malfunction.

6.1.4 Technology Demonstrations

The technology demonstration consists of these parts: advanced control law validation and trades, wave propagation experiment; and imaging experiments.

The objective of the advanced control law demonstration is to compare the various colocated, noncolocated, fixed gain and adaptive control laws developed for active control. Performance, as measured by LOS error, and stability margins are the key criteria. Comparing the performance of relative (eg., bending moment) and inertial (eg., proof-mass) control systems is also an objective. It is noted that only one or two of the most promising approaches are to be demonstrated on-orbit; the remaining will be discarded based on the results of the ground test.

The objective of the wave propagation experiment is to determine what type or combination of control approaches is best suited for optical missions with high disturbance sources. Currently, one can control at the disturbance source location by isolating it before its energy gets into the structure; one can control along the path of energy propagation through the structure with passive and active vibration suppression techniques; or one can control at the juncture between the optical train and the structure by using a high bandwidth autoalignment system. Trades between these systems are possible in terms of performance, cost, weight, complexity, and power. Again, only the most promising approach is intended for on-orbit test. The performance criteria is optical train motion and LOS error.

The final technology demonstration and trade is the imaging experiment. The objective here is to experimentally determine the relative merits between active optics (dithered or wavefront compensation) and active structural control. The intent is to determine the most advantageous, individual areas of application and combination. Image quality is to be evaluated by using truth targets. Only the most promising combination is to be evaluated on-orbit.

6.1.5 Miscellaneous

This set of experiments addresses the dynamical interaction between a large structure (Shuttle) and a payload, and, also slew-track-settle maneuvers.

The objectives of the dynamical interaction experiments are to i) model the Shuttle environment prior to performing any of the on-orbit experiments; and ii) test the analytical prediction capability of modal synthesis between two, dynamically complex structures.

The objectives of the rapid slew-track-settle experiment are to test some control coordination algorithms required in some missions. The algorithm arises when one tries to coordinate a slew maneuver (large dynamic range and small bandwidth) with structural control (medium dynamic range and bandwidth) and figure control (small dynamic range and high bandwidth). This control algorithm is necessarily non-linear, multivariable, and distributed in nature. Hence, it needs to be tested. The on-orbit experiment presents a good opportunity to do this since the Shuttle itself can be used in place of the typically very expensive attitude control system.

6.2 Relative Priority Between Experiments

Table 6-2 check lists the set of candidate experiments according to whether they have primary or secondary importance in a modeling intensive program, a technology verification intensive program or both. The "recommended" set is based on the analysts understanding of the current state of the technology. The actual experiments and procedures chosen from this candidate list are described in Appendix A.

Table 6-2. Relative Priority Between Experiments

	EXPERIMENTS NOTE: III' & IV' ARE SIMILAR TO III & IV, BUT ON-ORBIT.		NO.	MODELING INTENSIVE TEST		TECHNOLOGY VERIFICATION INTENSIVE TEST		RECOMMENDED	REMARKS ABOUT RECOMMENDATION
				PRIMARY	SECONDARY	PRIMARY	SECONDARY		
GROUND	COMPONENT TEST	MATERIAL	I.A	X		X		X	MAY ALREADY BE AVAILABLE.
		ACT. & SENS	B	X		X		X	SOME MAY ALREADY BE AVAILABLE.
		DISTRB.	C	X		X		X	
	SUBSTRUCTURE TESTS	PALLET	II.A	X			X	X	MAY ALREADY BE AVAILABLE.
		MIRROR	B	X			X	X	MAY ALREADY BE AVAILABLE.
		TEST STRUC.	C	X			X	X	
		MISC.	D	X			X	X	
	SYSTEM TEST	OPT. ALIGN	III.A	X		X		X	
		CENTROID ALIGN	B	X		X		X	
		ACT&SENS ALIGN	C	X		X		X	
		MODAL SYN.	D	X			X	X	
		DSTRB.VALIDATE	E		X	X		X	
		PASSIVE "	F	X			X		CAN INFER BEHAVIOR FROM III.G
		ACTIVE "	G	X		X		X	
	TECHNOLOGY DEMONSTRATION	ADV. CONTROL	IV.A		X	X		X	
		WAVE PROP.	B		X	X		X	
		IMAGING	C		X	X		X	
ON-ORBIT	MISCELLANEOUS	DYN. INTR.	V.A	X		X		X	
	SYSTEM TEST	OPT. ALIGN	III'.A	X		X		X	
		CENTROID ALIGN	B	X		X		X	
		ACT&SENS ALIGN	C	X			X		CONTROL SHOULD BE ROBUST ENOUGH TO HANDLE ERRORS.
		MODAL SYN	D	X			X	X	FEM VERSUS REAL DATA ID ONLY.
		DSTRB.VALIDATE	E		X	X		X	
		PASSIVE "	F		X		X	X	FEM VERSUS REAL DATA ID ONLY.
		ACTIVE "	G	X		X		X	FEM VERSUS REAL DATA ID ONLY.
	TECHNOLOGY DEMONSTRATION	ADV. CONTROL	IV'.A		X	X		X	JUST MOST PROMISING LAWS.
		WAVE PROP	B		X	X		X	JUST MOST PROMISING APPROACH
		IMAGING	C		X	X		X	JUST MOST PROMISING APPROACH.
	MISCELLANEOUS	SLEW-TRACK-SET	V.B		X		X		USE GROUND TEST.

6.3 The Control Subsystem

The control subsystem was designed to perform the various forms of control required by the experiments sequence described in Section 6.1. In order to be able to implement the required control forms, the control subsystem was divided into three functionally independent control modules. Each module is to be activated or disabled according to the experiment to be performed. This section also establishes the baseline location of actuators and sensors for each control module as well as hardware and software requirements to implement the defined control laws.

6.3.1 Control System Functions

The functional diagram of the control subsystem is shown in Figure 6-1. The three parts of the control systems are shown in the figure as follows:

(i) Passive Control System: This system consists of a series of dampers and isolators which can be locked and unlocked at any given time. These passive elements are placed in locations at which maximum energy dissipation, and thus maximum vibration suppressors, occurs. The passive control system will be used to demonstrate the ability to control the structure at the source of the disturbance.

(ii) Autoalignment System: The autoalignment system consists of actuators which adjust the position of the mirrors to minimize the LOS disturbances as measured by the LOS and figure sensors. The system has low and high bandwidth operating modes. The high bandwidth mode will be used to demonstrate the performance of the control subsystem while controlling the system at the destination during the wave propagation experiment.

The low bandwidth operation mode will be used in conjunction with other control modules, e.g. passive control, to assess the performance of a control approach combination.

(iii) Vibration Suppression System: This module is divided according to the control approach into either a inertial or relative structural control subsystems. The inertial system measures the absolute deflections at various

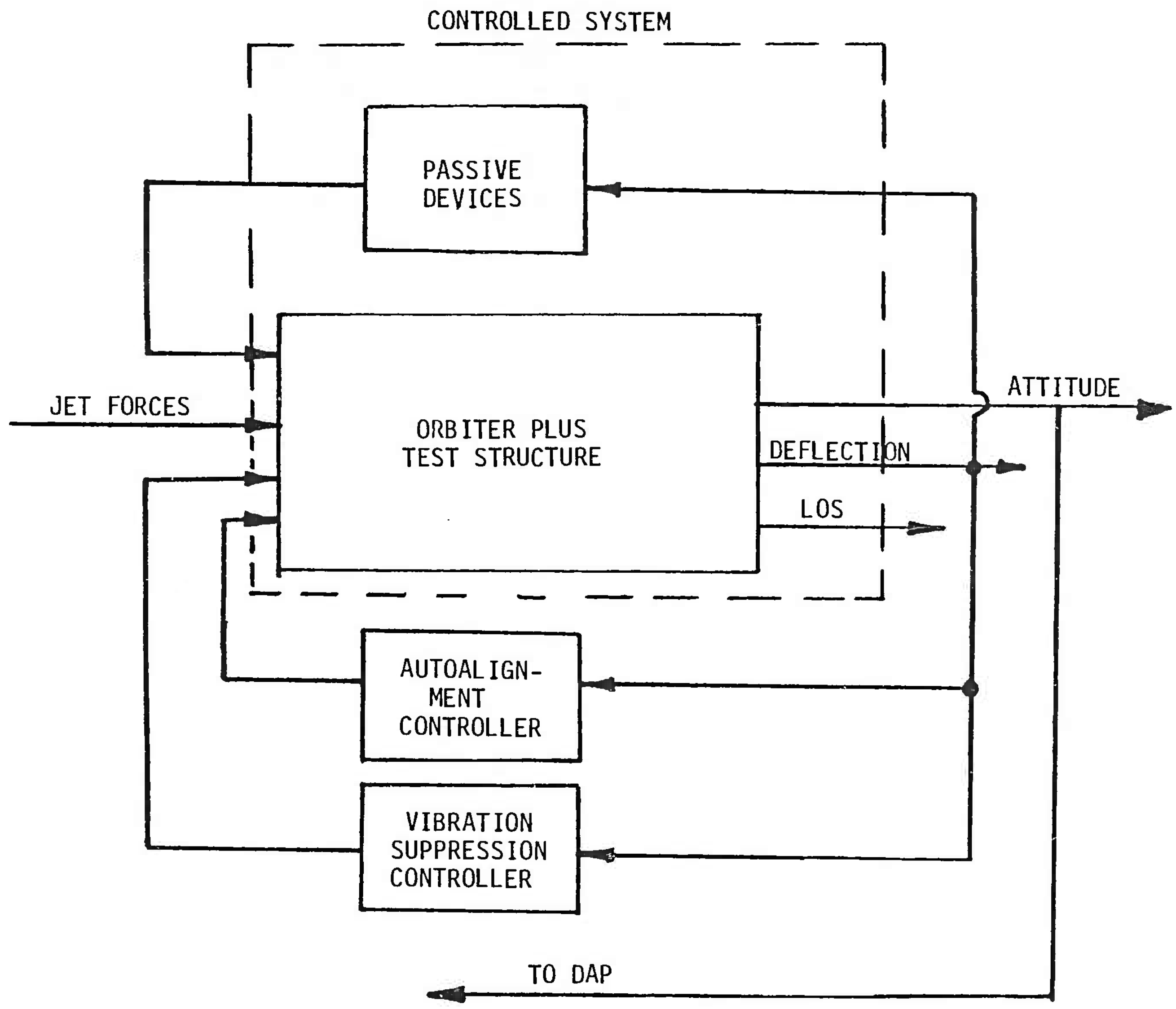

Figure 6-1. Control Subsystem

points and applies inertial forces to minimize the disturbance. Whereas the relative system measures the relative slopes between points on the structure and applies a set of bending moments to counteract the disturbance forces acting on the system. The vibration suppression system operating in either the inertial or relative operating modes will be used to demonstrate controlling the system along the propagation path (structural control) during the wave propagation experiment.

6.3.2 Actuator and Sensor Locations

The modal participation factor (g-factor) was used as a criterion for establishing the locations of the various actuators and sensors. The inertial g-factor for mode i at location j is defined by:

$$g_i = \frac{\phi_{ij}^2}{\omega_i^2} \tag{5.1}$$

The relative motion g-factor between locations j and k for mode i is given by:

$$g_i = \frac{(\phi_{ij} - \phi_{ik})^2}{\omega_i^2} \tag{5.2}$$

where ϕ is the mode shape.

A g-factor analysis was performed on the test structure using a TRW developed program MDLSFT. The program orders the nodes according to their g-factors, one ordering for each one of the modes and, if required, orders the modes according to the magnitude of the g-factor at a given node. The program performs this task in an interactive fashion and can calculate both inertial and relative g-factors as required.

The locations of the actuators and sensors for the different control modules are given next. The node locations are defined in Figure 5-3.

The inertial control system consists of linear momentum exchange devices located on the top of the mast (node 3) and at two support points of the primary mirror. The actuators located at the top of the mast act in the

x and y directions, and the actuators at nodes 14 and 15 act in the z-direction. Sensors in the form of accelerators are placed next to the actuators, creating a colocated system.

The relative control system consists of four bending moment actuators. Two actuators are connected between nodes 17 and 18 and supply torques T_y and T_x to control bending in the x and y-directions, respectively. The other two actuators are connected between nodes 10 and 14, and 10 and 15, supplying moments around the x axis, thus controlling the z deflection of the primary mirror. Sensors are located at the attachment points of the bending actuators, creating a colocated system.

The autoalignment system actuators are located at the supports of the two mirrors. Since each mirror has a kinematic mount, the mirrors' orientation can be adjusted by moving the support points without causing stresses in the structure.

The passive system includes isolators and dampers connected at the connection points of the relative control system i.e., nodes 17 and 18 for bending in the xz and yz planes and between joints 10 and 15, and 10 and 14. The passive system is tuned to dissipate energy from low frequency modes: the first two bending modes of the mast and the bending and torsional modes of the primary mirror and its support.

6.3.3 Hardware Requirements

A preliminary study of the hardware requirements for the various control loops was also performed. The results of this study are as follows:

(i) Inertial Control System: The baseline inertial control system's actuators are four linear momentum exchange devices. Each actuator is baselined to have a bandwidth of ω_B = 150 Hz with dynamic range $\pm$ 2N, accuracy of $\pm$0.02N, and resolution of 0.02N. Sensors in the form of piezoelectric accelerometers will be placed next to the actuators and thus will create a colocated control system. The sensors are baselined to have a bandwidth of 200 Hz, range $\pm$50g, and noise range of $\sim$0.0005g rms.

(ii) Relative Control System: The relative control system will consist of four bending moment actuators located in the places specified earlier. The actuator characteristics are $\omega_B \approx 200$ Hz, dynamic range $\pm$ 2Nm, and a resolution of $\pm$0.03 Nm. The sensors colocated with the actuators will have the following characteristics: bandwidth $\omega_B = 200$ Hz, dynamic range of ~1500 μm, and resolution of ~0.1 μm.

(iii) Autoalignment System: The autoalignment actuating system will consist of a stepper motor operating in a microstepping operation mode, 100:1 harmonic gear drive, and a sensitive ball screw system. An advantage of the microstepper is its easy interface with a digital controller. The autoalignment assembly is baselined to have a bandwidth of 100 Hz, a motion resolution of 0.1 μm, and a dynamic range of ~1500 μm. Since the autoalignment actuators are located at the support points of the mirrors, the control system will consist of six control loops.

6.3.4 Software Requirements

At the last stage of the control subsystem design study, the software requirements were estimated. These requirements are summarized in Table 6-3. Software estimates are based on the assumption that each control loop contains an n-th order filter with up to n-poles and n-zeroes. It is assumed that each filter is implemented using parallel realization which consist of second and first order filters. The assumptions on the number of operations of each filter were as follows: n first order and second order filters are as follows:

n - first order filters

3n+1	Multiplications
3n+1	Additions
8n	Logical instructions
4n+2	Storage locations for constants
8n	Storage locations for instructions

Table 6-3. Control Subsystem Software Requirements

	AUTOALIGNMENT SYSTEM	VIBRATION SUPPRESSION SYSTEM
NUMBER OF LOOPS	6	4
NUMBER OF ADDS	36	40
NUMBER OF MULTIPLIES	36	40
LOGICAL INSTRUCTIONS	96	96
STORAGE(LOCATIONS)	288	288
COMPUTATIONAL DELAY	0.2 msec	0.3 msec
D/A WORD SIZE	14 BIT	14 BIT
A/D WORD SIZE	14 BIT	14 BIT
A/D QUANTIZATION ERROR	0.1 μrad	0.1 μm
D/A QUANTIZATION ERROR	0.1 μm	0.1 μm

n - second order filters

5n+1	Multiplications
5n+1	Additions
16n	Logical instructions
9n+2	Storage locations for constants
16n	Storage locations for instructions

Assuming fixed point operations, the following assumptions are made concerning the timing of each operation:

Addition	1 cycle
Multiply	4 cycles
Logical instruction	1 cycle
Division	30 cycles
Trigonometric function	50 cycles

It is assumed that each cycle takes 1 μsec. The A/D converter's time is taken as 8 μsec and the ready and transfer time is assumed to be 2 μsec. The D/A converters delay time is assumed to be 3 μsec.

6.4 Parameter Estimation Subsystem

The parameter estimation subsystem serves many functions of the POC experiment. They are:

1) To provide an accurate on-orbit test structure model which can be related to analytical and ground test results. These relationships can help one learn how to model future large space structure more accurately.

2) To predict the performance and stability of high technology demonstration experiments before conducting them, thus ensuring the success and safety of the tests.

3) To validate the analytical method used to model passive and active control systems by considering the control systems as integral part of the structure whose damping and other dynamic properties are being determined.

Parameter estimation algorithms for LSS applications are already analyzed in our previous (ACOSS-8) study [19], which identifies the maximum likelihood method as the baseline approach and the frequency response method as a way of providing redundant information for cross-checking. Both methods are reviewed briefly in this report. Two important advances in the maximum likelihood method are made during the current study. One is the development of a substructure identification technique which allows one to identify the test structure in spite of Orbiter attachment and movement . The other is the utilization of a general purpose finite element analysis program in the identification loop; this allows the parameter estimation software to be easily adapted to any other structure.

Simulation studies of applying these methods to the ACOSS-14 test structure are conducted in order to obtain design data. Results show that the Orbiter dynamic interaction has minimal effect on the parameter estimation subsystem. The maximum likelihood method, as expected, gives very good estimates and the frequency response method yields good frequency estimates but is coarse on damping and mode shapes. The selected actuators and sensors are found to be able to generate adequate test data for parameter estimation. Most of the actuators and sensors are the same ones used in the

control subsystem. The data requirements are baselined from a study of the estimator performance as functions of sample rate and quantization.

6.4.1 Parameter Estimation Approaches

The maximum likelihood method has been chosen here as the baseline approach for its accuracy, shorter data requirement, and its ability to handle nonzero initial dynamic conditions. The method will be used to identify both the physical parameters and the modal parameters of the structure. The physical parameter estimates will provide a global description of the structure and the modal parameter estimates will "zero-in" on selected modes of particular interest.

The frequency response method gives very good estimates of the modal frequencies but only coarse estimates of the transfer function gains and the damping ratios. Also, the method is sensitive to nonzero initial dynamic conditions and generally requires longer data. Since the algorithm is very simple and can be implemented easily, it will be used here to provide redundant information for cross-checking the results from the maximum likelihood method.

6.4.1.1 Review of Maximum Likelihood Method

The underlying idea of the maximum likelihood method is to adjust the system parameters so that the model predicted response closely resembles, in some sense, the actual system response. This suggests that it has three basic parts: a parametrized model, a measure of closeness, and a parameter adjustment mechanism.

Let the dynamics of a LSS be modeled as:

$$\frac{d}{dt} x(t, \theta) = A(\theta)\, x(t, \theta) + B(\theta)\, u(t)$$

$$y(t, \theta) = C(\theta)\, x(t, \theta)$$

where θ is a vector of unknown parameters; A, B and C are system matrices; $u(t)$ is actuator input signal; and $y(t,\theta)$ is the model predicted output using parameter θ.

Let $z(t)$ be the actual sensor measurement signal which contains additive white Gaussian noise with zero mean and positive definite covariance matrix G.

Let z(t) be observed actual response of a LSS during time interval [0,T]. The closeness of model predicted response to the actual response is measured by the negative log likelihood function:

$$J(\theta, T) = \frac{1}{2} \int_0^T [z(t) - y(t, \theta)]^T G^{-1} [z(t) - y(t, \theta)] \, dt$$

The unknown parameter θ is adjusted so as to minimize the above function. The minimization is currently being performed by the modified Newton-Raphson method.

Physical and Modal Parameters

The unknown parameters of a LSS are directly related to its model representation. The LSS model is usually obtained through the finite element analysis which results in two equivalent ways of describing the LSS dynamics, each leading to a different set of parameters.

One model is the physical representation described in terms of the mass matrix M and the stiffness matrix K. The parameters of this model is naturally the elements of the M and K matrices, e.g., Young's modulus, Poisson ratio and lumped masses. The advantage of physical parameter is that one can identify the whole structure by estimating only a small number of parameters. But the estimation process is rather complicated since it iterates upon a finite element model of the LSS. In the current study, computer softwares are developed to incorporate existing general purpose finite element analysis program in the identification loop. This reduces some of the difficulties in estimating the physical parameters.

The other model is the modal representation obtained through an eigenvalue transformation from the physical representation. The parameters associated with this model are modal frequencies and mode shapes, called modal parameters. The estimation procedure for this set of parameters is much simpler but the large number of parameters restricts one to identify only a few critical modes.

6.4.1.2 Maximum Likelihood Identification of Substructure Parameters

To apply the physical parameter estimation technique described in the previous section to ACOSS-14 test structure, the estimator would need a detailed finite element model of the Orbiter with the test structure attached. Some difficulties with this approach are: 1) Orbiter finite element model is too complicated, 2) errors in the Orbiter finite element model degrade the accuracy of estimated test structure parameters, and 3) crew motion acts as unknown disturbance to the test structure. To circumvent these difficulties, a technique of "substructure identification", which identifies the test structure parameters independent of the Orbiter motions/vibrations, is developed.

The key step in substructural identification is to decouple the test structure dynamic equations from the Orbiter. The finite element model of the Orbiter with test structure attached can be written in the following partitioned form:

$$\left[\begin{array}{c|c|c} M_0 & \emptyset & \emptyset \\ \hline \emptyset & M_1 & \emptyset \\ \hline \emptyset & \emptyset & M_2 \end{array}\right] \frac{d}{dt} \left[\begin{array}{c} q_0 \\ \hline q_1 \\ \hline q_2 \end{array}\right] + \left[\begin{array}{c|c|c} K_{00} & K_{01} & \emptyset \\ \hline K_{10} & K_{11} & K_{12} \\ \hline \emptyset & K_{21} & K_{22} \end{array}\right] \left[\begin{array}{c} q_0 \\ \hline q_1 \\ \hline q_2 \end{array}\right] = \left[\begin{array}{c} F_0 \\ \hline F_1 \\ \hline F_2 \end{array}\right]$$

q_0 = Nodes of Orbiter

where q_1 = Node of Connecting Point

q_2 = Nodes of Test Structure

Let

$$\left[\begin{array}{c} q_0 \\ \hline q_1 \\ \hline q_2 \end{array}\right] = \left[\begin{array}{c|c|c} I & \emptyset & \emptyset \\ \hline \emptyset & I & \emptyset \\ \hline \emptyset & -K_{22}^{-1} K_{21} & I \end{array}\right] \left[\begin{array}{c} x_0 \\ \hline x_1 \\ \hline x_2 \end{array}\right] \quad \text{or} \quad \begin{array}{l} x_0 = q_0 \\ x_1 = q_1 \\ x_2 = q_2 + K_{22}^{-1} K_{21} q_1 \end{array}$$

Combining above two equations, the dynamic equation for the test structure in terms of the new variables becomes

$$M_2 \ddot{x}_2 + K_{22} x_2 = F_2 + M_2 K_{22}^{-1} K_{21} \ddot{x}_1$$

The above equation is independent of the Orbiter (x_0). If the accelerations at the connecting point ($\ddot{x}_1$) are measured, one can consider $\ddot{x}_1$ as an input to the test structure and use the above equation to identify the test structure parameters.

6.4.1.3 Frequency Response Method

Many versions of frequency response method exist in the literature. The one used in this study is as follows:

1) Establish the frequency response curve of an actuator-sensor pair by using Fast Fourier Transforms (FFT)

$$H(\omega) = \frac{\text{FFT (Output Signal)}}{\text{FFT (Input Signal)}}$$

2) Assume the transfer function of a particular bending mode is of the form (rate sensor)

$$H_i(\omega) = \frac{j\omega\, G_i}{-\omega^2 + j\, 2\zeta_i\, \omega_i\, \omega + \omega_i^2}$$

where G_i = transfer function gain; ζ_i = damping ratio; ω_i = modal frequency

3) For each sufficiently separated spike in the response curve, measure the frequency ω_{mi} and the magnitude of the spike M_i. Then

$$\omega_i = \omega_{mi} \text{ and } M_i = G_i/2\zeta_i\, \omega_i$$

4) Substitute above equations into $H_i(\omega)$ and determine the damping ratio ζ_i by minimizing the cost function

$$J(\zeta_i) = \int_{\omega_1}^{\omega_2} [|H(\omega)| - |H_i(\omega)|]^2\, d\omega$$

where ω_1 and ω_2 are chosen so that only one mode is involved.

5) After determining ζ_i, the transfer function gain is computed from

$$G_i = 2\zeta_i \omega_i M_i$$

6.4.2 Simulation Studies

The objective of the simulation studies is to obtain design data for baselining the identification subsystem hardware and software requirements.

6.4.2.1 Simulation Softwares

Computer software for parameter estimation simulation studies consist of two major parts - a detailed "true" system model and an identification algorithm. The true system is simulated using the computer programs developed in Section 4 for Orbiter dynamic interaction studies. The system dynamics are obtained by combining Orbiter and test structure modal data through the modal synthesis program KOMBINE. The DAP logic of firing vernier jets is also included to simulate Orbiter limit-cyclings. As in Section 5, the Orbiter attitudes are set initially at values shown in Table 5-4. This initial attitude causes frequent vernier jet firings and thus creates the worst case structural vibrations of the Orbiter and the test structure.

The system models used in the identification algorithms are much simpler: 1) the Orbiter and VRCS are omitted since their dynamic influence on the relative motions of the test structure has been determined to be much less than that of the test signals, and 2) it is truncated to have only the first six structural modes (the "true" system contains 30 modes).

All three identification algorithms mentioned before are programmed. The implementations of the frequency response method and the modal parameter estimation are fairly straightforward. The physical parameter estimation procedure requires the use of a finite-element modal analysis program in the identification loop. In previous studies (e.g., ACOSS-8), special subroutines were developed for the finite-element analysis of the particular structure of interest-a special subroutine for each structure to be analyzed. This is a tedious task which had to be repeated every time a new structure is considered. We resolve this problem by utilizing an existing general

purpose finite-element analysis program in the identification algorithm. The block diagram in Figure 6-2 shows how such a program (TRWSAP, TRW Structural Analysis Program) is used.

6.4.2.2 Selection of Actuators and Sensors for Parameter Estimation

The parameter estimation subsystem should make as much use as possible of the actuators and sensors already selected for the active control subsystem. The criterion of placing actuators and sensors for parameter estimation is very close to the one for active control, i.e., they should be placed at locations where all critical modes can be excited and measured. Additional actuators or sensors, however, may be required to enhance the identifiability of certain parameters.

The locations of actuators and sensors for parameter estimation are shown in Figure 6-3 and are also listed in Table 6-4. Other than the following two exceptions, all actuators and sensors are the same ones used in the active control subsystem.

1) Two additional linear momentum exchange devices are mounted at the mid-mast in the X_0 and Y_0 directions. These two actuators are used to excite the second-order mast bending modes (22.4 and 23.0 H_z), which are critical in distinguishing the masses at the secondary mirror and mid-mast.

2) Accelerometers and gyros are mounted at the base connecting the structure to the Orbiter. When this acceleration information is available, one can isolate the test structure dynamically from the Orbiter motions, permitting the use of the substructure identification technique described earlier.

6.4.2.3 Physical Parameter Estimation Results

Five structural parameters are determined as critical physical parameters that must be estimated. They are:

1) E — Young's modulus of the graphy epoxy material used to make the mast and most of the primary mirror support structure

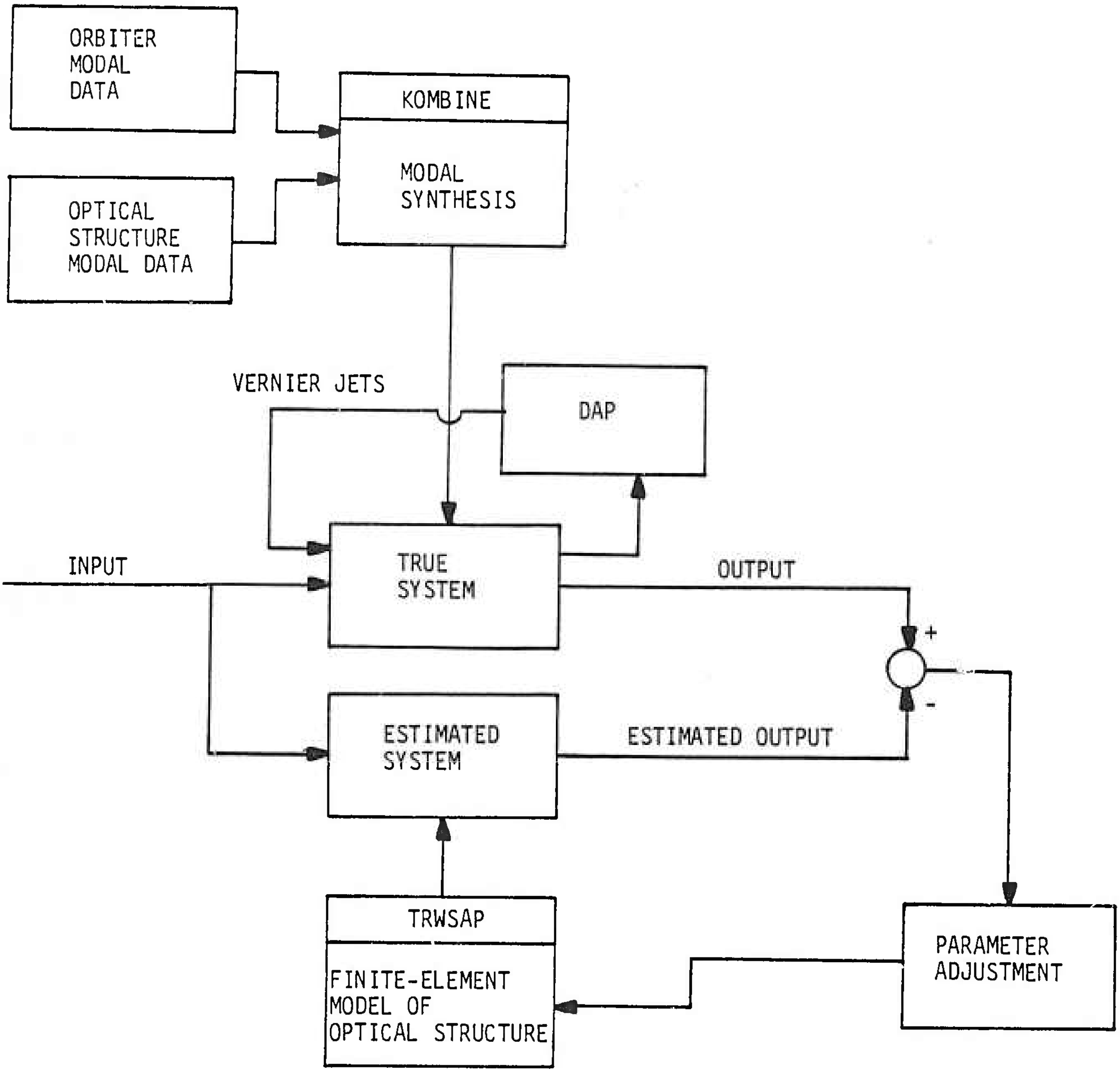

Figure 6-2. Simulation Software for Physical Parameter Estimation

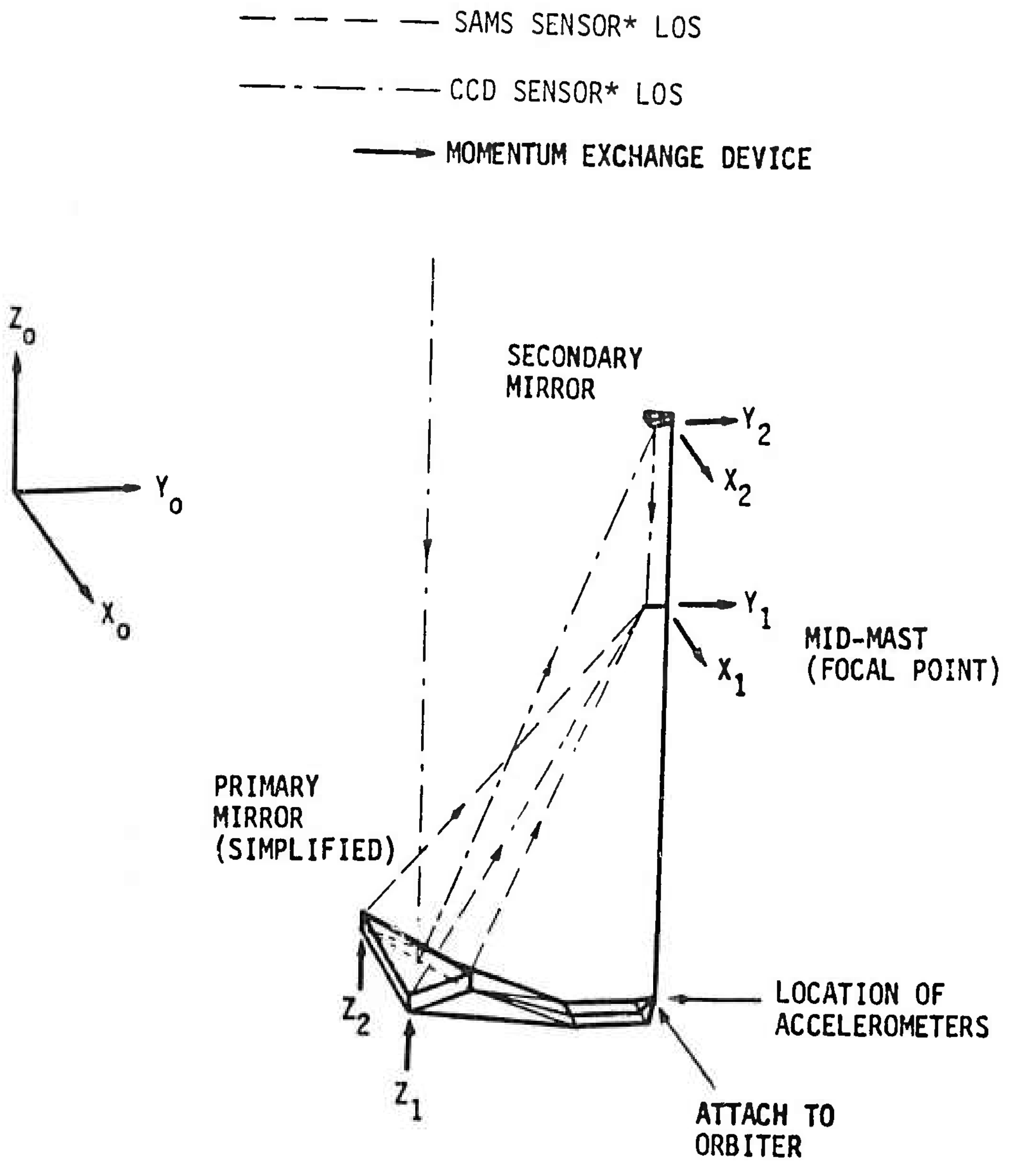

* Section 7

Figure 6-3. Actuator and Sensor Placement for Parameter Estimation

Table 6-4. Summary of Actuator/Sensor Used for Parameter Estimation

Actuator	Location	Direction	Type
1	Mid-mast	X	Linear Momentum Exchange
2	Mid-mast	Y	"
3	Secondary Mirror	X	"
4	Secondary Mirror	Y	"
5	Primary Mirror	Z	"
6	Primary Mirror	Z	"

Sensor	Measurement
SAMS	Distance from mid-mast to points on the Primary mirror (Section 7)
CCD Sensor	Motion of Optical Trim (Section 7)
Accelerometers (3)	Accelerations at the point connected to the Orbiter
Gyros (3)	Angular acceleration at the point connected to the Orbiter

2) ν the corresponding Poisson ratio of above material

3) M_{top} lumped mass of secondary mirror

4) M_{mid} lumped mass of instrument at focal plane (including CCD and SAMS sensors)

5) M_{prim} lumped mass of primary mirror.

The next step is to select a test signal that will make the unknown parameters more identifiable from structural responses. Table 6-5 lists the actuators, and the major structural modes and related physical parameters they make more identifiable.

There are procedures for computing the "optimal" test signal which maximizes the Fisher information matrix (high estimation accuracy), while satisfying some energy constraint. But optimal input design, in general, is a difficult problem to solve. The results depend on the unknown parameters and may violate the test structure load constraint or linearity assumption.

The approach taken in this study is to design a test signal which produces reasonably good estimates. Several test signals were tried. It was found that the masses of the secondary mirror and the mid-mast are difficult to distinguish if the second mast bending modes (modes 5 and 6) are not sufficiently excited. Also, the Poisson ratio and the mass of the primary mirror are highly correlated if the primary mirror torsional mode (mode 4) is not excited. A test signal that can excite modes 1-6 is, therefore, crucial. An example of such signals is shown in Figure 6-4.

Structural responses are measured using the SAMS sensor (Section 7), which measures the relative range from the mid-mast (focal point) to nodes 8, 14, and 15 of the primary mirror; these measurements are denoted as Y_1, Y_2, and Y_3, respectively. Gaussian white noise of 1 μm (1σ) is added to the measurement signal. The accelerations at the node connecting to the Orbiter are also measured; this permits one to identify the test structure parameters in spite of Orbiter structural vibrations and VRCS firings.

The physical parameter estimation technique is applied to 1 second of simulated data. Figure 6-5 shows the comparison of the measured data

Table 6-5. Actuator and Its Related Major Modes and Physical Parameters

Actuators	Major Modes	Physical Parameters
Secondary Mirror X_2, Y_2	2, 3	E, M_{top}
Primary Mirror Z_1, Z_2	1, 4	E, ν, M_{prim}
Mid-Mast X_1, Y_1	2, 3, 5, 6	E, M_{top}, M_{mid}

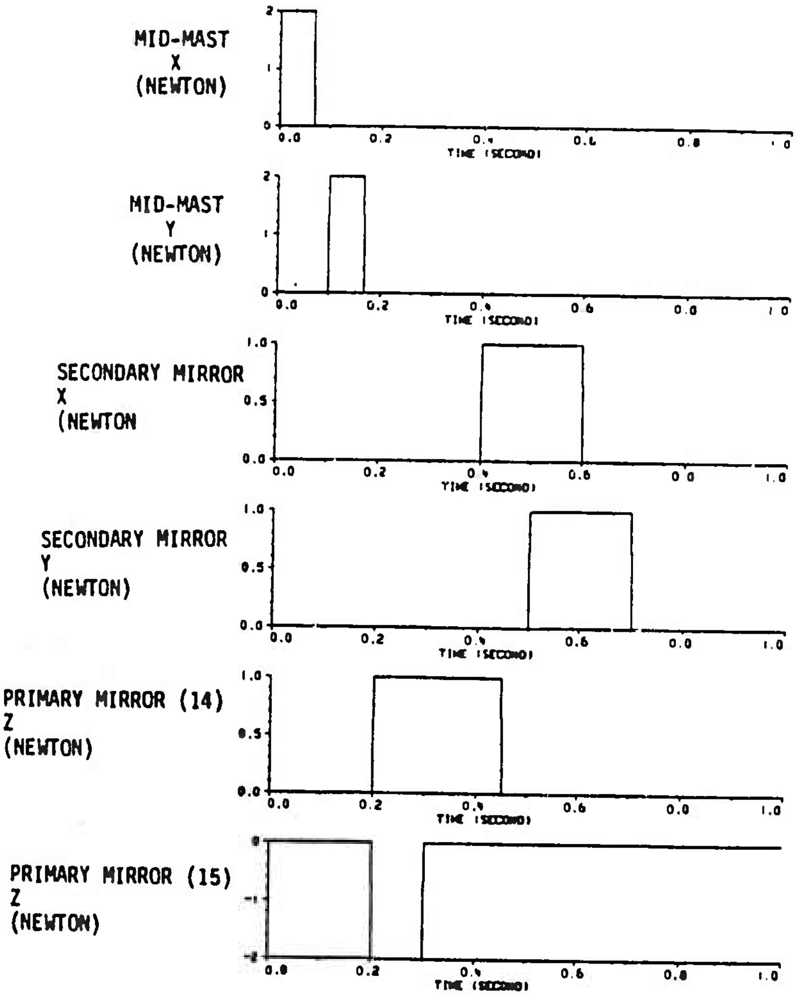

Figure 6-4. Test Signal for Physical Parameter Estimation

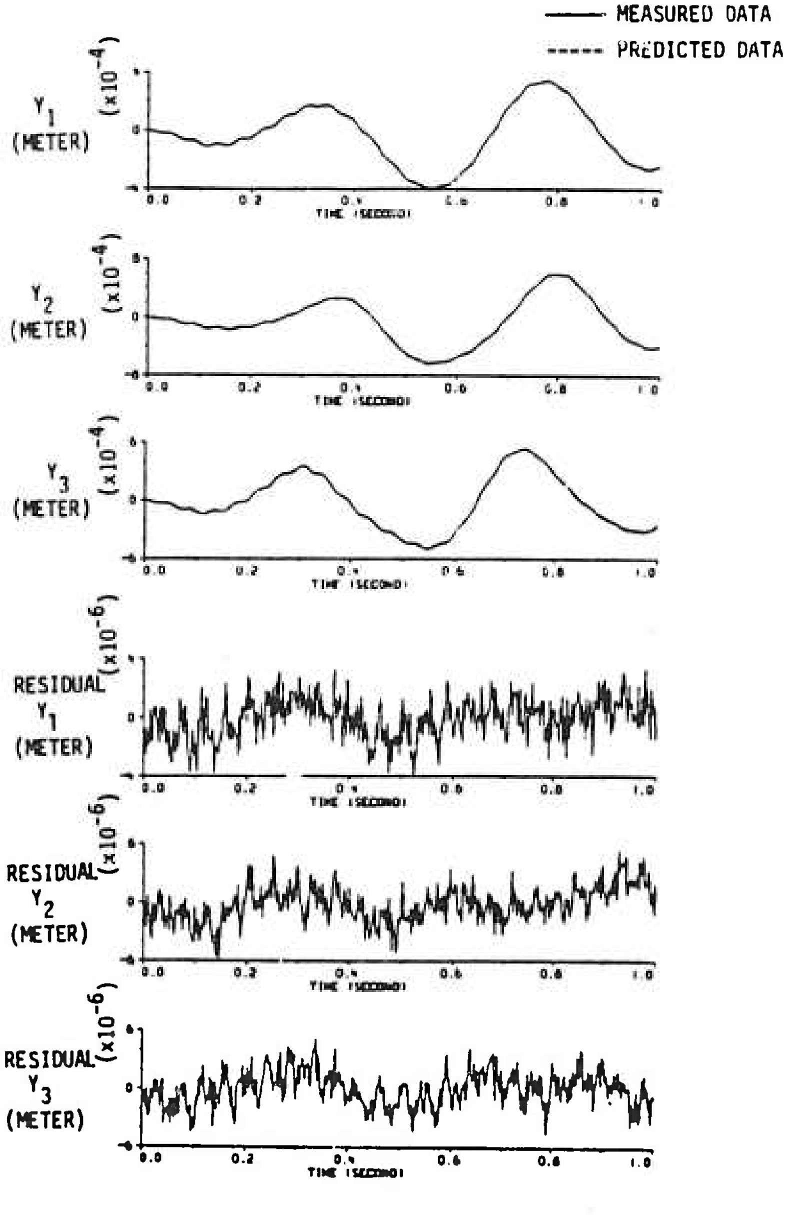

Figure 6-5. Comparison of the Measured Response with the Predicted Response for Physical Parameter Estimation

with the data predicted using the final estimated parameters. The differences are so small one can hardly tell them apart. The residuals which are the differences between measured signal and predicted signal are also shown in Figure 6-5. The estimated parameters in each of the Newton-Raphson iterations are shown in Figure 6-6.

The shape of the cost function which must be minimized to yield the maximum likelihood estimates depends on both the input signals and the physical parameters. For the input signal presented before, the cost function for some of the physical parameters are shown in Figure 6-7. In each case only one parameter is allowed to vary, all other parameters are fixed at their true values. As we have studied before in ACOSS-8, the cost function of longer data (2 seconds) has a sharper curve at the minimum point (which implies greater estimation accuracies) than that of shorter data (1 second). However, the region of convergence for 2 seconds of data is still very wide, so one can start the estimation algorithm with poor initial estimates and it will still converge.

6.4.2.4 Results of Modal Parameter Estimation

The modal parameters of the first four structural modes are obtained using 3 separate tests. In each test only one actuator is energized and the corresponding critical modes are estimated.

The time histories of data involved in a typical modal parameter estimation is shown in Figure 6-8. The input signal is a rectangular pulse with an amplitude of 1 Newton and duration of 0.3 second. The measured output is the relative rate of deflection of the secondary mirror in the x direction. The output measurement contains the responses due to Orbiter VRCS firings and the dynamic interaction with Orbiter structural modes. Also, for the particular case shown, the output measurement has nonzero initial dynamic conditions which have to be estimated along with other modal parameters. The predicted signals are computed using the resulting parameters after 5 Newton-Raphson iterations. Both the input and output signals are sampled at 50 Hz and quantized, with proper scaling, to 8 bits. Since it is planned that the parameter estimation be done on ground, the predicted signal is generated by a ground computer with a much higher

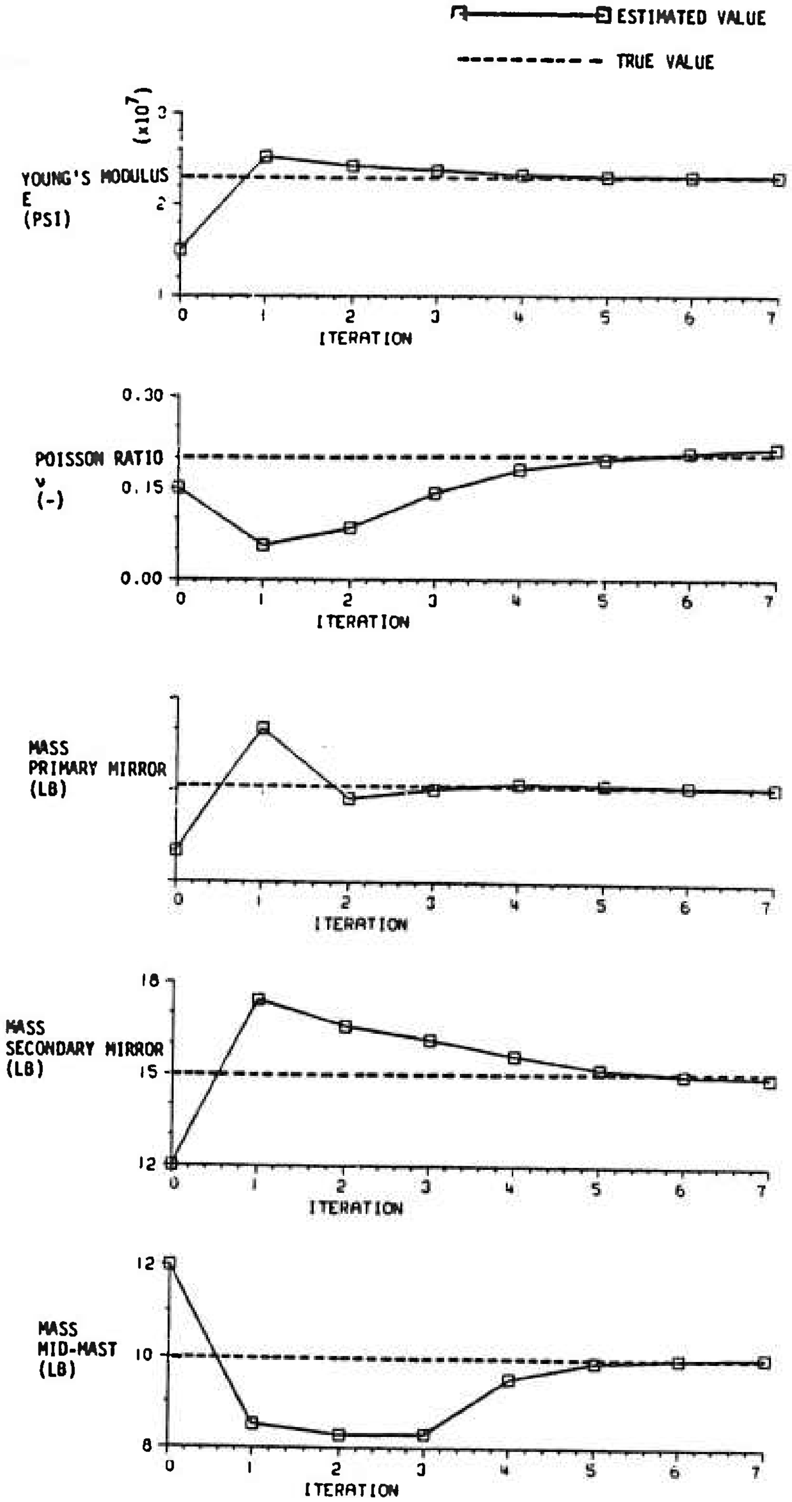

Figure 6-6. Convergence of Physical Parameters in Newton-Raphson Iterations

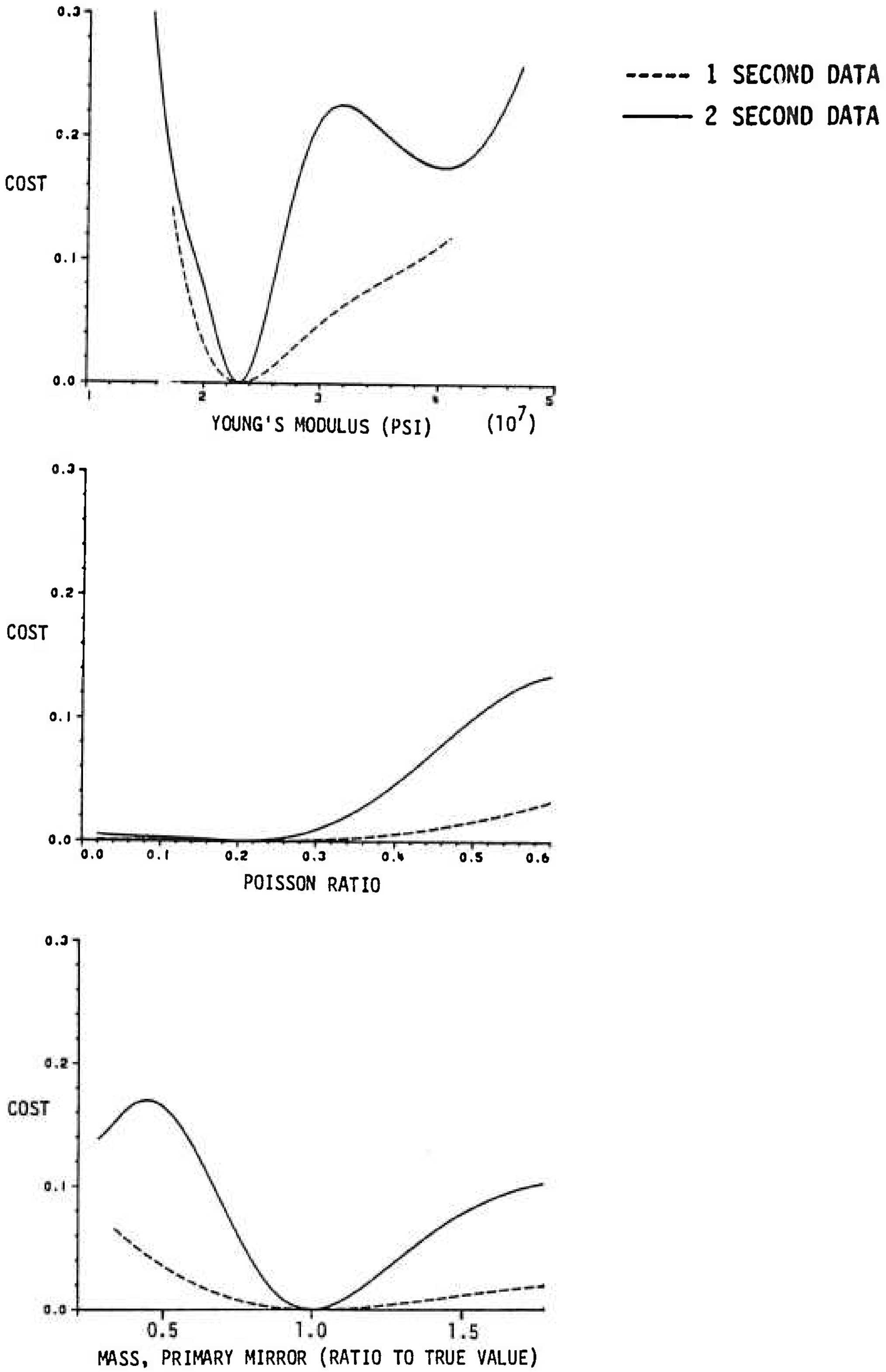

Figure 6-7. Cost as Function of Parameter Variations

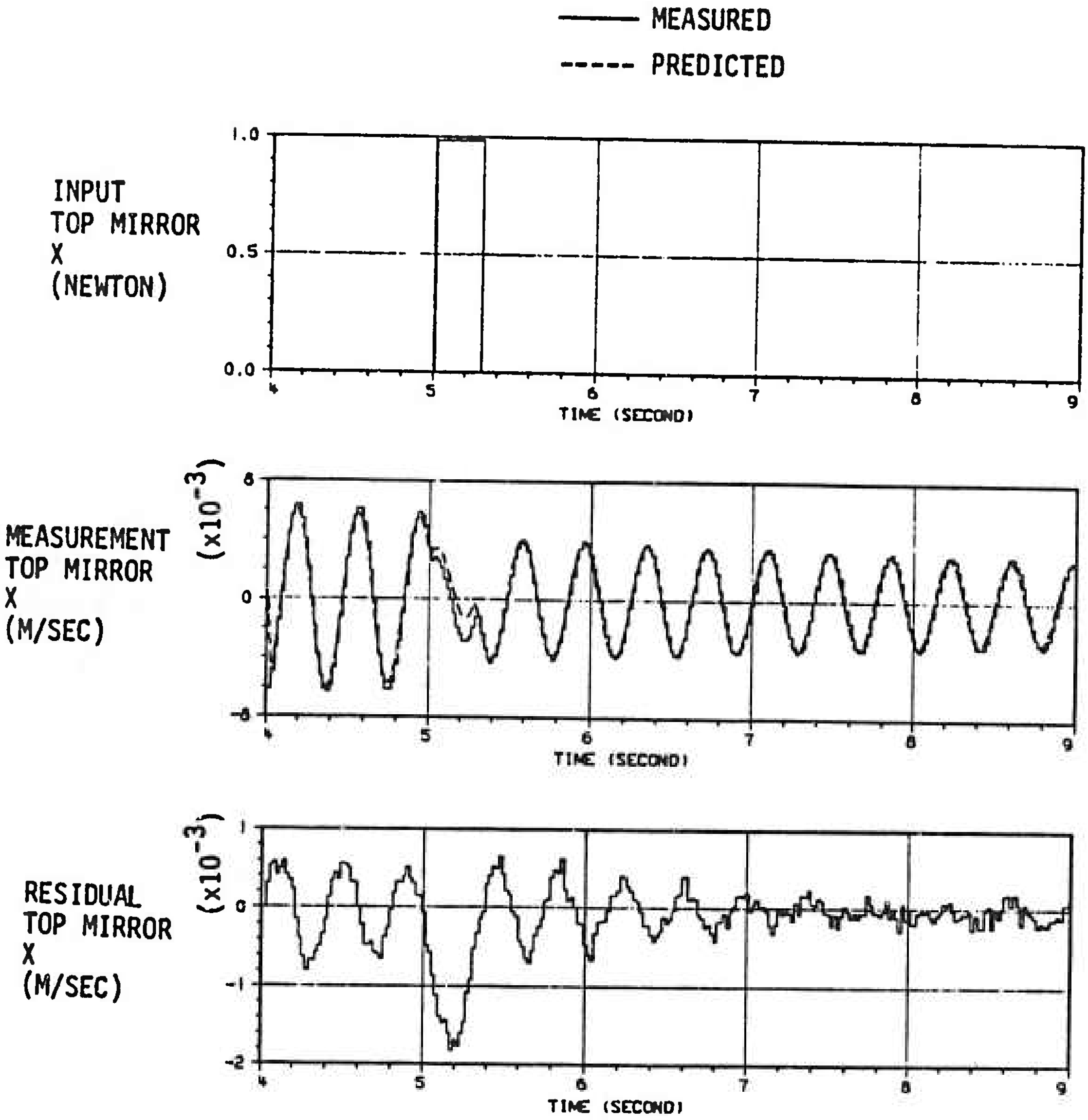

Figure 6-8. Time Histories of Data Used in Modal Parameter Estimations

quantization level. The impact of sample rate and quantization level on parameter estimation accuracy will be discussed later.

The results of the three modal parameter tests are summarized in Table 6-6. In some cases the initial dynamic conditions are also estimated. Since the initial condition is a function of the particular data starting point and not properties of the test structure, they are not shown.

6.4.2.5 Results of Frequency Response Method

Figure 6-9 shows the signals involved in estimating the second mode of the test structure. Band-limited (25 Hz) Gaussian random noise (a) is applied to the actuator at the secondary mirror in the X direction and the structural response at the same location is measured (b). The frequency contents in the first 20.48 second data of (a) and (b) are computed using the Fast Fourier Transforms (c and d). The frequency response curve (e) is obtained from the ratio of curves (d) and (c).

A computer program is developed to estimate the modal frequency, transfer function gain and damping ratio by fitting a second-order transfer function to the frequency response curve in the neighborhood of each modal spikes. Figure 6-10 shows the result of this frequency domain matching for the second mode.

The estimation results, summarized in Table 6-7, show very accurate modal frequency estimates but rather poor estimates of modal damping ratios and transfer function gains. These results are expected from our ACOSS-8 work and this is one reason for using this approach only as a cross-check.

6.4.2.6 Quantization and Sample Rate

Tests are made with various sample rates and quantization levels for the modal parameter estimation. Figure 6-11 shows the average (over unknown parameters) parameter error as function of sample rate for the cases of 8-bit and 16-bit fixed point quantization. The quantization level is selected so that all signal amplitudes are within its dynamic range. Both 8-bit and 16-bit quantization produce almost identical results in estimation accuracy which, however, degrades significantly for sample rate below 50 Hz. Thus, the baseline quantization level is specified at 14 bits and the sampling rate at 175 Hz.

Table 6-6. Summary of Modal Parameter Estimation

Test	Actuator	Mode	Parameter	Estimated Values: 5 sec	Estimated Values: 10 sec	True Value
1	Secondary Mirror X	2	ω_2 (Hz)	2.65	--	2.64
			ζ_2	0.43%	--	0.5%
			$C_{2,3x}$	-0.338	--	-0.340
			$C_{2,2x}$	-0.182	--	-C.184
2	Secondary Mirror Y	3	ω_3 (Hz)	2.66	--	2.65
			ζ_3	0.56%	--	0.5%
			$C_{3,3y}$	-0.336	--	-0.339
			$C_{3,2y}$	-0.181	--	-0.182
3	Primary Mirror Z	1	ω_1 (Hz)	1.97	1.97	1.97
			ζ_1	0.43%	0.49%	0.5%
			$C_{1,44z}$	0.145	0.141	0.146
			$C_{1,11z}$	0.089	0.086	0.090
			$C_{1,45z}$	0.147	0.141	0.146
		4	ω_4 (Hz)	4.89	4.88	4.88
			ζ_4	0.60%	0.62%	0.5%
			$C_{4,44z}$	0.119	0.119	0.120
			$C_{4,11z}$	0.0005	0.0008	0.00001
			$C_{4,45z}$	-0.119	-0.119	-0.120

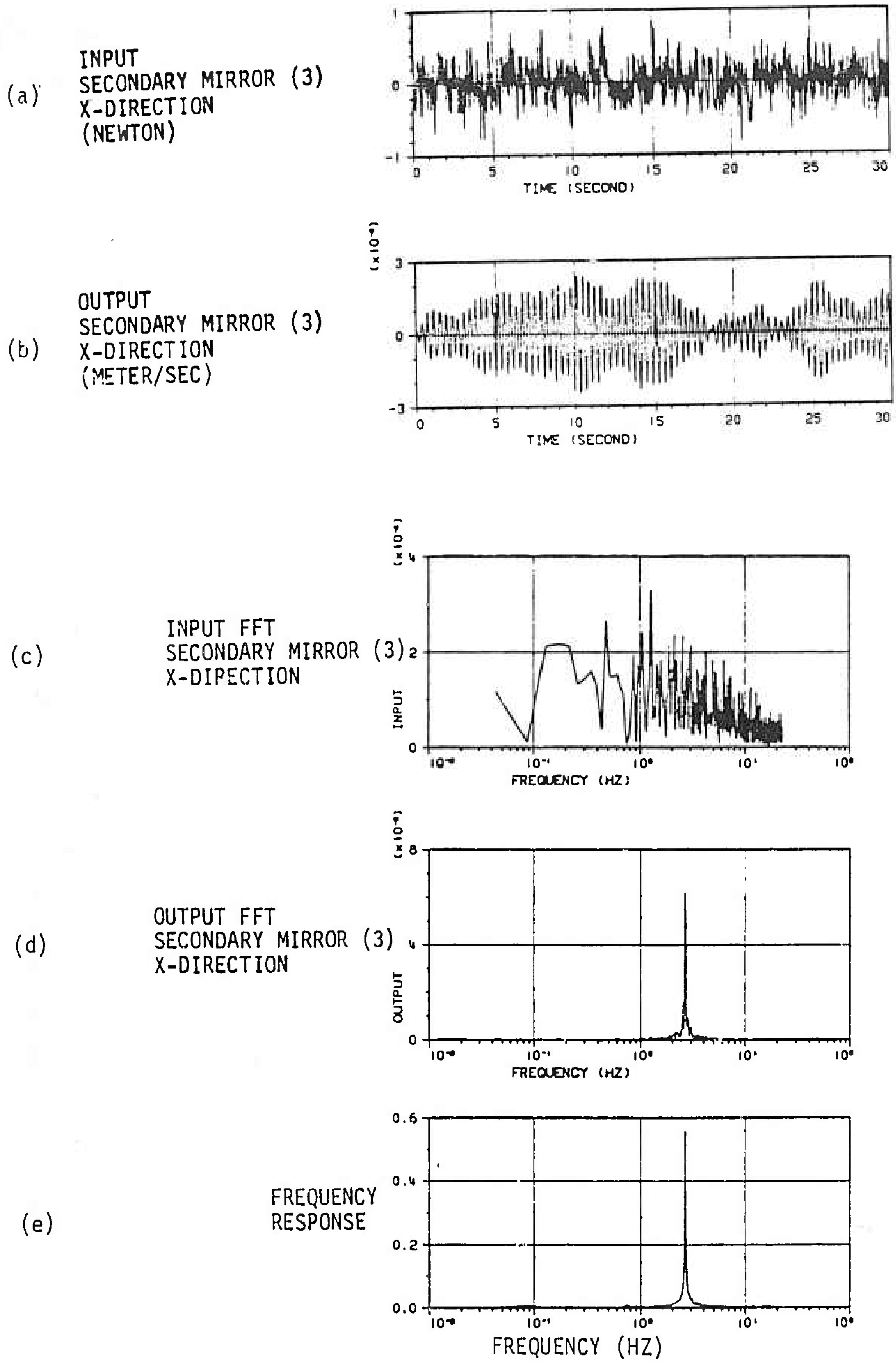

Figure 6-9. Time Histories of Input/Output Signal (a and b), Their Frequency Transforms (c and d), and the Frequency Response Curves (e)

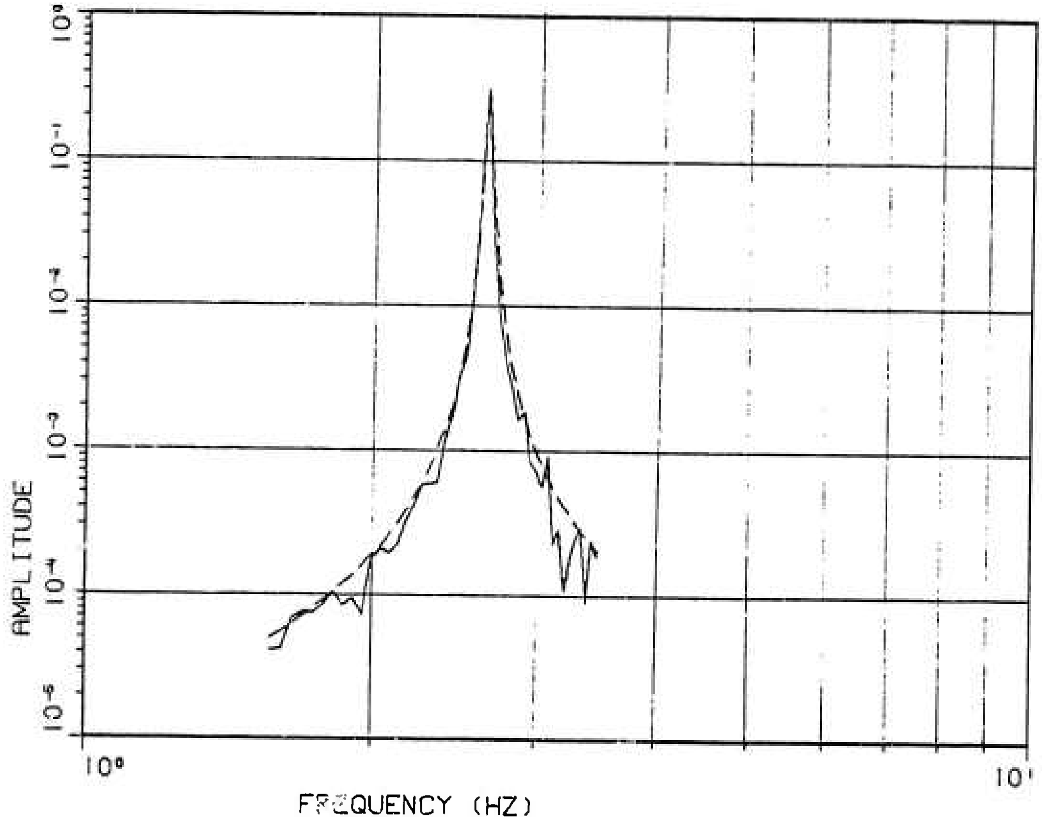

——————— Frequency Response Curve

- - - - - - - - - Second Order Transfer Function

Figure 6-10. Frequency Domain Matching of a Structural Mode

Table 6-7. Results of Frequency Response Method Using 20 Seconds of Data

INPUT	OUTPUT	MODE	FREQ. (HZ)		GAIN, G_i		DAMPING RATIO, ζ_i	
			TRUE	EST.	TRUE	EST.	TRUE	EST.
TOP MIRROR (3) X-FORCE	TOP MIRROR (3) X-RATE	2	2.64	2.65	0.115	0.123	0.005	0.007
	MID-MAST (2) X-RATE	2	2.64	2.65	0.062	0.070	0.005	0.007
PRIM. MIRROR (14) Z-FORCE	PRIM. MIRROR (14) Z-RATE	1	1.97	2.04	0.021	0.039	0.005	0.0122
		4	4.87	4.86	0.014	0.023	0.005	0.0039
	PRIM. MIRROR (8) Z-RATE	1	1.97	2.04	0.013	0.024	0.005	0.0122

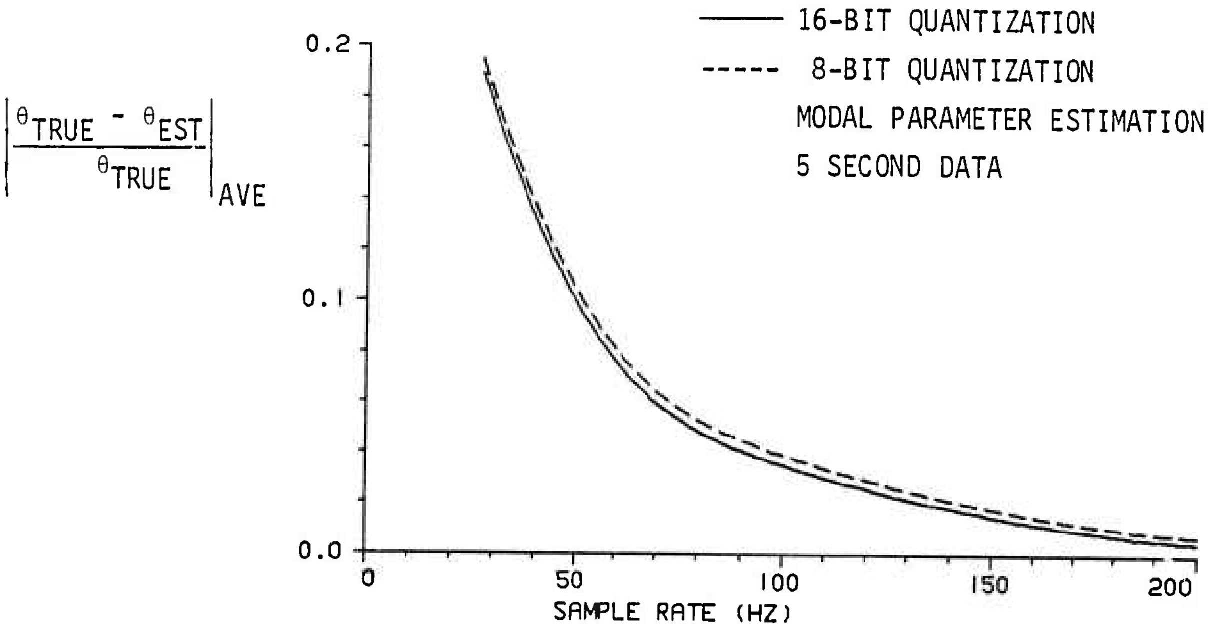

Figure 6-11. Average Parameter Estimation Error As a Function of Sample Rate for 8-Bit and 16-Bit Quantization

7.0 DATA ACQUISITION AND INSTRUMENTATION

With the establishment of the baseline concept and its basic compatibility with the Shuttle, finer details of the experiment system can be defined and analyzed. This section defines how experimental data is to be acquired, stored, and transmitted. The system's electrical and thermal requirements are also briefly assessed and compared with the capability of the Shuttle.

7.1 LOS Measurement and Optical Alignment

The performance criteria for the technology demonstrations will be optical element motion and LOS motion/image quality. A concept for measuring it is illustrated in Figure 7-1. The basic idea to measuring optical element motion is to deploy 8 Ga Al As laser diode (LED) transmitters on the perimeter of the primary mirror, preferably at rigid points subtending from the support. The six degree-of-freedom motion of these points (hence primary mirror rigid body motion) is then directly measured with a TRW Surface Accuracy Measurement Sensor (SAMS) rigidly attached to the focal plane. The motion of the secondary mirror is indirectly measured by observing the LED reflection off the secondary with CCD focal plane sensor and then subtracting the LED image motion caused by the primary. In order to make the LED light focus on the focal plane, four of the LEDs are lensed to focus at F.

The LOS and imaging performance of the system will be measured with the same charge-coupled-device (CCD) sensor system above, one similar to TRW's MADAN. LOS is directly measured by electronically tracking the centroid of a stellar or other point source truth target image in the sensor. Imaging quality is deduced by observing and electronically imaging a more complicated truth target and ground.

7.1.1 CCD Sensor Requirements

The LOS, imaging and secondary mirror range sensing functions defined above are performed by a CCD array. TRW is currently developing such a sensor (MADAN) for other applications, a picture of it is shown

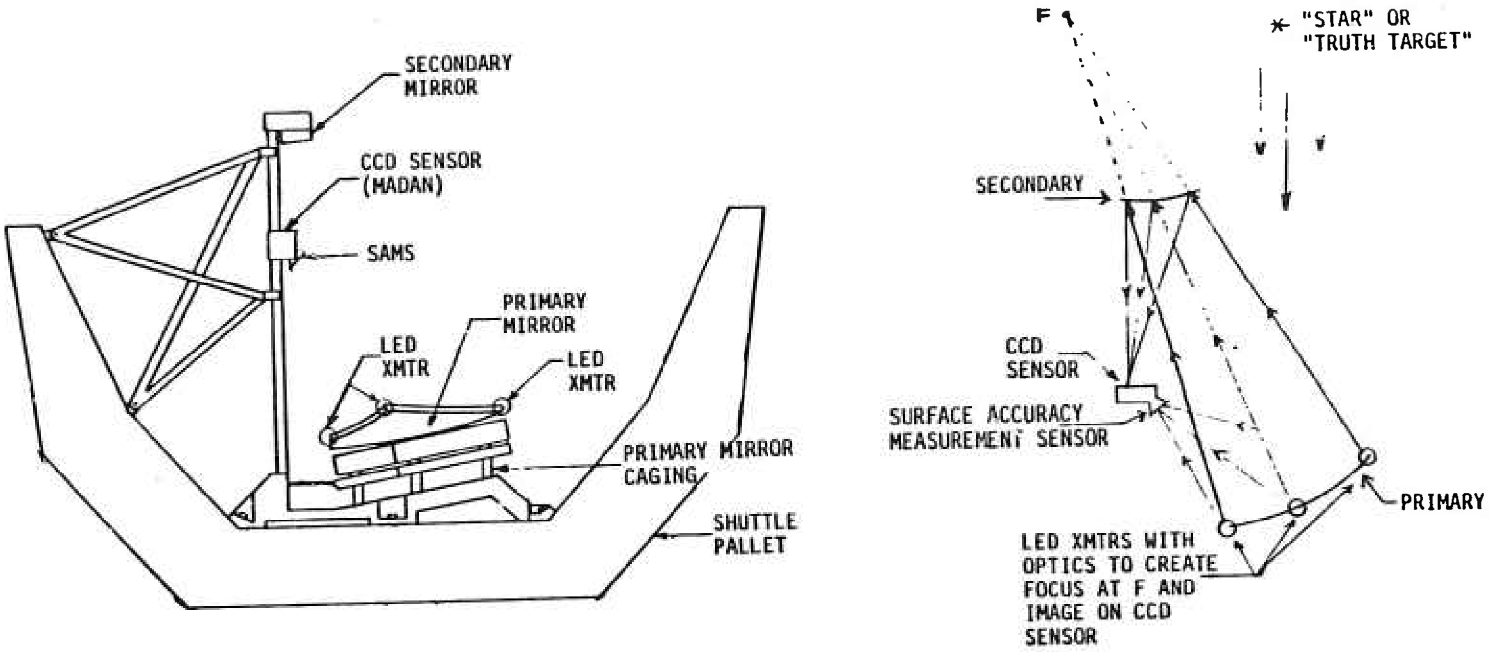

Figure 7-1. LOS Measurement and Optical Alignment Concept

in Figure 7-2. During the course of the study, the MADAN system designer was consulted to outline the requirements and modification required to make this sensor work for the present application. The optical requirement is to have a .01x.01 rad field of view with approximately .2 μrad resolution. The throughput requirement is to be able to sample "figure" at 175 Hz, and sample "image" at two frames/second.

The modification required to make the MADAN sensor meet these specifications are to replace the current quad arrangement of Hughes CCD arrays (see Figure 7-3) by four RCA53612 arrays. The RCA chips are 540x512 pixels each, so if one optically shutters the set and uses the standard .05 pixel interpolation algorithm, .2 μrad resolution is possible. One can further improve this resolution by using the preferred, .02 pixel interpolation algorithm. The resolution with this algorithm is .1 μrad.

In order to meet the throughput requirements, it is assumed that the laser diodes (designating critical structure locations) are aimed at pre-specified, nominal locations on the sensor. The area surrounding these locations are used only for structure measurements and not to image. The electronics then channels the pixel samples to either the image or structural measurement processor, depending on the location of the pixel on the chip. Pixel windowing is specified at 10x10 with all four chips running in parallel at .1 μsec/pixel. The windowed data is accumulated using .0015 seconds integration and then line dumped at .4 μsec/line. The signal strength provided by the laser diodes has been analyzed and it will permit 175 Hz samples of the structure with good S/N. Similarly, the light gathering capability of the telescope has been analyzed and it will permit two frame/second imaging rates.

The power consumption of the CCD sensor is conservatively estimated at 31 W, including data processing electronics. The total weight is less than 20 lbs.

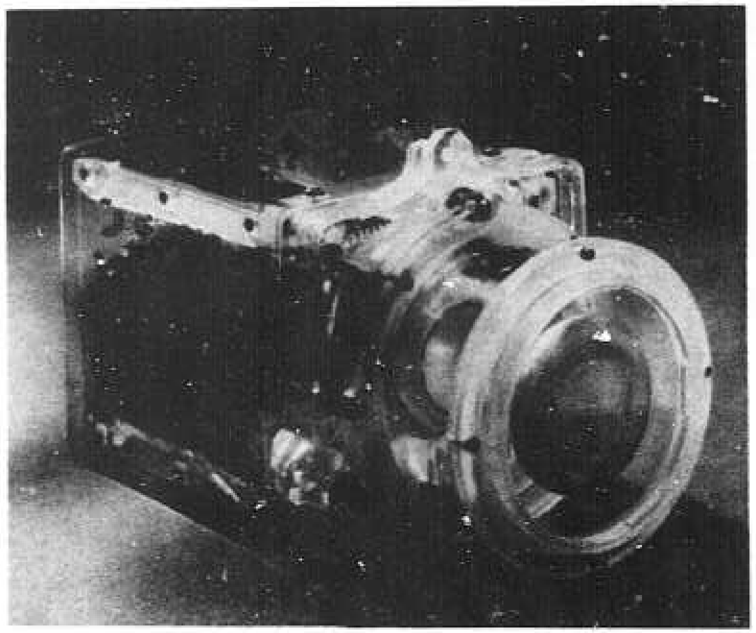

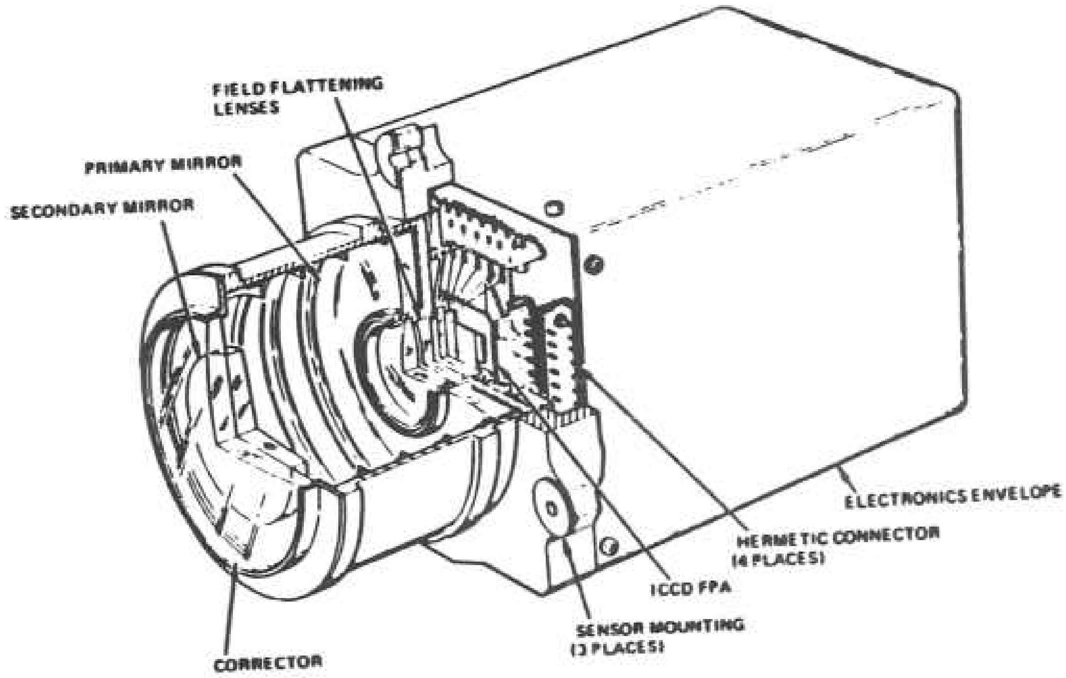

Figure 7-2. TRW Multimission Attitude Determination and Autonomous Navigation (MADAN) Sensor

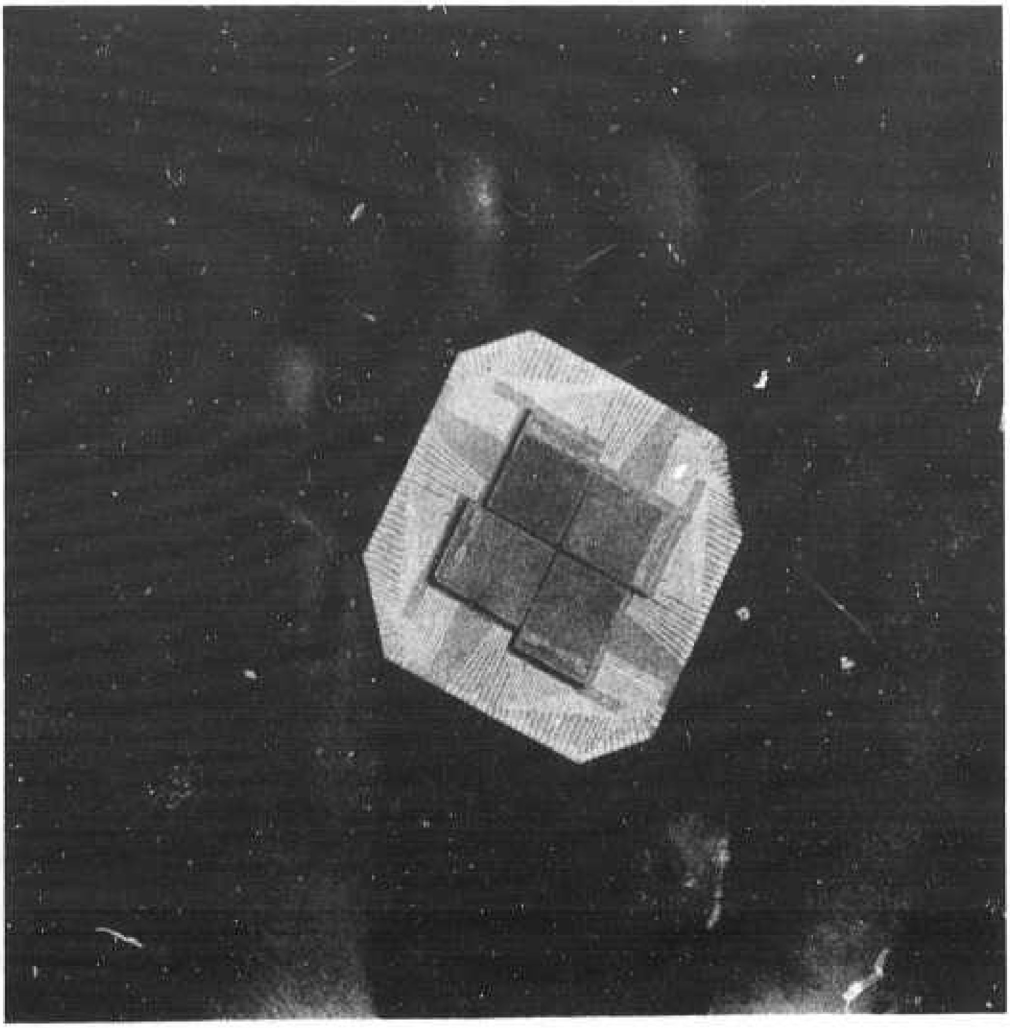

Figure 7-3. CCD Arrays in Quad Arrangement

7.1.2 Surface Accuracy Measurement Sensor (SAMS) Requirements

A modified SAMS has been baselined for ranging the primary mirror. The SAMS, shown in Figure 7-4 was originally developed by TRW for NASA Langley and was delivered to them in 1980. Since then, the sensor has continually been improved through better detectors, electronics, and element stabilization. The unique properties of the sensor are: its 5×10^4 dynamic range (independent of field of view); its excellent linearity properties; and bandwidth greater than 1 KHz. The sensor plus electronics consumes about 20W, and the space qualified sensor would weight 10 lbs.

For the present application the field of view of the sensor would be designed at 5000 μrad. This would allow a .1 μrad measurement accuracy. In order to simultaneously view all of the laser diodes on the primary mirror support, the optics on the sensor head will spacially multiplex the nominal range angles into the FOV. This will allow up to ± 400 μrad excursion at each range point. The approach has been successfully used elsewhere.

The SAMS sensor can only measure angles relative to its own coordinate frame. In order for it to range objects relative to itself, some additional information must be available. One approach to obtain this information is through the stadiametric ranging technique described in Figure 7-5. The approach is described for a planar coordinate frame for simplicity. The basic idea is that if one knows the relative distance between at least three points (four points for three dimensions) on an object, and, one knows the angles to the targets on the object, then the object can only lay in one of two positions. These are marked with solid and dashed lines in the figure. But note however, that in on case the angle to C is greater than the angle to B, and, in the other case the angle to B' is greater than to C'. So if one can associate the measured angle to the targets with the targets, the ambiguity is resolved, and the range to all three targets can be computed. The concept used in the SAMS is to uniquely tag the target by pulsing them at different rates.

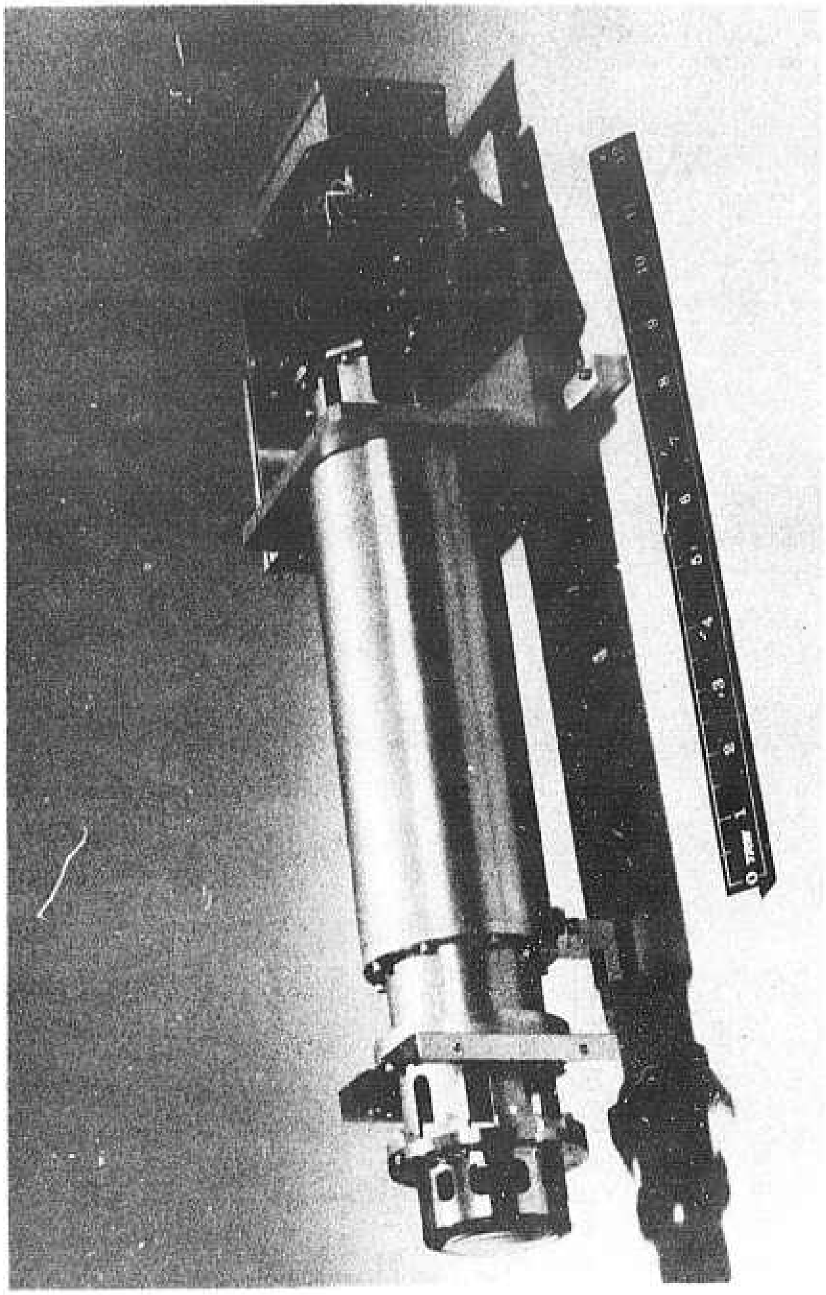

Figure 7-4. TRW SAMS Sensor

SAMS STADIAMETRIC RANGING

- RELATIVE DISTANCE BETWEEN LEDS A,B AND C ARE ASSUMED KNOWN I.E., KNOW S, R AND θ
- PULSE LEDS A, B AND C AT <u>DIFFERENT</u> RATES
- SAMS MEASURES ANGLES α, β and γ AND ASSOCIATES IT WITH LEDS A, B AND C
- A, B AND C CAN BE UNIQUELY RANGED GIVEN α, β, γ, S, R, θ AND THE TAGGING

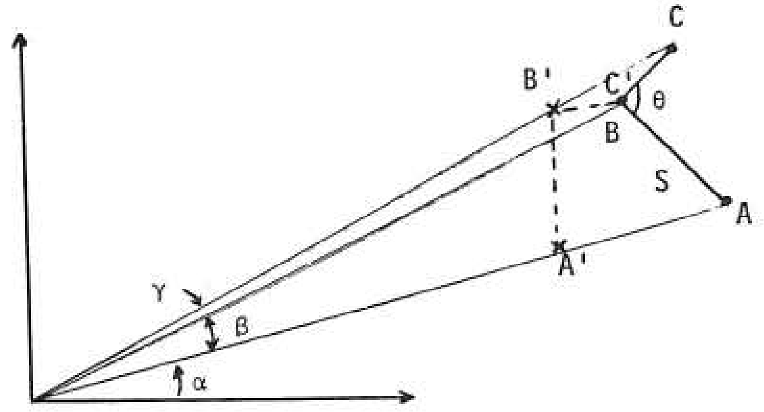

SAMS COORDINATE SYSTEM

● TRUE LOCATION OF LEDS

X RESOLVED AMBIGUOUS LOCATION

Figure 7-5. Stadiametric Ranging Technique Used in SAMS

7.1.3 Simulated Performance of the SAMS and CCD Sensor

Monte Carlo runs were used to determine the LOS and figure sensing capabilities of the baselined SAMS and CCD sensor systems. The simulation results of the SAMS showed that it will be able to stadiametrically range the position of point sources in the primary mirror to 0.16 μm (3σ) in all three axes. This result includes various expected random misalignments expected by the SAMS designer: referring to Figure 7-5, .1 μm, 1σ uncertainty in the reference distance S and R; .1 μrad, 1σ uncertainty in reference angle θ; and .1 μrad, 1σ measurement error in α, β and γ. This information was incorporated with the expected capability of the baselined CCD sensor in order to estimate the ranging sensitivity to the secondary mirror. This resulted in 0.2 μm(3σ), 3-axis ranging. Integrating this information into the baselined optical train sensitivity further resulted in a 0.8 μrad closed-loop vibration-control reference.

The CCD sensor itself is expected to resolve point-source LOS measurements to 0.1/0.2 μrad for 0.02/0.05 pixel interpolation, respectively. Hence, the CCD sensor will provide a closed-loop target tracking reference which will easily be able to measure the performance of the vibration control system.

7.2 Experiment Control and Data Handling System (CDHS)

All of the electrical, mechanical and optical hardware described (and to be described) interacts and is baselined to be controlled by the control and data handling system. Referring to Figure 7-6, the baseline architecture for this system is "top-down" with a special provision made to automate the experiment: Man interacts with the experiment through the Experiment Monitor Software package. Data entry is made by the astronaut through a data terminal (CRT, keyboard, etc.) or by ground through a radio link. The experiment monitor will enable either a manually controlled experiment or a complete set of pre-defined experiments. Manual control is allowed through a data bus to all experiment subsystems. Automated control is executed through an Automated Experiment Sequencer and Supervisor package. Whether manual or automatic, the experiments defined earlier (system tests, technology demonstrations

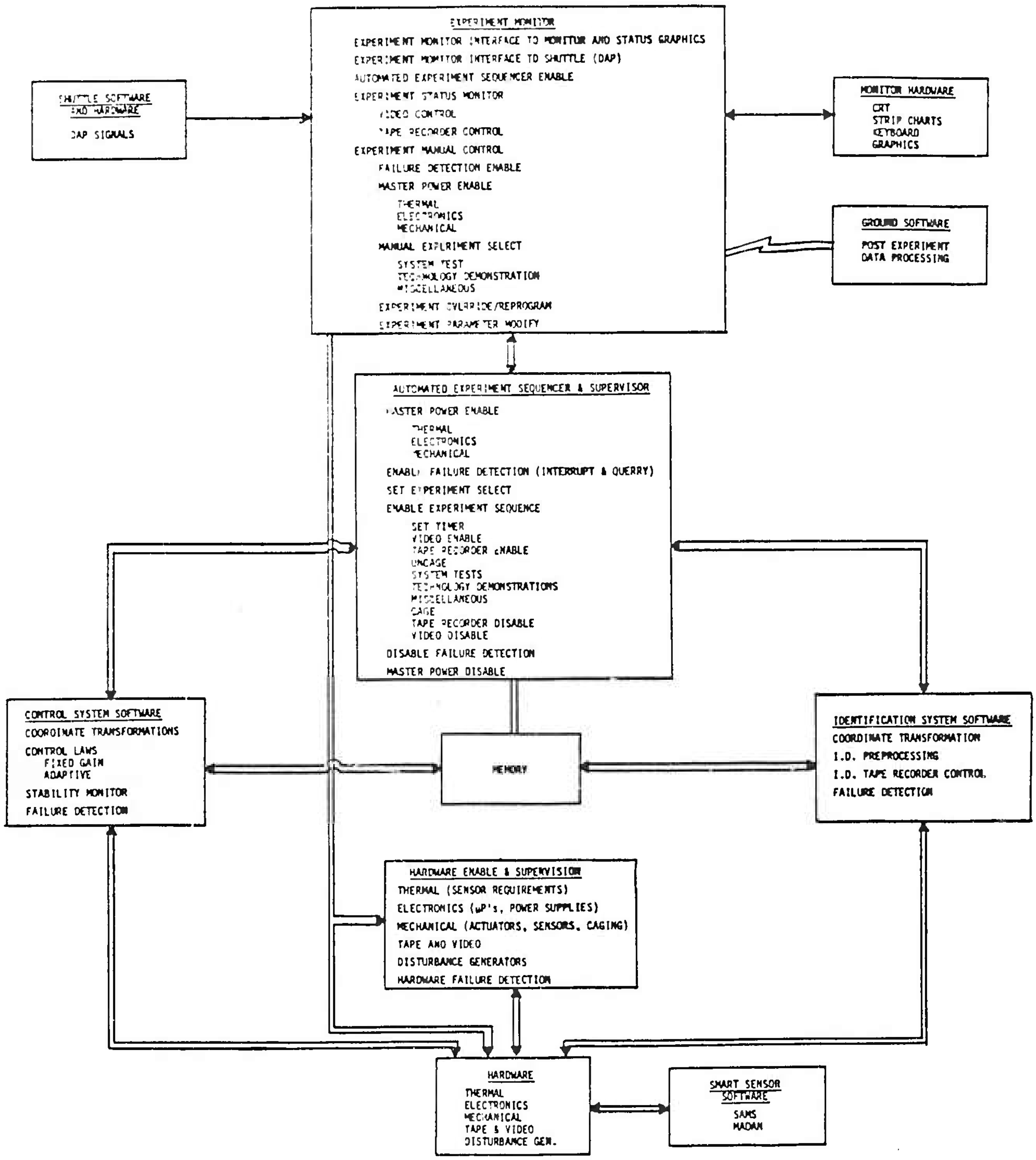

Figure 7-6. Baseline Control and Data Handling System Architecture

and miscellaneous) are stepped through by commanding the state of the hardware via a Hardware Enable and Supervision System. The purpose of the supervision system is to flag hardware anomalies to the experiment monitor so that corrective action can be taken. As the hardware is stepped through, the Control and Identification Software will execute according to manual or automatic algorithms stored in memory or in the Experiment Sequencer. Software failure detection with an overridable automatic shutoff is also provided here as an additional precaution.

During the execution of the experiments, we have identified 31 signals to be monitored and stored for ground processing. These include six disturbance/stimuli generators, four active control sensors, twelve optical autoalignment sensors, six inertial sensors, three digital-autopilot signals, and time. In addition to these, we have added another nine, as a pad, for a total of 40. The experiments command and data handling system (CDHS) will multiplex these measurements and communicate the data to the Shuttle payload tape recorder. The tape recorder is part of the Shuttle standard equipment, and will store all the information gathered during the duration of the experiment. After the experiments are completed, the data will be downlinked on the Shuttle's Ku-band channel. The signal is received by standard NASA links where it is then recorded on the ground, ready for processing.

The data recording requirements were computed to be 128K bits/second. This assumes forty data signals sampled at 200 Hz, each 16 bits long. The total data record time is upper bounded at 111 minutes, including various crosschecks and safety factors.

Two data recorder modes meeting the above specification were considered: 6 inches/second with fourteen parallel tracks recording a three-to-one multiplexed signal; and 30 inches/second with a single track recording a forty-to-one multiplexed signal. We are baselining the second mode as it appears to be simpler overall, and, it will be able to store data for 224 minutes at the required throughput rate.

The downlink operation will be automated and enabled by the CDHS. It will replay the recorded data at 120 inches/second with all fourteen

tracks in parallel, and relay it to the Shuttle's Ku-band interface. The Ku-band permits telemetry rates up to 50 M bits/second, making the tape recorder throughput the bottle neck. It will take approximately four minutes for the tape recorder to dump all of the recorded data.

7.3 "Blackbox" Hardware List and Requirements

A preliminary list of the major hardware required by the experiment has been compiled. The list will be used next to determine electrical and thermal requirements, and later to estimate the price of the experiment. Table 7-1 lists the hardware by major component headings, followed by the identifiable electric/electronic, optical, mechanical, and support equipment needed. Along side the identifiable hardware processors are listed the associated special software that must be supplied. The most expensive components identified are the line-of-sight (LOS) and figure sensors, the primary and secondary mirror, and the ground-based data processor.

The electrical requirements for the hardware itemized in Table 7-1 are tabulated in Table 7-2. It has been explicitly assumed that the power regulation efficiency is 80%, the power amplification efficiency is 75%, and, the standard Shuttle CRT, keyboard, and telemetry capabilities are used.

Table 7-3 estimates the total electrical and thermal requirements. Referring to the table, only the sensor packages require thermal support, but it is internally provided by the sensor package, and consumes little power (6 W). The total power requirement, 2600 W, is also modest, 76% of it is due to the estimated power consumption of the adaptive optics control system. The Shuttle can provide this power continuously for at least 7.5 hours. We have upper bounded the experiment requirements to be about 111 minutes of continuous consumption, and most likely it will be intermittent.

Table 7-1. Preliminary List of Major Hardware and Software Items Used in the Experiment

HARDWARE	ASSOCIATED SPECIAL SOFTWARE
LOS AND FIGURE SENSOR	
Surface Accuracy Measurement Sensor (SAMS)	
Optical Receiver	
Power Supply	
Thermal Support	
8 Laser Diodes + Beam Shape Optics	
Signal Processing Electronics - μP+	Stadiametric Ranging Software
CDHS Interface Electronics	
Imaging CCD Sensor (MADAN Like)	
Optical Receiver	
Power Supply	
Theromelectric Cooler	
Signal Processing Electronics - μP+	Nonlinearity Correction; Windowing; Image Processing
CDHS Interface Electronics	
SHUTTLE EXPERIMENT MONITOR	
Interface to Shuttle/Shuttle Ground Simulation	
Interface to CDHS	
Monitor - μP	Experiment Monitor
Power Supply	
Interface to Monitor Hardware	
CRT	
Stripcharts	
Keyboard	
Graphics	Smart Terminal
Failure Detection Circuit	
Video Recorder	
COMMAND DATA HANDLING SYSTEM	
Data Bus Electronics	
Memory	
Hardware Enable & Supervision - μP	Hardware Enable & Supervision
Failure Detection Sensors to Control, ID and Test Structure Hardware	
Automated Experiment Sequencer	Automated Experiment Sequences & Supervision
3 Supervisor - μP	
Power Supply	
TEST STRUCTURE HARDWARE	
Structure	
Caging Devices	
Primary Mirror & Figure Control System	Figure Control System
Secondary Mirror	
Sensor Supports	
Pallet	
Shuttle Payload Interfaces	

HARDWARE	ASSOCIATED SPECIAL SOFTWARE
CONTROL SYSTEM HARDWARE	
Control μP/'s	Control Laws; Coordinate Transformation Nonlinearity Correction; Stability Monitor, Self Performance Check
Autoalignment Actuators	
Power Supply	
D/A's	
Interfaces + Failure Detection	
Structural Control Actuators	
Power Supply	
D/A's	
Interfaces + Failure Detection	
Structural Control Sensors	
Power Supply	
A/D's	
Interfaces + Failure Detection	
Disturbance Broadcasting	
IDENTIFICATION SYSTEM HARDWARE (EXPERIMENT BORNE)	
I.D. μP/'s	Coordinate Transformation; Preprocessing, Nonlinearity Coorection, Tape Recorder Control; Self Performance Check
I.D. Actuators	
Power Supply	
D/A's	
Interfaces + Failure Detection	
I.D. Sensors	
Power Supply	
A/D's	
Interfaces + Failrue Detection	
Data Recorder/Memory	
Stimulation Recorder/Memory	
GROUND HARDWARE	
Data Processor	I.D. Software, Experiment Data Processing; Simulation; Analysis Support
Ground Receiver/Transmitter	
CRT	
Stripcharts	
Keyboard	
Graphics	

Table 7-2. Tabulation of Electrical Power Requirements

	Power(W)
SAMS	
Optical Receiver - 2W/channel	4.
8 Ga Al As Laser Diodes	1.6
μP + A/D + Signal Processing	8.
CDHS Interface	3.
Power Supply (η = .8)	3.3
	20.
CCD Sensor	
Optical Receiver	.5
Thermo Electric Cooler	6.
Signal Processing Electronics	18.
CDHS Interface	1.
Power Supply (η = .8)	5.1
	30.6
Shuttle Experiment Monitor	
Failure Detection	1.
Shuttle Interface	3.
CDHS Interface	2.
Interface to Monitor	4.
Monitor μP	6.
Graphics	25.
Stripchart (thermo electric)	25.
Power (η = .8)	13.
	79.
CDHS	
Data Bus Electronics	5.
Memory	8.
Hardware Enable Supervision	3.
Failure Detection	3.
Experiment Sequencer μP	3.
Power (η = .8)	5.
	27.

	Power (W)
Test Structure	
Caging Devices	9.
Figure Control	1200.
CDHS Interface	6.
Thermally Controlled Reference	30.
Amps (η = .75)	311.
Power (η = .8)	311.
	1868.
Control Subsystem	
μP's	6.
Autoalignment Actuators	80.
D/A's	11.
A/D's	10.
Structural Control Actuators	60.
Structural Control Sensors	6.
Disturbance Broadcasting (ROM)	2.
Interfaces, Power & Preamps (η = .75)	48.
Failure Detection	5.
Power Supply (η = .8)	47.5
	285.
ID Subsystem	
μP's	6.
Actuators	60.
D/A's	3.
A/D's	7.
Stimulation	2.
Interfaces, Power & Preamps (η = .75)	73.
Failure Detection	5.
Power Supply (η = .8)	73.
Sensors	9.
	138.

The tabulation assumes: 80% Power regulation efficiency
75% Power amplification efficiency
CRT, Keyboard, TV, and telemetry capabilities provided by Shuttle for payload are used.

Table 7-3. Summary of Electrical and Thermal Requirements

Items	Power Requirements	Thermal Requirements
Figure Sensing System	20W	Self contained
CCD Sensor System	31W	Self contained thermo-electric cooler
Experiment Monitor System	79W	--
Command Data Handling System	27W	--
Control System	285W	--
Parameter Estimation System	138W	--
Test Structure Plus Adaptive Optics Control System	1868W	--
Subtotal	2448W	
Total including 6% pad	2600W	

7.4 Miscellaneous

Sections two through seven of this report have provided a simplified, systems level analysis of the experiment system. Appendices A and B of this report complete some final details as requested in the statement of work.

8.0 DEVELOPMENT OF THEORY FOR NONCOLOCATED CONTROL

As a result of an earlier study performed by TRW (ACOSS-8), a stability ensuring design methodology was developed for LSS systems permitting the colocation of actuators and sensors. The design procedure has the advantage that it is relatively insensitive to modal parameters. It permits design objectives to be designed for and sought in both the time and frequency domains. And, the approach leads directly to solution that can be implemented using current microprocessor technology. In a number of applications of interest however, colocation is not possible and further theoretical development was required.

One objective of the current MOD contract study was to extend the ACOSS-8 theory to include noncolocated LSS systems. This section describes the approach taken to meet this objective and the resulting design extension. The plan was to re-examine the ACOSS-8 design approach, determine the properties that make it work, explore ways of synthesizing the desired properties, and derive the extended design procedure.

8.1 Review of ACOSS-8 Results

8.1.1 Stability Ensuring Design Method

The stability ensuring design methodology in ACOSS-8 makes use of positivity/energy dissipation theory to ensure the stability of the LSS. The key results were:

- The negative feedback connection of a positive system with a strictly positive system is stable
- An LSS with collocated actuators and ideal rate sensors is a positive system
- Embedding operations permit the treatment of non-positive systems

The power of the theory becomes apparent as one realizes that no assumptions are made about the dimensionality or linearity of the systems involved. It is for this reason that the theory permits the treatment of modal truncation, stability robustness and nonlinearities. The price one pays for the generality

is however, that designs tend to be conservative. It was therefore proposed in ACOSS-8 to use positivity in conjunction with on-orbit identification/control "tune-up": Positivity is used in the pre-flight design where there is a high parameter uncertainty; then as information is gathered on orbit, multivariable frequency domain techniques combined with positivity (to treat non-linearities) is used to tune the design for high performance.

It was clear that as system knowledge increases, the need for a conservative pre-flight design diminished. In cases where good pre-flight information is available over $\sim$ twice the control band, the positivity/frequency domain approach is to be applied directly without on-orbit identification.

8.1.2 Summary of Positivity Theory

The positivity method is a direct outgrowth of V. M. Popov's work on absolute and hyperstability. The basic underlying theory is general, makes extensive use of functional analysis, and is not restricted to linear time-invariant plants. In fact, the method has in the past been associated with the stability of nonlinear systems (Lur'e problem) where both the nonlinear and linear parts of the system must meet certain positivity conditions. These conditions are only sufficient conditions for stability and therefore tend to be conservative at times. Since well-known necessary and sufficient conditions exist to establish the stability of linear systems, it is apparent why positivity techniques have in the past generally not been applied to linear systems.

The stability problem in the control of large space structures (LSS) differs from more conventional linear systems, because the plant to be controlled is theoretically of infinite order (and practically of very high order), while the controller/estimator must, of necessity, be of relatively low order. It appears, therefore, desirable to use tests which do not require explicit evaluation of the closed loop system, but which impose conditions individually on the plant and the controller, assuring stability when the loop is closed by negative feedback. The stability theory based on positivity of operators is a powerful method having just this characteristic.

In order to summarize the theory, some definitions are required.

Let f(t) be a real, possibly vector valued function defined on $[0,\infty)$. The truncation of f(t) at t=T is defined as

$$f_T(t) = \begin{cases} f(t), & 0 \leq t \leq T \\ 0 \ , & t > T \end{cases}$$

Define the extended Hilbert Space H_e such that $f(t) \in H_e$ if and only if $f_T(t) \in$ Hilbert Space, H.

An operator with a domain and range in H_e is then defined to be (strictly) positive if for $f(t) \in H_e$,

$$\langle f_T(t), Hf_T(t) \rangle \geq 0 \ (>0), \quad \forall T \geq 0$$

Positive operators have the following useful properties:

1) The inverse of a positive operator is positive.

2) The sum of positive operators is positive.

3) Positivity Theorem [11, 12, 13]: The negative feedback system shown in Figure 8-1 is bounded-input-bounded-output BIBO stable for all inputs in H_e if both G and H are positive operators and at least one of them is also strictly positive.

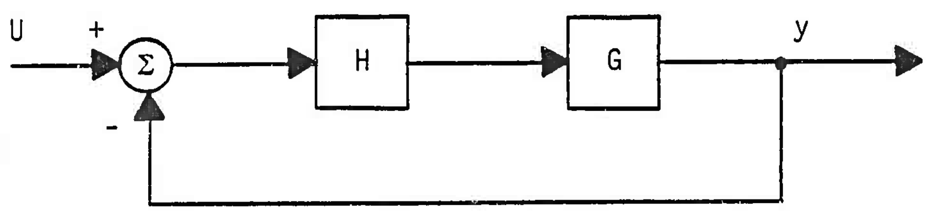

Figure 8-1. Cascade/Unity Feedback Interconnection

A positive operator may be interpreted physically as one that does not create energy (a strictly positive operator always dissipates energy). For this reason a positive operator is often referred to as a passive operator.

The term "Positive Real" is also often used to refer to a positive operator that is also convolutional and linear time-invariant (LTI). The term "Hyperstability" refers to the Positivity Theorem when at least one of the subsystems G or H is positive real, while the other may be nonlinear and/or time-varying.

A frequency domain test exists for testing the positivity of square operators which have a Laplace or Z-Transform representation [11,17]. Positivity is determined, using this test, by first computing the <u>positivity index</u> :

$$\delta_s(\omega) \triangleq \lambda_{min} \left\{ \frac{1}{2} [G(s=j\omega)+G^*(s=j\omega)] \right\} \omega\varepsilon, \quad [0,\infty)$$

or for discrete systems

$$\delta_z(\omega) \triangleq \lambda_{min} \left\{ \frac{1}{2} [G(z=e^{j\omega T})+G^*(z=e^{j\omega T})] \right\} \quad ,\omega\varepsilon[0, \pi)$$

where $\lambda_{min} \{\cdot\}$ denotes "minimum-eigenvalue-of" and "*" denotes complex-conjugate-transpose.

If

$\delta(\omega) > 0$ for all ω defined above, then G is strictly positive real

$\delta(\omega) \geq 0$ for all ω defined above, then G is positive real

$\delta(\omega) \leq 0$ for some ω in the defined range, then G is not positive.

The primary reason for approaching the LSS controller design problem from a Positivity perspective is that an LSS with colocated, ideal (infinite bandwidth) rate sensors and actuators is a positive operator. It was shown in ACOSS-8 (and is redescribed later) that this result is independent of modal parameters describing the structure. Therefore, according to the Positivity Theorem, <u>any</u> positive controller will preserve closed-loop stability—regardless of parameter uncertainty.

8.1.3 Operator Embedding

The condition imposed by the Positivity Theorem are often too restrictive in practice. For example when actuator and sensor dynamics are accounted for, or, when actuators and sensors are not colocated the LSS will no longer be positive. Therefore, the technique of operator embedding was introduced in ACOSS-8 in order to enlarge the class of plants that can be treated by the theorem.

Embedding transformations were defined in ACOSS-8 as the set of block diagram manipulations which do not alter a system's stability property.

Two types of embedding transformations were considered: "F" embedding refers to the cascade transformation in Figure 8-2.

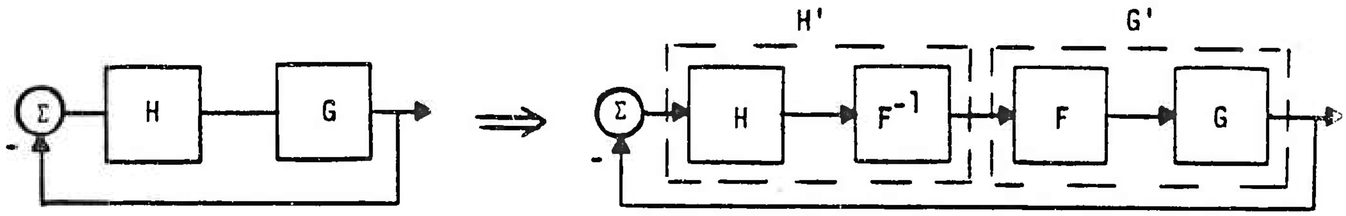

Figure 8-2. "F" Embedding

"D" embedding refers to the parallel transformation in Figure 8-3.

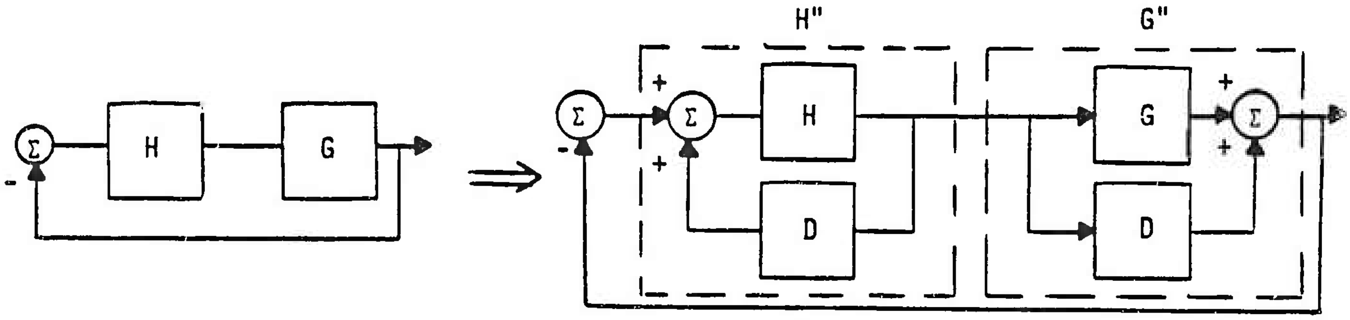

Figure 8-3. "D" Embedding

The important thing to realize about embedding transformations is they are only mathematical and are not physically implemented. The embedding may impose however, conditions on the controller which is to be physically implemented. For example, constant "D" embedding may impose that the gain of the controller must be less than some number at all frequencies.

Generally, embedding requires some knowledge of the plant to be controlled. For example, constant "D" embedding will require that one has estimated (albeit, crudely) the norm of the mode shapes and damping ratio of the high frequency modes. If one has additional knowledge of the plant, more complex embedding can be used to yield less conservative stability conditions. In a gross manner, embedding permits one to quantify stability conditions as a function of system knowledge.

8.1.4 Linear, Multivariable Frequency Domain Techniques

The linear multivariable frequency domain design approach was used in ACOSS-8 to guide the control system design whenever reasonably accurate system models are available. The combination of it with Positivity allows one to trade sensitivity properties for performance and vice-versa. The combinations will be summarized in Section 8.1.5.

The key to the extension of the classical Nyquist/Bode approach to the multivariable case are the characteristic gains of transfer function, G(S), describing the open-loop plant. The characteristic gain $\lambda(S)$ are defined as the solutions to the equation

$$DET\,[\lambda(S) \cdot I - G(S)] = 0; \quad S\varepsilon \quad [oj, \infty j)$$

This equation arises from the eigenvalue problem for a transfer matrix $G(S)_{mxm}$:

$$G(S)\, W_i\,(S) = \lambda_i(S)\, W_i\,(S) \text{ is evaluated for each } S\varepsilon \quad [0j, \infty j)$$

where

$\lambda_i(S)$ are called the characteristic gains of G(S)

$W_i(S)$ are called the characteristic vectors of G(S)

$V_i(S)$ are called the dual characteristic vectors of G(S)

The importance of the characteristic gains stem from the fact that the closed-loop characteristic gains of a unity feedback system are related to

the open-loop values in a manner analogous to single-input-single-output systems. i.e.,

$$\text{closed-loop gain} = \frac{\text{open-loop gain}}{1 + \text{open-loop gain}}$$

This fact can be demonstrated by considering the dyadic expansion of G(S):

$$G(S) = \sum_{i=1}^{m} \lambda_i(S)\, W_i(S)\, V_i^T(S) = W(S)\, [\lambda_i(S)]\, V(S)$$

If one now closes the loop around G (shown in Figure 8-4)

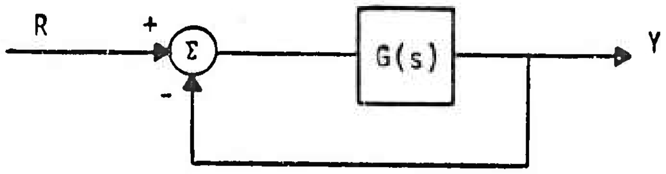

Figure 8-4. Unity Feedback System

and considers the dyadic expansion of the closed loop system G_c, then

$$G_c(S) = [I+G(S)]^{-1}G(S) = [I+W(S)\ \lambda(S)\ V(S)]^{-1}\, W(S)\ \lambda(S)\ V(S)$$

$$= [W(S)\, V(S) + W(S)\ \lambda(S)\ V(S)]^{-1} W(S)\, \lambda(S)\, V(S)$$

$$= W(S)\ [I+\lambda(S)]^{-1}\ \lambda(S)\ V(S)$$

$$= \sum_{i=1}^{m} \frac{\lambda_i(S)}{1+\lambda_i(S)}\, W_i(S)\, V_i^T(S)$$

Other key results using this technique are:

1) Generalized Nyquist Criterion: Closed-loop stability occurs if and only if the net sum of counter-clockwise encirclements of the (-1, 0.) by the characteristic gains is equal to the number of open-loop unstable poles.

2) To achieve low control interaction in a frequency band, it is sufficient that either all the characteristic gains have a large magnitude over that frequency band, or the dual eigenvectors are nearly orthogonal over that band.

3) In frequency bands of low interaction, the notions of gain margin and phase margin may be applied as a qualitative assessment of performance.

4) There is a relationship between tracking accuracy and the magnitude of the characteristic gains. Under the appropriate assumptions the relationship is analogous to the single-input-single-output case.

8.1.5 Positivity Design Steps

In practice, both positivity and frequency domain compensation* may be needed in order to meet stability and performance objectives. The two are combined by first determining the characteristic gains and positivity index of the plant and shaping them using techniques similar to those of Mac Farlane [15]. The shaping network is a precompensator M(s) which is designed for performance. Once the design of M(s) is completed, one can determine the D embedding operator that makes the precompensated plant positive. This is typically done by determining the positivity index $\delta(\omega)$ of the precompensated plant, finding its most negative peak δ_{min}, and choosing $D = \delta_o I$, $\delta_o > -\delta_{min} > 0$. The "H" part of the controller consists then merely of gains which must be set to less than or equal to $1/\delta_o$. The actually implemented controller satisfying the positivity design is then given by $(1/\delta_o)M(s)$ (See Figure 8-5).

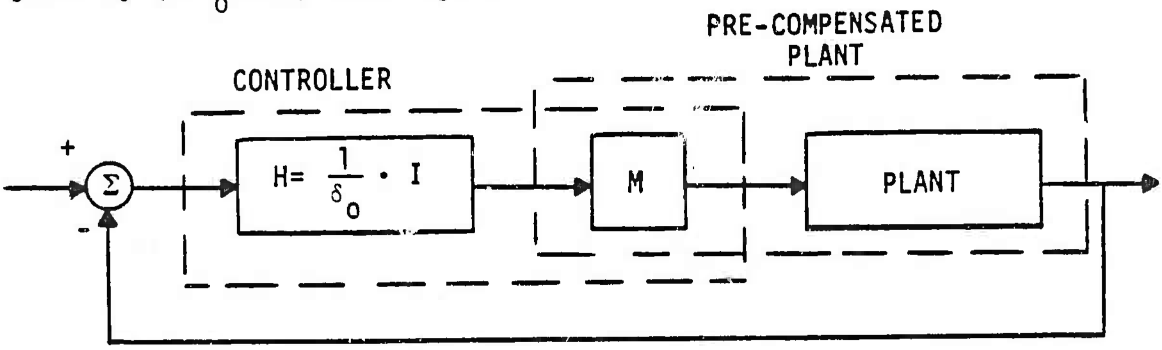

Figure 8-5. "D" Embedding a Precompensated Plant

* ACOSS-8 also describes a time domain alternative using optimal control theory. This study considers only the frequency domain approach.

The actual steps are:

1) Determine the characteristic gains $\lambda(\omega)$ and positivity index $\delta(\omega)$ of the plant + actuators + sensors

2) Shape characteristic gains and positivity index (cascade compensator M[s]) using Nyquist/Bode approach and CAD filter design program

   - Design for damping
   - Design for non modal sensitivity
   - Design for noise and disturbance rejection
   - Design high frequency roll-off characteristic
   - $\delta(\omega)$ is shaped for modal sensitivity

3) Evaluate positivity index $\delta(\omega)$ for entire pre-compensated system and determine δ_{min} (maximum negative peak)

4) Implement controller as $\frac{1}{\delta_o} \cdot M(s)$ where $\delta_o > -\delta_{min} > 0$

8.2 Generalizations Required for Noncolocated Control

In order to extend the ACOSS-8 approach, the distinguishing features of the noncolocated control problems were first isolated. It was found that the unique features are that an ideal, noncolocated LSS plant is not necessarily positive nor is it necessarily square (the number of system inputs and outputs are not necessarily equal).

The first possibility was considered benign with respect to stability as the ACOSS-8 theory was never restricted to positive systems at all. In theory the embedding operation required to make the embedded system positive can always be found, regardless of how negative the plant is. This was demonstrated in the ACOSS-8 examples. A more practical problem was to find however, the embedding operations which optimize performance in the noncolocated case. Recall that embedding can be interpreted as the possible excursions that the real plant can take from its nominal model. For colocated

systems both the real plant and the model were close to being positive. Hence, one could be fairly sloppy in choosing "F" embedding without much penalty on the performance. [Recall that embedding imposes constraints on the controller gains, and therefore affects performance.] Now, however, the nominal and real systems are possibly non-positive and the role of the "F" embedding becomes more important.

The second possibility was potentially more serious as both the positivity and frequency domain theory used in ACOSS-8 was for square systems. Fortunately, it was found that the frequency domain theory had been extended recently [16,17], but it was not easy to use yet. Moreover, the theory from which positivity was derived did not require the system to be square. The later finding was critical indeed as it is what ensures robustness.

The theoretical effort focused into three areas: generating a stability ensuring design condition for nonsquare plants; developing a procedure for making a nonsquare plant square (squaring procedure); and developing an embedding/compensation procedure for maximizing performance.

8.3 Generalizing Positivity

The first goal is to develop a stability-ensuring design criterion for nonsquare plants. This condition had to be simple and compatible to the conditions derived in ACOSS-8. The strategy to meet this goal was to revisit the derivation of the positivity condition, find the assumptions requiring square plants, remove them and then continue through the rest of the original derivation.

8.3.1 Conicity

It was found that the Positivity Theorem is a special case of the Conicity Theorem; and the Conicity Theorem can be derived by combining embedding with the Small Gain Theorem. Neither the Conicity or Small Gain Theorem require a square plant. The derivation below demonstrates this and follows the original work of Zames [13].

The Small Gain Theorem states that the GH system in Figure 8-6* is stable if for

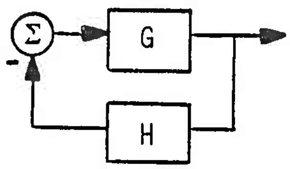

Figure 8-6. Feedback Interconnection

$$g(H) \triangleq \sup \frac{||Hf||}{||f||}, \quad \forall f \in \text{Extended Hilbert Space}$$

$g(H) \cdot g(G) < 1$. Note that this is a generalization of gain stabilization. If one now embeds the GH system, as shown in Figure 8-7, and applies the small gain condition, it is implicit that if

$$||\overline{G}|| = ||(G+D)\, F^{-1}|| < 1 \tag{8.1}$$

and

$$||\overline{H}|| = ||F\, (I-HD)^{-1} H|| < 1 \tag{8.2}$$

Then the GH and $\overline{GH}$ systems are stable. This is the linear version of the Conicity Theorem. The name comes from the fact that the inequalities (8.1) and (8.2) imply (if the inverses exist)

$$||(G+D)\, f|| < ||F\, f|| \quad \forall f$$

and

$$||(H^{-1}-D)\, f|| > ||F\, f|| \quad \forall f$$

* The Theorem is true whether or not the loop is closed with H in the feedback or cascade path.

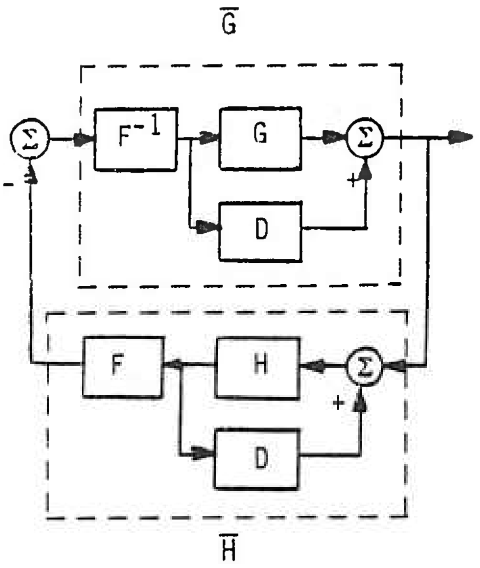

Figure 8-7. Embedding Used to Derive Conicity Theorem

which may be geometrically interpreted as: the gain of G must be inside the cone with center -D and radius F, and the gain of $-H^{-1}$ must be outside the cone with center -D and radius F. Zames then showed that if the additional constraints

$$D = I \cdot \text{constant}$$

$$F = I \cdot \text{constant}$$

$$-D-F = 0$$

$$-D+F \rightarrow I \cdot \infty$$

are imposed, then the identities (real inner-product space only)

$$||(G+D)\ f||^2 - ||F\ f||^2 < 0 \Leftrightarrow \langle (G+D+F)\ f,\ (G+D-F)\ f \rangle < 0$$

$$||(H^{-1}-D)\ f||^2 - ||F\ f||^2 > 0 \Leftrightarrow \langle (H^{-1}-D+F)\ f,\ (H^{-1}=D-F)\ f \rangle > 0$$

are equivalent to the conditions of the Positivity Theorem.

8.3.2 Sectors

Since Zames' early work on conicity, many new theories have been proposed. The concept of sectors [18] is to our knowledge the most general input-output stability result available. It includes everything described as a special case. The embedding operations are even explicitly accounted for as S_{11}, S_{12}, S_{21} and S_{22}:

An operator G is said to be inside/outside sector

$$S \triangleq \begin{bmatrix} S_{11} & S_{12} \\ S_{21} & S_{22} \end{bmatrix}$$

if $\langle S_{11}\, Gf + S_{12}\, f,\ S_{21}\, G\, f + S_{22}\, f \rangle < 0 \quad (>0)$.

The pertinent property of sectors that is particularly interesting is the Sector Stability Theorem - If G is inside a sector S and H^{-1} is outside the sector S, the closed loop GH system is stable. Hence, the Small Gain Theorem results when

$$S_{11} = S_{21} = S_{22} = I \text{ and } S_{12} = -I$$

The Conicity Theorem results when

$$S_{11} = S_{21} = I; \quad S_{12} = D-F \text{ and } S_{22} = D+F$$

The Positivity Theorem results when

$$S_{11} = S_{22} = 0; \quad S_{12} = -I \text{ and } S_{22} = I$$

Sectors also possess an algebra (summarized in Table 8-1) that makes their manipulation simpler than embedding. This makes it easy to derive stability ensuring design conditions on a case by case basis. Since generating particular results is not the intent of the study, conicity (or conic sector) will be used to generate the general results sought. Nevertheless, it is noted that the sector concept may be required in practical situations wherein performance cannot be sacrificed for an overly conservative stability robust design.

Table 8-1. Summary of Section Properties (Lemma 6.2 in [18])

1. Complimentary Sector

$$G \text{ inside sector} \begin{bmatrix} S_{11} & S_{12} \\ S_{21} & S_{22} \end{bmatrix} \Leftrightarrow G \text{ outside sector} \begin{bmatrix} I & 0 \\ 0 & -I \end{bmatrix} \cdot S$$

2. Multiplier

$$\text{sector} \begin{bmatrix} S_{11} & S_{12} \\ MS_{21} & MS_{22} \end{bmatrix} = \text{sector} \begin{bmatrix} aM^*S_{11} & aM^*S_{12} \\ b\ S_{21} & b\ S_{22} \end{bmatrix}$$

3. Inverse Relation

$$G \text{ inside sector} \begin{bmatrix} S_{11} & S_{12} \\ S_{21} & S_{22} \end{bmatrix} \Leftrightarrow G^{-1} \text{ inside sector } S \cdot \begin{bmatrix} 0 & I \\ I & 0 \end{bmatrix}$$

4. Sums of Relations

$$G_1 \text{ inside sector} \begin{bmatrix} S_{11} & S_{12} \\ S_{21} & S_{22} \end{bmatrix} \Leftrightarrow G_1 - G_2 \text{ inside sector } S \cdot \begin{bmatrix} I & G_2 \\ 0 & I \end{bmatrix}$$

5. Composition Products of Relation

a.

$$G_2G_1 \text{ inside sector} \begin{bmatrix} S_{11} & S_{12} \\ S_{21} & S_{22} \end{bmatrix} \Rightarrow G_1 \text{ inside sector } S \cdot \begin{bmatrix} G_2 & 0 \\ 0 & I \end{bmatrix}$$

b.

$$G_2G_1 \text{ inside sector} \begin{bmatrix} S_{11} & S_{12} \\ S_{21} & S_{22} \end{bmatrix} \Rightarrow G_2 \text{ inside sector } S \cdot \begin{bmatrix} I & 0 \\ 0 & G_1^{-1} \end{bmatrix}$$

c.

$$G_2 \text{ inside sector} \begin{bmatrix} S_{11}\ G_1 & S_{12} \\ S_{21}\ G_1 & S_{12} \end{bmatrix} \Rightarrow G_1 \cdot G_2 \text{ inside} \begin{bmatrix} S_{11} & S_{12} \\ S_{21} & S_{22} \end{bmatrix}$$

Notes: $a\ b > 0$; M^* is the adjoint of M; S_{ij} are operators mapping into extended inner-product spaces; $S_{ij}\ \underline{0} = \underline{0}$; properties 1-4 hold if inside is replaced by outside.

8.3.3 Stability-Ensuring Design Condition for Noncolocated Systems

The Conicity Theorem will now be used to derive a stability-ensuring design condition for noncolocated systems.

First, the uncertainty of the plant G is modeled as

$$||G+D|| < ||F||$$

This is the first condition of the Conicity Theorem and it states that the true system G differs from the nominal system -D by at most F (how it varies within the limit F is arbitrary). The plant G is then partitioned into $[G_1 \vdots G_2]$ for Case 1 (more inputs than outputs, Figure 8-8) and into $\begin{bmatrix} G_1 \\ \hline G_2 \end{bmatrix}$ for Case 2 (more outputs than inputs, Figure 8-9). The partitioning is not necessary but assigning G_1 to represent the colocated part of the plant and G_2 to represent the noncolocated part of the plant will allow an intuitive feel for the results. The assumption

$$||G_1 + D_1|| < ||F_1|| \text{ and } \quad ||G_2 + D_2|| < ||F_2||$$

can be interpreted, for example, as the uncertainty model for the colocated and noncolocated parts of the system. Now, in order for the Conicity Theorem to hold, the second condition

$$||F\,(I-HD)^{-1}\,H|| < 1$$

must be satisfied. Substituting the variables corresponding to Case 1 yields:

$$\left|\left|[F_1 \vdots F_2] \left\{ I + \begin{bmatrix} H_1 \\ \hline H_2 \end{bmatrix} [D_1 \vdots D_2] \right\}^{-1} \begin{bmatrix} H_1 \\ \hline H_2 \end{bmatrix} \right|\right| < 1$$

$$\left|\left|[F_1 \vdots F_2] \begin{bmatrix} H_1 \\ \hline H_2 \end{bmatrix} \left\{ I + [D_1 \vdots D_2] \begin{bmatrix} H_1 \\ \hline H_2 \end{bmatrix} \right\}^{-1} \right|\right| < 1$$

$$||(F_1\,H_1 + F_2\,H_2)(I + D_1\,H_1 + D_2\,H_2)^{-1}|| < 1$$

$$||F_1\,H_1 + F_2\,H_2|| < \frac{1}{||(I + D_1\,H_1 + D_2\,H_2)^{-1}||}$$

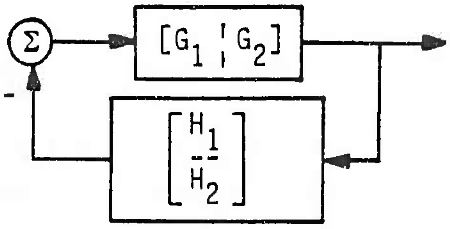

Figure 8-8. Noncolocated Control, Case 1: More Inputs than Outputs

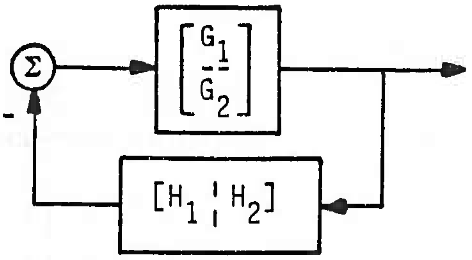

Figure 8-9. Noncolocated Control, Case 2: More Outputs than Inputs

Substituting the variables corresponding to Case 2 yields:

$$\left\| \begin{bmatrix} F_1 \\ \hline F_2 \end{bmatrix} \left\{ I + [H_1 \mid H_2] \begin{bmatrix} D_1 \\ \hline D_2 \end{bmatrix} \right\}^{-1} [H_1 \mid H_2] \right\| < 1$$

$$\left\| \begin{bmatrix} F_1 \\ \hline F_2 \end{bmatrix} [H_1 \mid H_2] \left\{ I + \begin{bmatrix} D_1 \\ \hline D_2 \end{bmatrix}^{-1} [H_1 \mid H_2] \right\}^{-1} \right\| < 1$$

$$\left\| \begin{bmatrix} F_1 H_1 & F_1 H_2 \\ F_2 H_1 & F_2 H_2 \end{bmatrix} \right\| < \frac{1}{\left\| \begin{bmatrix} I + H_1 D_1 & H_1 D_2 \\ H_2 D_1 & I + H_2 D_2 \end{bmatrix}^{-1} \right\|}$$

If one now chooses an ℓ_2 norm in these expressions, Parseval's Theorem may be used to evaluate them. This results in

Case 1:

$$\lambda_{max} \left\{ (F_1 H_1 + F_2 H_2)^* (F H_1 + F_2 H_2) \right\} < \lambda_{min} \left\{ (I + H_1 D_1 + H_2 D_2)^* (I + H_1 D_1 + H_2 D_2) \right\}$$

Case 2:

$$\lambda_{max} \left\{ \begin{bmatrix} F_1 H_1 & F_1 H_2 \\ \hline F_2 H_1 & F_2 H_2 \end{bmatrix}^* \begin{bmatrix} F_1 H_1 & F_1 H_2 \\ \hline F_2 H_1 & F_2 H_2 \end{bmatrix} \right\} < \lambda_{min} \left\{ \begin{bmatrix} I+H_1 D_1 & H_1 D_2 \\ \hline H_2 D_1 & I+H_2 D_2 \end{bmatrix}^* \begin{bmatrix} I+H_1 D_1 & H_1 D_2 \\ \hline H_2 D_1 & I+H_2 D_2 \end{bmatrix} \right\}$$

where $\lambda_{max} \{\cdot\}$ and $\lambda_{min} \{\cdot\}$ denotes take the maximum and minimum eigenvalues of $\{\cdot\}$, respectively.

Note that it has been assumed that G_1, G_2, F_1, F_2, D_1, D_2, H_1 and H_2 have a Laplace or Z-Transform representation, with the variable S or $Z=e^{ST}$ as the argument. The conditions are to be evaluated at every frequency S, where $S=j\omega$ and ω ranges from 0 to ∞ for continuous systems and from 0 to π/T for sample data systems.

Note also that these conditions degenerate to the positivity conditions in ACOSS-8 if the system is square and the conditions on page 8-12 are imposed. The latter are not possible to enforce, however, in the nonsquare case.

8.4 Squaring Down Procedure

As explained before, the design technique adopted by TRW combines positivity theory with the multivariable frequency domain approach. Both of these techniques were originally defined for square systems, i.e., systems for which the number of actuators equals the number of sensors. Since in many large space structures this is not the case, the system should be "squared down" before the usual design procedure is followed. Thus, the design procedure for rectangular systems calls for the following two stage procedure.

(i) Calculation of the Square Down Filter. The square down filter $K(Z)$ is chosen to improve on the performance of the system. This is done by designing $K(Z)$ to discriminate against modes which have limited influence on the performance of the system, e.g., do not affect the motion of line of sight (LOS), in favor of modes which affect the performance the most. In addition, $K(Z)$ should be constructed to enhance the stability and robustness characteristics of the system which are both related to its positivity index. This can be done by designing $K(Z)$ in a way which makes the resultant square system as close as possible to a positive real system. As usual in design problems, a suitable compromise must be made between the conflicting requirements of stability and performance.

(ii) Design of Controller. After the system is squared down, a compensator $G_c(Z)$ is designed using the positivity design approach. Since the square down filter $K(Z)$ is designed to enhance performance, the important modes will be prominently represented in the feedback signal. As a result, the damping of these modes can be increased using lower controller gains.

It should be noted that dividing the control system into two separate parts, controller + square down filter, is artificial and was introduced here only for the explanation of the proposed design procedure. The complete control law which is finally implemented is given by $H(Z) = G_c(Z)\ K(Z)$ where $H(Z)$ is a rectangular digital filter, as shown in Figure 8-10.

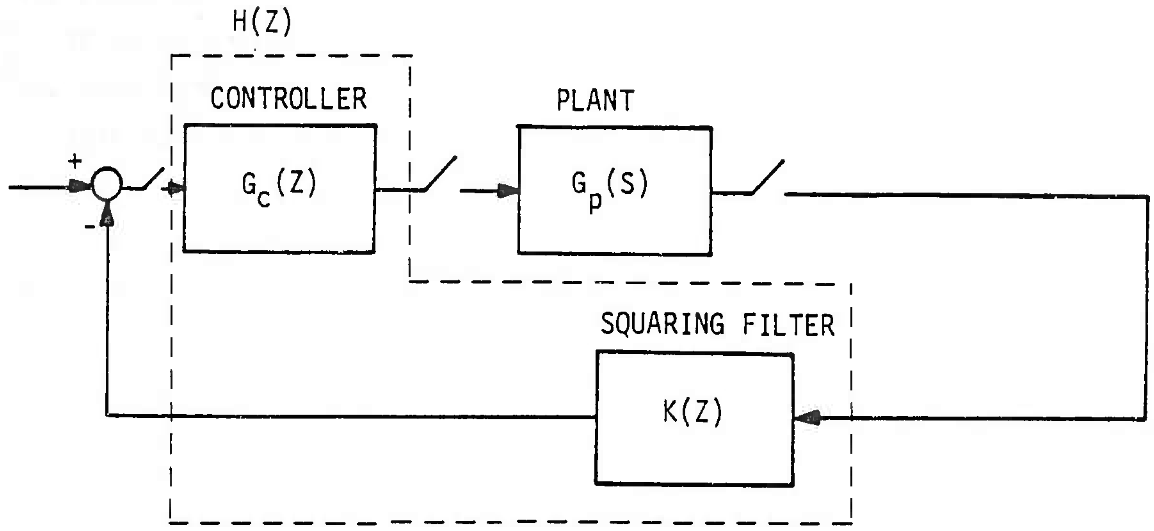

Figure 8-10. Topology of a "Squared Down" System

It should be also noted that the squaring down procedure can also be used to augment the representation of the important modes in the feedback signal of a square noncolocated system. This can be done prior to designing the controller, thus facilitating the task of damping augmentation.

8.4.1 Positivity Properties of Large Space Structures

Before explaining how colocation of actuators and sensors makes LSS behave as a positive operator, various dynamic representations of vibrational systems will be introduced. These dynamic descriptions will be later used in defining various characteristics of the system at hand.

In the following, three different descriptions of a large space structure will be used alternately.

(i) Modal Representation. Motion of a linear vibratory system is given by:

$$M\ddot{q} + Kq = u \tag{8.3}$$

where M is a positive definite $n \times n$ mass matrix, K is a non-negative, symmetric $n \times n$ stiffness matrix and u is a time dependent forcing function.

For a complicated structure, the matrices M and K are defined using the finite element approximation method. Modal analysis is then performed to compute a transformation matrix ϕ which relates the physical coordinates q to the modal coordinates η—$q = \phi\eta$. The equations of motion can be then written as:

$$\ddot{\eta} + \Omega\eta = \phi^T u \tag{8.4}$$

where $\Omega = \text{diag}\,(\omega_1^2, \ldots, \omega_n^2)$

Let the actuators and sensors locations be: $a_1 \ldots a_m$, and $s_1 \ldots s_r$ respectively. Then after including modal damping and assuming rate measurements, the equations of motion take the form:

$$\ddot{\eta}_i + 2\zeta\omega_i \dot{\eta}_i + \omega_i^2 \eta_i = \phi_i(a_1)\, u_1 + \ldots + \phi_i(a_m)\, u_m \tag{8.5}$$

$$y_k = \phi_1(s_i)\, \dot{\eta}_1 + \ldots \phi_n(s_k)\, \dot{\eta}_n \tag{8.6}$$

$$i = 1 \ldots n$$
$$k = 1 \ldots r$$

where ζ is the damping coefficient and y is the observation vector.

(ii) State Space Representation

Defining $x \triangleq (\eta_1, \dot{\eta}_1 \ldots \eta_n, \dot{\eta}_n)$ equations (8.5) and (8.6) can be written as:

$$\dot{x} = Ax + Bu \tag{8.7}$$

$$y = Cx \tag{8.8}$$

where:

$$A = \begin{bmatrix} A_1 & & \\ & \ddots & \\ & & A_n \end{bmatrix}, \quad A_i = \begin{bmatrix} 0 & 1 \\ -\omega_i^2 & -2\zeta\omega_i \end{bmatrix}$$

$$B=\begin{bmatrix} 0 \\ B_1 \\ 0 \\ B_2 \\ \vdots \\ 0 \\ B_n \end{bmatrix}, \qquad B_i=\left[\phi_i\,(a_1)\ldots.\phi_i\,(a_m)\right]$$

$$C=\left[0\ C_1\ 0\ C_2..0\ C_n\right] \qquad C_i=\begin{bmatrix} \phi_i\,(s_1) \\ \cdot \\ \cdot \\ \cdot \\ \phi_i\,(s_r) \end{bmatrix}$$

(iii) Transfer Matrix Representation

By definition the transfer function of a system defined by equations (8.7) and (8.8) is given by:

$$G_p(s) = C\,(sI-A)^{-1}\,B \tag{8.9}$$

Defining

$$B^*=\begin{bmatrix} B_1 \\ \cdot \\ \cdot \\ \cdot \\ B_n \end{bmatrix}, \qquad C^*=\left[C_1.\ .\ .\ .C_n\right]$$

equation (8.9) can be written as:

$$G_p(s) = C^*\,D(s)\,B^*,\ D(s) = \text{diag}\left(\frac{s}{s^2+2\zeta\omega_i s+\omega_i^2}\right) \tag{8.10}$$

As explained in Section 8.1.2, the positivity of a square system can be tested according to the definition by evaluating the matrix $G(j\omega) + G^*(j\omega)$ for continuous systems [or $G(e^{j\omega T}) + G^*(e^{j\omega T})$ for discrete systems] for $0 < \omega < \infty$, and evaluating the positivity index. For multi-input multi-output (MIMO) systems the frequency domain approach requires, however, extensive computing effort to calculate the eigenvalues of the above matrices for many frequency values. To overcome this difficulty B.D.O Anderson developed a relatively simple positivity test

in the time domain. The theorem on which the test is based is a generalization of the Kalman - Yakubovich lemma for single-input single output (SISO) systems and can be stated as follows:

Theorem: Let $G(s)$ be a square matrix of rational transfer functions such that $G(\infty)$ is finite and G has poles which lie in $Re[s] < 0$ or are simple on $Re[s] = 0$. Let $\{A, B, C, G(\infty)\}$ be a minimal realization of G. Then $G(s)$ is positive real if and only if there exists a symmetric positive definite matrix P and matrices W_o and L such that

(i) $PA + A^T P = -LL^T$

(ii) $W_o^T W_o = G(\infty) + G^T(\infty)$

(iii) $C^T = PB + LW_o$

Further, $G(s)$ is strictly positive real if LL^T is positive definite.

In the case of a large space structures $G(\infty)=0$, equation (ii) reduces to $W_0=0$ which results in equation (iii):

$$C^T = PB \qquad (8.11)$$

Positivity of a system with colocated actuators and sensors can be established in the frequency domain by observing that for a colocated actuators and rate sensors one has:

$$C^{*T} = B^* \qquad (8.12)$$

Hence from equation (8.10)

$$G_p(j\omega) + G_p^*(j\omega) = B^{*T} E(\omega) B^* \qquad (8.13)$$

where

$$E(\omega) = \text{diag}\left[Re\left(\frac{j\omega}{-\omega^2+2\zeta j\omega\omega_i+\omega_i^2}\right)\right]$$

$E(\omega)$ is positive definite for all ω and thus $G_p(j\omega) + G_p^*(j\omega)$ is also positive definite.

In the time domain it can be shown that:

$$P = \begin{bmatrix} P_1 & & 0 \\ & \ddots & \\ 0 & & P_n \end{bmatrix} \quad \text{and} \quad L = \begin{bmatrix} L_1 & & \\ & \ddots & \\ & & L_n \end{bmatrix} \tag{8.14}$$

where

$$P_i = \begin{bmatrix} \omega_i^2 \, p_i & 0 \\ 0 & p_i \end{bmatrix}, \quad L_i = \begin{bmatrix} 0 & 0 \\ 0 & 2\sqrt{\alpha p_i} \end{bmatrix}, \quad p_i = 1 \tag{8.15}$$

is a solution to the equations of Anderson's theorem. This is provided the actuators and rate sensors are colocated and have infinite bandwiths.

The above solution is valid for any number of modes. Hence, if the dynamics of the actuators and rate sensors are not included, the spillover modes cannot destabilize the system. This is because any number of spillover modes form a positive system, i.e., a system which is energy dissipative and therefore stable.

The situation for noncolocated systems is not that fortunate. For SISO noncolocated systems if sign $[\phi_i(a_1)]$ = sign $[\phi_i(s_1)]$ (8.16) then the system is positive. This can be shown by taking $p_i = \dfrac{\phi_i(s_1)}{\phi_i(a_1)}$ for i = 1,..... This gives p_i which is positive definite and a $\sqrt{p_i}$ which is real. Obviously, there are some high frequency modes for which this condition cannot be satisfied. However, with a judicious placement of actuators and sensors these modes can be placed outside the control bandwidth and therefore will not affect system stability.

Intuitively, one would like to extend the above result to MIMO noncolocated systems. Unfortunately it can be shown that satisfying the equation

$$\text{sign}\ [\phi_i(a_j)] = \text{sign}\ [\phi_i(s_j)] \quad i=1,.. \tag{8.17}$$

for j=1,...m does not assure a positive system.

MIMO structures which can be shown to be positive are classes of structures with colocated actuators and sensors. Although non-colocated MIMO structures are not generally positive, it can be shown that when a loop is closed on a noncolocated system, the system is <u>stable</u> provided $(B^T C^T + C B)$ is a semipositive definite matrix.

8.4.2 <u>Squaring Down: Time Domain Approach</u>

The time domain square down procedure makes use of Anderson's theorem for establishing positivity. If the number of controlled modes n_c satisfies $n_c = \max(r, m)$, a constant square down matrix K which makes the system positive can be obtained. If $n_c = r$, then using Anderson's lemma one can write:

$$P B = C^T K^T \tag{8.18}$$

P is chosen as in equations (8.14) and (8.15) and because of the peculiar form of B, equation (8.18) reduces to:

$$K^T = (C^{*T})^{-1} B^* \tag{8.19}$$

Similarly if $n_c = m$, it can be shown that the a square down matrix which makes the system positive is given by:

$$K = B^{*-1} C^T \tag{8.20}$$

The requirement $n_c = \max(r,m)$ leads to a high number of sensors (or actuators). If one is forced to limit the number of sensors and actuators, the time domain approach can still be pursued by creating a square system which is "close" to a square positive system. Let $n_c = r$ then using the Moore - Penrose pseudo inverse, the square down constant matrix is given by

$$K = (C^*)^+ \; B^* \tag{8.21}$$

where + denotes a pseudo-inverse. Using K as given by equation (8.21) generates a square system that is closest to a positive square system in a Euclidean norm sense. In the program which implemented this approach, the pseudo inverse was calculated using a singular value subroutine taken from the LINPACK library.

In the time domain approach the square down criterion is to make the system as positive as possible without paying attention to the performance requirements. The performance characteristics of the system are designed for in the second stage of the design by calculating an approximate compensation filter $G_c(z)$.

8.4.3 Squaring Down: Frequency Domain Approach

In this approach the square down matrix is allowed to depend on frequency. Although it is possible to calculate K for any given frequency, the calculation will be carried out only at the natural frequencies because at these frequencies a sudden jump in system's gains occurs. In the approach taken here, a DC value of K, $K_o = K(o)$ is first calculated and then a digital filter is added to adjust the compensator's gain at modal frequencies.

The DC value of the squaring matrix K is calculated from the equation:

$$K_o \, G_p(o) = R_o \tag{8.22}$$

The matrix $G_p(o)$ is the value of the transfer matrix at $\omega = 0$ and is given by:

$$G_{pij}(o) = \sum_{k=1}^{n} \phi_k \, (s_i)\phi_k(a_j) \tag{8.23}$$

Another interpretation of each element of $G_p(o)$, $G_{pij}(o)$, is that it expresses the motion at location s_i due to a unit force at location a_j. The purpose of this square down scheme is to scale the feedback signals according to the motion of the LOS. This is done by calculating a diagonal matrix R_o according to the equation:

$$r_{jj} = \sum_{k=1}^{n} \phi_k(a_j) \sqrt{\phi_{k1x}^2 + \phi_{k1y}^2 + \phi_{k1z}^2}, \; j=1...m \tag{8.24}$$

r_{jj} - is the motion exerted by a unit force at actuator j on the LOS.

Since K_0 is a rectangular matrix the system of equations defined by (8.22) is underdetermined and many solutions are possible. In the computer program based on this approach, the matrix K_0 is calculated using a singular value decomposition which results in a minimum norm solution.

In the second part of the square down procedure the frequency dependence of the matrix K is computed. This is done by calculating the norm of the transfer matrix at the natural frequencies, σ_i and equating it to the modal participation factor $-g_i$ at the LOS evaluated at this frequency. The norm of the transfer matrix $||K_0\ G(\omega_i)||$ at a given frequency is taken as the maximum singular value. Since the underlying assumption is that the modal damping is very low, there is only one singular value of $K_0\ G(\omega_i)$ which is different from zero.

The modal participation factor is given by:

$$g_i = \frac{\phi_{ilx}^2 + \phi_{ily}^2 + \phi_{ilz}^2}{\omega_1^2} \tag{8.25}$$

The ratio $\frac{g_i}{\sigma_i}$ gives the gain required at each frequency. This gain should be looked upon as a measure of the relative importance of various modes as reflected in the LOS motion. After this calculation is completed for $\omega = \omega_i$, i = 1...n a sequence of gains is obtained. The next step is to approximate this series of gains $\alpha(\omega_i)$, i = 1...n by a realizable digital filter $\alpha(z)$. The resulting square down matrix is given by $\alpha(z)\cdot K_0$. Since frequency domain design approach results in a diagonal controller

$$G_c(z) = \beta(z) \cdot I \tag{24}$$

The resulting complete controller H(z) is given by

$$H(z) = \alpha(z)\ \beta(z)\ K_0 \tag{25}$$

The main criterion of the square down procedure based in the frequency domain is to enhance system performance. The relative stability characteristics of the closed loop system still has to be established while designing the compensator $G_0(z)$. Therefore, this procedure can be employed to increase the representation of the important modes for

square noncolocated systems prior to the usual compensator design procedure.

An important special case of non-square systems is the case of a system which possesses a colocated subsystem of actuators and sensors. This is a very realistic case since the main difficulty in creating a colocated control system is in placing the actuators due to size and power limitations. For this class of structures a preferred design approach is first to create a colocated system by placing sensors at the actuators locations and then place additional sensors at critical locations (e.g., at LOS) to enhance system's closed loop performance.

For the class of systems with partly colocated actuators and sensors, the structure of the square down filter is set to preserve the favorable stability characteristics of the colocated subsystem.

Assume that the complete system possesses r sensors of which m are colocated with the m actuators. Calculating the square down matrix as in Section 8.4.3 would destroy the positivity of the colocated subsystem. Instead let K have the following structure

$$K(z) = \left[I \; \vdots \; L\,(z) \right] \tag{8.28}$$

The above structure will ensure that the colocated subsystem remains positive real. This form of K will be referred to as "partial square down" matrix. Figure 8-11 shows the functional diagrams of both the full and partially squared down systems.

If $r < 2m$ the system of equations to determine the DC value of L, L_o, is underdetermined. In this case a least square procedure is employed.

A digital program based on the frequency domain approach square down technique was used on the flat plate and tetrahedron examples. The flowchart of this program is shown in Figure 8-12. The program is interactive and allows for both the general and partial squaring down matrix calculation. The program reads the system state space description from a preassigned tape and the user supplies the format of the desired square down matrix. The output of the program consists of a DC matrix K_o (or L_o) and the gains of the modal frequencies. In addition, the state

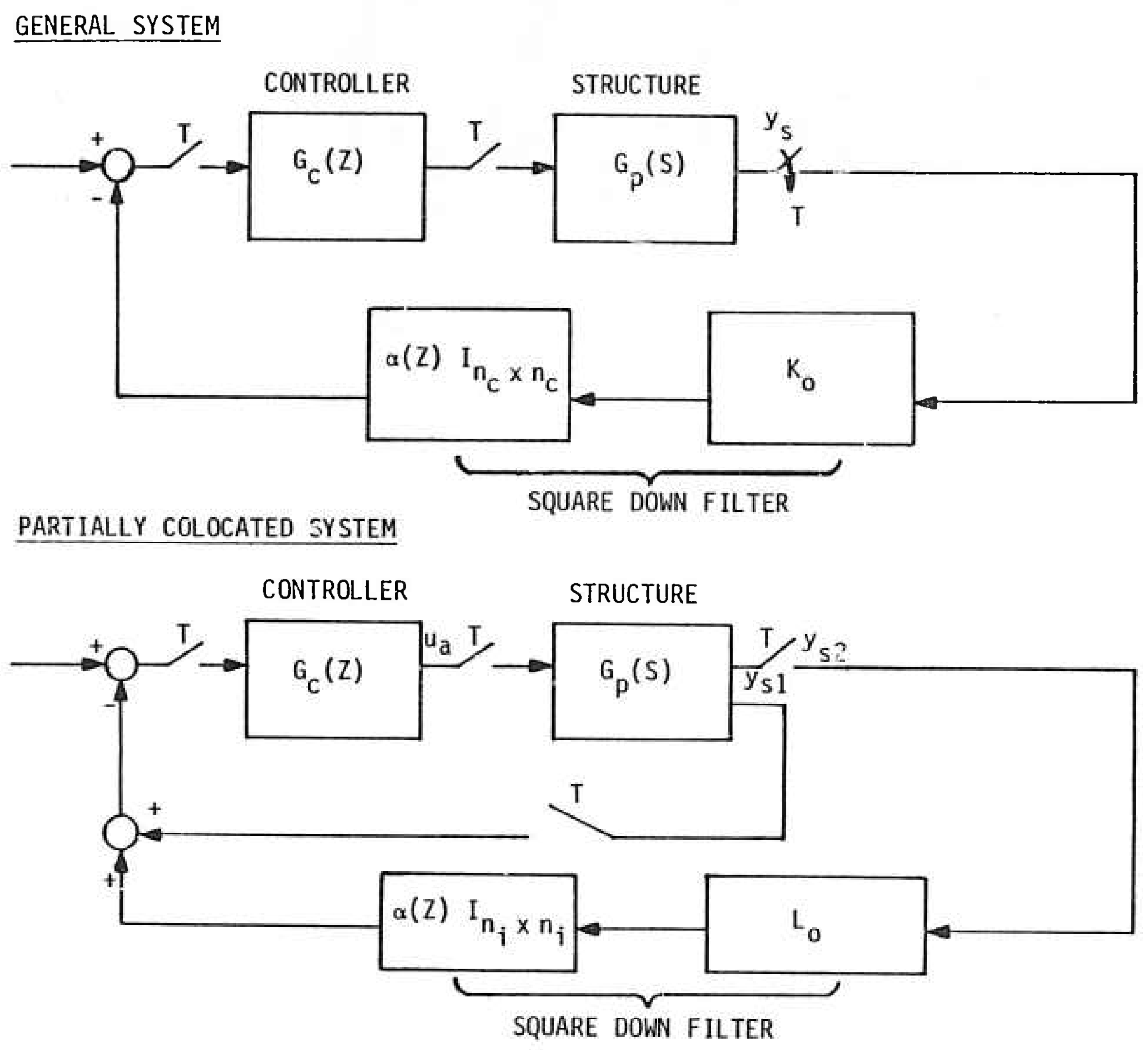

Figure 8-11. Squared Down System Topology

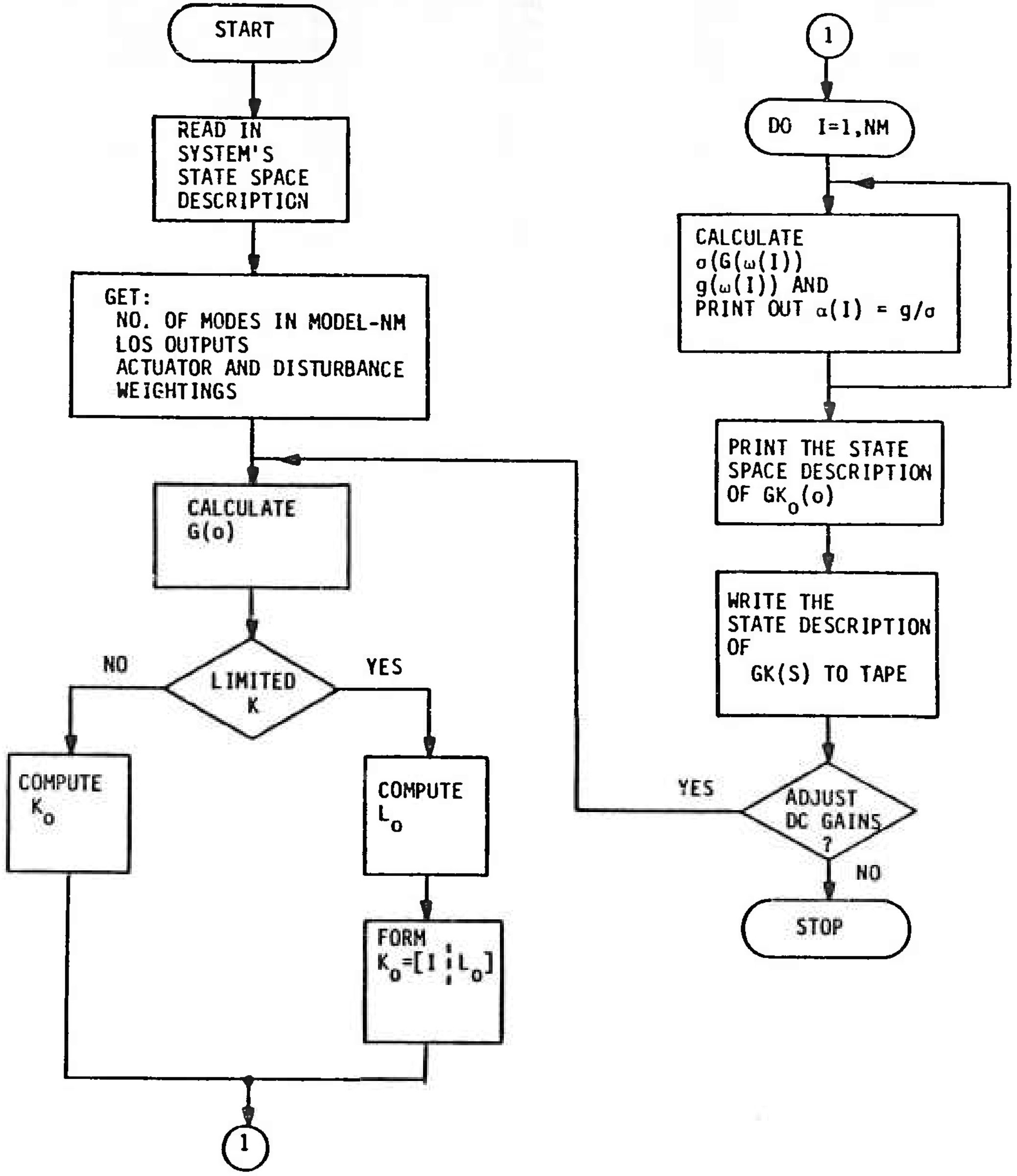

Figure 8-12. Flow Chart of the Square Down Program

space representation of $K_0\ G(s)$ is written onto a tape in a format compatible with the linear analysis program FLYNSYS.

9.0 DESIGN EXAMPLES AND EVALUATION

Two design examples were selected to demonstrate the approach discussed in Chapter 8. The two examples chosen are the TRW flat plate and the Draper Tetrahedron. The design in both examples use noncolocated control systems and thus are suitable for demonstrating the proposed design procedure. In the following, the structures will be described, then the design steps will be explained; robustness properties of the designs will be evaluated, and finally the performance of the proposed control systems for each structure will be evaluated using digital simulation.

9.1 The TRW Flat Plate Example

The flat plate design example is an existing experimental set up shown in Figure 9-1. The plate is 1.73 x 1.22 meters and is made of 1.6 mm aluminum. The top edge of the plate is clamped to a supporting structure which is rigidly attached to the wall. Control is applied to the plate by using the bending moment actuators shown in the figure. Each actuator has a built in magnetic sensor which measures relative deflections and rates.

The model used to design the controller was generated using TRW's finite element program TRWSAP. The modal frequencies of this "nominal model" are shown in Table 9-1. Next to these theoretical frequencies are the true frequencies of the plate (our "perturbed model"). The assumed and actual damping are also shown.

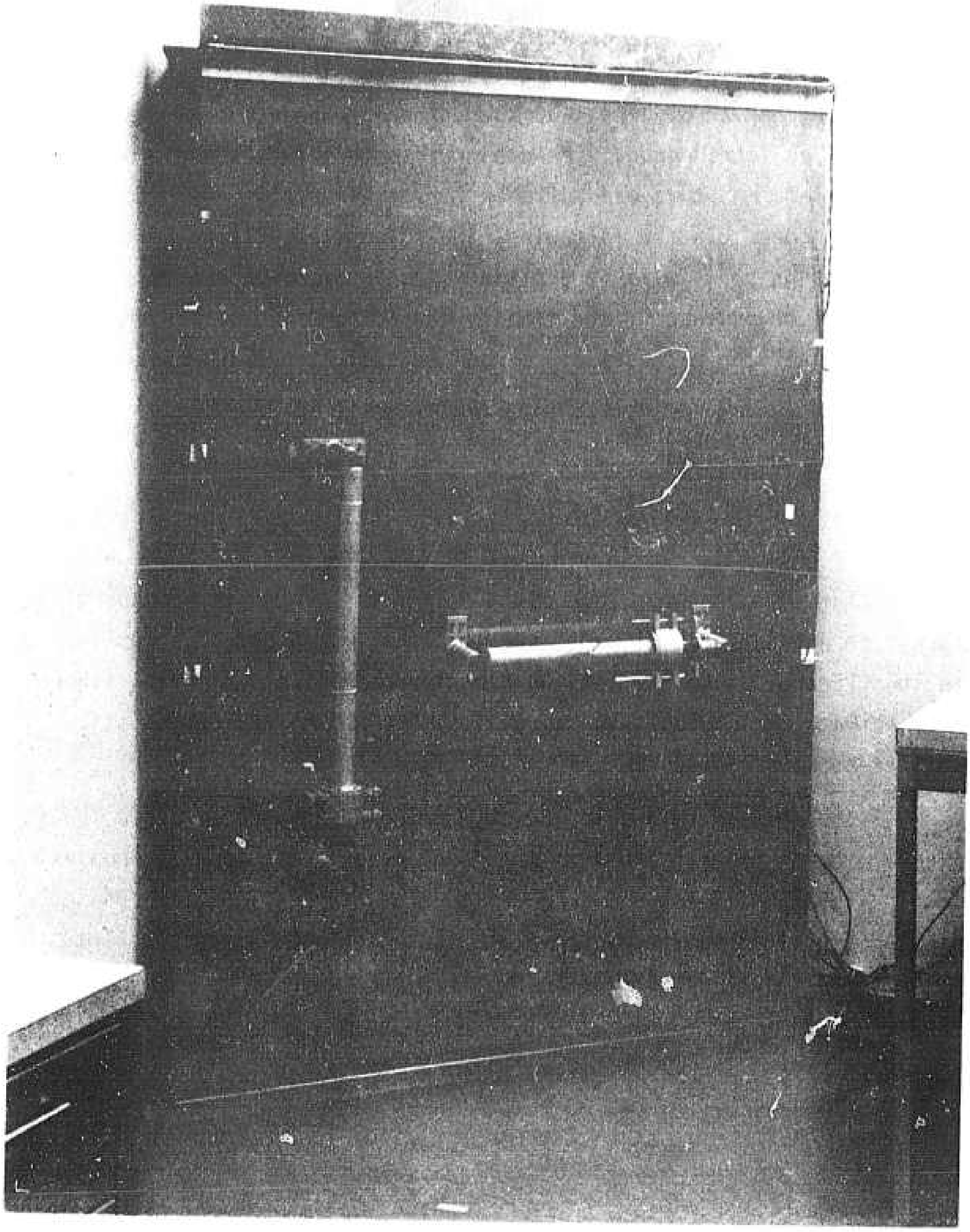

Figure 9-1. TRW Flat Plate

Table 9-1. Theoretical and Experimental Model Frequencies and Damping Coefficients

Mode #	Theoretical Freq (Hz)	Model Damping	Experimental Freq (Hz)	Model Damping
1	.413	.03	.67	.06
2	1.27	.03	1.67	.009
3	2.83	.03	2.75	.003
4	4.96	.03	5.14	.032
5	5.87	.03	5.43	.042
6	8.08	.03	8.0	.023
7	10.08	.03	9.7	.062
8	10.5	.03	11.0	.013
9	12.3	.03	12.25	unknown

9.1.1 Flat Plate: Control System Design

In this section the designs using colocated and noncolocated control systems are described and evaluated. The design is done using the multi-variable frequency domain technique combined with the positivity approach. The square down procedure described in Section 8 is also used for the noncolocated design. The design evaluation criteria used are the singular value decomposition (SVD) of the return difference and the positivity under the system. Both measure the system's robustness.

The assumption used in the colocated design was that only the two colocated actuators and sensors shown in Figure 9-1 are to be used for controlling the X and Y motions of the plate. In the noncolocated design, an additional sensor and an inertial rate sensor were placed at the bottom right corner of the plate (this sensor has not been implemented yet on the experimental set up). This location was chosen for the additional sensor because there, the low frequency modes are more observable.

The goal of both the colocated and noncolocated designs are to augment the modal damping so that the plate motion settles quickly, in response to initial conditions.

9.1.2 The Colocated Flat Plate Controller

The colocated controller developed in TRW for the experimental set up shown in Figure 9-1 is given by:

$$60.94 + \frac{12.4Z - 12.1}{Z^2 - 1.77Z + 0.884}$$

The controller operates in each of the two system's channel with sampling time $T_s = 0.01$ seconds. The design was performed using the positivity and multivariable frequency domain approach. The open loop characteristic gains for the compensated and uncompensated colocated systems in the ω-plane are shown in Figure 9-2. The minimum and maximum singular values of the return difference and a plot of the positivity index are shown in Figure 9-3.

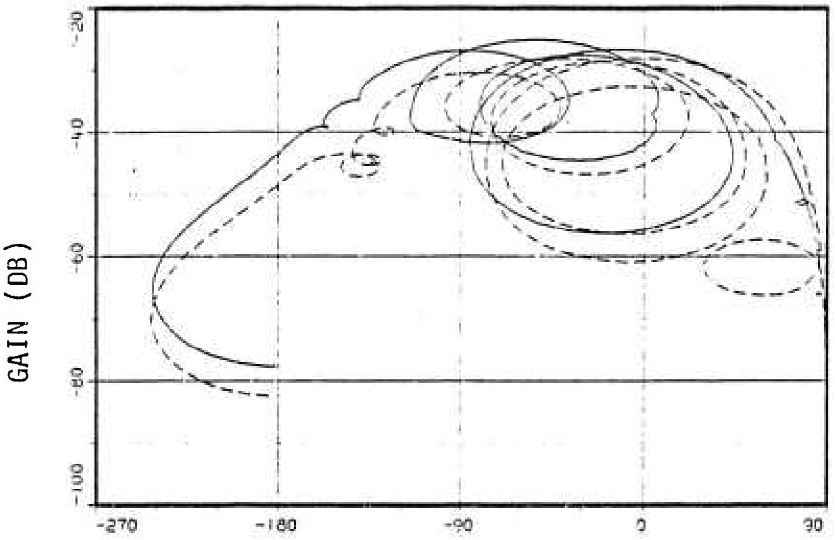

(a) $\lambda(\nu)$ OF OPEN-LOOP, UNCOMPENSATED COLOCATED SYSTEM
PHASE (DEG)

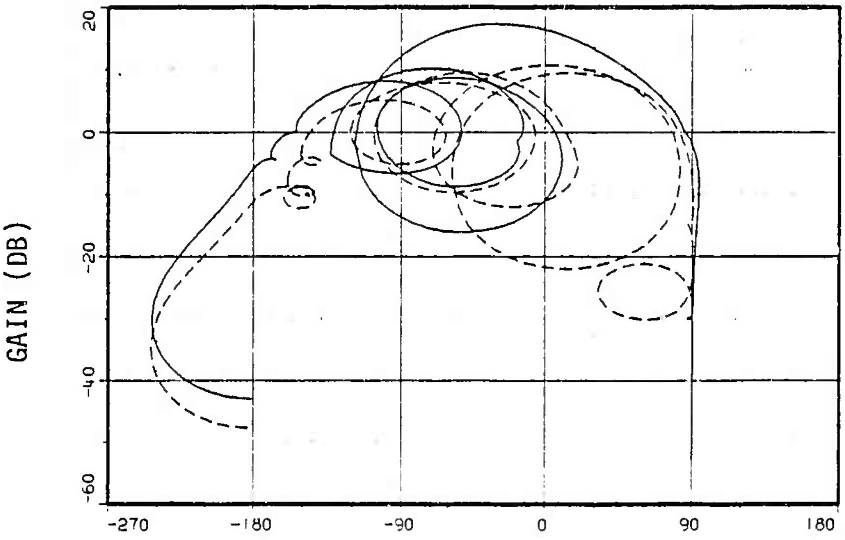

(b) $\lambda(\nu)$ OF OPEN LOOP, COMPENSATED COLOCATED SYSTEM
PHASE (DEG)

Figure 9-2. Open Loop Colocated System's Characteristic Gains

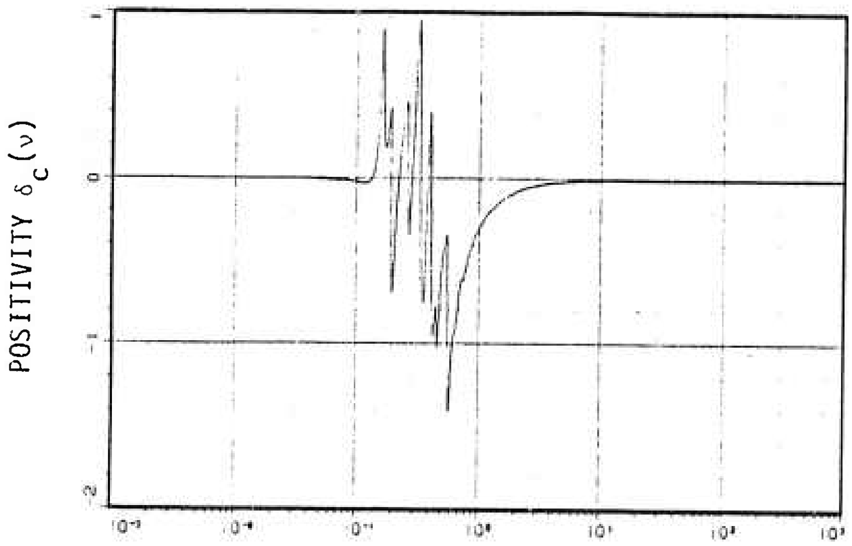

(a) POSITIVITY INDEX

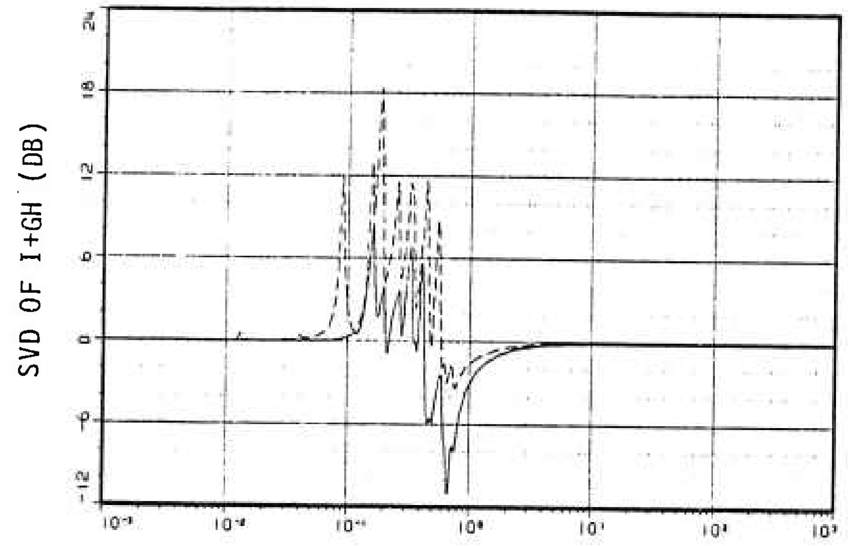

(b) MINIMUM AND MAXIMUM SINGULAR VALUE OF THE RETURN DIFFERENCE

Figure 9-3. Positivity Index and SVD of the Return Difference for the Colocated Design

9.1.3 Noncolocated Flat Plate Design

As explained in Section 8.4, the first step of the noncolocated design is to square down the system. This was done by applying the procedure described in Section 8.4.3 and using the program based on it. The square down of the sytem was performed using the corner sensor response as the performance criterion. This criterion emphasizes the first two vibrational modes. The resultant square down matrix is given by:

$$K = \begin{bmatrix} 1.4 & 0 & -30.834 \\ 0 & 10. & -16.977 \end{bmatrix}$$

The second step of the design is to compute the characteristic gains $\lambda(\nu)$ of the resultant squared down open loop system in the w-plane. They are shown in Figure 9-4(a). Note that the characteristic gains are computed after the squaring down procedure of step 1 since they are defined only for square systems.

The third step of the design is to shape the characteristic gains and the plant's positivity under to augment modal damping and the robustness properties of the system. The resultant compensator is:

$$B(Z) = \frac{0.0193Z^2 + 0.032437Z + 0.016218}{Z^2 - 1.64706Z + 0.716807} \cdot I_{2x2} \quad (9.3)$$

Hence the complete controller is given by:

$$H(Z) = \frac{0.0193Z^2 + 0.032437Z + 0.016218}{Z^2 - 1.64706Z + 0.716807} \begin{bmatrix} 1.4 & 0 & -30.834 \\ 0 & 10. & -16.977 \end{bmatrix} \quad (9.4)$$

The compensated systems characteristic gains are shown in Figure 9-4(b). The maximum and minimum singular values of the return difference and the positivity index plot of the noncollocated system are shown in Figure 9-5.

9.1.4 Noncolocated Flat Plate Design Evaluation: Robustness Properties and Closed Loop Poles

The robustness properties of the closed loop system were assessed by two methods: the positivity index $\delta(\omega)$ and by computing the minimum and maximum singular values of the return difference matrix. The

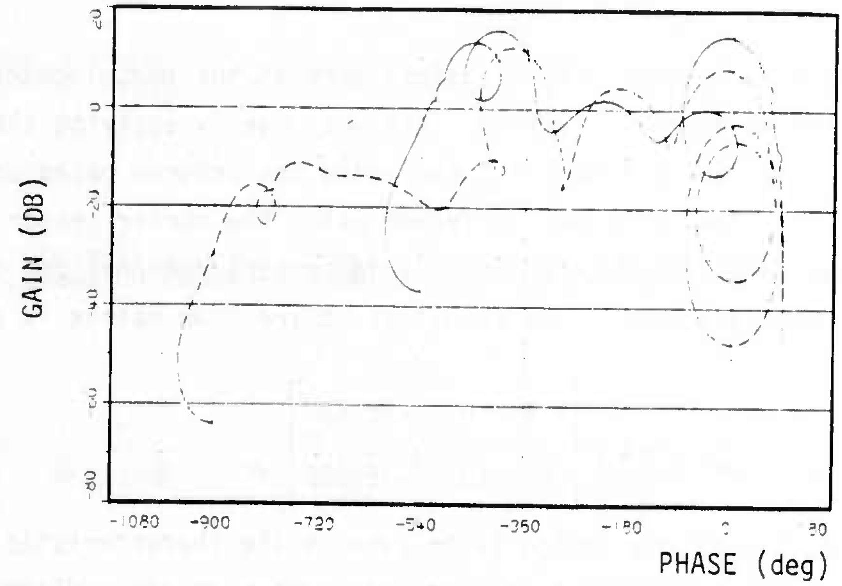

(a) $\lambda(\nu)$ OF OPEN-LOOP, SQUARED, NONCOLOCATED SYSTEM

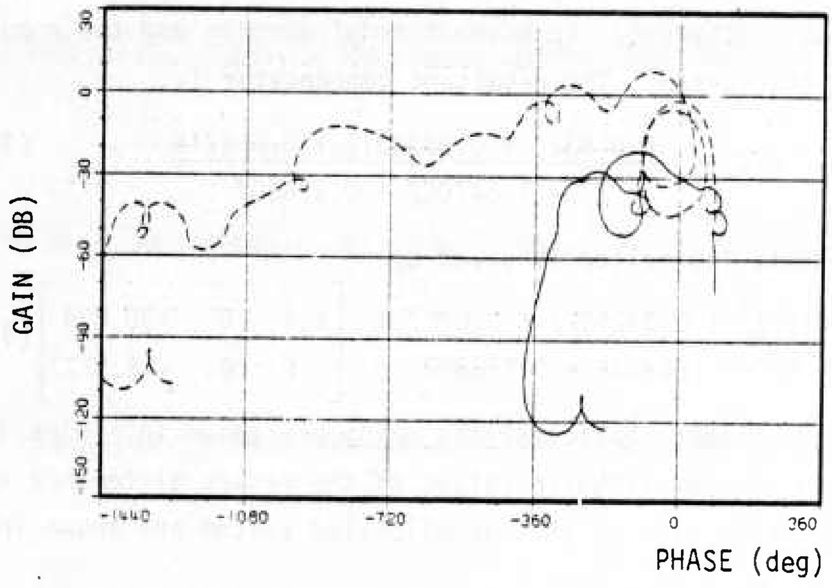

(b) $\lambda(\nu)$ OF OPEN-LOOP, COMPENSATED, NONCOLOCATED SYSTEM

Figure 9-4. Characteristic Gains of the Uncompensated and Compensated Systems

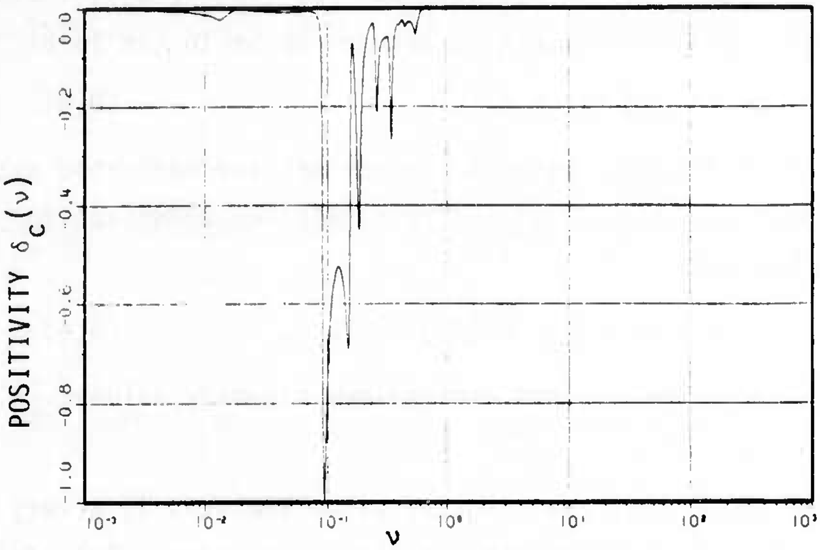

(a) POSITIVITY INDEX

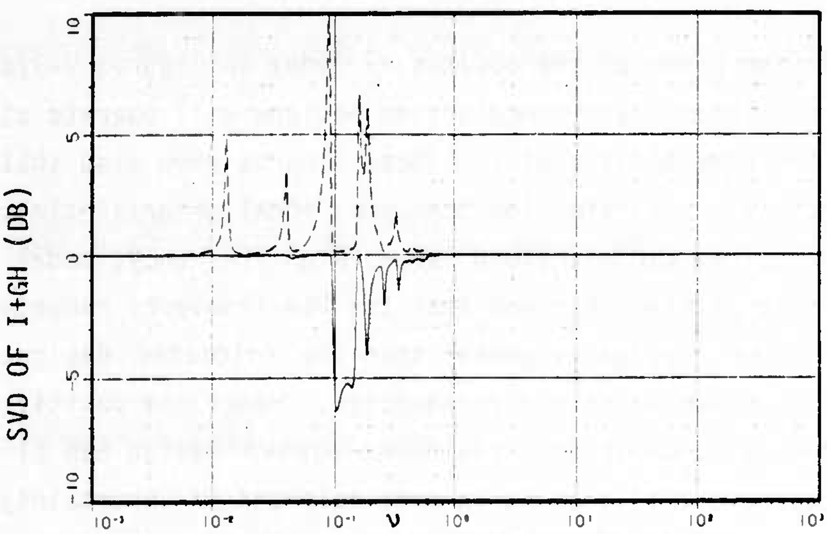

(b) MINIMUM AND MAXIMUM SINGULAR VALUES OF THE RETURN DIFFERENCE

Figure 9-5. Positivity Index and SVD of the Return Difference for the Squared Noncolocated Design

singular value analysis was performed on the return difference matrix since an additive perturbation was assumed (see [22], [23]), i.e. the perturbed system's transfer matrix is assumed to be in the form:

$$\tilde{G}(s) = G(s) + E(s) \qquad (9.5)$$

Where E(s) is the difference between the nominal and perturbed system It can be shown (see [22], [23],) that a sufficient condition for stability is given by:

$$\underline{\sigma}\,[I + G(j\omega)] > \bar{\sigma}\,[E(j\omega)] \ \forall\omega > 0 \qquad (9.6)$$

where $\underline{\sigma}$ and $\bar{\sigma}$ denote the minimum and maximum singular values, respectively.

It should be noted that the singular value analysis is a very conservative test of robustness for oscillatory systems. This is due to the existence of many lightly damped vibrational modes that result in sharp peaks in the frequency plot of $\bar{\sigma}\,[E(j\omega)]$. Since $\sigma_{min}[I + G(j\omega)]$ has to be larger than $\sigma_{max}\,[E(j\omega)]$ <u>for all frequencies</u>, the resonance peaks impose very conservative bounds on robustness.

As shown in the plots of the positivity index in Figures 9-3(a) and 9-5(a), the colocated and noncolocated designs will operate at approximately the same DC gain of 1. These figures show also that both systems tolerate moderate, low frequency modal uncertainties. Moreover, both designs can withstand large, high frequency, modal uncertainties. It is also observed that the low frequency robustness of the noncolocated design is poorer than the colocated design, but, this situation is reversed at mid frequencies. Hence the positivity index analysis conclusion is that the noncolocated design has slightly better robustness properties as it is more tolerant of uncertainty at the mid and high frequencies where the model <u>is</u> less certain.

The singular value plots of the colocated and noncolocated designs shown in Figures 9-3(b) and 9-5(b), reinforces the conclusion of the positivity index analysis. The plots show that the colocated design will tolerate moderate, additive, but otherwise unstructured uncertainties over the band $\nu = 0.$ to 0.1. Whereas the noncolocated system will withstand moderate perturbations over the band $\nu = 0.$ to 0.4. For about

a decade later, both control systems can tolerate small unstructured uncertainties. Finally, at high frequencies, the location of the negative peaks in the plots leads to the same conclusion as the positivity under analysis, namely, that overall the noncolocated design is slightly better.

To complete the evaluation of the proposed control designs, the poles of the closed loop system were computed. The list of the closed loop poles for both the colocated and noncolocated designs, using the theoretical model, is given in Table 9-2. It can be observed that the noncolocated design has better low frequency damping characteristics than the colocated system but the situation reverses at mid frequencies. At high frequencies, the nearly positive character of the colocated system becomes evident, having the high frequency modes much better damped.

9.1.5 Simulation Study Results for the Flat Plate Example

A digital simulation study was conducted to evaluate the performance of the colocated and noncolocated control systems using both the theoretical and perturbed ("real") models. Figure 9-6 compares the uncompensated response of the flat plate with those of the colocated and noncolocated designs for the theoretical model of the plate. The plots shown are the modal position response of the plate when the initial condition of the first ten modes is set to 1. They verify the analysis and clearly demonstrate the improved damping character of the noncolocated design: the first two modes are decaying much faster than in the colocated case. Figure 9-7 shows the corresponding responses of modes 6 to 15 for the noncolocated design with the initial condition as above. It is clear that all the high frequency modes are stable. The conclusion is, therefore, that the simulation study verifies the analysis results for the theoretical model as far as stability, and modal damping of the modes are concerned.

A similar simulation study was performed on the perturbed flat plate model. Figure 9-8 shows the comparison between the open loop performance and noncolocated designs as applied to the "real" plate. It is evident that the qualitative performance of noncolocated designs remains the same: it has good low frequency damping. Also, it is clear that all the modes remain stable despite the mismodelling, as shown in Figure 9-9.

Table 9-2. Closed Loop Z-Plane Eigenvalues for the Colocated and Noncolocated Design

Colocated Design

MODE #		REAL PART	IMAGINARY PART	DAMPING RATIO
	1)	.18734E-02,	.00000	1.00000
	2)	.27357E+00,	.92356E+00	.02920
	4)	.28184E+00,	.92160E+00	.02898
	6)	-.84031E-02,	.00000	.83562
	7)	-.11288E-01,	.00000	.81901
	8)	.37904E+00,	.88555E+00	.03208
	10)	.43034E+00,	.86198E+00	.03361
	12)	.47459E+00,	.84371E+00	.03069
	14)	.60048E+00,	.75344E+00	.04142
	16)	.64423E+00,	.70601E+00	.05436
	18)	.30868E+00,	.00000	1.00000
	19)	.37238E+00,	.00000	1.00000
10	20)	.74140E+00,	.62659E+00	.04233
9	22)	.76632E+00,	.60158E+00	.03920
8	24)	.84288E+00,	.49808E+00	.03968
7	26)	.90008E+00,	.38891E+00	.04821
6	28)	.91887E+00,	.32587E+00	.07426
4	30)	.90804E+00,	.27069E+00	.18292
5	32)	.88802E+00,	.26552E+00	.25290
3	34)	.96306E+00,	.17372E+00	.12031
2	36)	.99433E+00,	.79755E-01	.03094
1	38)	.99884E+00,	.25921E-01	.03174

Noncolocated Design

MODE #		REAL PART	IMAGINARY PART	DAMPING RATIO
	1)	.27746E+00,	.92148E+00	.03001
	3)	.29502E+00,	.91674E+00	.02989
	5)	.41530E+00,	.87305E+00	.02996
	7)	.47713E+00,	.84378E+00	.02947
	9)	.51685E+00,	.82217E+00	.02900
10	11)	.65361E+00,	.72310E+00	.03062
9	13)	.69932E+00,	.68324E+00	.02915
	15)	.15550E+00,	.00000	1.00000
	16)	.15301E+00,	.00000	1.00000
8	17)	.77929E+00,	.60715E+00	.01841
7	19)	.78544E+00,	.57661E+00	.04097
6	21)	.86399E+00,	.48110E+00	.02195
5	23)	.92066E+00,	.34770E+00	.04427
4	25)	.93204E+00,	.26384E+00	.11463
	27)	.81731E+00,	.19299E+00	.60154
	29)	.85884E+00,	.21056E+00	.45542
3	31)	.95598E+00,	.20523E+00	.10573
2	33)	.99267E+00,	.80399E-01	.05056
1	35)	.99801E+00,	.26005E-01	.06316
	37)	.16622E-02,	.00000	1.00000
	38)	.18401E-02,	.00000	1.00000
	39)	.18734E-02,	.00000	1.00000

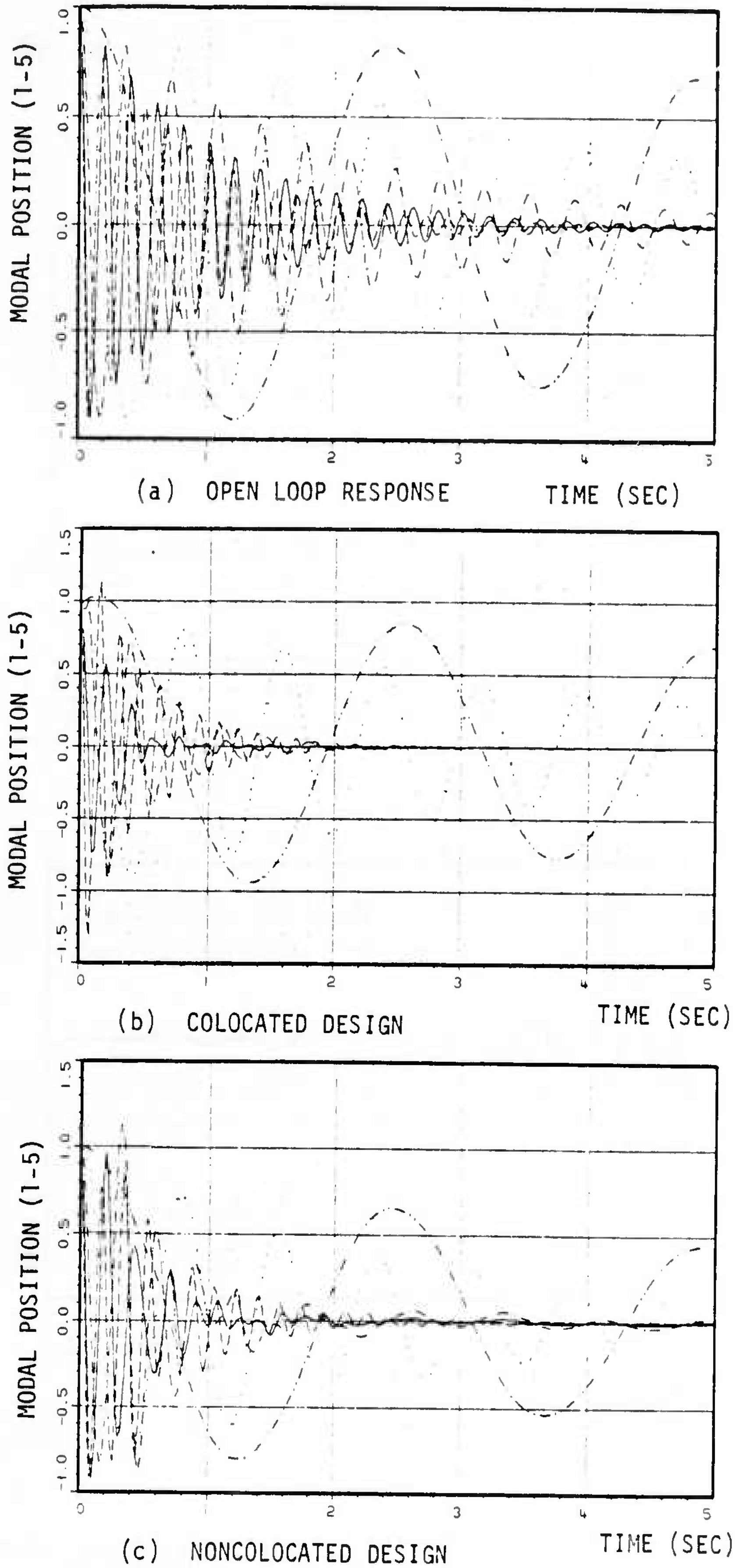

Figure 9-6. Simulation Results for Theoretical Model: Comparison Between Open-Loop and Colocated and Noncolocated Design

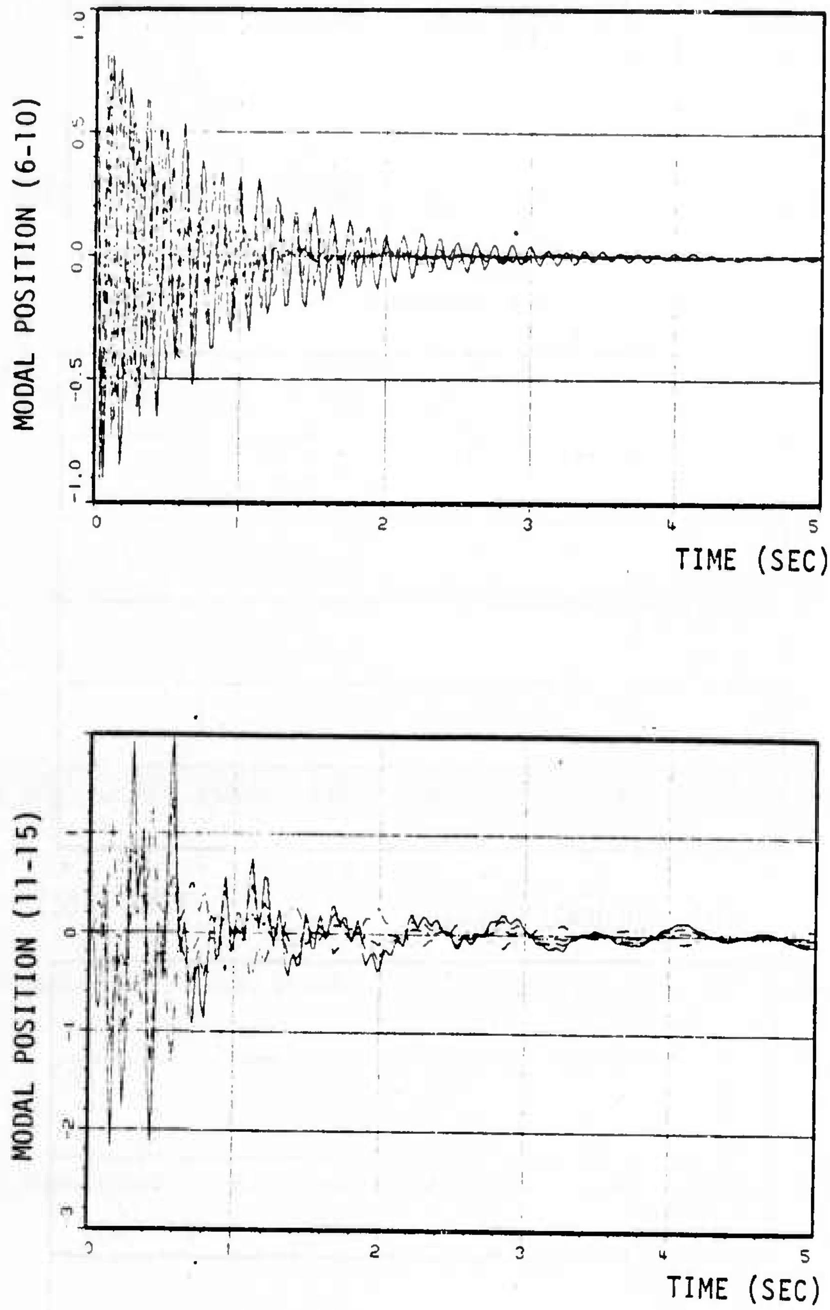

Figure 9-7. Modal Response of the Theoretical Model with Noncolocated Control System: Modes 6-15

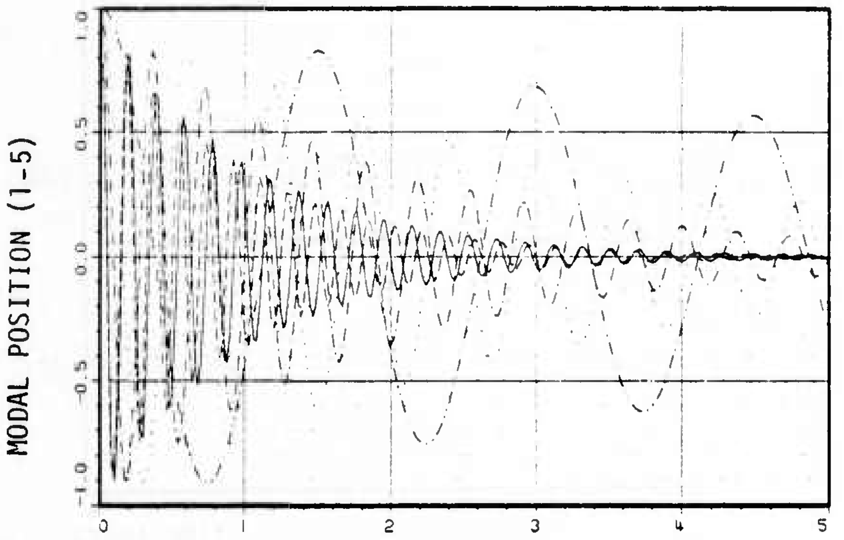

(a) OPEN-LOOP SYSTEM

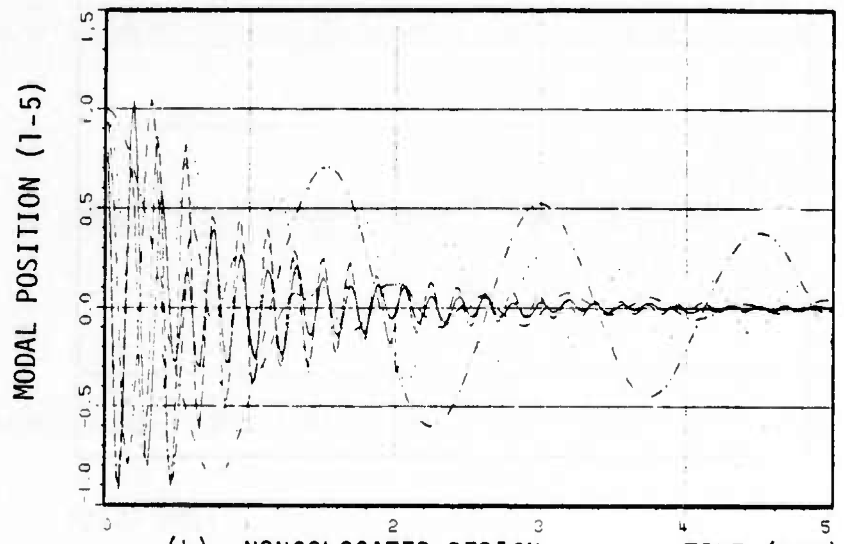

(b) NONCOLOCATED DESIGN

Figure 9-8. Simulations Results for the Perturbed Model: Open-Loop and Noncolocated System's Responses

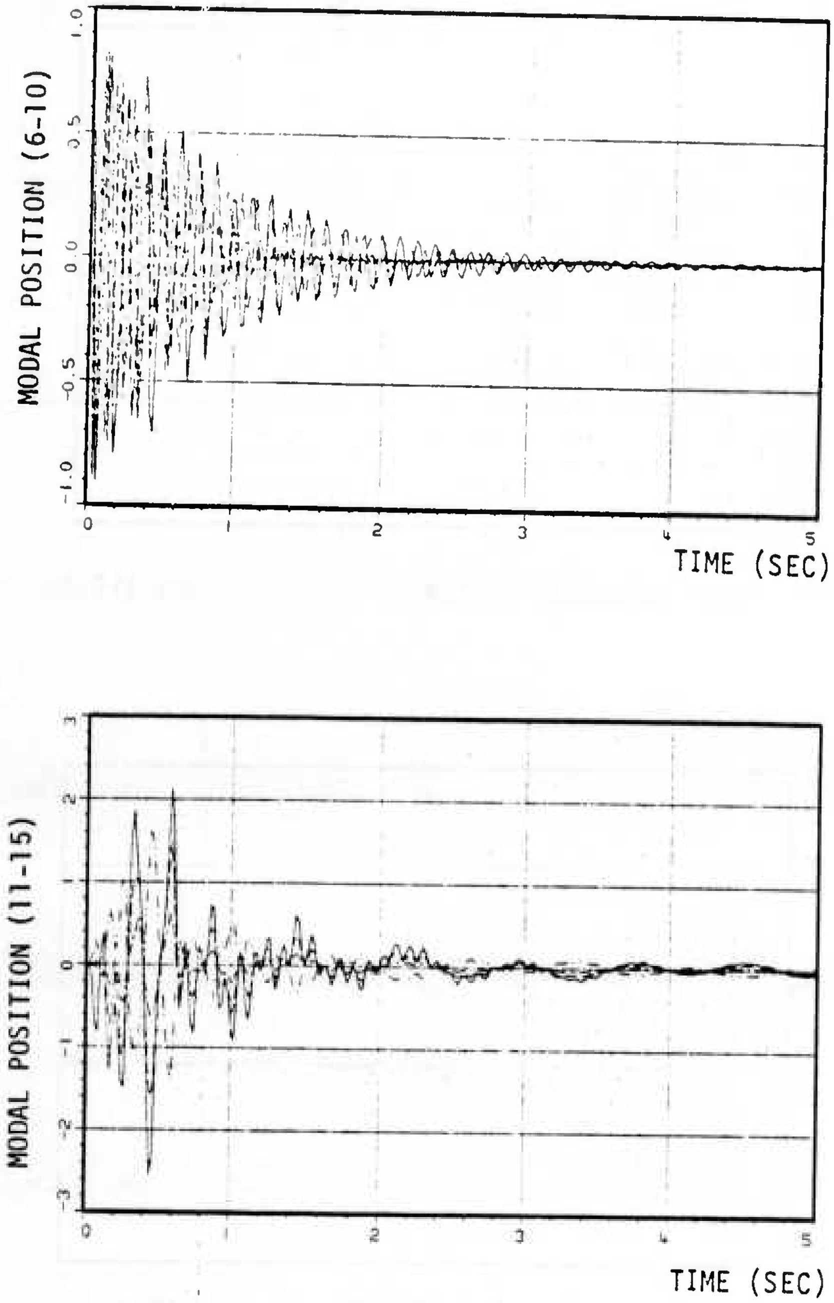

Figure 9-9. Modal Response of the Perturbed Model with Noncolocated Control System: Modes 6-15

9.2 The Draper Tetrahedral Truss Example

The Tetrahedral Truss, shown in Figure 9-10, was selected as the second test example the noncolocated design approach. This structure was devised by Draper Labs [24] as one of the simplest non-planar geometries capable of representing a large space structure. Despite its apparent simplicity, it models the feed-tower in a generic class of large antenna application. The tetrahedral apex represents the antenna feed, members 1-6 are a part of the feed support structure, and bi-peds 7-8, 9-10, and 11-12 are supports/controls attached to an inertially stabilized (assumed) antenna dish.

The finite element method was used to model the tetrahedron. Referring to Figure 9-10, the model contains ten nodes, each with three degrees of freedom, and twelve truss members. All truss members are pin connected and are flexible in the axial direction only. Nodes 5 through 10 are pinned to a rigid support. Masses are lumped at nodes 1 through 4, each with 3 degrees of freedom. Tables 9-3 and 9-4 show the elements areas and the lumped mass for both the nominal and perturbed models and Table 9-5 shows the modal frequencies for both these models. Modal damping of $\sim 0.5\%$ was assumed for all modes.

9.2.1 Control System Design for the Tetrahedral Truss

The goal of the control system design was to come up with a controller designed according to the first 8 modes of the nominal structure. The design was evaluated by robustness measures such as positivity index and SVD analysis and by the closed loop eigenvalues. In addition, the time history response to the initial conditions given in Table 9-6 was simulated. The objective is that the X-LOS error and Y-LOS error are less than $4. \times 10^{-4}$ and 2.5×10^{-4} respectively in 20 seconds. The design will be evaluated with respect to the 12 mode full models of the nominal and perturbed structures.

Two control system designs are compared:

(i) A colocated system design - Six colocated sensors and actuators are assumed to act as member dampers in parallel with members 7 through 12. The member dampers were assumed capable of sensing relative position and velocity and exerting force in the axial direction only.

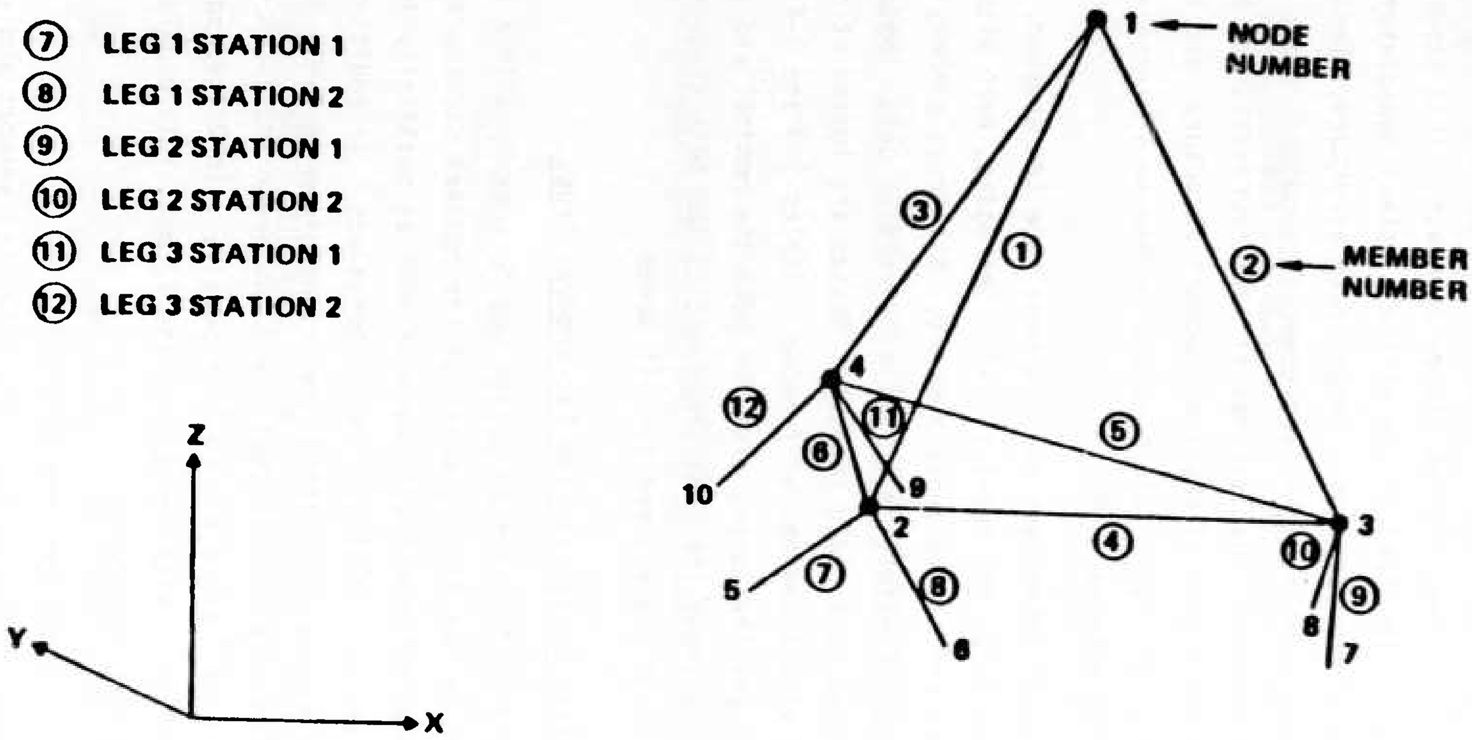

Figure 9-10. Draper Tetrahedral Truss

Table 9-3. Tetrahedron Model's Element Areas

Element	Nominal structure cross-section	Perturbed structure cross-section
1	1000	1200
2	100	150
3	100	150
4	1000	1200
5	1000	1200
6	1000	1200
7	100	150
8	100	150
9	100	150
10	100	150
11	100	150
12	100	150

Table 9-4. Tetrahedron Model's Lumped Masses

Node	Nominal structure mass	Perturbed structure mass
1	2	4
2	2	2
3	2	2
4	2	2

Table 9-5. Tetrahedron's Modal Frequencies

Mode No.	Nominal Model	Perturbed Model
1	.214	.186
2	.265	.233
3	.460	.472
4	.471	.566
5	.541	.612
6	.669	.820
7	.742	.903
8	.757	.909
9	1.359	1.423
10	1.472	1.640
11	1.637	1.739
12	2.054	2.223

Table 9-6. Initial Conditions for the Tetrahedron Design Evaluation

Mode	Displacement (η)	Velocity ($\dot{\eta}$)
1	-.001	-.003
2	.006	.01
3	.001	.03
4	-.009	-.02
5	.008	.02
6	-.001	-.02
7	-.002	-.003
8	.002	.004
9	.0	.0
10	.0	.0
11	.0	.0
12	.0	.0

(ii) Noncolocated system design - In addition to the colocated system, two sensors which measure X-LOS and Y-LOS motions were assumed. This created a noncolocated control system with 6 actuators and 8 sensors.

9.2.2 The Colocated Controller for the Tetrahedron

The colocated controller for the tetrahedron was developed using the design methodology developed in Section 8 and is given in Appendix D. The sampling rate was chosen to be 0.2 seconds. This rate is approximately three times faster than the highest controlled mode. In order to achieve the desired rate of decay, the colocated controller was designed using an α-shifted plane as explained in Appendix D. The digital filter was designed using the generalized Nyquist Theorem for multivariable systems. The decentralized controller resulting from the design in the w-plane is:

$$H(Z) = I_{6x6} \cdot 11.492 + \frac{3.921162Z - 3.9863812}{Z^2 - 1.70921Z + .846578}$$

The open loop characteristic gains for the compensated, colocated system are given in Figure 9-11. The minimum and maximum singular values of the return difference matrix and a plot of the positivity under are given in Figure 9-12. The closed loop eigenvalues are shown in Table 9-7.

9.2.3 Design of the Noncolocated Control System for the Tetrahedral Truss

As in the flat plate example,the first step in the design of a noncolocated nonsquare control system is to square down the plant by calculating on appropriate matrix K_0. Both a full order and partial squaring down matrices were generated and are given in Table 9-8 (i) and (ii). Appropriate filters were also generated to improve the system's performance. As it will be shown later, these filters are not needed in the design and constant matrices yield good closed-loop performance which meets requirements. Figure 9-13 compares the frequency responses of the colocated system to two squared down systems which were squared down as follows:

With Compensator

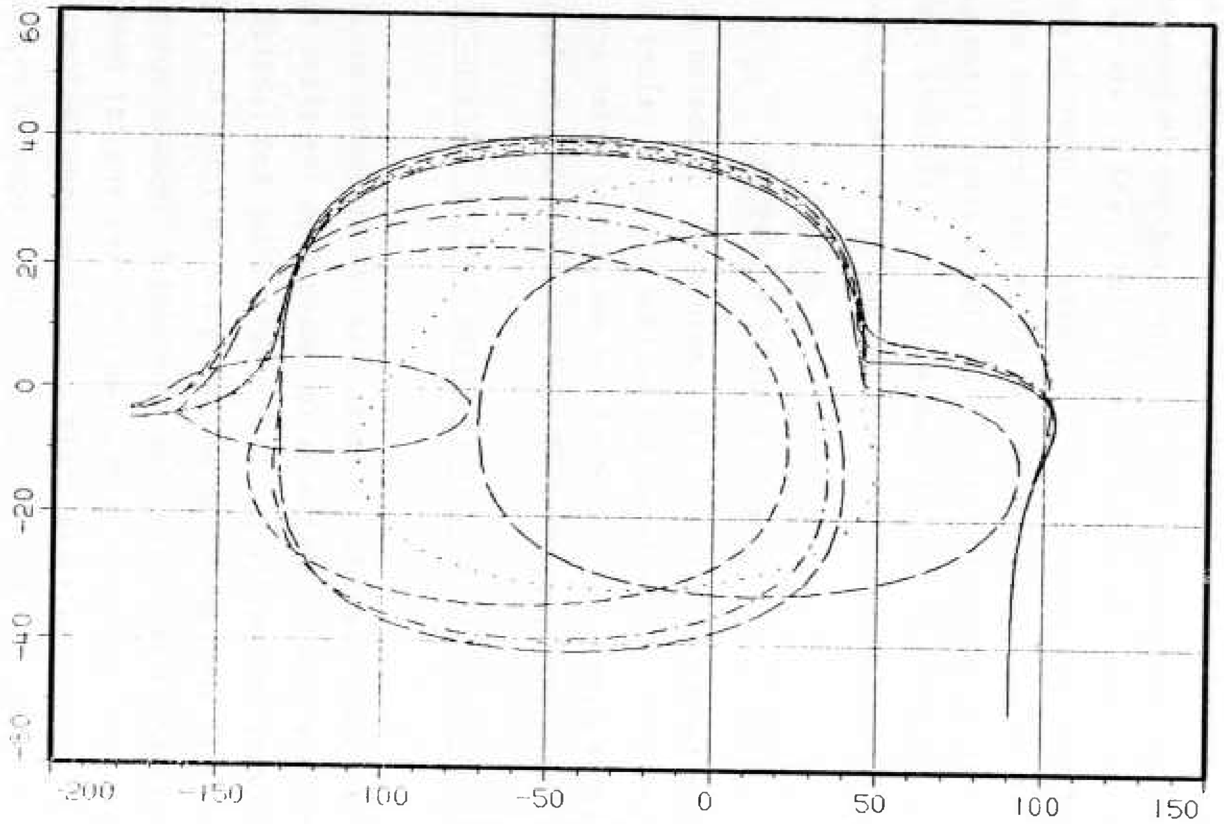

Figure 9-11. Characteristic Gains for the Compensated Colocated System

With Compensator

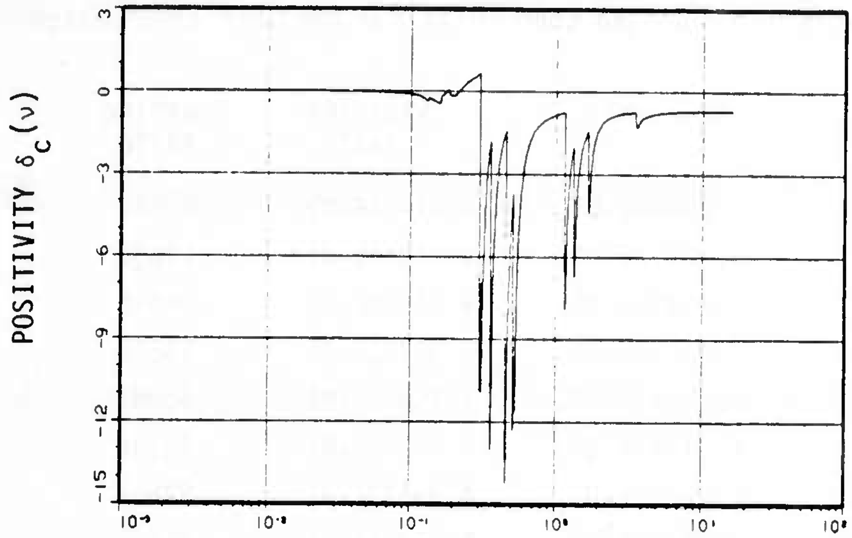

(a) POSITIVITY INDEX

With Compensator

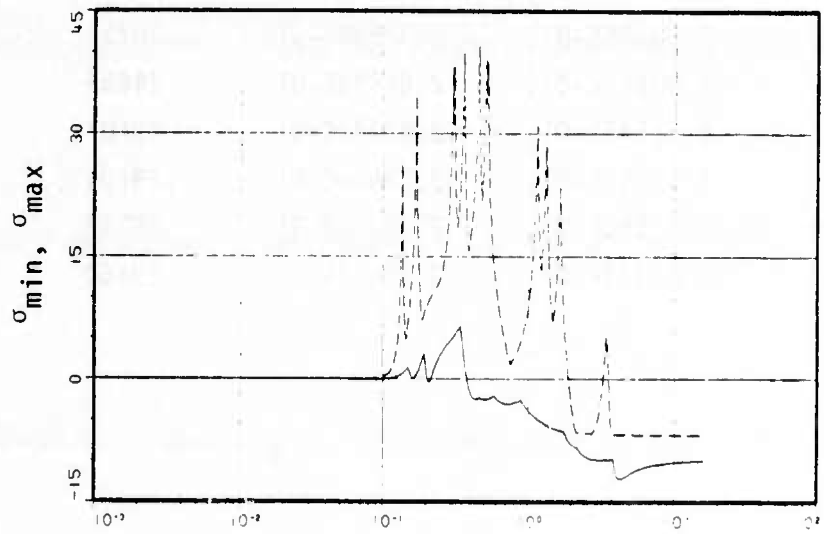

(b) The minimum and maximum singular values of the return difference

Figure 9-12. Positivity and SVD of the Return Difference for the Colocated Design

Table 9-7. Closed Loop Poles for the Colocated Design

	REAL PART	IMAGINARY PART	DAMPING RATIO
1)	-8.26864E-01,	4.61434E-01	.02072
3)	-4.60310E-01,	5.71054E-01	.13652
5)	-5.49398E-01,	6.24499E-01	.08010
7)	-3.84056E-01,	5.99832E-01	.15656
9)	1.01249E-01,	4.74242E-01	.46967
11)	1.01941E-01,	4.78232E-01	.46536
13)	1.48772E-01,	4.39533E-01	.52509
15)	6.07551E-01,	5.86374E-01	.21521
17)	4.41817E-01,	5.87595E-01	.31527
19)	6.67944E-01,	5.86729E-01	.16104
21)	9.37237E-01,	2.60093E-01	.10188
23)	8.92957E-01,	3.74850E-01	.08042
25)	8.80506E-01,	3.04850E-01	.20737
27)	8.90611E-01,	2.64750E-01	.24655
29)	8.62547E-01,	2.83442E-01	.29107
31)	8.65940E-01,	2.78600E-01	.29104
33)	8.65500E-01,	2.79053E-01	.29137
35)	8.64333E-01,	2.80603E-01	.29160

Table 9-8. Noncolocated Design for the Tetrahedron: Squaring Down Matrices and a Constant Controller

(i) Full Squaring down matrix

$$K_o = \begin{matrix}
2.200397E+00 & -2.520930E-01 & 3.148287E-01 & 7.466842E-01 & 2.849142E-01 & -4.465127E-01 & -8.457131E-01 & 1.180849E-01 \\
-2.521063E-01 & 2.200368E+00 & -4.466463E-01 & 2.848772E-01 & 7.466571E-01 & 3.147453E-01 & -3.206069E-01 & -7.915183E-01 \\
1.861677E-01 & -3.869148E-01 & 1.854454E+00 & -1.607475E-01 & 2.845484E-01 & 5.767142E-01 & 1.552142E-01 & -6.416451E-01 \\
7.593358E-01 & 3.391750E-01 & -2.327921E-01 & 2.429030E+00 & -4.790156E-01 & 2.655159E-01 & 7.782062E-01 & 1.563027E-01 \\
3.391984E-01 & 7.592648E-01 & 2.653881E-01 & -4.789763E-01 & 2.428884E+00 & -2.327506E-01 & 5.244262E-01 & 5.957704E-01 \\
-3.868089E-01 & 1.861121E-01 & 5.767280E-01 & 2.846522E-01 & -1.607214E-01 & 1.854558E+00 & -4.780327E-01 & 4.552007E-01
\end{matrix}$$

(ii) Partial squaring down matrix

$$K_o = \begin{array}{cccccccc}
 & & & & & & \multicolumn{2}{c}{\overbrace{\hspace{6em}}^{L_o}} \\
1.000000E+00 & 0.000000 & 0.000000 & 0.000000 & 0.000000 & 0.000000 & -1.110261E+00 & 1.071245E-01 \\
0.000000 & 1.000000E+00 & 0.000000 & 0.000000 & 0.000000 & 0.000000 & -4.622898E-01 & -1.015125E+00 \\
0.000000 & 0.000000 & 1.000000E+00 & 0.000000 & 0.000000 & 0.000000 & 4.636716E-01 & -1.025712E+00 \\
0.000000 & 0.000000 & 0.000000 & 1.000000E+00 & 0.000000 & 0.000000 & 1.077917E+00 & 7.707819E-02 \\
0.000000 & 0.000000 & 0.000000 & 0.000000 & 1.000000E+00 & 0.000000 & 6.057096E-01 & 8.949230E-01 \\
0.000000 & 0.000000 & 0.000000 & 0.000000 & 0.000000 & 1.000000E+00 & -6.563728E-01 & 9.143774E-01
\end{array}$$

(iii) A constant gain controller: $4 \cdot I \cdot [I \vdots L_o]$

$$H = \begin{matrix}
4.000000E+00 & 0.000000 & 0.000000 & 0.000000 & 0.000000 & 0.000000 & -4.441045E+00 & 4.284981E-01 \\
0.000000 & 4.000000E+00 & 0.000000 & 0.000000 & 0.000000 & 0.000000 & -1.849159E+00 & -4.060499E+00 \\
0.000000 & 0.000000 & 4.000000E+00 & 0.000000 & 0.000000 & 0.000000 & 1.854686E+00 & -4.102848E+00 \\
0.000000 & 0.000000 & 0.000000 & 4.000000E+00 & 0.000000 & 0.000000 & 4.311669E+00 & 3.083127E-01 \\
0.000000 & 0.000000 & 0.000000 & 0.000000 & 4.000000E+00 & 0.000000 & 2.422838E+00 & 3.579692E+00 \\
0.000000 & 0.000000 & 0.000000 & 0.000000 & 0.000000 & 4.000000E+00 & -2.625491E+00 & 3.657510E+00
\end{matrix}$$

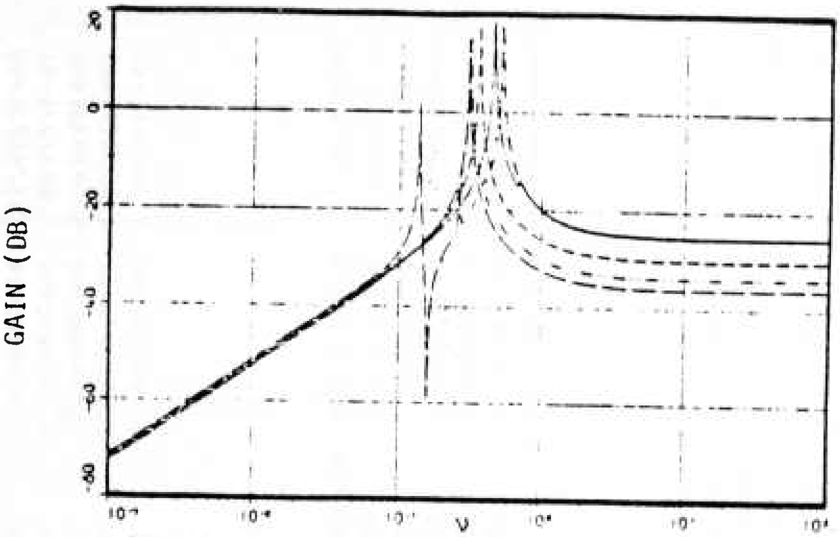

(a) FREE COLOCATED SYSTEM

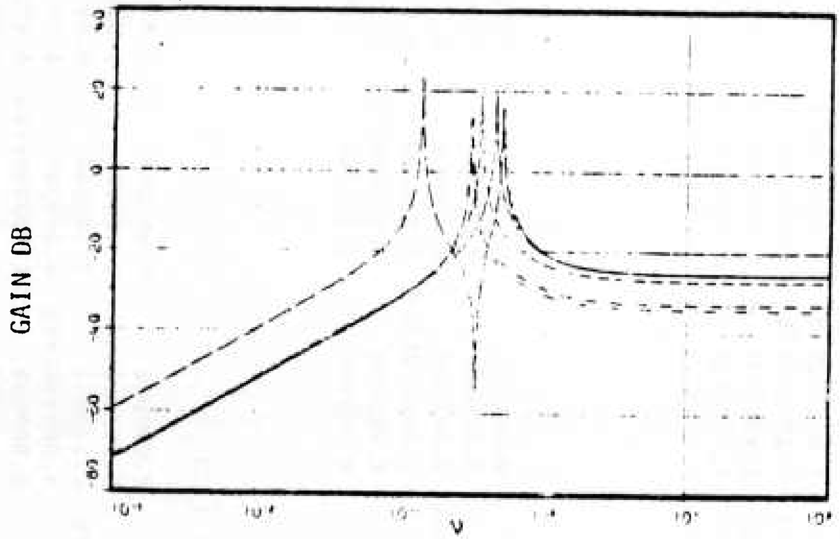

(b) PARTIAL SQUARE DOWN

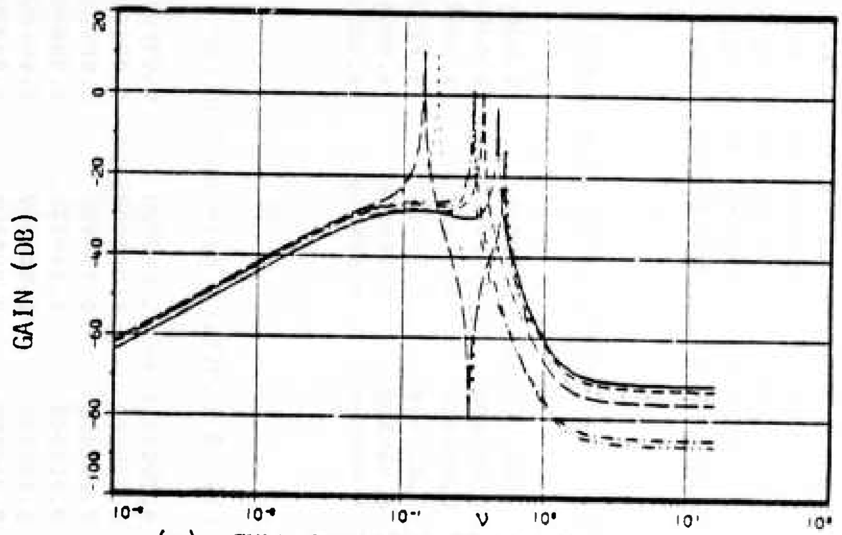

(c) FULL SQUARING DOWN + FILTER

Figure 9-13. Squaring Down Comparison

(i) Full-Order Square Down Matrix + Third-Order Filter: The square down matrix is given by $\alpha(Z)\ K_0$. K_0 is given in Table 9-8(i) and the digital filter is given by

$$\alpha(Z) = \frac{1.82 \cdot 10^{-3}\ Z^3 + 5.46 \cdot 10^{-3}\ Z^2 + 5.43 \cdot 10^{-3}\ Z + 1.82 \cdot 10^{-3}}{Z^3 - 2.267\ Z^2 + 1.713\ Z - 4.317}$$

(ii) Partial Square Down Matrix - The square down matrix is given by

$$K_0 = [I \ \vdots \ L_0] \quad \text{as given in Table 9-8(ii)}$$

As it can be observed in Figure 9-13 the gains of the two first modes are increased relative to the other modes when the square down procedure is applied. This is true both in the case of a limited gain matrix and the case of a full gain matrix + third-order filter. The filter gives more weight to the important modes (modes 1 and 2), however, it introduces lag into the system which complicates the design of a control.

It was found that the squared down noncolocated system can have its poles acquire the needed amount of damping by using a constant diagonal compensator. This is true for both the partial square down matrix $K_0 = [I \quad L_0]$ and the full matrix K_0. Since the partial matrix results in a more simple control system, this design will be explained and compared to the colocated design. The square down matrix is as in Table 9-8(ii) and a compensator 4·I was included to improve performance. The resultant complete controller is in Table 9-8(iii). The functional diagram of the noncolocated control system is given in Figure 9-14.

Since a constant gain controller yields a closed loop system with adequately damped poles, no additional filtering is necessary. This simplification of the controller's structure is due to the squaring down matrix, it amplified the representation of important modes in the feedback signal. This, in turn, allowed for damping augmentation with a constant gain without destabilizing the high frequency modes. Table 9-9 shows the closed loop poles of the noncolocated system with the controller as given in Table 9-8(iii). As it can be observed, both the nominal

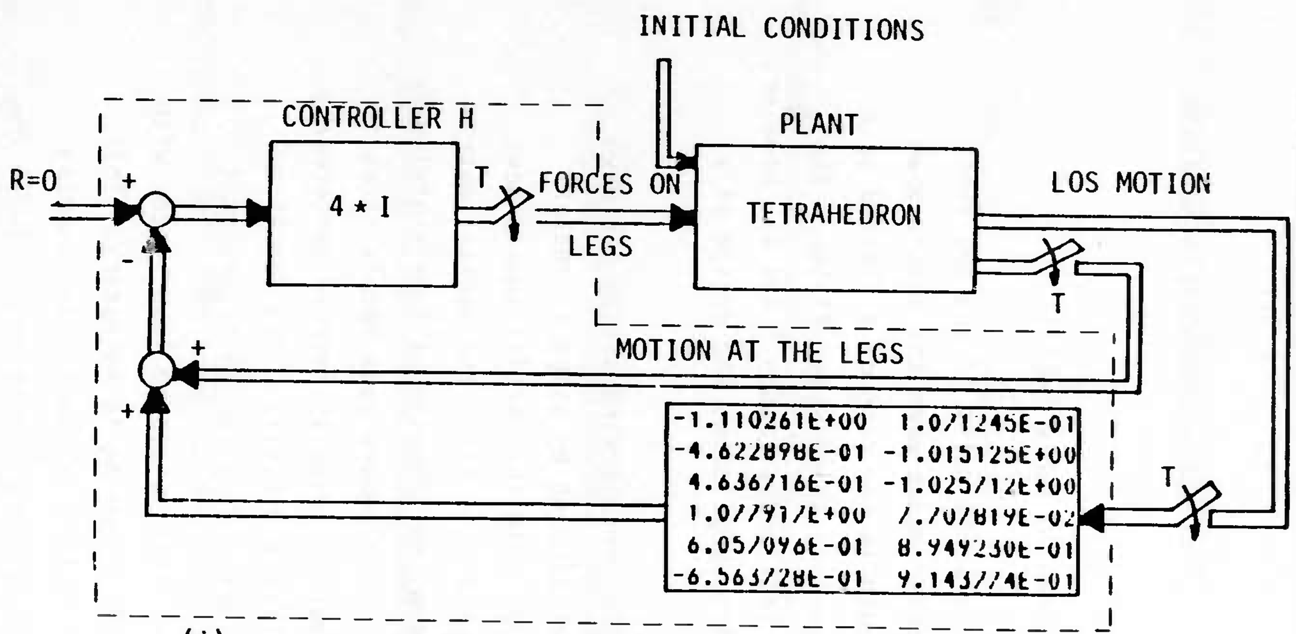

(i) Functional Diagram of the Noncolocated Control System

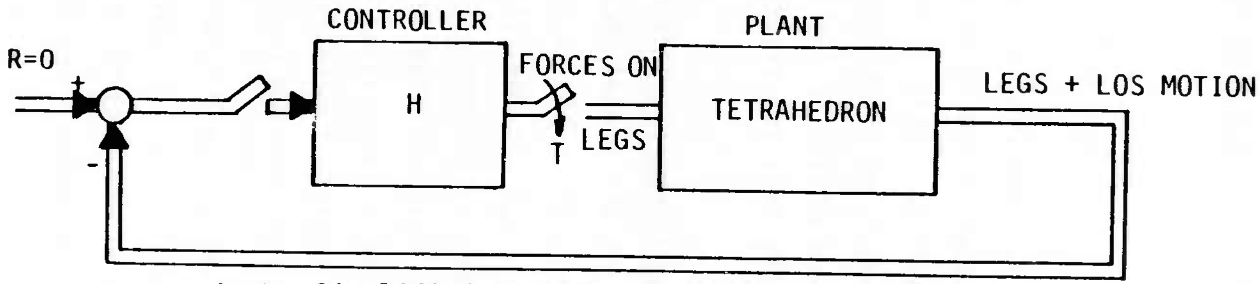

(ii) Simplified Diagram of the Noncolocated System

Figure 9-14. Functional Diagram of the Noncolocated Control System

Table 9-9. Noncolocated Design for the Tetrahedron: Closed Loop Eigenvalues

NOMINAL MODEL				PERTURBED MODEL			
MODE NO.	REAL PART	IMAGINARY PART	DAMPING RATIO	MODE NO.	REAL PART	IMAGINARY PART	DAMPING RATIO
12	-8.36060E-01,	5.19399E-01	.00613	12	-9.30047E-01,	3.32128E-01	.00447
10	-3.35591E-01,	8.46896E-01	.04781	10	-5.20228E-01,	7.65558E-01	.03565
11	-4.89047E-01,	8.11337E-01	.02560	11	-6.07722E-01,	7.09748E-01	.02977
9	-1.76840E-01,	9.23107E-01	.03520	9	-2.35851E-01,	9.44989E-01	.01452
1	8.93068E-01,	2.50093E-01	.26600	1	9.39023E-01,	2.27119E-01	.14382
7	4.74255E-01,	6.97765E-01	.17195	2	9.07373E-01,	2.81288E-01	.16829
8	4.44674E-01,	7.07356E-01	.17524	4	6.91026E-01,	6.26838E-01	.09375
6	4.87042E-01,	6.32348E-01	.23935	3	7.82332E-01,	5.36903E-01	.08697
2	8.36757E-01,	3.02534E-01	.31905	5	6.23057E-01,	6.50462E-01	.12850
4	7.63258E-01,	5.40298E-01	.10823	7	2.84903E-01,	7.87679E-01	.14330
3	7.83291E-01,	5.27559E-01	.09609	8	2.69223E-01,	7.86649E-01	.14712
5	6.48394E-01,	5.52743E-01	.22123	6	3.47020E-01,	7.34707E-01	.18076

and perturbed models acquire considerable modal damping. It is especially important that modes 1 and 2 have high damping coefficients since they contribute the most to the LOS motion. It should be noted, a sensitivity study showed that the closed loop modal damping characteristics are not sensitive to the compensator's gain: a change of the nominal gain (4·I) by 6 db gave damping within specifications. See also Section 9.2.4.

Figures 9-15 and 9-16 show the characteristic gains, the positivity index and the SVD analysis for the compensated noncolocated system. The conclusions one can draw from the comparison of the colocated design given in Figures 9-11 and 9-12 and the noncolocated design shown in Figures 9-15 and 9-16, reinforces the results obtained for the plate example:

(i) The colocated and noncolocated systems will operate at approximately the same DC gain.

(ii) Both systems can tolerate moderate, low frequency modal uncertainties.

(iii) Both systems can withstand large high frequency modal uncertainties.

(iv) The colocated system has better robustness properties at low frequencies. The situation is reversed in mid frequencies.

9.2.4 <u>Simulation Study Results for the Tetrahedral Truss</u>

A simulation study, similar to the flat plate study was conducted. The study evaluated the performance of the colocated and noncolocated designs for both the theoretical and perturbed models. The evaluation was done by studying the time response to the modal initial conditions given in Table 9-6 (see Section 9.2.1). The response of the nominal tetrahedral model for both the colocated and noncolocated designs are shown in Figure 9-17. As it can be seen the LOS transient requirements are used for both designs, however, the noncolocated design has a superior performance. As can be observed, the LOS displacement for the noncolocated design in both the X and Y directions is within the required band in about 6 seconds, which is in about 30% of the required

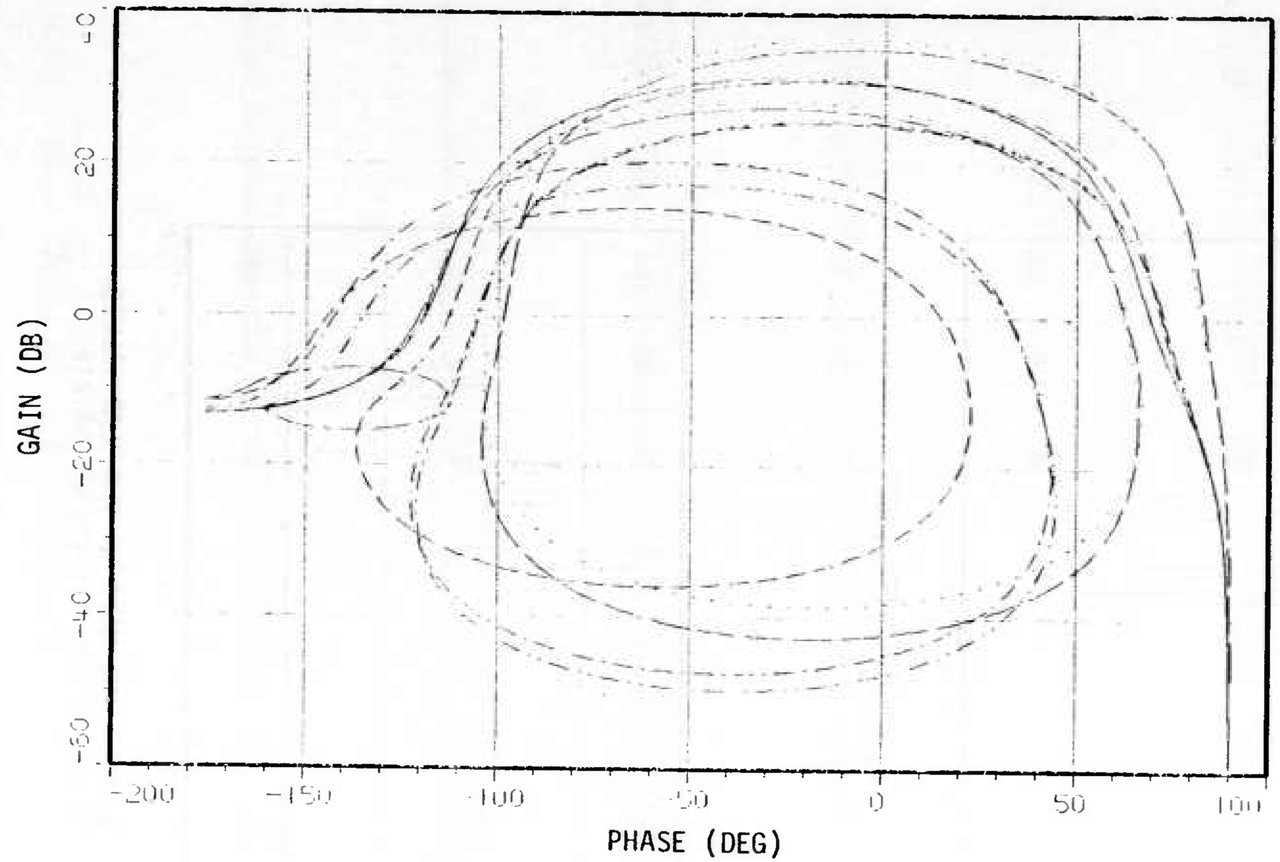

Figure 9-15. Noncolocated Design for the Tetrahedron: Characteristic Gains of the Compensated System

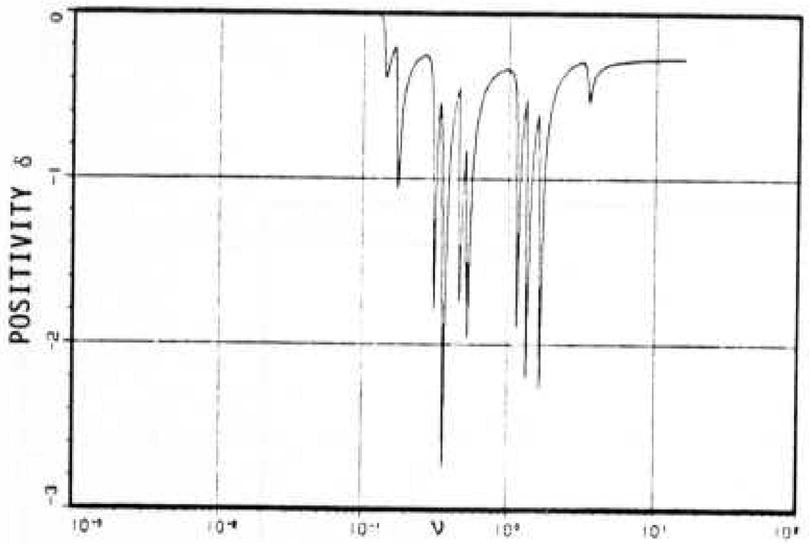

(a) POSITIVITY INDEX

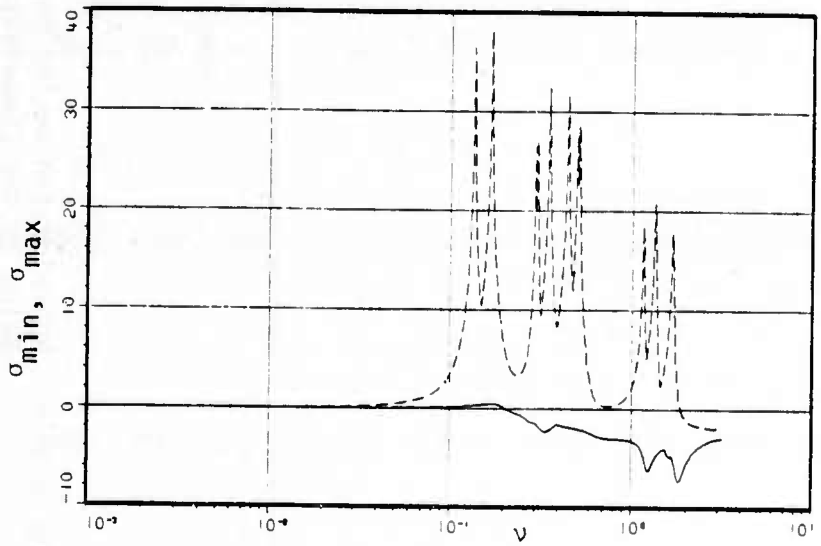

(b) MINIMUM AND MAXIMUM SINGULAR VALUES
OF THE RETURN DIFFERENCE MATRIX

Figure 9-16. Noncolocated Design for the Tetrahedron: Positivity Index and Singular Value Analysis of the Return Difference

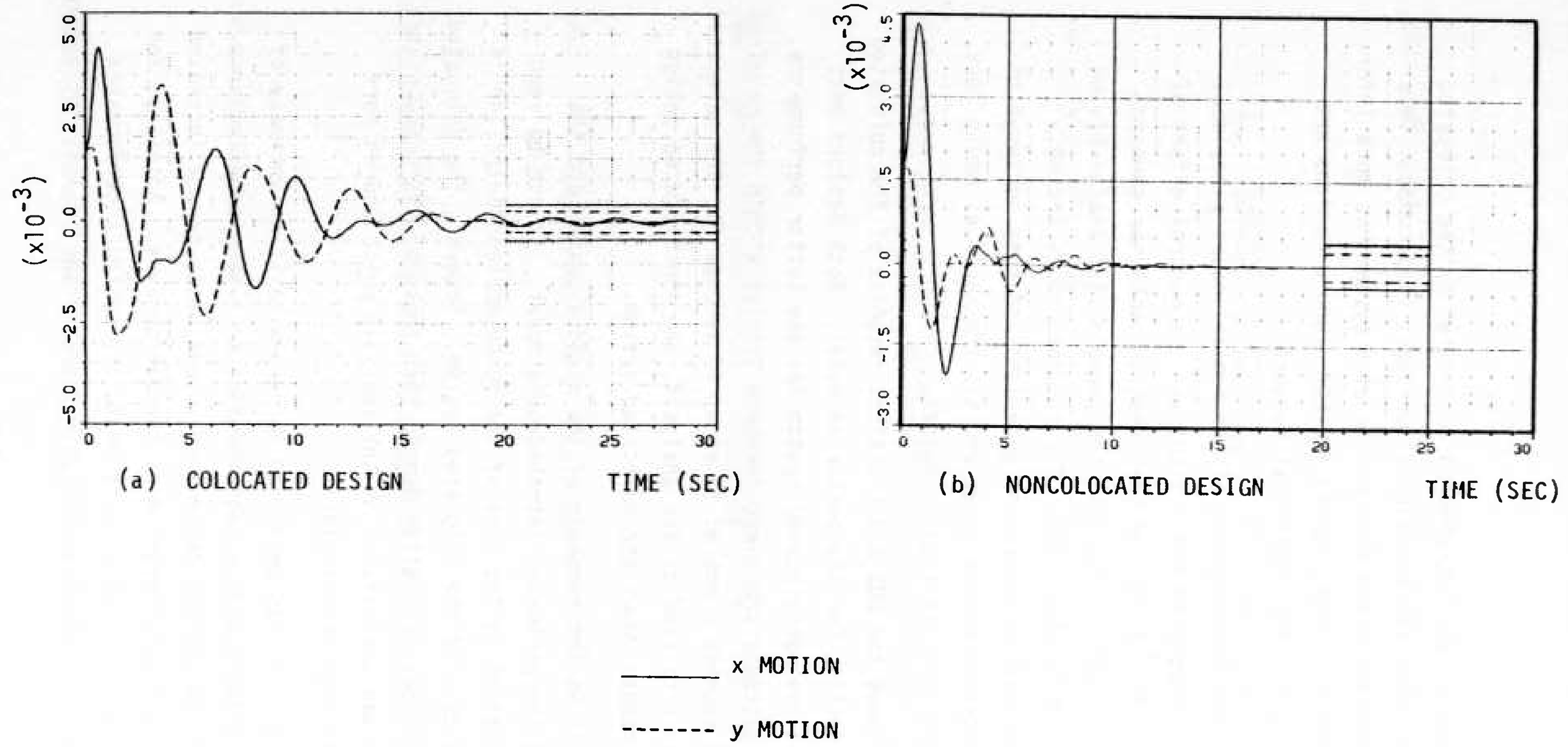

Figure 9-17. Nominal Model Transient Response of the Colocated and Noncolocated Control Systems for the Tetrahedron

time. The transient of the tetrahedron controlled by the colocated system reaches the required band only after about 15 seconds. This could have been expected since the noncolocated system has more information in the feedback signal, namely the LOS x and y motions are measured directly by the two additional sensors.

Figure 9-18 shows the response of the nominal model's residual modes (modes not included in the design) and the control effort of the actuator at leg #1. It can be seen that the actuator command forces are modest in both cases, with the noncolocated design having a lower control force by about 40%. The residual modes are only slightly excited by both control configurations and they converge to zero. The noncolocated control sytem excites the residual modes less, but a high frequency mode is lightly damped.

Figure 9-19 shows the LOS and transient response of the colocated and noncolocated designs for the perturbed model. Both designs meet specification, but the noncolocated system has the better performance. The noncolocated system's transient response settles within the required band in about 9.5 seconds compared to about 20 seconds for the colocated system. Hence, as predicted by the analysis, the noncolocated design is slightly more robust than the colocated system.

Figure 9-20 shows the response of the residual modes and the control effort of the perturbed tetrahedron's model. It can be seen that the control effort in the case of the noncolocated controller is lower than in the case of the colocated system. However, the colocated system's residual modes are better damped than those of the noncolocated controller. This was anticipated by the analysis which showed more uniform damping at high frequencies.

A sensitivity study was performed to determine if an increase of the controller's gains causes a deterioration in system's performance. It was found that the nominal controller's gain, 4.I, can be increased to about 12.I without deterioration of the performance. Actually, for certain higher values of controller's gain, the system's performance improves. Figure 9-21 compares the LOS motions of the nominal tetrahedron

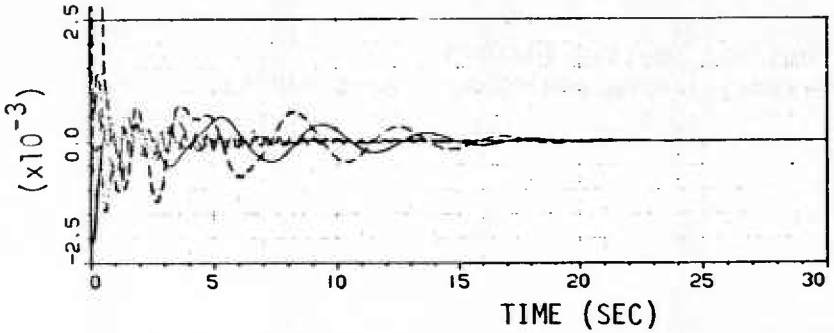

(a) COLOCATED DESIGN: RESIDUAL MODES TRANSIENT RESPONSE

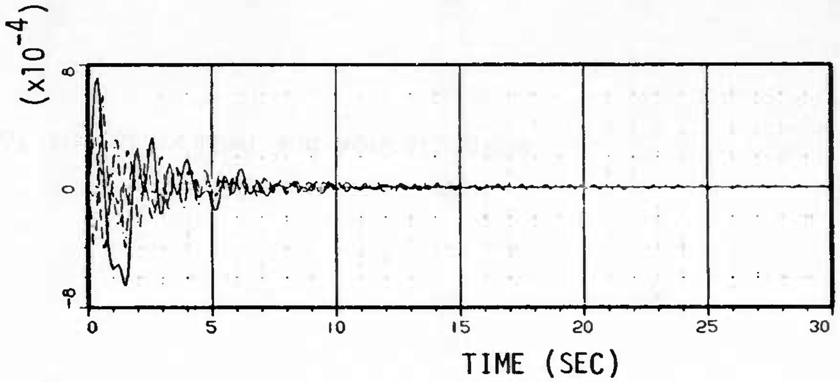

(c) NONCOLOCATED DESIGN: RESIDUAL MODES TRANSIENT RESPONSE

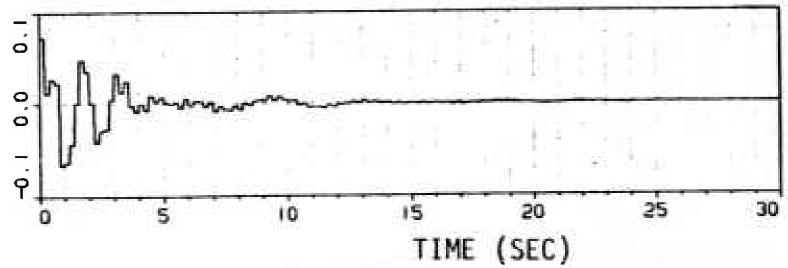

(b) COLOCATED DESIGN: CONTROL EFFORT AT LEG #1

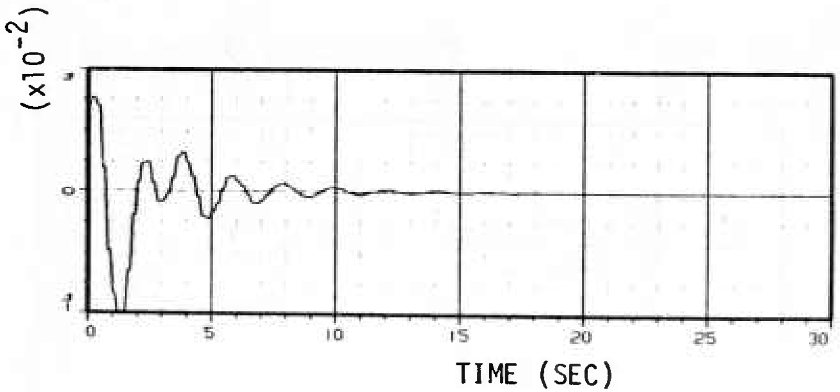

(d) NONCOLOCATED DESIGN: CONTROL EFFORT AT LEG #1

Figure 9-18. Nominal Model: Residual Modes' Response and Control Effort for Colocated and Noncolocated Designs

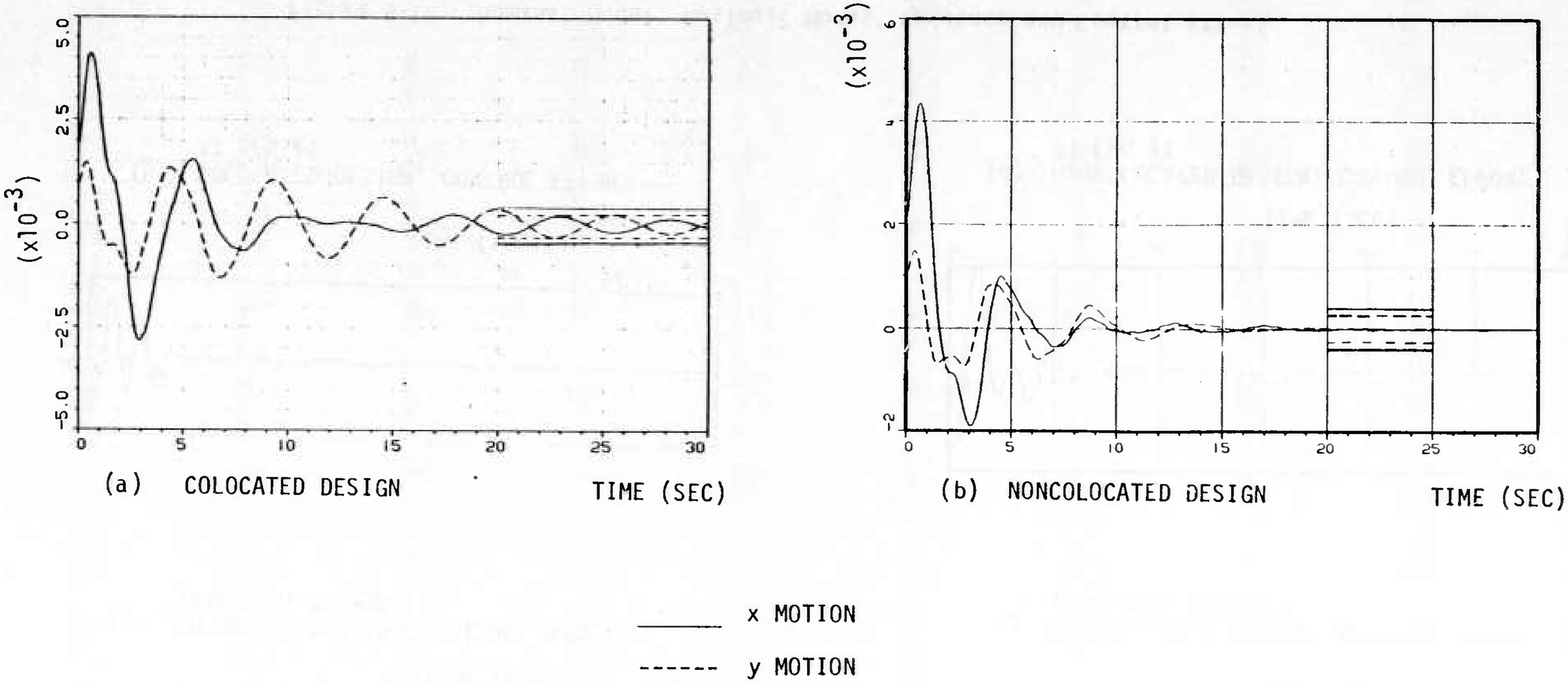

Figure 9-19. Perturbed Model: Transient Response of the Colocated and Noncolocated Control Systems for the Tetrahedron

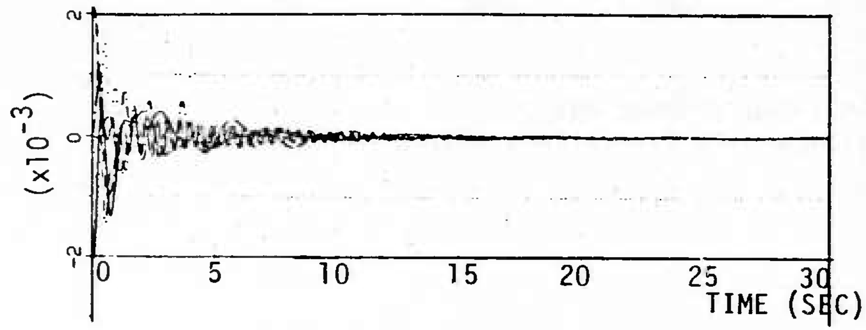

(a) COLOCATED DESIGN: RESIDUAL MODES' TRANSIENT RESPONSE

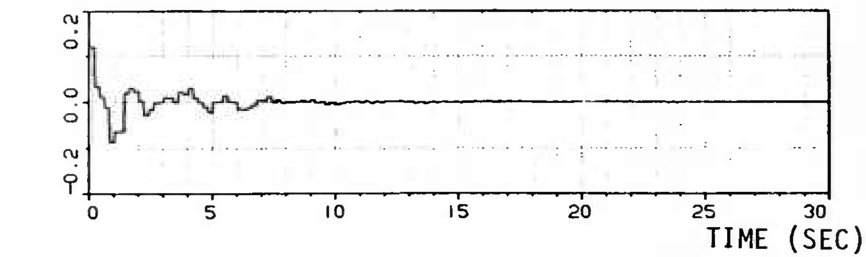

(b) COLOCATED DESIGN: CONTROL EFFORT AT LEG #1

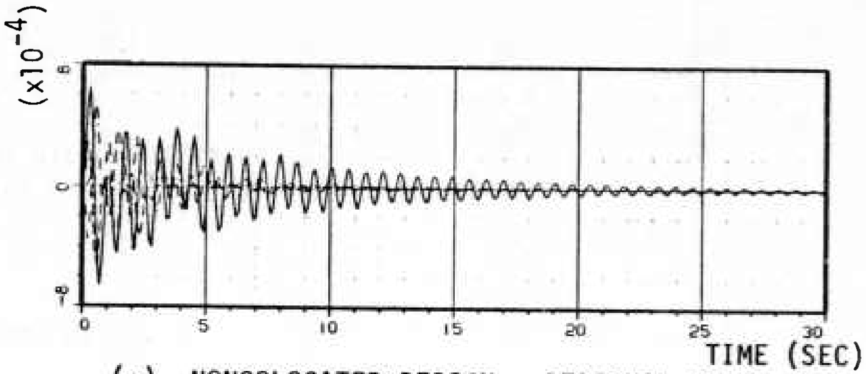

(c) NONCOLOCATED DESIGN: RESIDUAL MODES TRANSIENT RESPONSE

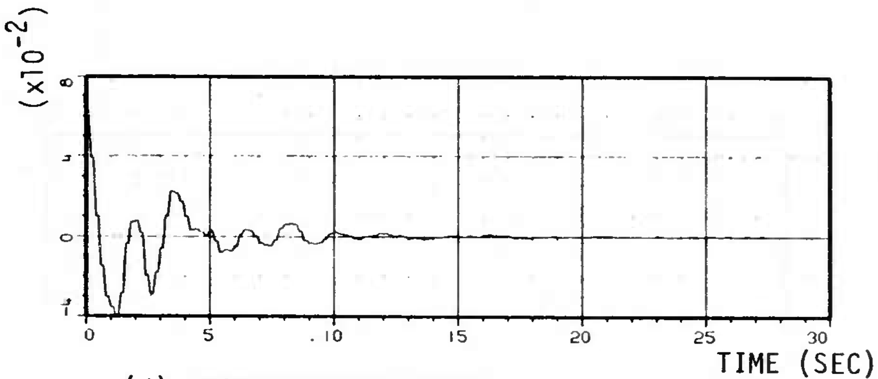

(d) NONCOLOCATED DESIGN: CONTROL EFFORT AT LEG #1

Figure 9-20. Perturbed Model: Residual Modes' Response and Control Effort for Colocated and Noncolocated Designs

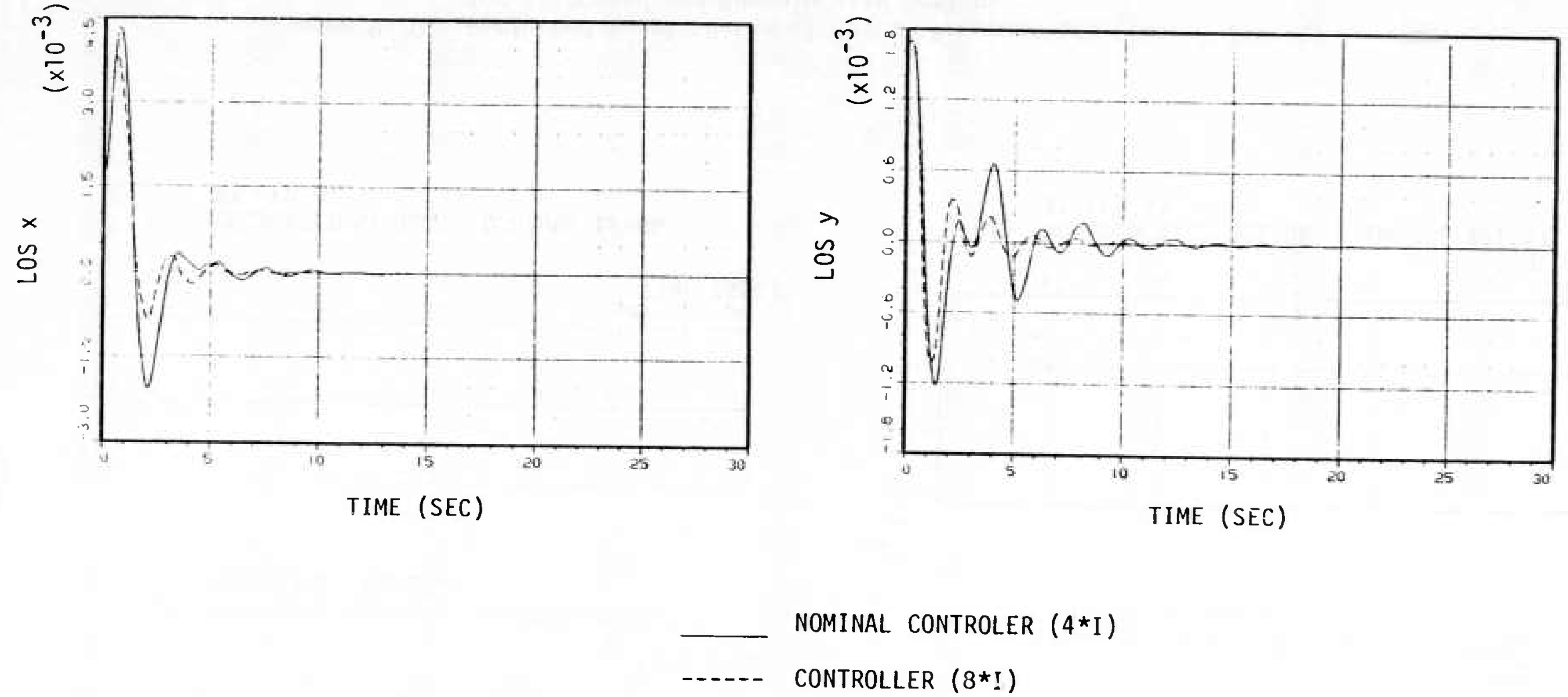

Figure 9-21. Sensitivity to Controller Gain Variation: Transient Response of the Nominal Model with Two Different Gains

model, with the nominal controller 4·I, and with controller 8·I. It can be seen that the performance of the system with the higher gain is better and the LOS transient motion reaches the required band in less than 3 seconds.

9.3 Conclusions of the Design Examples Study

Section 9 described the application of the positivity theory and multivariable frequency domain techniques to the design of noncolocated control systems. The study showed that the developed squaring down procedure gives good results and can be incorporated into the positivity/frequency domain methodology.

Comparison of colocated and noncolocated systems led to the following conclusions:

(i) The noncolocated design provides better damping of the important modes, i.e. modes which influence the performance the most.

(ii) The colocated design provides more uniform damping of the modes and therefore, modes not included in the design model are better damped.

(iii) The colocated and noncolocated designs for the examples presented have similar robustness properties with a slight advantage to the noncolocated design. However, this is not a general conclusion and is specific to the examples at hand.

(iv) The computational requirements for both systems are comparable.

REFERENCES

[1] "NASA Space Systems Technology Model," Volumes I-III, NASA OAST, May 1980

[2] This reference will be made available to qualified military and government agencies on request from RADC (OCSE), Griffiss AFB NY 13441.

[3] "NASA Literature Search Number 45835: Space Shuttle Payloads," requested by R. J. Benhabib, April 30, 1981. Also, "Supplemental Material 1978-1981" and "Supplemental Material K-Series"

[4] "Advanced System Concepts and Their Orbital Support Needs," Aerospace Corporation, 1976

[5] "Space Resources and Space Settlements," NASA SP-428, 1979

[6] "Space Horizons," JPL, 1979

[7] "Post LANDSAT-D, Advanced Concept Evaluation," General Electric, 1978

[8] "Coordinate Systems for the Space Shuttle Program," NASA JSC, TMX-58153, October 1974

[9] "Space Shuttle Orbiter, Orbital Flight Test Level C; Functional Subsystem Software Requirements, Guidance Navigation, and Control Part C; Flight Control, Orbit 2," Rockwell International, SD 76-SH-0009A, 15 April 1979

[10] "Space Transportation System" Reimbursement Guide," NASA, JSC-11802, May 1980

[11] Benhabib, Iwens and Jackson, "Stability of Distributed Control for Large Flexible Structures Using Positivity Concepts," J. Guidance and Control, Volume 4, No. 5, October 1981

[12] Iwens, R. P., "Input-Output Stability of Continuous and Discrete Time Nonlinear Systems," Ph.D. Dissertation, University of California, Berkeley, California, March 1967

[13] Zames, G., "On the Input-Output Stability of Time Varying Nonlinear Systems - Part I ...," IEEE AC-11, No. 2, April 1966

[14] Iwens, Benhabib and Jackson, "A Unified Approach to the Design of Large Space Structure Control Systems," 1980 JACC, San Francisco, California, August 1980

REFERENCES (Continued)

[15] Mac Farlane, et. al., "Complex Variable Methods for Multivariable Feedback Systems Analysis and Design," in Alternatives for Linear Multivariable Control, NEC, Illinois, 1978

[16] Stevens, R. K., "A Generalization of the Nyquist Stability Criterion," IEEE AC-26, June 1981

[17] Stevens, R. K., "A Nyquist Criterion for Distributed Systems Subject to a One Parameter Family of Feedback Compensators," IEEE AC-27, June 1982

[18] Safanov and Athens, "On Stability Theory," IEEE Conference on Decision and Control, San Diego, California, January 1979

[19] "ACOSS Eight, Phase II - TRW," RADC-TR-81-242, September 1981

[20] "Payload/Cargo Integration Schedules/Planning Guidelines," NASA JSC, 1981

[21] "Study of Electrical and Chemical Propulsion Systems for Auxiliary Propulsion of Large Space Systems, Final Report," Boeing Aerospace, March 1981

[22] Lehtomaki, N. A., Castanon, D., Levy, B., Stein, G., Sandell Jr, N. R., and Athans, M., "Robustness Tests Utilizing the Structure of Modelling Error," IEEE Conference on Decision and Control, 1981, San Diego

[23] Benhabib, R. J. and Iwens, R. P., "Robust Control of High Order Systems Using Positivity," Workshop on the Application of Distributed System Theory to the Control of Large Space Structures, JPL, July 1982

[24] Strunce, R., "Description of Draper Example Structure Model," Charles Stark Draper Laboratories

APPENDIX A. TEST AND FLIGHT EXPERIMENT PROGRAM PLAN

The objectives of the test plan are to determine how and in what sequence the experiments are to be conducted. This includes determination of how the experiments are to be controlled and what kind of on-orbit operations are required. The test plan also addresses the testing and correlation of analytical models with the post-flight experimental data.

A.1 Baseline Experiment Sequence

The plan below describes how and in what sequence the experiments are to be executed. Referring to the timeline in Figure A-1, it will take approximately two hours to sequence through the experiments, including triply redundant data gathering.

POC Structure Dynamical Interaction with Orbiter-180 Seconds

Function:
1) Validate analytical method used to model the dynamic interaction between the POC structure and the shuttle.
2) Validate the shuttle environment model.

Operations:
1) Monitor the temperature of structure, the shuttle DAP, the inertial/base sensor, and control system sensors.
2) Record POC structural motion.
3) Stimulate structure with pulses; stimulate with frequency sweep; stimulate with disturbances; threshold against ground; record POC structural motion, base sensor output and DAP commands.
4) Apply maximum likelihood modal parameter estimation technique and crosscheck with FFT.

Optical Element Alignment-420 Seconds

Function:
1) Center and DC calibrate ranging sensors.
2) Establish "Disturbance Free" behavior.

Operations:
1) Use six mirror alignment actuators to center laser diodes in the FOV of the SAMS and CCD sensor.
2) Monitor the temperature of the structure, the Shuttle DAP and the inertial/base sensors.

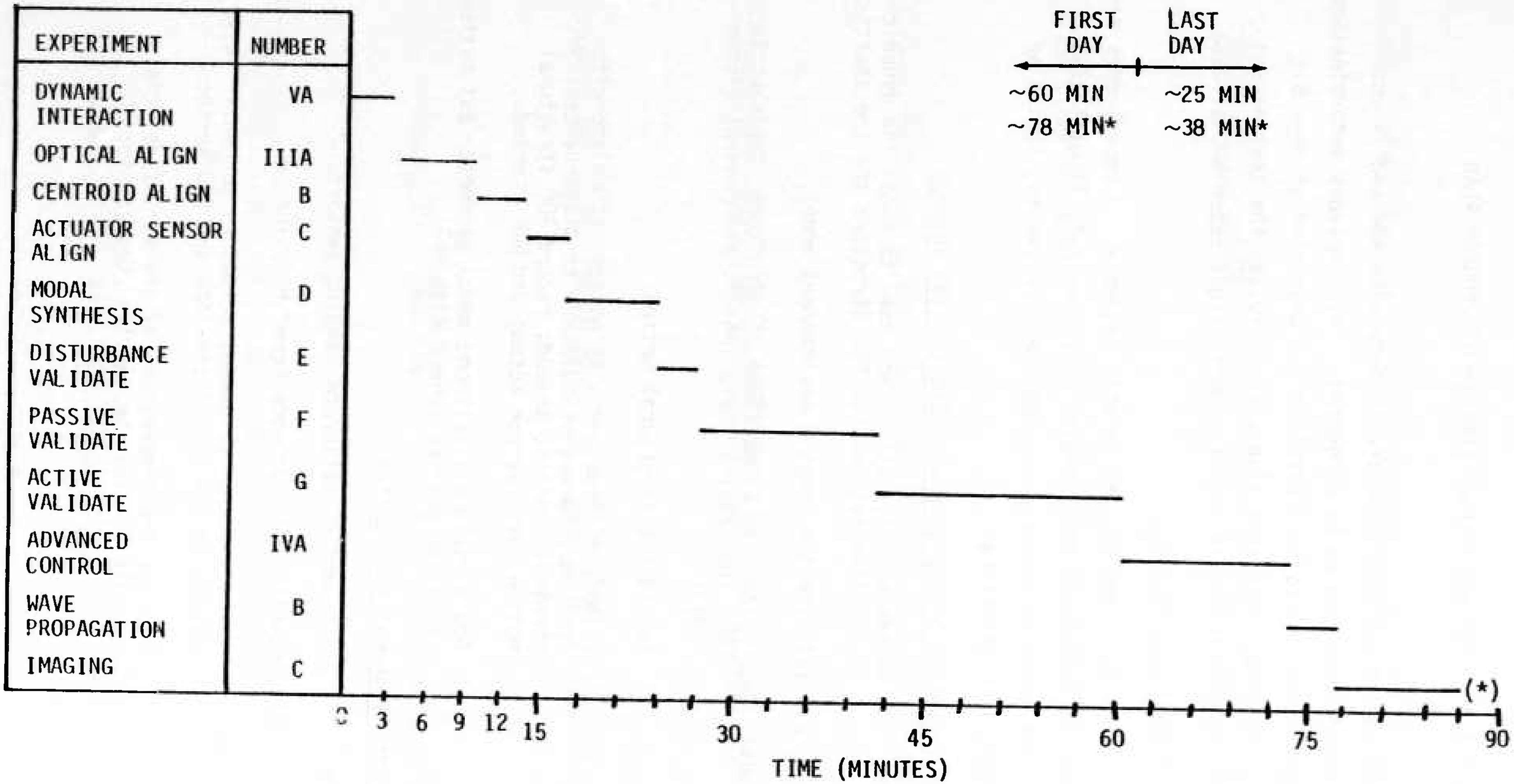

* Total time is 85.3 minutes, but we added a 30% pad to get 111 minutes.

Figure A-1. Baseline Experiment Sequence Timeline

3) Individually perturb each mirror alignment actuator through 10 DC levels. Low pass and time average to establish linearity behavior. Threshold against ground values.

4) Observe behavior of mirrors and structure as Shuttle limit cycles (3 cycles).

LOS Centroid Alignment-260 Seconds

Function: 1) Calibrate image motion sensing system.

2) Calibrate optical element motion to LOS motion transformation.

Operation: 1) Acquire bright star and center by translating CCD sensor.

2) Monitor the temperature of the structure, the shuttle DAP and the inertial/base sensors.

3) Individually perturb each optical alignment actuator through 6 DC levels. Low pass and time average centroid motion. Threshold against ground values.

Structural Control Actuator and Sensor Alignment-180 Seconds

Function: Calibrate actuator to sensor transformation

Operations: 1) Fix on star acquired earlier.

2) Monitor the temperature of the structure, the Shuttle DAP, the inertial/base sensors, LOS motion and control sensor signals.

3) Individually step each structural control actuator through 6 DC levels. Low pass and time average all sensor signals. Subtract Shuttle motion to get DC gains. Threshold against ground values.

Modal Synthesis Experiment-210 Seconds

Function: Validate model synthesis as a technique for modeling LSS from smaller substructures.

Operations: 1) Monitor the temperature of the structure, the Shuttle DAP, the inertial/base sensors, mirror motion and control system sensors.

2) Stimulate structure with pulses and store response for ground processing.

3) Stimulate structure with sinusoidal frequency sweep and mark peaks. Individually stimulate with sinusoids at critical frequencies. Store free-vibration decay for ground processing.

4) Apply maximum likelihood (ML) modal parameter estimation technique and crosscheck against free-vibration decay. Apply ML physical parameter estimation and compare with assumed physical values.

<u>Disturbance Recording Validation-180 Seconds</u>

Function: Verify that disturbance "Recording" is representative of expected disturbances.

Operations:

1) Monitor the temperature of the structure, the shuttle DAP, the inertial/base sensors, and control system sensors.

2) Turn on each disturbance actuator (shaker) individually. Cross-correlate with ground value and threshold.

<u>Lumped Passive Element Modeling and Control Experiment-960 Seconds</u>

Function: Validate analytical methods used to model structures with integrated, lumped, passive elements.

Operations:

1) Fix on star acquired earlier.

2) Monitor the temperature of the structure, the Shuttle DAP motion, the inertial/base sensors, control system sensors, and LOS sensor.

3) Turn on disturbances and record response.

4) Individually unlock each passive isolator, then all simultaneously. Record response.

5) Lock all isolators.

6) Turn off disturbances.

7) Unlock all passive elements. Stimulate with pulse. Stimulate with sinusoidal frequency sweep and mark peaks. Stimulate with sinusoids at critical modes, record free vibration decay and threshold against ground values.

8) Turn on disturbances and record data.

9) Unlock all passive elements and record disturbance response. Threshold against ground values.

10) Same as step 4 in Modal Synthesis experiment.

Active Structural Control System Modeling Experiment-960 Seconds

Function: Validate analytical methods used to model active control

Operations:

1) Fix on star acquired earlier.

2) Monitor the temperature of structure, the Shuttle DAP, the inertial/base sensors, control system sensors, and LOS sensor,

3) Individually turn on insensitive inertial and relative control systems. For each one: measure diagonal gain and phase margin, and threshold against ground values; stimulate with pulse; stimulate with sinusoidal frequency sweep and mark peaks; stimulate with sinusoids at critical modes, record free-vibration decay and threshold against ground values.

4) Turn on both inertial and relative control systems. Repeat procedure in step 3.

5) Turn on disturbances.

6) Individually turn on inertial and relative control system. Measure LOS error and figure.

7) Turn on both inertial and relative control systems. Measure LOS and figure.

8) Same as step 4 in Modal Synthesis experiment.

Advanced Control Law Demonstration-780 Seconds

Function: Determine stability and performance limitations of the two most promising control laws.

Operations:

1) Calibrate SAMS and LOS motion sensors.

2) Acquire bright star and center unto CCD array.

3) Monitor the temperature of structure, the Shuttle DAP, the inertial/base sensor, control system sensors, and LOS sensor.

4) For each of two control laws: measure diagonal gain and phase margin, and threshold against ground values; stimulate with pulse; stimulate with sinusoidal frequency sweep and mark peaks; stimulate with sinusoids at critical modes, record free vibration decay and threshold against ground values.

5) Turn on disturbances.

6) Record LOS and mirror motions and threshold against ground values.

7) Same as step 4 in Modal Synthesis experiment.

Have Propagation Experiment-180 Seconds

Function: Determine performance of high bandwidth autoalignment system.

Operations:
1) Fix on star acquired earlier.

2) Monitor the temperature of the structure, the Shuttle DAP, inertial/base sensors, control system sensors and LOS sensor.

3) Turn on high bandwidth autoalignment system and record nominal figure and LOS motion. Threshold against ground values.

4) Turn on disturbances and record figure and LOS motion. Threshold against ground values.

Imaging Experiment-600 Seconds

Function: Establish performance limitations and relative merits of two competing technologies.

Operations:
1) Point telescope at space.

2) Monitor the temperature of structure, the Shuttle DAP, the inertial/base sensor, control system sensors and LOS sensor.

3) For each of two competing technologies: store image for one Shuttle limit cycle; turn on disturbances; and store image for one Shuttle limit cycle.

4) Maneuver Shuttle to point telescope at earth.

5) Repeat step 3.

The baselined experiment sequence and timeline will not require any unusual time slot requirements as the total experiment lasts 111 minutes. Seventy-eight continuous minutes one day and 33 continuous minutes three days later. The primary reason for the break is to allow for ground validation of structural modeling, low gain feedback behavior and predicted

subsystem performance prior to conducting the high technology demonstration. The approach ensures that all the bugs are out and that the demonstration is successful the first time.

A.2 Control of the Experiments

The baseline test structure fits comfortably in the Shuttle cargo bay and its dynamic interaction with the Orbiter is immeasurable to the Shuttle attitude control system. For this reason the baseline design also does not require any deployment/erection activities, extra vehicular activity (EVA), use of the remote manipulator arm, restowage, nor an emergency jettison procedure. The role of the astronauts during the experiments will therefore be relatively minor: the structure fits into the shuttle cargo bay so it needs no deployment assistance nor astronaut extra vehicular activity; the CDHS system baselined has an automated experiment sequencer to prepare, execute, monitor, and step through the experiments; the structure's caging mechanism is electromechanical and is controlled by the sequencer; and the subsystems failure detection and shutoff, data validation, and transmission of data are all accounted for in the automated CDHS architecture. The only roles, therefore, that one can currently baseline for the astronauts are to monitor the execution of the experiments as they are cycled; to provide real-time data entry/modification if failure is detected; and to point the shuttle cargo bay away and towards the earth during the imaging experiments.

A.3 Concept for Correlating Analytical Models with Test Data

One of the reasons for performing the experiments is to learn how to model structures more accurately. There are two immediate goals in mind. One is to determine the relationship between ground and on-orbit structural behavior. The second is to learn how to combine the dynamics of components to create the dynamics of the total system. The questions that must be answered in order to do this have both a functional and a parametric nature:

Does the open-loop composed system behave as predicted by the modal synthesis procedure?

Is the linear feedback model (almost always assumed) a reasonably good predictor of closed-loop system behavior? Or, does the feedback enter in a more complicated manner?

For a given system model functional, does the parameter which creates the best data fit equal the physical values in the sub-components?

It is necessary to determine that the answer to the posed questions is affirmative, even for micron and nanometer motion.

Figure A-2 conceptualizes a possible approach for finding the answers. The idea is to validate the modal synthesis procedure by comparing its form with the global FEM model. Both models are then validated by showing that the parameters providing the best data fit are realistic physical values. The analytical models will be constructed from the material properties of the components, the actuator and sensor dynamics, and the control laws (things one can model well). The model construction/functional is initially assumed to be linear then adjusted along with the parameterization until both the model predictions and the parameters match the true values.

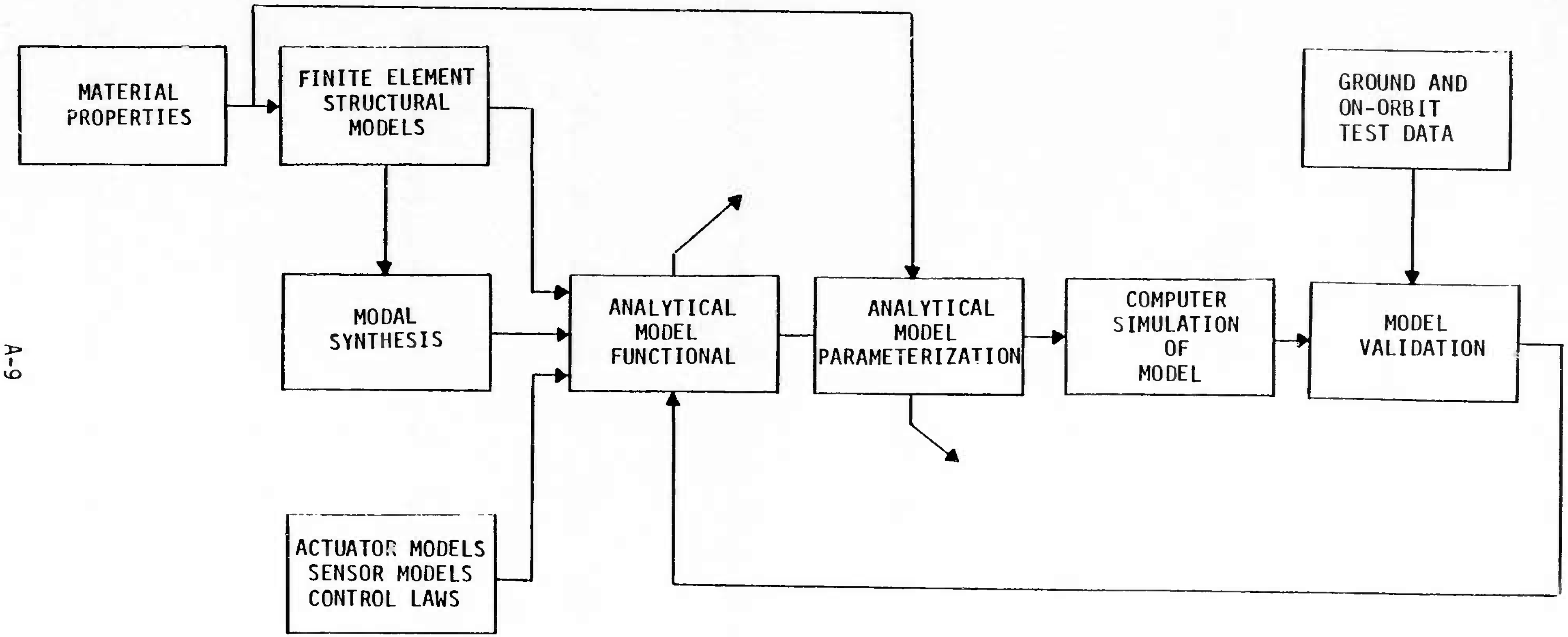

Figure A-2. Concept for Correlating Analytical Models with Test Data

APPENDIX B. EXPERIMENT MILESTONES, SCHEDULE AND COST

The final objective of the PREMOD contract was to outline the milestones, schedule and rough-order-of-magnitude (ROM) cost estimates required for the government to accomplish experiment objectives.

B.1 Milestones and Schedule

Figure B-1 summarizes the experiment milestones and schedule. The total program is baselined to last four years. The first year will be spent primarily on subsystem and component design work, planning subsystem tests and integration, and on specifying the experiment tests and test conditions. The second year will be used to build the hardware, program and debug software, test and integrate the subsystem components and on planning the system and Shuttle integration and test. The first half of the third year will be used to complete the integration of the ground experiment and the second half will be used to execute and process the ground experiments. The fourth year will be spent integrating the experiment into the Shuttle, with a planned launch and on-orbit experiment execution following in the third quarter. The on-orbit experiment data processing is planned for the fourth quarter of the fourth year.

B.2 ROM Costs

The rough-order-of-magnitude cost estimate for the total program is shown in Table B-1.

Table B-1. ROM Cost Estimate

COST ITEM	SIMPLIFIED GROUND EXPERIMENT ($K IN 1982)	COMPLETE GROUND AND ON-ORBIT EXPERIMENT ($K IN 1982)
TOTAL FOR HARDWARE	1514	9024
TOTAL FOR SHUTTLE USE	-	14,834
TOTAL FOR LABOR	3750	9000
PROFIT (15%)	790	4929
MARGIN FOR ERROR (15%)	908	5668
TOTAL	$6962K	$43,455K

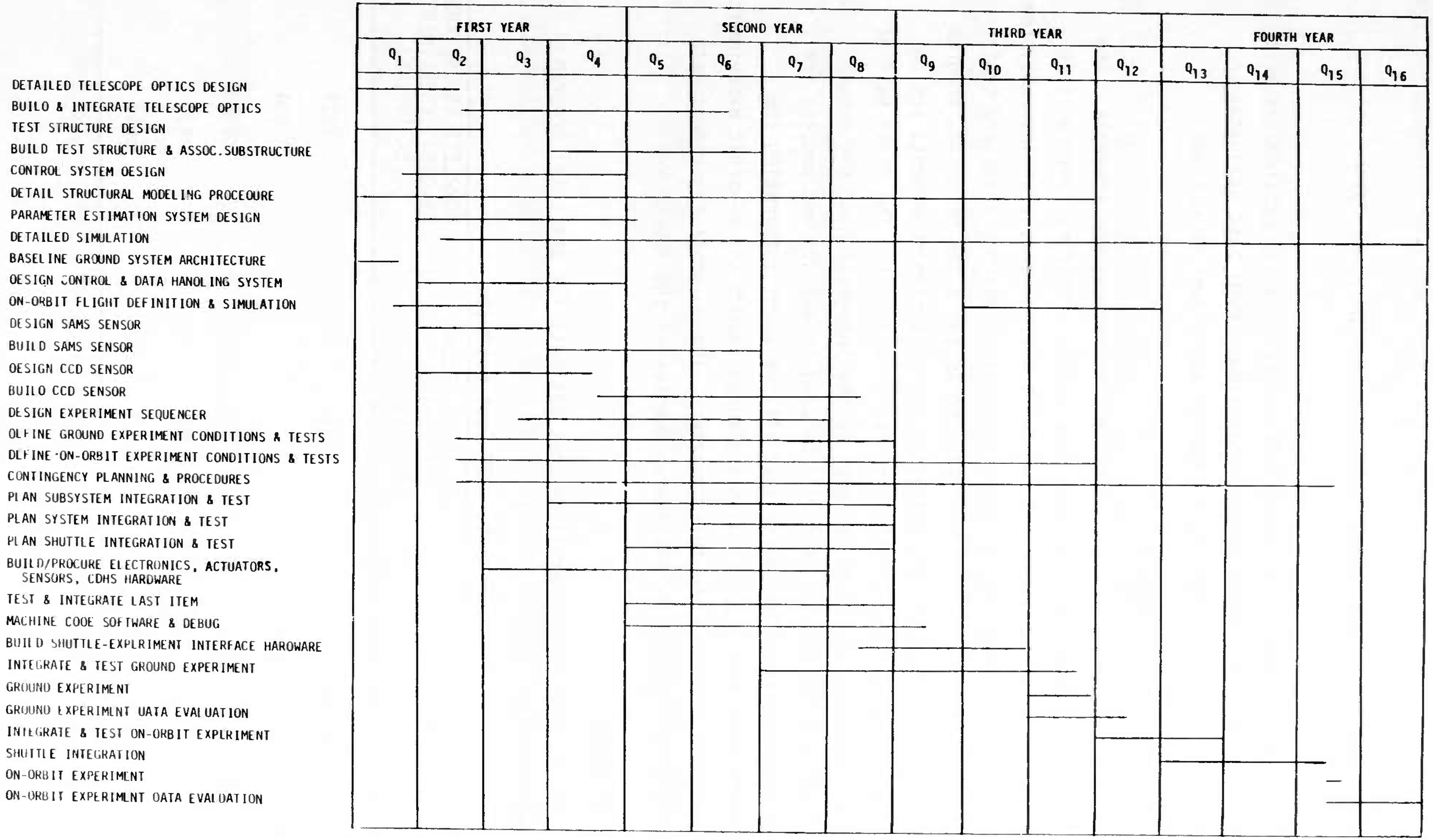

Figure B-1. Experiment Milestones and Schedule

The cost breakdown for the total experiment is shown in the Table B-2 and is approximately $9M for hardware, $14.8M for Shuttle costs, $9M for labor costs, $4.9M profit, and $5.7M (15%) for error margin. The total cost is $43.5M. The Shuttle cost estimate is detailed further in Table B-3. The driving cost ($10.3M) is primarily due to the cost of standard services for a complete pallet flight, (one user on the pallet, all other Shuttle facilities are shared). The key assumptions used in making the estimate are the accuracy of the "Civilian Reimbursement Guidelines" document dated May 1980 [10] and the assumed 10% inflation factor. All estimates quoted are in 1982 dollars. In reality this experiment is a DOD flight, having a lower negotiated cost with NASA than other government users. Therefore, the real cost of flight may be slightly lower. The actual figures were being negotiated, however, by DOD and NASA at the time the estimate was made.

Table B-2. ROM Cost Estimate Breakdown

COST ITEM	SIMPLIFIED GROUND EXPERIMENT ($K in 1982)	COMPLETE GROUND & ON-ORBIT EXPERIMENT ($K in 1982)
HARDWARE		
SAM Sensor	410	410
CCD Sensor	--	2510
Experiment Monitor	90	90
CDHS System	155	155
Control System	291	291
Identification System	123	123
Test Structure & Supporting Hardware	115	115
Ground Test Equipment Monitor	330	330
Primary Mirror & Figure Control	--	4500
Secondary Mirror & Assoc. Optics	--	500
TOTAL FOR HARDWARE	$1514K	$9024K
SHUTTLE COSTS*		
Standard Fees		10247
Element Use Fees		1789
Optional Services		2798
TOTAL FOR SHUTTLE USE	--	$14834K
LABOR COSTS	$3750	9000
SUBTOTAL	$5264K	$32858K
PROFIT (15%)	790	4929
MARGIN FOR ERROR (15%)	908	5668
TOTAL	$6962K	$43455K

* Assumes complete pallet flight, civilian reimbursement guidelines dated May 1980, 10% inflation factor.

Table B-3. Breakdown of Shuttle Cost Estimate*

ITEM		COST $M 1975	COST $M, 1982 10% INFLATION/YR
STANDARD SERVICES - LOAD FACTOR = 0.23			
Shuttle Operations		4.14	
Shuttle Use Fee		0.99	
Facilities and Equipment Use Fee		0.06	
Payload Specialist		0.07	
TOTAL COST OF STANDARD SERVICES		$5.26M	$10.3M
ELEMENT SERVICES			
Operations - Complete Pallet		0.89	
Element Use Fee - Complete Pallet		0.03	
TOTAL COST OF ELEMENT SERVICES		$0.92M	$1.8M
OPTIONAL SERVICES			
Vandenberg Flight			
Unique Integration Requirements			
Additional Resources			
Special Access to Payload Operation			
Special Software in Command & Data Management Subsystem			
Data Transmission Outside of JSC Payload Control Center	Est.	0.75	
Transmission of Spacelab Data Not Contained in the STS Operational Instrumentation Telemetry Link			
Payload Specialist and Training		0.1	
Thermal Loads Analysis		0.15	
Structural Loads Analysis		0.08	
Additional Days of STS Support (1 Day)		0.1	
Payload Operations Control Center in Most Mode - Est		0.1	
Optional Transportation Services - Est		0.02	
Optional Security Services - Est		0.02	
Optional Photographic Services - Est		0.02	
Guaranteed Launch Date		0.1	
TOTAL COST OF OPTIONAL SERVICES		$1.44M	$2.8M
TOTAL SHUTTLE LAUNCH COST			$14.8M

* "Space Transportation System Reimbursement Guide," May 1980 [10].

APPENDIX C. A MODEL OF THE SHUTTLE DIGITAL AUTOPILOT (DAP)

This appendix briefly describes the DAP model implemented in the dynamic interaction study. The model was based on the description given in [9] with up-to-date parameters obtained from Johnson Space Center. In the following, explanation of the various model subroutines is given and some of the logic is explained. For more detailed description see [9].

C.1 Phase Plane Logic

The phase plane logic implemented in the Shuttle Orbiter DAP is based on a time optimal control law. It assumes low coupling between the axes and, hence, the dynamics of the system around each axis can be approximated as double integrator. The time optimal feedback solution for this problem is well known. However, the optimal control law cannot be implemented precisely because of the following imperfections: attitude and rate measurement errors, measurement disturbances and noise, and quantization errors - both quantization of the jet firing time and the quantization of the attitude and rate measurement in the A/D converter from IMU. Hence, implementation of the optimal control law would lead to continuous limit cycle and to fuel waste. To avoid these problems, the phase plane logic was designed to hit the smallest limit cycle in one pass and minimize fuel waste. Moreover, the logic was further developed to take into account the coupling between the axes when the system is in the hysteresis region.

Figure C-1 shows the various regions in the phase plane of the Orbiter's axis. This logic is implemented for each control axis, with the three commands forming the command control vector. The control vector is then fed into the jet selection logic subroutine to choose the jets which generate the control torque.

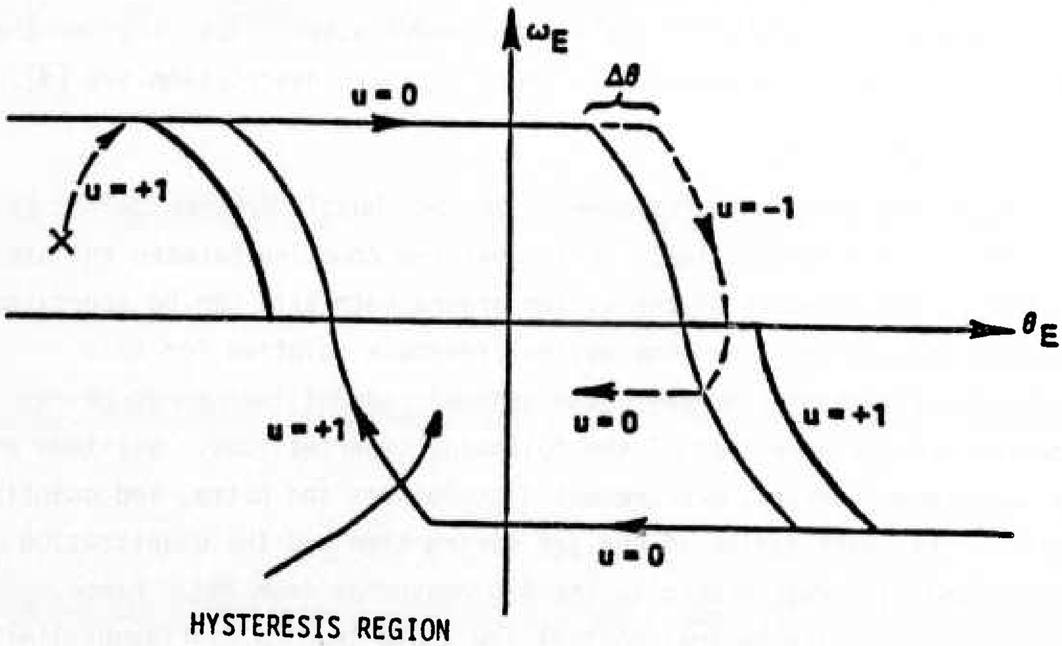

Figure C-1. Phase Plane Logic Regions

C.2 Vernier Jet Selection Logic

Since the Shuttle was assumed to be in its normal operation mode, only the vernier jet selection logic was simulated. The vernier jet selection logic obtains the commanded command vector, $-A_R$, from the phase plane logic module and computes a dot product, D_j, of A_R with the angular increment vector a_j of thruster j for j=1,....,6. See Figure C-2. The thruster with maximum D_j is designated D_1 and is fired. If the next largest D_j, call it D_2, is greater than $T_1 \cdot D_1$ this jet is fired. The next largest D_j, say D_3, is fired if $D_3 > T_2 . D_1$. Hence, a maximum of three vernier thrusters fire at one time. It should also be noted that when the Shuttle is in vernier operation mode, the element of commanded vector A_R can be different from $\pm$ 1.

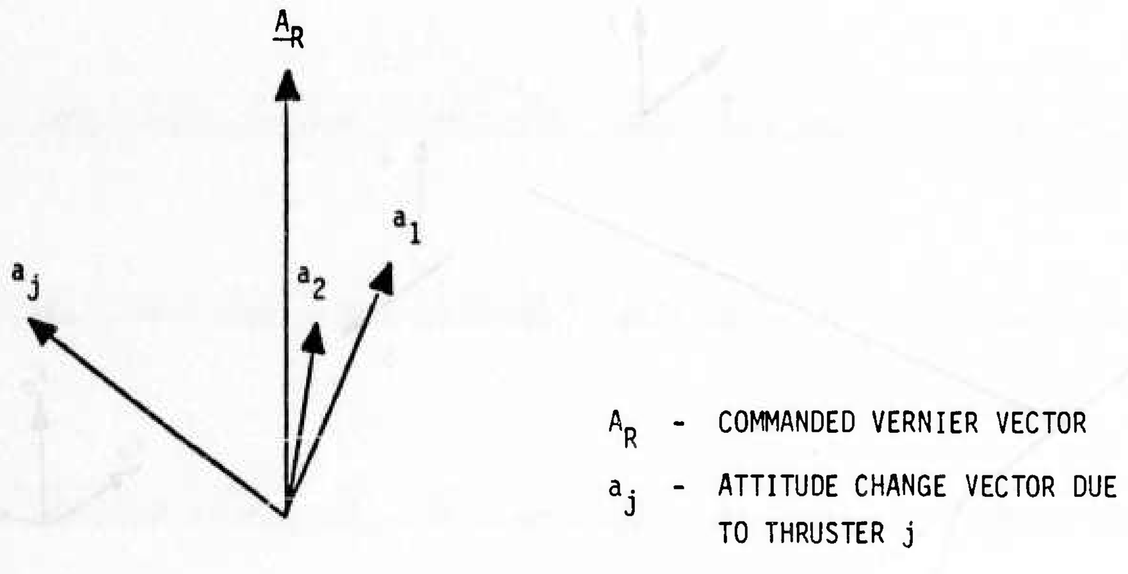

Figure C-2. A Command Vector and Angular Increment Directions

Table C-1 summarizes the features of the vernier thrusters. The firing directions of various vernier thrusters are shown in Figure C-3. The Orbiter possesses six vernier thrusters which produce a thrust of ~24 lbf each. Two thrusters are located in the front and generate thrust in the xy plane, forming an angle of 45° with the x-axis. The rear thrusters consist of two pairs. One pair fires in the +z direction and the other in the $\pm$y direction. The vernier thrusters are not designed to produce forces in -z or x directions. Thus, any altitude change or drag makeup has to be performed using the primary thrusters.

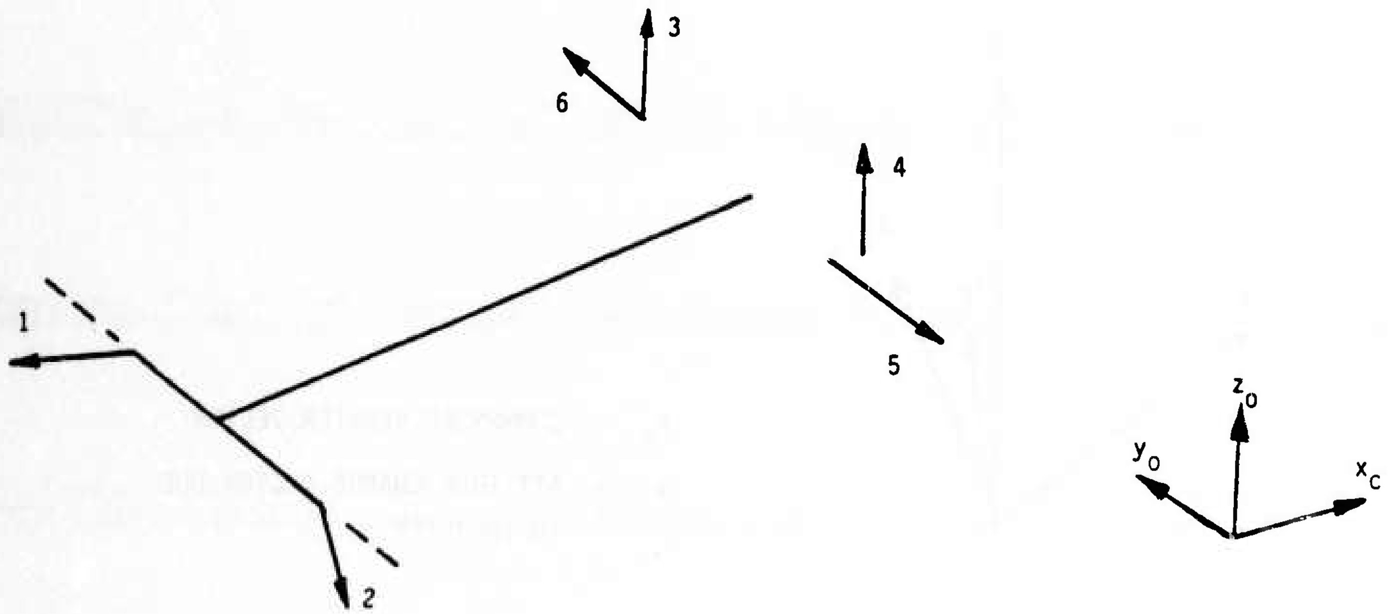

Figure C-3. Vernier Thrusters Firing Directions

Table C-1. Vernier Jet Locations and Thrust Directions

SYMBOL	ARRAY NUMBER	NO. IN PROGRAM	LOCATION* (INCHES)			FORCE (LB)			ANGULAR INCREMENTS ($\times 10^{-4}$ RAD/SEC)		
			x_o	y_o	z_o	F_x	F_y	F_z	$\dot{\theta}_x$	$\dot{\theta}_y$	$\dot{\theta}_z$
F5R	39	1	324.35	59.70	350.12	0.8	-17	17.6	3.52	9.28	8.66
F5L	40	2	324.35	-59.70	350.12	0.8	17	17.6	-3.52	9.28	8.66
L5D	44	3	1565.00	-118.00	455.44	0	0	24.0	-14.68	-7.54	0.
R5D	43	4	1565.00	118.00	455.44	0	0	24.0	14.68	-7.54	0.
L5L	42	5	1565.00	-149.87	459.00	0	24	0.6	-11.29	-0.19	7.29
R5R	41	6	1565.00	149.87	459.00	0	-24	0.6	11.29	0.19	-7.29

*IN THE REFERENCE COORDINATE SYSTEM.

C.3 State Estimator

The state estimator consists of two parallel Kalman-type filters, one for acceleration estimation and one for rate estimation. The S-plane formulation for the acceleration estimate is

$$\hat{\alpha}(S) = \frac{\frac{1}{T_M^2}\left[\frac{2K_{\alpha a}}{2-K_{\omega a}}\right]\alpha(S)}{S^2 + \left[\frac{2K_{\omega a} - K_{\alpha a}}{(2-K_{\omega a})T_M}\right] S + \frac{1}{T_M^2}\left[\frac{2K_{\alpha a}}{2-K_{\omega a}}\right]}$$

where

T_M = measurement update

$K_{\alpha a}$ = acceleration gain

$K_{\omega a}$ = rate gain

The S-plane formulation for the rate estimate is

$$\hat{\omega}(S) = \frac{\frac{K_{\omega r}}{K_o T_M^2}\omega(S)}{S^2 + \frac{K_{\theta r}}{K_o T_M} S + \frac{K_{\omega r}}{K_o T_M^2}} + \frac{\left[S + \frac{K_{\theta r}}{K_o T_M}\right]\hat{\alpha}(S)}{S^2 + \frac{K_{\theta r}}{K_o T_M} S + \frac{K_{\omega r}}{K_o T_M^2}}$$

where

T_M = measurement update (PART1-FILTER) period = TMEAS

$K_{\theta r}$ = attitude gain

$K_{\omega r}$ = rate gain

$K_o = 1 - \frac{K_{\theta r}}{2} - \frac{K_{\omega r}}{4}$

Each of two filters is divided into a measurement incorporation section and an extrapolation section. Measurement incorporation for both filters is performed at the attitude measurement update rate (6.25 Hz) by FILTER1.

Extrapolation for both filters is performed at 12.5 Hz by FILTER2. In addition, FILTER1 provides a 25-Hz extrapolation of the measured-attitude variable ATTITUDE. This variable is reset to a pure measurement value by FILTER1 at 6.25 Hz.

APPENDIX D

Discrete-Time Large Space Structure Control System Design Using Positivity

by

R. J. Benhabib

Presented at the 20th IEEE Conference on Decision and Control, San Diego, California, December 1981.

DISCRETE LARGE SPACE STRUCTURE CONTROL SYSTEM DESIGN USING POSITIVITY

R. J. Benhabib

TRW Defense and Space Systems Group
Redondo Beach, California 90278

Abstract

Because of the cost and flexibility advantages offered by microprocessors, any control system to be considered for Large Space Structures (LSS) will likely be digital. This short paper proposes a combined positivity and W-plane, frequency domain design procedure for synthesizing the control of these structures. Positivity theory is used to ensure the stability and stability robustness of digital designs, inclusive of modal truncation and aliasing. Shaping the characteristic gains in an α-shifted W-plane synthesizes the required performance. The combined approach has the advantage that it leads directly to robust and implementable low-order controllers. A design example using an LSS like structure concludes the paper.

I. Introduction

Of the existing control problems, the active control of large space structures (LSS) perhaps most clearly demonstrates the difficulties involved in designing for stability and performance robustness while restricting oneself to using only control laws of implementable complexity. The LSS "plant" is unique in the sense that it exhibits high (theoretically infinite) state dimensionality, very low damping, only poor "plant" models are available, and the disturbance set is widely varied.

Briefly, the LSS's dynamics centered about the "rigid" body motion can be approximated by the modal state representation:

$$\dot{x}_i = A_i x_i + B_i u$$
$$y = \sum_{i=1}^{n} C_i x_i \qquad (1)$$

where

$$x_i \triangleq \begin{bmatrix} \text{position of ith mode} \\ \text{rate of ith mode} \end{bmatrix}$$

$$A_i \triangleq \begin{bmatrix} 0 & 1 \\ -\omega_i^2 & -2\delta_i\omega_i \end{bmatrix} \in \mathbb{R}^{2\times 2}$$

$$B_i \triangleq \begin{bmatrix} 0 \\ \hline \text{input influence coeff. for ith mode} \end{bmatrix} \in \mathbb{R}^{2\times m}$$

$$C_i \triangleq \begin{bmatrix} 0 & \begin{array}{|l} \text{output rate measurement} \\ \text{coefficients for ith mode} \end{array} \end{bmatrix} \in \mathbb{R}^{r\times 2}$$

$m \triangleq$ number of actuators

$r \triangleq$ number of sensors

and n is theoretically infinite or, more practically, very large order (>100 states). The parameters in this representation are generally computed by solving the eigenvalue problem resulting from finite element modelling of the structure [1]. This approach is currently the best practical method for modelling the structure, yet the resulting fidelity of the parameters ω_i, B_i and C_i degrades drastically with increasing i (>100% error in some cases). Independent of the finite element approach, the damping, δ_i, of the structure is poorly known and is very small (.001 - .01). Small uncertainties in the finite element model may therefore induce very large, non-monotonic changes in the input/output map. The phenomenon occurs even when one is careful and uses a frequency dependent norm which restricts the bandwidth of the input signal set,e.g., think of the response of (1) to a sinusoid just on and just off an assumed resonant frequency. For this reason model order reduction within the control bandwidth, based only on open-loop measures, is very difficult and a large order plant model often has to be retained. The impact of this difficulty becomes most evident whenever one attempts to base and implement robust control laws whose order is fundamentally tied to the dimension of the plant's state space.

The disturbance set about which the LSS is to be regulated is non-trivial. The more common disturbances constant (e.g., gravity gradients) and random (e.g., equivalent noise of reaction wheel bearings) are encountered together with impulsive (e.g., rapid slew maneuvers) and periodic* (e.g., reaction wheel imbalance). This wide variety of disturbances makes designs employing the placement of disturbance-to-error transmission zeros potentially too sensitive and complex.

In order to obtain robustness with an implementable controller, in spite of the difficulties represented by an LSS, this paper proposes a combined positivity/frequency domain approach to synthesizing digital LSS control systems. The

* not necessarily sinusoidal

characteristic gains of the LSS are shaped in an α-shifted W-plane in order to synthesize performance. Positivity theory is used to ensure the stability robustness of the design. The paper will first summarize the main results from positivity and multi-variable frequency-domain design* theory. These results are then interpreted in context with the LSS plant. This is followed by the design procedure and concluded with a design example using a tetrahedral truss.

II. Synopsis of Positivity Theory

First, some definitions are required.

Let f(t) be a real, possibly vector valued function defined on $[0,\infty)$. The truncation of f(t) at t=T is defined as

$$f_T(t) = \begin{cases} f(t), & 0 \le t \le T \\ 0, & t > T \end{cases}$$

Define the extended Hilbert Space H_e such that $f(t) \in H_e$ if and only if $f_T(t) \in$ Hilbert Space, H.

An operator with a domain and range in H_e is then defined to be (strictly) positive if for $f(t) \in H_e$,

$$\langle f_T(t),\ Hf_T(t)\rangle \ge 0 \quad (>0)$$

Positive operators are useful because they have the following properties:

1) The inverse of a positive operator is positive.
2) The sum of positive operators is positive.
3) Positivity Theorem [2,3,4]: The negative feedback systems shown in Figures 1 and 2 are bounded-input-bounded-output BIBO stable for all inputs in H_e if both G and H are positive operators and at least one of them is also strictly positive. The main advantage of the theorem is that conditions are imposed individually on G and H, ensuring stability when the loop is closed by negative feedback.

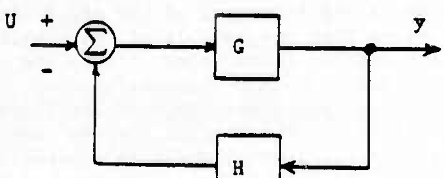

Figure 1. Feedback Interconnection

* We restrict ourselves only to generalized Nyquist/Bode methods.

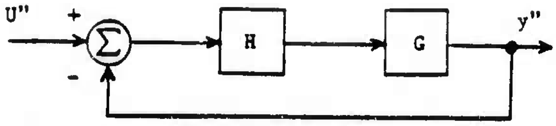

Figure 2. Cascade/Unity Feedback Interconnection

A positive operator may be interpreted physically as one that does not create energy (a strictly positive operator always dissipates energy). For this reason, a positive operator is often referred to as a passive operator.

The term "Positive Real" is also often used to refer to a positive operator that is also convolutional and linear time-invariant (LTI). The term "Hyperstability" refers to the Positivity Theorem when at least one of the subsystems G or H is positive real, while the other may be nonlinear and/or time-varying.

A frequency domain test exists for testing the positivity of square operators which have a Laplace or Z-Transform representation [4,5]. Positivity is determined, using this test, by first computing the positivity index:

$$\delta(\omega) \triangleq \lambda_{min}\left\{\frac{1}{2}\left[G(s=j\omega)+G^*(s=j\omega)\right]\right\},\ \omega\in[0,\infty)$$

or for discrete systems

$$\delta(\omega) \triangleq \lambda_{min}\left\{\frac{1}{2}\left[G(z=e^{j\omega T})+G^*(z=e^{j\omega T})\right]\right\},\ \omega\in[0,\ \pi)$$

where $\lambda_{min}\{\cdot\}$ denotes "minimum-eigenvalue-of" and "*" denotes complex-conjugate-transpose.

If

$\delta(\omega) > 0$ for all ω defined above, then G is strictly positive real

$\delta(\omega) \ge 0$ for all ω defined above, then G is positive real

$\delta(\omega) \le 0$ for some ω in the defined range, then G is not positive.

Finally, there is a strong relationship between the Small-Gain Theorem*, the Positivity Theorem, and the concept of conicity [2]. The link is the set of stability invariant transformations called embedding. As Appendix A shows, if G and H are LTI, then the stability of the system in Figure 1 implies the stability of the embedded system in Figure 3 and vice-versa. This stability invariant property however, does not in any way imply input-output equivalence. The relationship between small-gain, positivity, and conicity can now be

* The system in Figures 1 and 2 are BIBO if for

$$g(H) \triangleq \sup \frac{\|H\ f_T\|}{\|f_T\|},\ g(H)\cdot g(G) < 1.$$

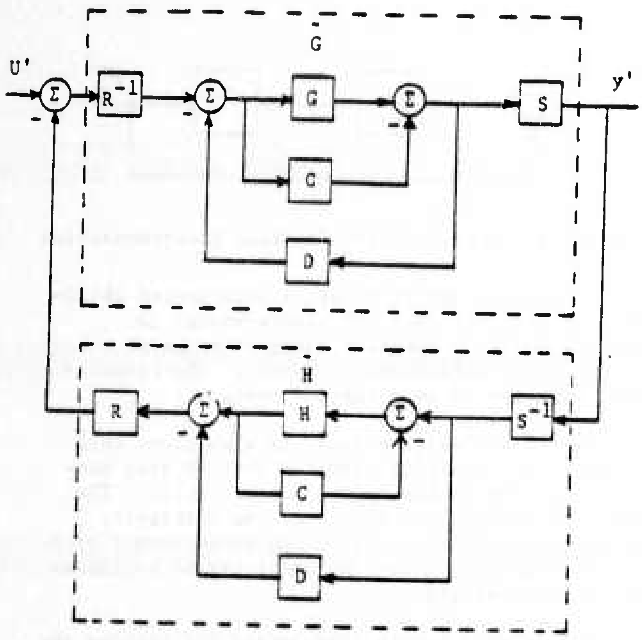

Figure 3. **Example of Embedded Feedback Interconnection**

demonstrated. Using the small gain theorem on the system in Figure 3 (with $D \equiv 0$ and $S \equiv I$) implies if

$$\|\tilde{G}\| = \|(G-C)\,R^{-1}\| < 1 \tag{2}$$

and

$$\|\tilde{H}\| = \|R\,(I+HC)^{-1}\,H\| < 1 \tag{3}$$

Then the system in Figure 1 is stable*. But Eq. (2) implies

$$\|(G-C)\,f_T\| < \|R\,f_T\| \;\; \forall\, f_T$$

This equation may be geometrically interpreted as a cone with center C and radius R. If the additional constraints

$$C = I \cdot \text{constant}$$
$$R = I \cdot \text{constant}$$
$$C - R = 0$$
$$C + R \to I \cdot \infty$$

are placed on Equation (2), then the identity (real-inner product space only)

$$\|(G-C)\,f_T\| - \|Rf_T\| < 0 \Leftrightarrow \langle (G-C+R)f_T, (G-C-R)f_T \rangle < 0$$

is equivalent to the positivity condition. It is important to note, however, that had we demanded that $\tilde{G}$ and $\tilde{H}$ in Eq. (2) and (3) satisfy the positivity condition (i.e., either $\tilde{G} > 0$ and $\tilde{H} \geq 0$, or $\tilde{H} > 0$ and $\tilde{G} \geq 0$), the stability of the system in Figure 1 could still be inferred even though the geometry can no longer be interpreted as a cone.

It is interesting to note therefore that various interpretations can be given to each embedding transformation. The interpretation depending on the stability theorem with which it is used. Some interpretations of the mathematics include modeling of plant uncertainty, distance from passive systems, bounding of unmodeled dynamics, and the model-reference interpretation given in [7].

* Similar transformation can be applied to the system in Figure 2.

III. Summary of Multivariable Frequency-Domain Design

The objective in frequency domain design is to meet and/or optimize performance goals under the constraint that the closed-loop system be stable. The key to extending this classical Nyquist/Bode approach to the multivariable case [8] are the characteristic gains of the square transfer matrix G(s), describing the open-loop plant. The characteristic gains $\lambda(s)$ are the eigenvalues of G(s) as function of frequency, i.e., the solution to

$$G(s)\; v(s) = \lambda(s)\; v(s) \tag{4}$$

The importance of $\lambda(s)$ stems from the fact that the $\lambda_c(s)$ of a closed-loop unity feedback system are related to the open-loop $\lambda_o(s)$ in a manner that is analogous to single-input-single-output systems, i.e.,

$$\text{closed-loop gain} = \frac{\text{open-loop gain}}{1 + \text{open-loop gain}}$$

Using and shaping the open-loop $\lambda(s)$ and v(s):

1) Multivariable Nyquist Theorem [8]. A closed-loop system is stable if and only if the net sum of counter-clockwise encirclements of the (-1.,0.) point by the characteristic gains are equal to the number of open-loop unstable poles.

2) With proper interpretation, any closed contour can be taken while applying the multivariable Nyquist Theorem. The basic concept one is exploiting in the Nyquist Theorem is the Principal of the Argument [9]. This means that one can either conformally map any desired closed contour into the Nyquist Path and then evaluate Eq. (4), or evaluate (4) along the desired closed contour directly. The Nyquist Theorem then gives conditions under which no closed-loop poles will be in the region represented by the closed contour. Figure 4 shows two of the possible mappings which can be used to ensure that satisfaction of the Theorem will imply that closed-loop transients exponentiall decay faster than some desired value a.

3) To achieve low control interaction in a frequency band it is sufficient to ensure either that all the open-loop $\lambda_o(s)$ have a large magnitude over that band, or, that all the open-loop v(s) are nearly orthogonal over that band.

4) In frequency bands of low interaction, the notion of gain margin and phase margin may be applied as a qualitative assessment of performance. Furthermore, in these bands, the plot of the open-loop $\lambda_o(s)$ in the Nichols chart can provide a direct measure of sensitivity, tracking accuracy, and disturbance rejection along directions computable from v(s)*.

IV. LSS Plant from a Positivity and Frequency-Domain Perspective

There are several reasons for approaching the LSS controller design problem from a Positivity/Frequency-Domain perspective. Foremost is the fact that an LSS with collocated, ideal (infinite bandwidth) rate sensors and actuators is a positive operator [4]. This result is independent of the parameters characterizing the LSS. From equation (1), the transfer function of the idealized LSS also has reciprocity properties (i.e. in modal coordinates $B^T=C$, so the transfer function from input i to output j is the same as from input j to output i). As a consequence of positivity and reciprocity under ideal conditions, tha LSS transfer function with collocated finite bandwidth actuators and rate sensors exhibits nearly orthogonal eigenvectors (v(s) in equation 4) and positivity over most of the actuator/sensor bandwidth. For small negative excursions of $\delta(\omega)$ or when the actuators and sensors begin to add significant phase shift, the Positivity Theorem is applied with embedding [5].

It is also reasonable to use conicity concepts in treating the LSS problem but there are some difficulties. The LSS plant has closely spaced modes with almost no damping. This makes the singular values of G(s) behave violently at the resonant frequencies. Also, while conicity has in general the potential for providing a tighter bound (assuming embedding is <u>not</u> permitted in the Positivity Theorem), in practice, the uncertainty in LSS modal frequencies is so high that the cone parameters nearly degenerate to the positivity conditions. In other words, the LSS undergoes 180° phase shifts (-40 dB to +40 dB with $\xi=.005$) a large number of times and at closely spaced frequencies whose center location is very uncertain. The uncertainty of the center and behavior bound are therefore modeled by conicity parameters which are practically equal to the positivity conditions.

It therefore makes sense to analyze LSS behavior in terms of its proximity to a positive system. This is measured by the positivity index $\delta(\omega)$ in the sense that

$$G - \delta(\omega) \cdot I$$

is a positive operator. Hence $\delta(\omega) \cdot I$ is an appropriate "C" operator in a positivity interpreted embedding procedure. The implied Theorem conditions which the controller $\tilde{H} > 0$ satisfies (R=I; S=I; D=0) is that it can phase stabilize all frequencies where $\delta(\omega) > 0$, but, must gain stabilize wherever $\delta(\omega) < 0$.

In general, <u>any</u> skew Hermitian matrix can also be added to [redacted] H without affecting stability.

- α-shifted s-plane design
  1) Let $S' = S-\alpha$
  2) Compute $\lambda(G(S'))$, $S'=j\omega$, $\omega\in[0,\infty)$
  3) Apply encirclement criterion
  4) Compensate in S'-plane
  5) Map controller back to $S=S=S+\alpha$
- α-shifted Z-plane design
  1) Let $Z' = r_o Z$, $r_o = e^{-\alpha T_{samp}}$
  2) Compute $\lambda\{\mathcal{Z}[G(S)]|_{Z'=r_o Z}\}$, $Z = e^{j\omega T_{samp}}$, $\omega\in[0,\pi)$
  3) Map into W'-pane and use encirclement criterion
  4) Design compensator in W'-plane. Note:

$$W = \frac{(1+r_o)\,W' + (1-r_o)}{(1-r_o)\,W' + (1+r_o)} = \frac{Z' - r_o}{Z' + r_o}$$

  5) Map controller back to Z:

$$Z = \frac{W' + 1}{r_o(1-W')}$$

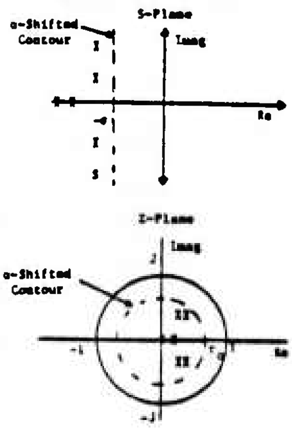

Figure 4. Linear MIMO Frequency Domain Design: Specified Degree of Stability Via α-Shift

* It is acknowledged that sensitivity and disturbance rejection are generally best measured using singular-value analysis, but the LSS plant, as will be shown later, has some very interesting properties.

V. Recipe for Sample-Data LSS Control Design in the W-plane

1. Compute the characteristic gains $\lambda(w)$ and the positivity index $\delta(\omega)$ for the open-loop, sampled plant. i.e., solve

$$\mathrm{DET}\left\{\mathcal{W}\{\mathcal{Z}[G(s)]\} - \lambda(w)\cdot I\right\} = 0 \qquad (5)$$

and

$$\delta(w) = \lambda_{\min}\left\{\frac{1}{2}\left\{\mathcal{W}\{\mathcal{Z}[G(s)]\}+\mathcal{W}^*\{\mathcal{Z}[G(s)]\}\right\}\right\} \qquad (6)$$

where

$\mathcal{Z}[\cdot]$ denotes "take the z-transform of $[\cdot]$"

$\mathcal{W}\{\cdot\}$ denotes "substitute $\frac{w+1}{1-w}$ for z in $\{\cdot\}$"

$*$ denotes "take the complex conjugate transpose"

$\lambda_{\min}\{\cdot\}$ denotes "take the minimum eigen-value of"

and $\lambda(w)$ and $\delta(w)$ is solved for with

$$w = jv, \quad v\,\varepsilon\,[0,\infty)$$

2. Shape $\lambda(w)$ to meet sensitivity and disturbance rejection requirements in the bandwidth of interest*. Non-modal sensitivity and disturbance rejection are approximated by

$$\left|\frac{1}{1+\lambda_s(w)}\right|, \quad \lambda_s(w) \triangleq \text{"shaped" } \lambda(w)$$

$\delta(w)$ can be advantageously used here to indicate the class of shaping compensstors which will preserve stability inclusive of modal errors and any model order reduction which may have been used. I.e., $\delta(w)$ can be used to measure the permissible low frequency multiplicative perturbstions and high frequency additive perturbations. The minimum of $\delta(w)$ and $\delta_p(w)$ [the positivity index for the worst case perturbed system] as function of w bounds the gains of the permissible positive filters/controllers.

Note: δ_p is never really computed. It is estimated, like the conicity parameters, from physical information like rsnge in damping ratio, modal data uncertainty, and actuator/sensor bsndwidth vsriation.

If the desired gains for $\lambda_s(w)$ cannot be sttained together with stability and a $\delta(w)$ indicstive that the worst case plant can be encompsssed, then a solution to the problem posed is not possible. One must then trade reductions of performance and/or system uncertainty with increaaes in actuator/sensor bandwidth. With ideal, collocated actuator/sensor pairs, the worst case always has a $\delta_p(w)\geq 0$. An indication thst any positive controller will preserve closed-loop stability, independent of modal data and order reduction.

3. Determine the "α-line" that will reflect desirable pole locations (e.g. based on desired transient response) and compute the characteristic gains $\lambda(w')$ for the α-shifted system. i.e., evsluate (6) using the $\mathcal{W}'$ operator instead of $\mathcal{W}$.

$\mathcal{W}'\{\cdot\}$ denotes "substitute $\frac{w'+1}{r_o(1-w')}$ for z in $\{\cdot\}$"

where

$$r_o = e^{-\alpha T_{SAMP}}$$

4. If necessary, shape $\lambda(w')$ to satisfy the Nyquist Theorem over the bsndwidth of interest. This ensures that modes within the control bandwidth have a desirable rate of decay.

Map the w' controller back to the Z-domain.

5. Compute $\lambda_c(w)$ and $\delta_c(w)$, the open-loop λ and δ for the plant plus controller. If everything was done correctly, $\lambda_c(w)$ will indicate stability and $\delta_c(w)$ will indicate s perturbation margin that encompasses the worst case plant.

Note that because positivity retains the convexity properties of conicity, satisfaction of the nominal and worst case implies satisfaction of all convex perturbations in-between.

6. Simulate to verify that disturbance rejection goals have been satisfied. It should be very close. Otherwise the gains along the diagonal of the compensator can be increased, without loss of stability (including perturbations) by an amount computable from $\delta_c(w)$ and $\delta_p(w)$.

VI. Tetrahedron Example

The Tetrahedral Truss, shown in Figure 6 will now be used to illustrate the idess presented. This structure was devised by Draper Labs [10] as one of the simplest non-planar geometries capable of representing a large space structure. Despite its apparent simplicity, it models the feed-tower in a generic clasa of large antenna applications. The tetrahedral apex represents the antenna feed, members 1-6 are part of the feed support structure, and bi-peds 7-8, 9-10 and 11-12 are supports/controls attached to an inertially stabilized (assumed) antenna dish. Because of the nature of the resl problem, the motion of the feed (apex) must be controlled through actuators and sensors placed at the bi-peds, none can be placed at the feed. The latter constitutes the control problem: i.e., control the feed precisely despite large modeling uncertainty and without resorting to direct measurement or control of its motion.

* This is done using a Nichols chart and a computer-sided filter design program.

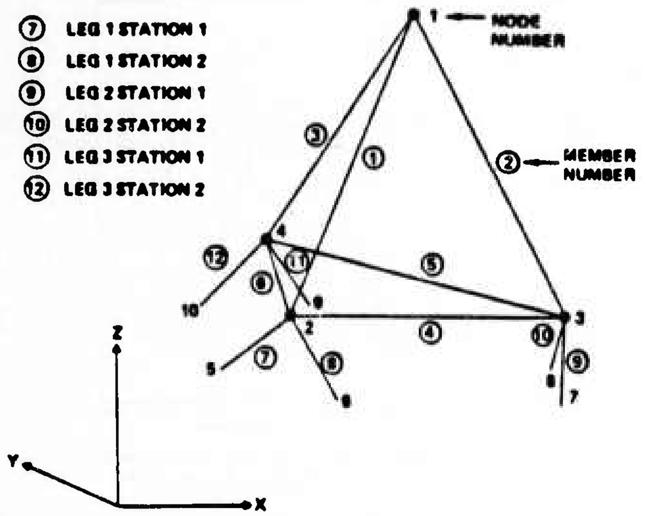

Figure 6. Draper Tetrahedral Truss

The finite element method was used to model the tetrahedron. Referring to Figure 6, the model contains ten nodes, each with three degrees of freedom, and twelve truss members. Node coordinates and element connectiveness for the "nominal" model are listed in Table 1. These elements are assumed to be capable of resisting axial forces only. The masses were assumed to be lumped at the nodes one through four.

Table 1. Tetrahedron Structural Model Parameters (Nominal)

Node Point Locations

Node	X	Y	Z
1	0.0	0.0	10.165
2	-5.0	-2.887	2.0
3	5.0	-2.887	2.0
4	0.0	5.7735	2.0
5	-6.0	-1.1547	0.0
6	-4.0	-4.6188	0.0
7	4.0	-4.6188	0.0
8	6.0	-1.1547	0.0
9	2.0	5.7735	0.0
10	-2.0	5.7735	0.0

Restraints X, Y, & Z at nodes 5-10

Element Connectivities and Properties

Element	Node 1	Node 2	Area
1	1	2	1000.
2	1	3	100.
3	1	4	100.
4	2	3	1000.
5	3	4	1000.
6	2	4	1000.
7	2	5	100.
8	2	6	100.
9	3	7	100.
10	3	8	100.
11	4	9	100.
12	4	10	100.

Material E = 1.0

Lumped Masses

Node	Mass
1	2.0
2	2.0
3	2.0
4	2.0

Six colocated sensors/actuators were assumed to act as member dampers in parallel with members 7 through 12. The member dampers were assumed capable of sensing relative position and velocity and exerting force in the axial direction only.

The objective was to design a robust controller and evaluate the resulting controller on the full order nominal model. A second evaluation was then conducted using the true tetrahedral system parameters shown in Table 2.

Table 2. Tetrahedron Parameter Variation

Masses

Node	Mass
1	4.0

Element Property Changes

Element	Area
1	1200.0
2	150.0
3	150.0
4	1200.0
5	1200.0
6	1200.0
7	150.0
8	150.0
9	150.0
10	150.0
11	150.0
12	150.0

Both evaluations were based on the initial conditions given in Table 3. The goal was to damp the line-of-sight motion of Node 1 in the x and y directions to less than 0.0004 and 0.00025 units, respectively, in 20 seconds.

Table 3. Initial Conditions for Control Design Evaluations

Mode	Displacement (η)	Velocity $(\dot{\eta})$
1	-.001	-.003
2	.006	.01
3	.001	.03
4	-.009	-.02
5	.008	.02
6	-.001	-.02
7	-.002	-.003
8	.002	.004
9	.0	.0
10	.0	.0
11	.0	.0
12	.0	.0

The sampling rate was chosen to be 0.2 seconds. This rate is approximately three times faster than the rate required to reconstruct the highest controlled mode, 0.909 Hz. [Note 0.909 Hz is not the highest mode modeled. There are several modes at higher frequencies which even get aliased.] Using 0.2 sec, one can compute the characteristic gains and positivity index for the nominal plant. These are shown in Figures 7 and 8.

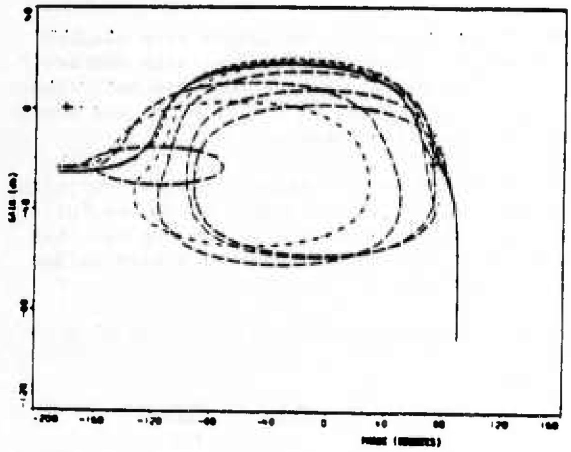

Figure 7. Characteristic Gains of the Tetrahedron in the W-Plane

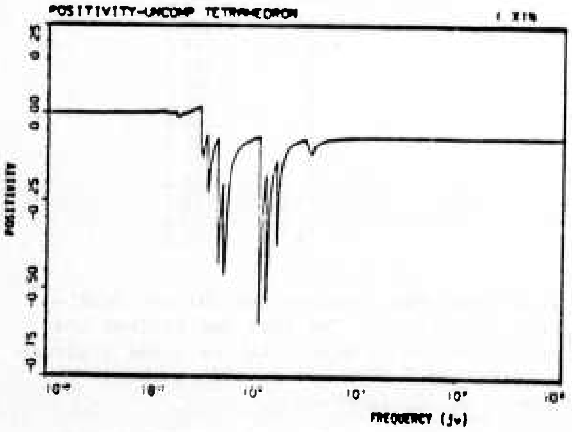

Figure 8. Positivity Index of Uncompensated System (W-Plane)

The disturbances for this system were not specified in [10] so one can go directly into the α-shifted plane in order to design for the required rate of decay. It can be computed that $\alpha = 0.230$/sec will decay the specified initial conditions to levels desired after 20 seconds. So after adding a little feedback, $7.8 \cdot I$ to a-priori shift the majority of poles inside the α region, the α-shifted characteristic gains are computed. Figure 9 shows that in order to obtain the required rate of decay, modes #1 and #2 must encircle the point (180°, 0 db). The reason for requiring the encirclement is that these modes are open-loop "unstable" in the α-shifted plane, so the encirclement condition of the Nyquist Theorem applies. Note that mode #12 is also unstable in the α-plane (stable in the regular plane), but does not have to encircle the (-180 , 0 db) point because it lies outside the control bandwidth. The compensator

$$I_{6x6} \cdot 11.492 + \frac{3.921162Z - 3.9863812}{Z^2 - 1.70921Z + .846578}$$

can be shown to shape the characteristic gains in the desired manner.

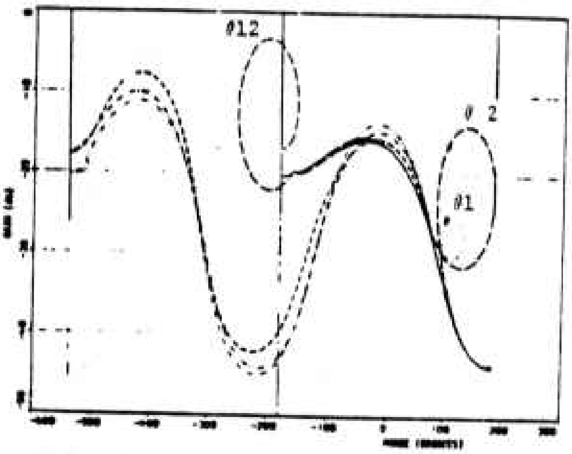

Figure 9. Characteristic Gains of the Tetrahedron in the α-Shifted W-Plane, $R_o = 0.955$

Figures 10 and 11 show the characteristic gains and the positivity index for the open-loop plant plus the compensator. The characteristic gains show that the system is stable. The positivity index shows that large perturbation are permitted at low and high frequencies.

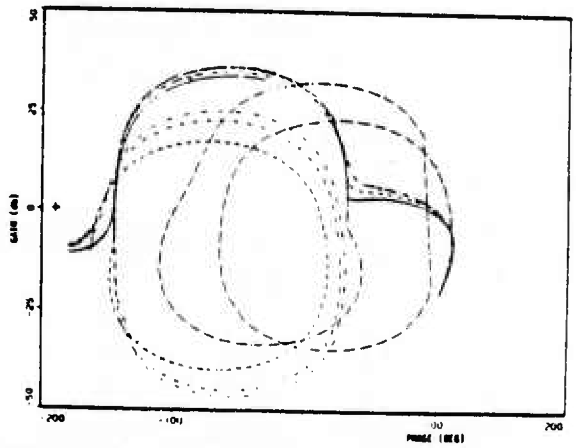

Figure 10. Frequency Response of Compensated Open-Loop System in the W-Plane

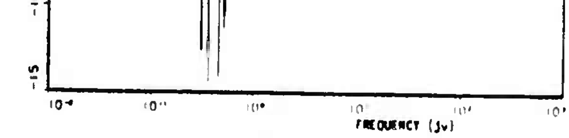

Figure 11. Positivity Index of Compensated System (W-Plane)

At intermediate frequencies, the system remains relatively insensitive to the modal data (additive unmodeled modal perturbation), but, multiplicative phase shifts could destabilize the system. The perturbed tetrahedron, however, primarily consists of changes in the modal data and it can be computed that the perturbed model plus all convex combinations in between are well within the permissible perturbation region.

Figures 12 through 17 show the simulated transient responses of the nominal and perturbed systems to the initial conditions given in Table 3. Figures 12 and 13 show that the unmodelled modes are stable despite the use of the low order decentralized controller. Figures 14 and 15 show that the nominal system meets design specifications but that there is a small loss of performance using the perturbed model. Figures 16 and 17 show that actuator command forces are modest.

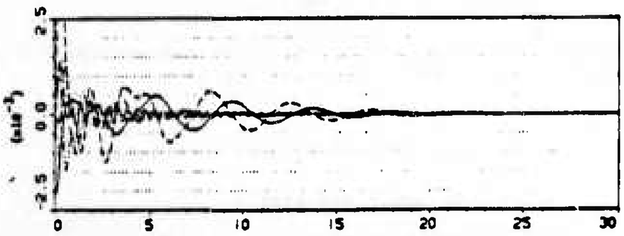

Figure 12. Response of Residual Modes (Nominal System)

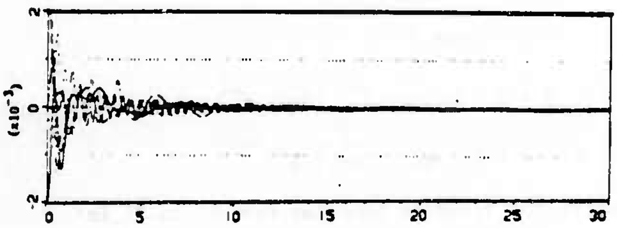

Figure 13. Response of Residual Modes (Perturbed System)

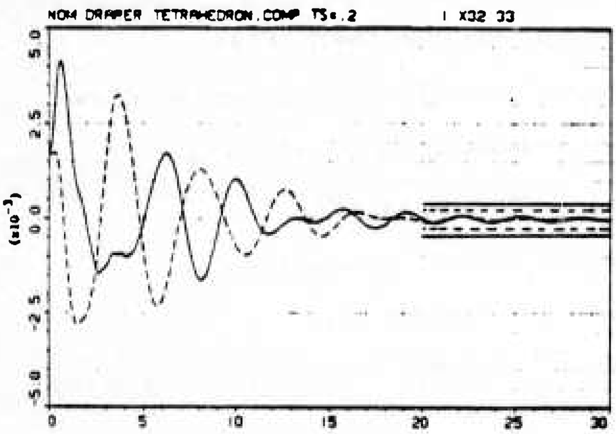

Figure 14. Transient Response of Nominal System to Initial Conditions

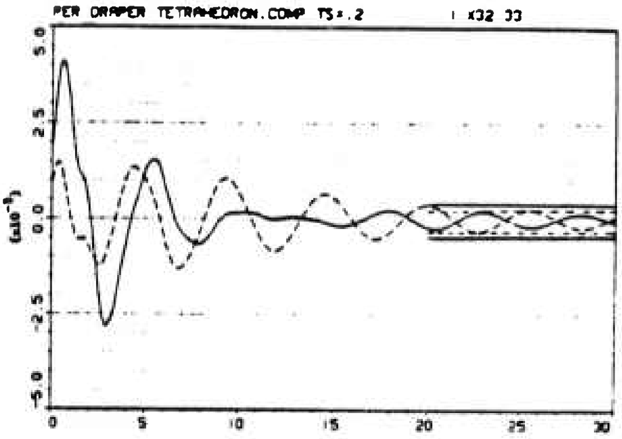

Figure 15. Transient Response of Perturbed System to Initial Conditions

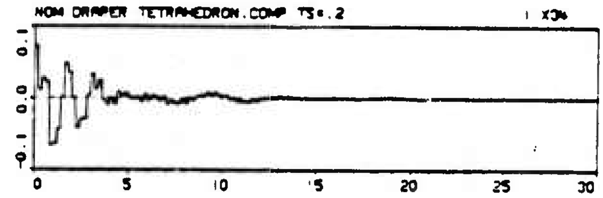

Figure 16. Actuator Force at Leg 1, Station 1 (Nominal System)

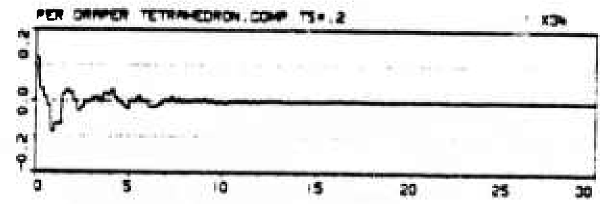

Figure 17. Actuator Force at Leg 1, Station 1 (Perturbed System)

VII. Summary/Future Work

This paper has summarized those aspects of Positivity and Frequency Domain Theory which are useful in the design of LSS control systems. A design procedure combining the two was described. An example illustrated the approach and good results were obtained.

A future paper will further detail how the basic ideas have been used to design the control system for a much more realistic structure. Future efforts will be directed at applying the concepts to "non-square" LSS plants where colocation of actuators and sensor is not permitted.

References

[1] Przemieniecky, J.S., Theory of Matrix Structural Analysis, McGraw-Hill, 1958.

[2] Zames, G., "On the Input-Output Stability of Time-Varying Nonlinear Feedback Systems - Part I ...," IEEE AC-11, No. 2, April 1966.

[3] Iwens, R.P., "Input-Output Stability of Continuous and Discrete Time Nonlinear Control Systems," Ph.D. Dissertation, University of California, Berkeley, CA, March 1967.

[4] Benhabib, Iwens, and Jackson, "Stability of Distributed Control for Large Flexible Structure Using Positivity Concepts," AIAA Guidance and Control Conference, Boulder, CO, August 1979.

[5] Iwens, Benhabib, and Jackson, "A Unified Approach to the Design of Large Space Structure Control Systems," JACC, San Francisco, CA, August 1980.

[6] Benhabib, Iwens, and Jackson, "Adaptive Control for Large Space Structures," IEEE CDC, Ft. Lauderdale, FL, June 1979.

[7] Zames, G., "Feedback and Optimal Sensitivity. Model Reference Transformations, Multiplicative Seminorms and Approximate Inverses," IEEE AC-26, No. 2, April 1981.

[8] Mac Farlane, et. al., "Complex Variable Methods for Multivariable Systems Analysis and Design," in Alternatives for Linear Multivariable Control," NEC, Chicago, IL, 1978.

[9] Churchill, R.V., Complex Variables and Applications, 2nd ed., McGraw-Hill, New York, 1960.

[10] Description of Draper Example Structure Model from R. Strunce, Charles Stark Draper Labs.

Appendix

In this Appendix the stability equivalence of the system in Figures 1 and 3 are established for linear systems. The proof relies on the following two identities:

1) If $I \pm A$ is invertible, then

$$I \mp A\,(I \pm A)^{-1} = (I \pm A)^{-1}$$

Proof: $$(I \pm A) \mp A \equiv I$$

so pre-operating on both sides of the identity by

$$(I \pm A)^{-1}$$

yields the desired result.

2) If G and H are linear*, and, I+HG and I+GH are invertible, then

$$G(I+HG)^{-1} = (I+GH)^{-1}\,G$$

Proof: $$G+GH\overset{G}{\cancel{G}} \equiv G+GHG$$

therefore,

$$G(I+HG) = (I+GH)\,G$$

so pre-operating on both sides by $(I+HG)^{-1}$ yields

$$G = (I+GH)\,G\,(I+HG)^{-1}$$

and post-operating on both sides yields

$$(I+GH)^{-1}\,G = G\,(I+HG)^{-1}.$$

Assertion: The stability of either of the systems in Figure 1 and 3 imply the stability of the other if

a) $(I+CH)$ and $[I+(G-C)\,D]$ have inverses,

b) G,H,C,D,R, and S are stable,

and

c) The system in both figures are controllable and observable.

Proof: From Figure 3:

$$\tilde{G} = S\,[I+(G-C)D]^{-1}\,(G-C)\,R^{-1}$$

$$\tilde{H} = R\,[(I+HC)^{-1}\,H-D]\,S^{-1}$$

Therefore the transfer function from U' to Y' is:

$$[I+\tilde{G}\tilde{H}]^{-1}\,\tilde{G} =$$

$$\left\{I+S[I+(G-C)D]^{-1}\,(G-C)\;[(I+HC)^{-1}\,H-D]S^{-1}\right\}^{-1}\,\tilde{G} =$$

$$S\left\{I+[I+(G-C)D]^{-1}\,(G-C)\,[(I+HC)^{-1}\,H-D\,]\right\}^{-1}\,S^{-1}\,\tilde{G} =$$

$$S\left\{I-[I+(G-C)D]^{-1}\,(G-C)D+[I+(G-C)D]^{-1}\,(G-C)(I+HC)^{-1}\,H\right\}^{-1}\,S^{-1}\,\tilde{G} =$$

$$S\left\{[I+(G-C)D]^{-1}+[I+(G-C)D]^{-1}\,(G-C)(I+HC)^{-1}H\right\}^{-1}\,S^{-1}\,\tilde{G} =$$

$$S[I+(G-C)(I+HC)^{-1}H]^{-1}\,[I+(G-C)D]\,S^{-1}\,\tilde{G} =$$

$$S[I+GH(I+CH)^{-1}-CH(I+CH)^{-1}]^{-1}\,[I+(G-C)D]\,S^{-1}\,\tilde{G} =$$

$$S[(I+GH)\,(I+CH)^{-1}]^{-1}\,[I+(G-C)D]\,S^{-1}\,\tilde{G} =$$

$$S(I+CH)(I+GH)^{-1}\,[I+(G-C)D]\,S^{-1}\,\tilde{G} =$$

$$S(I+CH)(I+GH)^{-1}(G-C)\,R^{-1} = [I+\tilde{G}\tilde{H}]^{-1}\,\tilde{G}$$

* Linearity is not really necessary. All that is needed is that the distributive law used be permitted. This fact can and has been used to derive the nonlinear error equation in a reduced-order model-reference adaptive control [6].

It follows from this development that if the quantities

$$(I+CH) \text{ and } I+(G-C)D$$

have inverses and G,H,C,D,R, and S are stable, then stability of a controllable/observable $\tilde{G},\tilde{H}$ system implies the stability of the G,H system.

By rewriting the algebraic statements in the proof backward, the converse is also easily established under the same assumption, i.e., the stability of the G,H system implies the stability of the $\tilde{G},\tilde{H}$ system.

Addresses	number of copies
R. Carman RADC/OCSE	5
RADC/TSLD GRIFFISS AFB NY 13441	1
RADC/DAP GRIFFISS AFB NY 13441	2
ADMINISTRATOR DEF TECH INF CTR ATTN: DTIC-DDA CAMERON STA BG 5 ALEXANDRIA VA 22314	12
TRW One Space Park Redondo Beach, CA 90278	5
Charles Stark Draper Lab Attn: Dr. Keto Soosar 555 Technology Square M.S. -95 Cambridge, MA 02139	1
NASA Headquarters ATTN: Mr. J. B. Dahlgren Code RTH-6 Washington, DC 20546	1
Charles Stark Draper Lab Attn: Mr. R. Strunce 555 Technology Square M.S. -60 Cambridge, MA 02139	1

Charles Stark Draper Lab Attn: Dr. Daniel R. Hegg 555 Technology Square M.S. -60 Cambridge, MA 02139	1
ARPA/STO Attn: Lt Col A. Herzberg 1400 Wilson Blvd Arlington, VA 22209	1
ARPA/STO Attn: Maj E. Dietz 1400 Wilson Blvd Arlington, VA 22209	1
Riverside Research Institute Attn. Mr. A. DeVilliers 1701 N. Ft. Myer Drive, Suite 711 Arlington, VA 22209	2
Riverside Research Attn: HALO Library, Mr. Bob Passut 1701 N.Ft. Myer Drive Arlington, VA 22209	1
Itek Corp Optical Systems Division 10 Maguire Rd. Lexington, MA 02173	1
Perkin Elmer Corp Attn: Mr. H. Levenstein Electro Optical Division Main Avenue Norwalk, CT 06856	1
Hughes Aircraft Company Attn: Mr. George Speak M.S. B_156 Culver City, CA 09230	1

Hughes Aircraft Company 1
Attn: Mr. Ken Beale
Centinela Teale Sts
Culver City, CA 90230

Air Force Flight Dynamics Lab 1
Attn+ Dr. Lynn Rogers
Wright Patterson AFB, OH 45433

AFWL/FIBG 1
Attn: Mr. Jerome Pearson
Wright Patterson AFB, OH 45433

Air Force Wright Aero Lab. FIGC 1
Attn. Siva S. Banda
Wright Patterson AFB, OH 45433

Air Force Institute of Technology 1
Attn: Prof. R. Calico/ENY
Wright Patterson AFB, OH 45433

Aerospace Corp. 2
Attn: Dr. G.T. Tseng
2350 E. El Segundo Blvd
El Segundo, CA 90245

Aerospace Corp. 1
Attn: Mr. J. Mosich
2350 E. El Segundo Blvd
El Segundo, CA 90245

Aerospace Corp/Bldg 125/1054 1
Attn: Mr. Steve Burrin
Advanced Systems Tech Div.
2400 E El Segundo Blvd
El Segundo, CA 90245

SD/SD/YLVS
Attn: Mr. Lawrence Weeks
P.O. Box 92960
Worldway Postal Center
Los Angeles CA 90009 1

SD/YCD
Attn: YCPT/Capt Gajewski
P.O. Box 92960
Worldway Postal Center
Los Angelel, CA 90009 1

Grumman Aerospace Corp
Attn: Dr. A. Mendelson
South Oyster Bay Road
Bethpage, NY 11714 1

OUSDR&E/DS
Attn. Mr. A. Bertapelli
Room 3D136
Pentagon, Washington, DC 20301 1

Jet Propulsion Laboratory
Dr. S. Szermay
4800 Oak Grove Drive
Pasadena, CA 91103 2

MIT/Lincoln Laboratory
Attn: S. Wright
P.O. Box 73
Lexington, MA 02173 1

Lockheed Space Missile Corp.
Attn: A. A. Woods, Jr., 0/62-E6
P.O. Box 504
Sunnyvale, California 94088-3504 5

Lockheed Missiles Space Co.
Attn: Mr. Paul Williamson
3251 Hanover St.
Palo Alto, CA 94304 1

General Dynamics Attn: Ray Halstenberg Convair Division 5001 Keary Villa Rd San Diego, CA 92123	1
STI Attn: Mr. R.C. Stroud 20065 Stevens Creek Blvd. Cupertiono, CA 95014	1
NASA Langley Research Ctr Attn: Dr. Earle K. Huckins III Dr. M. F. Card Langley Station, Bldg 1293B, MS 230 Hampton, VA 23665	2
NASA Johnson Space Center Attn: Robert Piland Ms. EA Houston, TX 77058	1
McDonald Douglas Corp Attn: Mr. Read Johnson Douglas Missile Space Systems Div 5301 Bulsa Ave Huntington Beach, CA 92607	1
Integrated Systems Inc. Attn: Dr. N. K. Gupta and M. G. Lyons 151 University Avenue, Suite 400 Palo Alto, California 94301	2
Boeing Aerospace Company Attn: Mr. Leo Cline P.O. Box 3999 Seattle, WA 98124 MS 8 W-23	1
TRW Defense Space Sys Group Inc. Attn: Ralph Iwens Bldg 82/2054 One Space Park Redondo Beach, CA 90278	1

TRW 1
Attn: Mr. Len Pincus
Bldg R-5, Room 2031
Redondo Beach, CA 90278

Department of the navy 1
Attn: Dr. K.T. Alfriend
Naval Research Laboratory
Code 7920
Washington, DC 20375

Airesearch Manuf. Co. of Calif. 1
Attn: Mr. Oscar Buchmann
2525 West 190th St.
Torrance, CA 90509

Analytic Decisions, Inc. 1
Attn: Mr. Gary Glaser
1401 Wilson Blv.
Arlington, VA 22209

Ford Aerospace & Communications Corp. 1
Drs. I. P. Leliakov and P. Barba, MS/G80
3939 Fabian way
Palo Alto, California 94304

Center for Analysis 1
Attn: Mr. jim Justice
13 Corporate Plaza
Newport Beach, CA 92660

W. J. Schafer Associates 1
Dr. R. Kappesser
Suite 800
1901 Fort Meyer Drive
Arlington, VA 22209

General Research Corp 1
Attn: Mr. Thomas Zakrzewski
7655 Old Springhouse Road
McLean, VA 22101

Air Force Weapons Laboratory 2
Attn: Lt Col D. Washburn
ARAA
Kirtland AFB, NM 87117

Karman Sciences Corp. 1
Attn: Dr. Walter E. Ware
1500 Garden of the Gods Road
P.O. Box 7463
Colorado Springs, CO 80933

MRJ, Inc. 1
10400 Eaton Place
Suite 300
Fairfax, VA 22030

Photon Research Associates 1
Attn: mr. Jim Myer
P.O. Box 1318
La Jolla, CA 92038

Rockwell International 1
Attn: Russell Loftman (Space Systems Group)
(Mail Code - SL56)
12214 Lakewood Blvd.
Downey, CA 90241

Science Applications, Inc. 1
Attn: Mr. Richard Ryan
3 Preston Court
Bedford, MA 01730

U.S. Army Missile Command 1
Attn: DRSMI-RAS/Mr. Fred Haak
Redstone Arsenal, AL

Naval Electronic Systems Command 1
Attn: Mr. Charles Good
PME_106-4
National Center I
Washington, DC 20360

Lockheed Palo Alto Research Laboratory 2
Attn: Dr. J. N. Aubrun, 0/52-56
3251 Hanover Street
Palo Alto, California 94304-1187

U.S. Army/DARCOM 1
Attn: Mr. Bernie Chasnov
AMC Bldg
5001 Eisenhower Ave
Alexandria, VA 22333

Defense Documentation Center 1
Cameron Station
Alexandria, VA 22314

Honeywell Inc. 2
Attn: Dr. Thomas B. Cunningham
Attn: Dr. Michael F. Barrett
2600 Ridgway Parkway MN 17-2375
Minneapolis, MN 55413

NASA Marshal Space Flight Center 2
Attn. Dr. J. C. Blair, ED01
Henry B. Waites
Marshal Space Flight Center, AL 35812

TRW
Attn: Robert Benhabib
Bldg 82/2024
One Space Park
Redondo Beach, CA 90278

NASA Langley Research Center 1
Attn: Dr. L. Pinson
MS - 230
Hampton, VA 23665

MIT/Lincoln Laboratory
ATTN: Dr. D. Hyland
P. O. Box 73
Lexington MA 02173 1

MIT/Lincoln Laboratory
ATTN: Dr. N. Smith
P. O. Box 73
Lexington MA 02173 11

Control Dynamics Co.
ATTN; Dr. Sherman Seltzer
Suite 1414 Executive Plaza
555 Sparkman Drive
Huntsville AL 35805 1

MISSION
of
Rome Air Development Center

RADC plans and executes research, development, test and selected acquisition programs in support of Command, Control Communications and Intelligence (C^3I) activities. Technical and engineering support within areas of technical competence is provided to ESD Program Offices (POs) and other ESD elements. The principal technical mission areas are communications, electromagnetic guidance and control, surveillance of ground and aerospace objects, intelligence data collection and handling, information system technology, ionospheric propagation, solid state sciences, microwave physics and electronic reliability, maintainability and compatibility.